

Diss. ETH No. 20574

**New Analysis Method to Confirm the Upper Limit
of the Branching Ratio $\mathcal{B}(\mu^+ \rightarrow e^+ + \gamma)$
from the MEG Experiment**

A dissertation submitted to
ETH ZURICH
for the degree of
DOCTOR OF SCIENCES

presented by
JEANINE ADAM
Dipl. Phys. ETH
born on March 23, 1985
citizen of Oberdorf SO

accepted on the recommendation of

| | |
|------------------------------|-------------|
| Prof. Dr. Günther Dissertori | examiner |
| Prof. Dr. Klaus Kirch | co-examiner |
| Prof. Dr. André Schöning | co-examiner |

2012

Abstract

The Standard Model of particle physics does not allow lepton flavor violating decays of charged leptons as neutrinos are supposed to be massless. However, as recent experiments have shown that neutrinos have a tiny non-vanishing mass, such decays of charged leptons are in principle possible via neutrino oscillations. The expected branching ratios are extremely small so that observations of lepton flavor violating decays of charged leptons would be impossible with current experimental methods. During the last years, new theoretical models have been developed that describe physics beyond the Standard Model. It is widely expected that such models can answer the open questions in particle physics as, for example, the matter-antimatter asymmetry. Some of these new theories predict branching ratios for the lepton flavor violating decays of charged leptons that can be measured with state-of-the-art experimental methods. An observation of such a lepton flavor violating decay would be an important hint for the existence of physics beyond the Standard Model.

An international collaboration has recently developed a high precision experiment, the so-called MEG experiment, to search for the lepton flavor violating decay $\mu^+ \rightarrow e^+ + \gamma$. The MEG collaboration is aiming for a sensitivity of 10^{-13} , which would lower the previously best upper limit of the branching ratio $\mathcal{B}(\mu^+ \rightarrow e^+ + \gamma)$ by two orders of magnitude. The MEG experiment started physics data taking in 2008 and the analysis of the combined data sets collected in 2009 and 2010 results in a branching ratio of $\mathcal{B}(\mu^+ \rightarrow e^+ + \gamma) < 2.4 \cdot 10^{-12}$ (90 % C.L.), which is the most stringent limit on this decay to date.

This thesis deals with various aspects of the MEG experiment including the experimental apparatus and physics analysis. The results presented in this thesis are based on data collected during the data taking runs of 2009 and 2010.

Improvements of the MEG drift chamber system concerning the pressure control system, the high voltage system, and the geometrical alignment to enhance the performance stability and the measurement accuracy are detailed in the first part of this thesis. Furthermore, a measuring technique to determine the timing resolution of a DRS4 chip with a precision of 3 ps is proposed. The viability of this method is shown by studying the influence of several parameters on the timing resolution as, for example, the influence of electronic noise. In order to analyze the performance of the liquid xenon detector under variable beam conditions, a new monitoring tool based on a neutron generator was applied for the first time in 2010. In this thesis, the data analysis methods of this monitoring tool are discussed and the results are presented.

The second part of this thesis proposes analysis methods to verify that the detection and analysis processes of the MEG experiment behave as expected. In particular, a new analysis method based on goodness of fit checks is discussed that verifies the consistency of measured event distributions and background probability density functions. In addition, event distributions are studied to identify unexpected dependencies or event clusters. Finally, to confirm the results obtained with the official MEG analysis, all information about the collected events are transformed from the multidimensional parameter space to the one-dimensional space of a discriminant variable, namely the relative signal likelihood. In this thesis, new analysis methods based on the relative signal likelihood are proposed to calculate the confidence interval limits of the branching ratio $\mathcal{B}(\mu^+ \rightarrow e^+ + \gamma)$. First, a cut analysis is detailed that can be performed much quicker than the official MEG analysis. The cut analysis results in a branching ratio of $\mathcal{B}(\mu^+ \rightarrow e^+ + \gamma) < 2.9 \cdot 10^{-12}$ (90 % C.L.) for the combined 2009 and 2010 data sets and confirms therefore the result of the official MEG analysis. Second, an alternative analysis method is proposed that uses a maximum likelihood analysis and the Feldman-Cousins unified approach with profile likelihood ordering. The alternative analysis method is more than 400 times faster than the official MEG analysis method and results in a branching ratio of $\mathcal{B}(\mu^+ \rightarrow e^+ + \gamma) < 2.4 \cdot 10^{-12}$ (90 % C.L.) for the combined data sets of 2009 and 2010. Therefore, the newly proposed analysis method provides the same confidence interval limit as the official MEG analysis method.

Zusammenfassung

Sogenannte Lepton-Flavor verletzende Zerfälle von geladenen Leptonen sind im Standardmodell der Teilchenphysik nicht erlaubt, da Neutrinos als masselos angesehen werden. Neuste Experimente haben jedoch gezeigt, dass Neutrinos eine kleine, nicht verschwindende Masse besitzen. Entsprechend sind Lepton-Flavor verletzende Zerfälle von geladenen Leptonen mittels Neutrinooszillationen prinzipiell möglich. Die erwarteten Werte für die jeweiligen Verzweigungsverhältnisse sind jedoch äusserst klein und können mit heutigen experimentellen Messmethoden nicht beobachtet werden. In den letzten Jahren wurden neue theoretische Modelle entwickelt, welche neue Physik jenseits des Standardmodells beschreiben. Diese Theorien sollen die noch ungeklärten Fragen der Teilchenphysik beantworten, beispielsweise der Grund für die Materie-Antimaterie Asymmetrie. Manche dieser Theorien prognostizieren Verzweigungsverhältnisse für Lepton-Flavor verletzende Zerfälle von geladenen Leptonen, die mit neusten experimentellen Methoden nachgewiesen werden könnten. Die Entdeckung eines solchen Zerfalls wäre ein wichtiger Hinweis dafür, dass neue Physik jenseits des Standardmodells existiert.

Eine internationale Kollaboration untersucht derzeit den Lepton-Flavor verletzenden Zerfall $\mu^+ \rightarrow e^+ + \gamma$ mittels eines am Paul Scherrer Institut aufgebauten Hochpräzisionsexperiments (MEG Experiment). Das Ziel der MEG Kollaboration ist es, eine Sensitivität von 10^{-13} zu erreichen, um die bisherig beste Obergrenze für das Verzweigungsverhältnis $\mathcal{B}(\mu^+ \rightarrow e^+ + \gamma)$ um zwei Grössenordnungen zu verbessern. Das MEG Experiment startete 2008 mit der Datenaufnahme und die Analyse der kombinierten Daten von 2009 und 2010 resultiert in ein Verzweigungsverhältnis von $\mathcal{B}(\mu^+ \rightarrow e^+ + \gamma) < 2.4 \cdot 10^{-12}$ (90 % C.L.), welches die momentan genaueste Obergrenze für dieses Verzweigungsverhältnis darstellt.

Diese Arbeit beinhaltet verschiedene Aspekte des MEG Experiments und betrifft sowohl den Detektor als auch die Datenanalyse. Die Resultate, welche in dieser Arbeit präsentiert werden, basieren auf den Daten von 2009 und 2010.

Im ersten Teil dieser Arbeit werden Verbesserungen des MEG Driftkammernsystems beschrieben, welche das Druckkontrollsystem, das Hochspannungssystem und die optische Vermessung betreffen. Des Weiteren wird eine Messtechnik vorgestellt, welche die Zeitauflösung eines DRS4 Chips mit einer Genauigkeit von 3 ps bestimmt. Die Messtechnik wird anschliessend benutzt, um den Einfluss von verschiedensten Parametern auf die Zeitauflösung zu untersuchen, wie beispielsweise der Einfluss von elektronischem Rauschen. Im Jahr 2010 wurde zum ersten Mal eine Überwachungsmethode eingesetzt, welche auf einem Neutronengenerator beruht und die Leistungsfähigkeit des MEG Photonendetektors bei verschiedenen Strahlintensitäten

überprüft. In dieser Arbeit werden die Datenanalysetechniken dieser Überwachungsmethode diskutiert und deren Resultate vorgestellt.

Um zu überprüfen, ob die Detektions- und Analyseprozesse des MEG Experiments richtig funktionieren, werden im zweiten Teil dieser Arbeit verschiedene Analysemethoden diskutiert. Insbesondere wird eine Analysemethode basierend auf sogenannten Goodness-of-Fit-Tests besprochen, welche die Konsistenz der gemessenen Ereignisverteilungen und Wahrscheinlichkeitsdichten des Untergrunds überprüft. Zusätzlich werden die gemessenen Ereignisverteilungen auf unerwartete Abhängigkeiten oder Ereignisanhäufungen untersucht. Zuletzt werden die Resultate der offiziellen MEG Analyse überprüft, indem die Informationen über die gemessenen Ereignisse vom mehrdimensionalen Parameterraum in den eindimensionalen Raum der relativen Signalwahrscheinlichkeit transformiert werden. In dieser Arbeit werden zwei Analysemethoden vorgestellt, welche die Grenzen des Konfidenzintervalls für das Verzweigungsverhältnis $\mathcal{B}(\mu^+ \rightarrow e^+ + \gamma)$ berechnen. Beide Methoden beruhen auf der relativen Signalwahrscheinlichkeit. Zuerst wird eine sehr schnelle Cut-Analyse vorgestellt. Diese Cut-Analyse resultiert in ein Verzweigungsverhältnis von $\mathcal{B}(\mu^+ \rightarrow e^+ + \gamma) < 2.9 \cdot 10^{-12}$ (90 % C.L.) für die kombinierten Daten von 2009 und 2010. Die Cut-Analyse bestätigt daher das Resultat der offiziellen MEG Analyse. Anschliessend wird eine alternative Analysemethode diskutiert, welche eine Maximum-Likelihood-Analyse mit dem Ansatz von Feldman-Cousins kombiniert. Die alternative Analysemethode ist über 400 mal schneller als die offizielle MEG Analyse und ergibt ein Verzweigungsverhältnis von $\mathcal{B}(\mu^+ \rightarrow e^+ + \gamma) < 2.4 \cdot 10^{-12}$ (90 % C.L.) für die kombinierten Daten von 2009 und 2010. Die neu eingeführte alternative Analysemethode liefert entsprechend das gleiche Resultat wie die offizielle MEG Analyse.

Contents

| | |
|-----------------------------------------------------------------------------|------------|
| Abstract | III |
| Zusammenfassung | V |
| 1 Introduction | 1 |
| 1.1 Theoretical Background | 2 |
| 1.1.1 The Standard Model of Particle Physics | 2 |
| 1.1.2 Neutrino Masses | 4 |
| 1.1.3 Physics Beyond the Standard Model | 5 |
| 1.2 The $\mu^+ \rightarrow e^+ + \gamma$ Search | 6 |
| 1.2.1 Past $\mu^+ \rightarrow e^+ + \gamma$ Search Experiments | 7 |
| 1.2.2 Event and Background Signature | 9 |
| 1.2.3 Requirements of the $\mu^+ \rightarrow e^+ + \gamma$ Search | 9 |
| 1.3 Related Work | 10 |
| 1.4 Thesis Outline | 11 |
| I Experimental Apparatus | 13 |
| 2 The MEG Experiment | 15 |
| 2.1 Detector Overview | 15 |
| 2.2 Beam and Target | 16 |
| 2.3 Positron Spectrometer | 17 |
| 2.3.1 COBRA Magnet | 18 |
| 2.3.2 Drift Chamber System | 19 |

| | | |
|----------|---------------------------------------------------------------------------|-----------|
| 2.3.3 | Timing Counters | 21 |
| 2.4 | Photon Detector | 21 |
| 2.5 | Electronics and Data Acquisition | 24 |
| 2.5.1 | Data Acquisition System | 24 |
| 2.5.2 | Trigger | 24 |
| 2.5.3 | Domino Ring Sampler | 25 |
| 2.5.4 | Slow Control | 25 |
| 2.6 | Simulation and Analysis Software | 26 |
| 2.7 | Calibration and Monitoring Hardware | 27 |
| 2.7.1 | Stationary Calibration Devices inside the Liquid Xenon Detector | 27 |
| 2.7.2 | Cockcroft-Walton Proton Accelerator | 28 |
| 2.7.3 | Charge Exchange Calibration Apparatus | 28 |
| 2.7.4 | Neutron Generator | 29 |
| 2.8 | Data Taking | 30 |
| 2.8.1 | Data Taking at the Paul Scherrer Institute | 30 |
| 2.8.2 | Data Taking Periods | 30 |
| 2.8.3 | Detector Performance | 32 |
| 2.9 | Summary | 32 |
| 3 | Drift Chamber System | 35 |
| 3.1 | Pressure Control System | 35 |
| 3.2 | High Voltage System | 38 |
| 3.3 | Optical Survey | 41 |
| 3.4 | Summary | 45 |
| 4 | DRS4 Chip | 47 |
| 4.1 | Timing Resolution Measurements | 47 |
| 4.1.1 | Timing Calibration | 47 |
| 4.1.2 | Measuring Principle | 48 |
| 4.1.3 | Results | 50 |
| 4.2 | Influence of Clock Cables | 54 |
| 4.3 | Summary | 57 |

| | | |
|-----------|--------------------------------------------------------------------|-----------|
| 5 | Liquid Xenon Monitoring with a Neutron Generator | 59 |
| 5.1 | Experimental Setup | 59 |
| 5.2 | Data Analysis | 60 |
| 5.3 | Dead Channel Recovery | 63 |
| 5.4 | Summary | 64 |
| | | |
| II | Physics Analysis | 67 |
| | | |
| 6 | $\mu^+ \rightarrow e^+ + \gamma$ Search Analysis | 69 |
| 6.1 | Definitions | 69 |
| 6.1.1 | Kinematic Variables | 70 |
| 6.1.2 | Data Sets | 70 |
| 6.1.3 | Pre-Selection | 71 |
| 6.1.4 | Blind Box | 71 |
| 6.1.5 | Analysis Window | 72 |
| 6.1.6 | Estimations from Sideband Data | 73 |
| 6.2 | Maximum Likelihood Analysis | 74 |
| 6.3 | Probability Density Functions | 75 |
| 6.3.1 | Signal | 75 |
| 6.3.2 | Radiative Muon Decay | 77 |
| 6.3.3 | Accidental Background | 77 |
| 6.4 | Confidence Interval | 78 |
| 6.5 | Normalization | 80 |
| 6.6 | Sensitivity | 81 |
| 6.6.1 | Expected Confidence Interval Limit | 81 |
| 6.6.2 | Results of the Timing Sideband Analysis | 83 |
| 6.7 | Results of the 2009 and 2010 Data Analysis | 84 |
| 6.7.1 | Results of the Maximum Likelihood Analysis | 84 |
| 6.7.2 | Results of the Confidence Level Calculation | 85 |
| 6.8 | Systematic Uncertainties | 89 |
| 6.9 | Summary | 91 |

| | | |
|----------|-------------------------------------------------------------------------------------------------------|------------|
| 7 | Event and Background Distribution Checks | 93 |
| 7.1 | Background Distributions | 93 |
| 7.1.1 | Goodness of Fit Methods | 94 |
| 7.1.2 | Accidental Background Probability Density Function Validation using Timing Sideband Data | 96 |
| 7.1.3 | Background Distribution in the Analysis Window | 97 |
| 7.2 | Event Distributions | 100 |
| 7.2.1 | Definition of High Ranked Events | 100 |
| 7.2.2 | Event Distributions of the 2009 and 2010 Data Sets | 100 |
| 7.3 | Summary | 105 |
| 8 | Relative Signal Likelihood Analysis | 107 |
| 8.1 | The Relative Signal Likelihood R_{sig} | 107 |
| 8.1.1 | Probability Density Functions of R_{sig} | 108 |
| 8.1.2 | The R_{sig} Condition | 109 |
| 8.1.3 | Goodness of Fit Checks | 110 |
| 8.2 | The R_{sig} Cut Analysis | 114 |
| 8.2.1 | Cut Analysis Method | 114 |
| 8.2.2 | Results of the Cut Analysis | 116 |
| 8.3 | The R_{sig} Alternative Analysis | 119 |
| 8.3.1 | Basic Idea | 119 |
| 8.3.2 | Expected Background | 121 |
| 8.3.3 | Analysis Method | 121 |
| 8.3.4 | Sensitivity | 124 |
| 8.3.5 | Uncertainties | 127 |
| 8.3.6 | Results of the R_{sig} Alternative Analysis | 129 |
| 8.3.7 | Comparison of Results | 133 |
| 8.3.8 | Prospects | 133 |
| 8.4 | Summary | 136 |
| 9 | Conclusion and Outlook | 139 |
| A | Graphs of the Event and Background Distribution Checks | 143 |

| | |
|-------------------------|------------|
| List of Figures | 155 |
| List of Tables | 159 |
| Bibliography | 161 |
| Acknowledgements | 169 |
| Curriculum Vitae | 171 |

Chapter 1

Introduction

The Standard Model of particle physics describes all known elementary particles as well as their interactions. The elementary particles are classified in three flavor generations. It is experimentally proven that flavor violating processes exist, namely in the quark sector and in the neutral lepton sector. But until now, no flavor violating process has been observed in the charged lepton sector composed of the electron (e), the muon (μ), and the tau particle (τ). This means that lepton flavor violating decays of charged leptons such as $\mu \rightarrow e + \gamma$, $\mu \rightarrow e + e + e$, $\tau \rightarrow e + \gamma$, or $\tau \rightarrow \mu + \gamma$ have never been observed.

In the Standard Model, the neutrino masses are supposed to be zero. As a consequence, lepton flavor violating processes are forbidden and the lepton flavor numbers are conserved. Even if neutrino masses are introduced, the expected branching ratios for such processes are strongly suppressed due to small neutrino masses. It is therefore not possible to observe lepton flavor violating decays of charged leptons with current measuring techniques.

During the last years, new theories beyond the Standard Model became more important as it is expected that such theories may answer the open questions of particle physics such as the matter-antimatter asymmetry. Even though different experiments are trying to prove the existence of such theoretical models, no evidence for new physics has been found so far. However, such new theories predict branching ratios for lepton flavor violating decays of charged leptons that are measurable with experimental methods. The search for lepton flavor violating decays of charged leptons is therefore equivalent to the search for new physics beyond the Standard Model.

The decay of an antimuon¹ into a positron and a photon ($\mu^+ \rightarrow e^+ + \gamma$) is one of the simplest lepton flavor violating processes. In 1999, the best upper limit of the branching ratio $\mathcal{B}(\mu^+ \rightarrow e^+ + \gamma)$ was found by the MEGA experiment and was given by $\mathcal{B}(\mu^+ \rightarrow e^+ + \gamma) < 1.2 \cdot 10^{-11}$ at 90% C.L. [1]. In the same year, a research proposal [2] was approved by the Research Committee for Particle Physics of the Paul Scherrer Institute (PSI, [3]) in Switzerland. An international collaboration called MEG (“Muon to Electron and Gamma”, [4]) of approximately 60 physicists from Italy, Japan, Russia, Switzerland, and the United States

¹For the remainder of this thesis, the term “muon” will be used even if an antimuon is meant.

started to develop a new high precision experiment to search for the decay $\mu^+ \rightarrow e^+ + \gamma$. The goal of the MEG collaboration is to lower the limit of the branching ratio found by the MEGA experiment by two orders of magnitude to 10^{-13} . The aimed sensitivity of the MEG experiment allows to achieve a branching ratio $\mathcal{B}(\mu^+ \rightarrow e^+ + \gamma)$ that is predicted by new theoretical models. In other words, the MEG experiment will either observe the decay $\mu^+ \rightarrow e^+ + \gamma$ and therefore prove the existence of new physics beyond the Standard Model or it will find a new limit of the branching ratio $\mathcal{B}(\mu^+ \rightarrow e^+ + \gamma)$ that will put stringent constraints on the allowed parameter space of new theories.

This thesis deals with various aspects of the MEG experiment including the experimental apparatus and physics analysis. This thesis focuses on improvements of the MEG drift chamber system, the timing resolution of a DRS4 chip, and a neutron generator monitoring tool for the MEG liquid xenon detector. Furthermore, goodness of fit checks are performed and event distributions are studied. Finally, new analysis methods based on the relative signal likelihood are proposed to calculate the confidence interval limits of the branching ratio $\mathcal{B}(\mu^+ \rightarrow e^+ + \gamma)$ and to confirm the results obtained with the official MEG analysis.

The remainder of this chapter is structured as follows: The theoretical background about Standard Model, neutrino masses, and physics beyond the Standard Model is detailed in Section 1.1. An overview of past experiments searching for the decay $\mu^+ \rightarrow e^+ + \gamma$, the event and background signature, and the requirements to search for this decay are presented in Section 1.2. Section 1.3 gives an overview of experiments searching for other lepton flavor violating decays of charged leptons. Finally, Section 1.4 describes the structure of this thesis.

1.1 Theoretical Background

The theoretical background of the lepton flavor violating decay $\mu^+ \rightarrow e^+ + \gamma$ in the Standard Model, in the Standard Model including neutrino masses, and in theoretical models about physics beyond the Standard Model is detailed in Section 1.1.1, Section 1.1.2, and Section 1.1.3, respectively. This section describes commonly known particle physics models. For general references for the Standard Model of particle physics, neutrino physics, and supersymmetric theories, the reader is referred to [5–7].

1.1.1 The Standard Model of Particle Physics

The Standard Model (SM) of particle physics describes the known elementary particles and their interactions. To date, 12 elementary spin 1/2 fermions (particles with half integer spin) are known, namely six leptons (electron (e), electron neutrino (ν_e), muon (μ), muon neutrino (ν_μ), tau (τ), tau neutrino (ν_τ)) and six quarks (up (u), down (d), strange (s), charm (c),

bottom (b), top (t)). These fermions are classified in three flavor generations:

$$\begin{array}{rcccl}
 \text{Quark} & \begin{pmatrix} u \\ d \end{pmatrix} & \begin{pmatrix} c \\ s \end{pmatrix} & \begin{pmatrix} t \\ b \end{pmatrix} & \\
 \text{Lepton} & \begin{pmatrix} \nu_e \\ e \end{pmatrix} & \begin{pmatrix} \nu_\mu \\ \mu \end{pmatrix} & \begin{pmatrix} \nu_\tau \\ \tau \end{pmatrix} & \\
 \text{Generation} & I & II & III &
 \end{array}$$

The SM also describes the interactions between the fermions, namely the electromagnetic, the weak, and the strong interaction. All interactions are carried by spin 1 gauge bosons (particles with integer spin). The photon (γ) is the gauge boson of the electromagnetic interaction, the W^\pm - and Z^0 -bosons are the gauge bosons of the weak interaction, and eight gluons are the gauge bosons of the strong interaction. The gravitational interaction is not described by the SM and a corresponding gauge boson (“graviton”) has not been observed so far. The gauge theory of the SM is therefore described by the group

$$\text{SU}(3)_C \times \text{SU}(2)_L \times \text{U}(1)_Y \quad (1.1)$$

where $\text{SU}(3)_C$ describes the strong interaction and $\text{SU}(2)_L \times \text{U}(1)_Y$ describes the unification of the electromagnetic and the weak interaction (electroweak interaction). An open question of the SM of particle physics is why elementary particles are massive. In the particle physics community, the most popular theory is the Higgs mechanism, which states that the electroweak group is spontaneously broken. This theory postulates a new particle, namely the Higgs boson. The ATLAS and CMS experiments at the Large Hadron Collider (LHC) at CERN have recently discovered a new particle with a mass near 125 GeV that could be the Higgs boson [8].

As mentioned before, quarks and leptons are classified in three flavor generations. It is experimentally verified that flavor-violating processes occur in the quark sector. They are described by the unitary Cabibbo-Kobayashi-Maskawa (CKM) matrix V with

$$\begin{pmatrix} d' \\ s' \\ b' \end{pmatrix} = \begin{pmatrix} V_{ud} & V_{us} & V_{ub} \\ V_{cd} & V_{cs} & V_{cb} \\ V_{td} & V_{ts} & V_{tb} \end{pmatrix} \cdot \begin{pmatrix} d \\ s \\ b \end{pmatrix} \quad (1.2)$$

where the vector (d', s', b') denotes the weak interaction eigenstates (flavor eigenstates) and (d, s, b) denotes the mass eigenstates of the corresponding quarks. The probability of the transition from a quark i to another quark j is given by the square of the corresponding mixing matrix element $|V_{ij}|^2$.

As measurements of the neutrino masses only resulted in small upper bounds that are limited by the precision of the measurements, it was assumed for a long time that neutrinos are massless. As a consequence, the corresponding lepton mixing matrix is diagonal, that is, lepton flavor mixing is not allowed. Therefore, each lepton flavor number L_e , L_μ , and L_τ with

$$L_l = \begin{cases} 1 & \text{if } l^- \text{ or } \nu_l \\ -1 & \text{if } l^+ \text{ or } \bar{\nu}_l \\ 0 & \text{else} \end{cases} \quad l = e, \mu, \tau \quad (1.3)$$

is conserved in every process. Consequently, the lepton flavor violating decay $\mu^+ \rightarrow e^+ + \gamma$ is not allowed in the SM. Nevertheless, the SM predicts lepton flavor conserving decays of muons and various experiments proved their existence and measured the branching ratios. The most important muon decays with the corresponding branching ratios are listed in Table 1.1. The muon decay $\mu^- \rightarrow e^- + \bar{\nu}_e + \nu_\mu$ is known as Michel decay and $\mu^- \rightarrow e^- + \bar{\nu}_e + \nu_\mu + \gamma$ is the radiative muon decay.

Table 1.1: Muon decay modes and the corresponding branching ratios [9]. The μ^+ decay modes are charge conjugates of the listed decay modes.

| Muon Decay Mode | Branching Ratio | Reference |
|-------------------------------------------------------------|-------------------------------|-----------|
| $\mu^- \rightarrow e^- + \bar{\nu}_e + \nu_\mu$ | $\approx 100\%$ | |
| $\mu^- \rightarrow e^- + \bar{\nu}_e + \nu_\mu + \gamma$ | $(1.4 \pm 0.4)\%$ | [10] |
| $\mu^- \rightarrow e^- + \bar{\nu}_e + \nu_\mu + e^+ + e^-$ | $(3.4 \pm 0.4) \cdot 10^{-5}$ | [11] |

1.1.2 Neutrino Masses

In the SM, neutrinos are supposed to be massless. However, if neutrinos have a non-zero mass, their mass eigenstates and flavor eigenstates are connected via a non-diagonal matrix U with

$$\begin{pmatrix} \nu_e \\ \nu_\mu \\ \nu_\tau \end{pmatrix} = \begin{pmatrix} U_{e1} & U_{e2} & U_{e3} \\ U_{\mu1} & U_{\mu2} & U_{\mu3} \\ U_{\tau1} & U_{\tau2} & U_{\tau3} \end{pmatrix} \cdot \begin{pmatrix} \nu_1 \\ \nu_2 \\ \nu_3 \end{pmatrix} \quad (1.4)$$

where the vector $(\nu_e, \nu_\mu, \nu_\tau)$ denotes the flavor eigenstates and (ν_1, ν_2, ν_3) denotes the mass eigenstates of the corresponding neutrinos. The unitary matrix U is known as the Pontecorvo-Maki-Nakagawa-Sakata (PMNS) matrix. The probability to have a muon neutrino ν_μ in an electron neutrino ν_e beam at a distance L from the beam source (also referred to as “neutrino oscillation”) is given by [6]

$$P(\nu_e \rightarrow \nu_\mu) = \sin^2(\theta) \cdot \sin^2 \left(\frac{1.27 \cdot (\Delta m^2/\text{eV}^2) \cdot (L/\text{m})}{(E/\text{MeV})} \right) \quad (1.5)$$

with θ the mixing angle calculated from the PMNS matrix, Δm^2 the squared neutrino mass difference, and E the neutrino energy. An observation of such a neutrino oscillation $P(\nu_e \rightarrow \nu_\mu) > 0$ would imply a neutrino mass difference of $\Delta m^2 > 0$ and therefore non-zero neutrino masses.

During the last years, various experiments such as Super-Kamiokande [12], SNO [13], or Daya Bay [14] observed neutrino oscillations so that the assumption of massless neutrinos is no longer tenable. The presence of massive neutrinos and therefore neutrino oscillations enables the lepton flavor violating decay $\mu^+ \rightarrow e^+ + \gamma$. Figure 1.1 shows Feynman diagrams contributing to the decay $\mu^+ \rightarrow e^+ + \gamma$ in the SM with neutrino oscillations. The branching

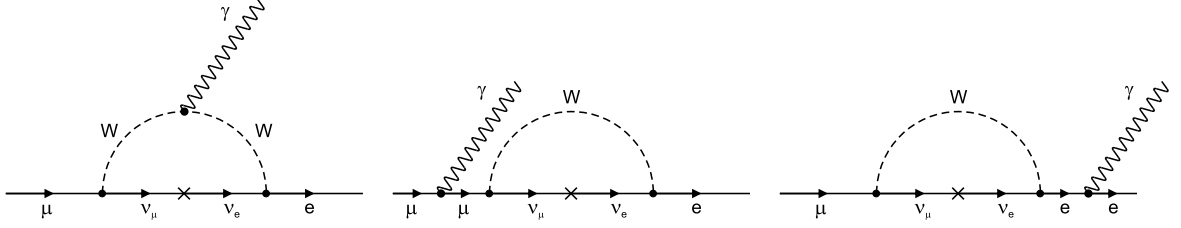


Figure 1.1: Feynman diagrams contributing to the decay $\mu^+ \rightarrow e^+ + \gamma$ in the SM with neutrino oscillations.

ratio $\mathcal{B}(\mu^+ \rightarrow e^+ + \gamma)$ is given by [15]

$$\mathcal{B}(\mu^+ \rightarrow e^+ + \gamma) = \frac{3}{32} \cdot \frac{\alpha}{\pi} \cdot \left(\frac{\Delta m^2}{M_W^2} \right)^2 \cdot \sin^2(\theta) \cdot \cos^2(\theta) \quad (1.6)$$

with M_W the mass of the W -boson, Δm^2 the squared neutrino mass difference, and $\sin^2(\theta) \cdot \cos^2(\theta)$ the mixing factor $\sin^2(\theta) \cdot \cos^2(\theta) = |\sum_i U_{\mu i} \cdot U_{ei}|^2$. The branching ratio for the lepton flavor violating decay $\mu^+ \rightarrow e^+ + \gamma$ is therefore extremely small for tiny neutrino mass differences [15]:

$$\begin{aligned} \mathcal{B}(\mu^+ \rightarrow e^+ + \gamma) &= 5 \cdot 10^{-48} \cdot (\Delta m^2 / \text{eV}^2)^2 \cdot \sin^2(\theta) \cdot \cos^2(\theta) \\ &\approx 10^{-55}. \end{aligned} \quad (1.7)$$

As a consequence, the lepton flavor violating decay $\mu^+ \rightarrow e^+ + \gamma$ as described in the SM with neutrino oscillations cannot be observed with experimental methods as the expected branching ratio is many orders of magnitude smaller than the reachable sensitivity of such experiments.

1.1.3 Physics Beyond the Standard Model

The SM of particle physics is a very successful model and was able to predict certain particles before they were actually observed. Nevertheless, the SM does not answer all open questions of particle physics. For example, the SM does not describe gravitation, it does not explain the matter-antimatter asymmetry, and it cannot answer the question what dark matter is. All those open questions lead to the assumption that there exists a universal theory beyond the SM that can provide the missing answers. During the last years, several theoretical extensions to the SM were developed such as grand unified theories (GUT) to unify all kinds of interactions at high energies or supersymmetric (SUSY) models that predict new supersymmetric particles. Even though particle physics experiments all over the world are trying to prove the existence of such models, no evidence for new physics beyond the SM has been found so far.

The simplest GUT model is the minimal SU(5) model. But as the predicted proton decay time is shorter than the experimental limit [16], the minimal SU(5) model is already excluded. Nevertheless, the combination of the minimal SU(5) model with SUSY is still not discarded. It was shown in [17] that the lepton flavor violating decay $\mu^+ \rightarrow e^+ + \gamma$ can be induced

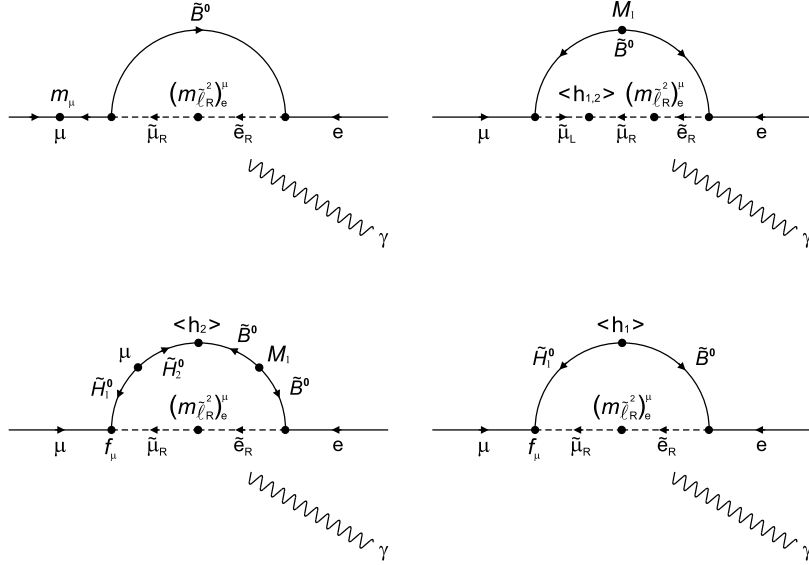


Figure 1.2: Feynman diagrams for the decay $\mu^+ \rightarrow e^+ + \gamma$ in the SU(5) SUSY GUT model. The supersymmetric particles $\tilde{\mu}_L$, $\tilde{\mu}_R$, \tilde{e}_R , \tilde{B}^0 , and \tilde{H}^0 are the left-handed smuon, right-handed smuon, right-handed selectron, bino, and neutral higgsino, respectively. The blobs on the lines and the corresponding terms are the mixing masses. The figure is adopted from [17].

by processes illustrated with Feynman diagrams shown in Fig. 1.2. In a certain parameter space, the expected branching ratio $\mathcal{B}(\mu^+ \rightarrow e^+ + \gamma)$ reaches up to 10^{-12} and is therefore one order of magnitude below the experimental limit from MEGA that is given by $1.2 \cdot 10^{-11}$ [1]. Lowering the experimental limit by one or two orders of magnitude can either prove the existence of physics beyond the SM or restrict the allowed parameter space.

The lepton flavor violation in a SO(10) SUSY GUT model is also discussed in the literature [18]. The SO(10) model has some advantages over SU(5) models such as the neutrino masses, which are naturally present in the SO(10) model. This model predicts branching ratios of lepton flavor violating muon decays that are just below the experimental limits. The results of the analysis presented in [18] are shown in Fig. 1.3. The MEG experiment will be able to test the currently discussed theoretical models and to put stringent constraints on them. The MEG experiment makes therefore an important contribution to the worldwide search for physics beyond the SM.

1.2 The $\mu^+ \rightarrow e^+ + \gamma$ Search

An overview of past experiments that searched for the lepton flavor violating decay $\mu^+ \rightarrow e^+ + \gamma$ is given in Section 1.2.1. In addition, the event and background signatures are described in Section 1.2.2 and the requirements of the $\mu^+ \rightarrow e^+ + \gamma$ search are listed in Section 1.2.3.

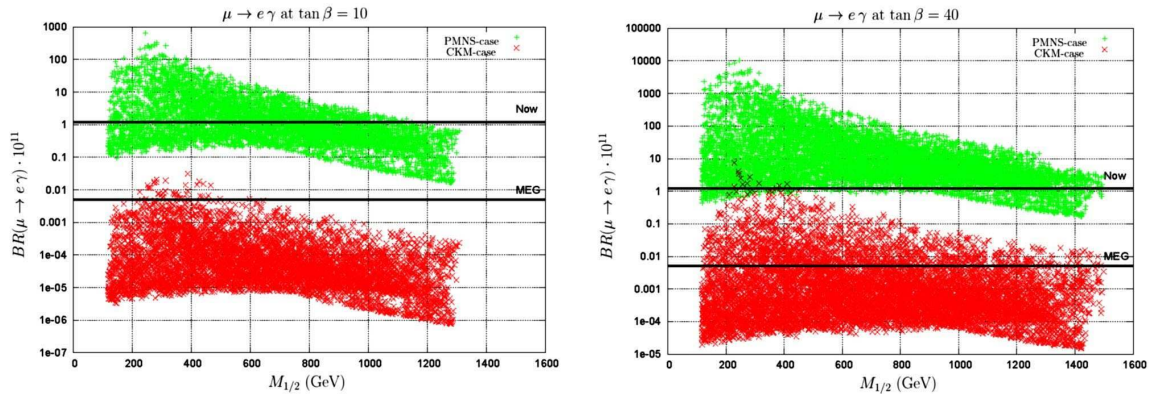


Figure 1.3: Branching ratio of the lepton flavor violating decay $\mu^+ \rightarrow e^+ + \gamma$ as a function of the unified gaugino mass $M_{1/2}$ in the SO(10) SUSY GUT model for two fixed values for $\tan\beta$. The parameter $\tan\beta$ is the ratio of the two vacuum expectation values of the two neutral Higgs bosons. Each plot shows two scenarios, namely the PMNS- and the CKM-case. The points of the scatter plots are obtained by scanning the SUSY GUT parameter space that is accessible with the LHC at CERN. The horizontal line with the label “Now” indicates the upper limit of the branching ratio $\mathcal{B}(\mu^+ \rightarrow e^+ + \gamma)$ found by MEGA and the line with the label “MEG” indicates the limit reachable by the MEG experiment. The plots originate from [18].

1.2.1 Past $\mu^+ \rightarrow e^+ + \gamma$ Search Experiments

The muon was discovered in cosmic radiation in 1937 [19]. At this time, it was not yet known that the muon is an elementary particle and it was assumed that the muon would decay in an electron and a photon if the muon is an excited state of the electron. The first experiment searching for the decay $\mu^+ \rightarrow e^+ + \gamma$ was made by Hincks and Pontecorvo in 1947 with cosmic ray muons [20]. They found an upper limit of the branching ratio $\mathcal{B}(\mu^+ \rightarrow e^+ + \gamma)$ of less than 10%. During the following years, the sensitivities of $\mu^+ \rightarrow e^+ + \gamma$ search experiments significantly improved due to the fact that the experiments had access to muons produced by accelerators. First, the experiments used muons produced by stopped pion beams. Later, the experiments directly used muon beams. The sensitivities of the experiments increased with better muon sources. However, to deal with the increased number of background events, $\mu^+ \rightarrow e^+ + \gamma$ search experiments require a good background rejection capability. Figure 1.4 shows the upper limits of the branching ratio $\mathcal{B}(\mu^+ \rightarrow e^+ + \gamma)$ obtained with past $\mu^+ \rightarrow e^+ + \gamma$ search experiments and the most important results are summarized in Table 1.2. Before the MEG experiment started physics data taking, the best upper limit of the branching ratio $\mathcal{B}(\mu^+ \rightarrow e^+ + \gamma)$ was provided by the MEGA experiment and was given by $1.2 \cdot 10^{-11}$ at 90% C.L. [1]. The MEG experiment is aiming a sensitivity of 10^{-13} , which would lower the limit of MEGA by two orders of magnitude.

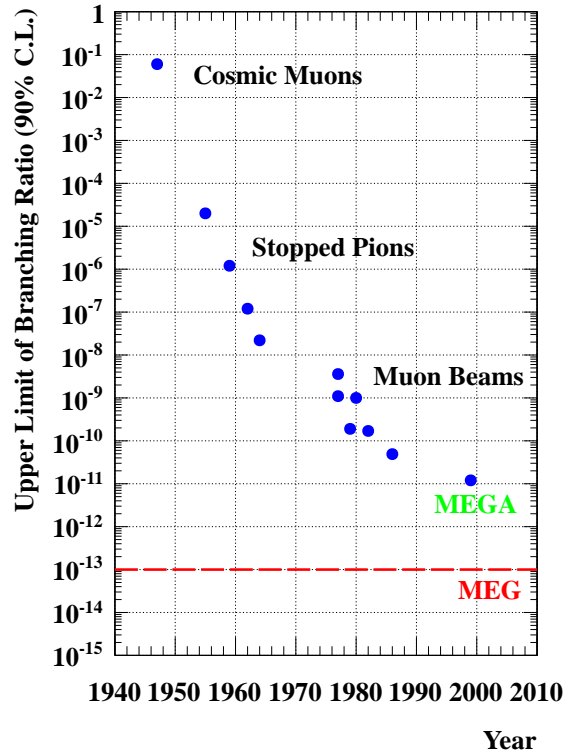


Figure 1.4: Upper limits of the branching ratio $\mathcal{B}(\mu^+ \rightarrow e^+ + \gamma)$ obtained with past experiments as a function of the publication year. The labels “Cosmic Muons”, “Stopped Pions”, and “Muon Beams” denote the techniques that were used by the experiments. The last entry corresponds to the result of the MEGA experiment. The aimed sensitivity of the MEG experiment is 10^{-13} and is indicated with a horizontal line.

Table 1.2: Overview of past $\mu^+ \rightarrow e^+ + \gamma$ search experiments. The name of the experiment or the location is listed with the publication year and the reached upper limit of the branching ratio $\mathcal{B}(\mu^+ \rightarrow e^+ + \gamma)$.

| Experiment/Place | Year | Upper Limit at 90 % C.L. | Reference |
|------------------|------|--------------------------|-----------|
| TRIUMF | 1977 | $3.6 \cdot 10^{-9}$ | [21] |
| SIN | 1980 | $1.0 \cdot 10^{-9}$ | [22] |
| LANL | 1982 | $1.7 \cdot 10^{-10}$ | [23] |
| Crystal Box | 1986 | $4.9 \cdot 10^{-11}$ | [24] |
| MEGA | 1999 | $1.2 \cdot 10^{-11}$ | [1] |

1.2.2 Event and Background Signature

As negatively charged muons would be captured by nuclei if they are stopped in the target, a positively charged muon beam is used for the MEG experiment. The muon beam is stopped in a target and the muons decay at rest. The signature of $\mu^+ \rightarrow e^+ + \gamma$ events is characterized by:

- The energies of the emitted positron and photon are equal to half of the muon mass, that is, $E_e = m_\mu/2 = 52.8 \text{ MeV}$ (positron energy) and $E_\gamma = m_\mu/2 = 52.8 \text{ MeV}$ (photon energy).
- Positron and photon are emitted back-to-back, that is, $\phi_{e\gamma} = 0 \text{ rad}$ (relative azimuthal angle) and $\theta_{e\gamma} = 0 \text{ rad}$ (relative polar angle). The definitions of $\phi_{e\gamma}$ and $\theta_{e\gamma}$ are explained in Chapter 6.
- Positron and photon are emitted coincident in time, that is, $t_{e\gamma} = 0 \text{ s}$ (relative timing).

There exist two kinds of background events for the event signature described before. The first one are radiative muon decays where neutrinos carry away only little energy. The kinematics of radiative muon decays are well known and it has been shown that the background of radiative muon decays is not a serious problem for the MEG experiment as long as detector resolutions similar to past $\mu^+ \rightarrow e^+ + \gamma$ search experiments are achieved [25]. The second kind of background events are accidental coincidences of a positron from a Michel decay and one or more overlapping photons with an energy of approximately 52.8 MeV from another source. This source might be radiative muon decays, annihilation-in-flight, or bremsstrahlung of positrons from Michel decays. The higher the muon stopping rate, the higher is the probability of accidental coincidences, and the more serious is the impact of this kind of background events. As a consequence, good background rejection capabilities and therefore excellent detector resolutions are necessary to search for the decay $\mu^+ \rightarrow e^+ + \gamma$. It has been shown that accidental coincidences are the dominant background for the MEG experiment and that they limit the reachable sensitivity [25].

1.2.3 Requirements of the $\mu^+ \rightarrow e^+ + \gamma$ Search

To be sensitive for the lepton flavor violating decay $\mu^+ \rightarrow e^+ + \gamma$ within three or four years of physics data taking, a high muon stopping rate is required. Unfortunately, the probability of accidental coincidences of positrons and photons increases quadratically with higher muon stopping rate. It was shown before that such accidental coincidences will limit the $\mu^+ \rightarrow e^+ + \gamma$ search of the MEG experiment. A pulsed muon beam is therefore not suited for the $\mu^+ \rightarrow e^+ + \gamma$ search. To have a high muon stopping rate and to minimize the accidental background, a high intense and continuous muon beam is required. In addition, the kinematics of positrons and photons have to be measured with high resolution. It was shown in [2] that the branching ratio of the accidental background \mathcal{B}_A is approximately given by the formula

$$\mathcal{B}_A \propto \delta E_e \cdot \delta t_{e\gamma} \cdot (\delta E_\gamma)^2 \cdot (\delta \Theta_{e\gamma})^2 \quad (1.8)$$

with δE_e , $\delta t_{e\gamma}$, δE_γ , and $\delta\Theta_{e\gamma}$ the resolutions of the positron energy, timing, photon energy, and opening angle, respectively. Therefore, it is especially important to have a high performance photon detector with a good energy resolution and a positron detector with a high performance even in a high rate environment. To meet the demands of the $\mu^+ \rightarrow e^+ + \gamma$ search, the MEG collaboration developed a high precision detector including new, innovative, and precise measuring methods and technologies. The experimental apparatus as well as calibration and monitoring methods are described in the first part of this thesis and the analysis techniques are explained in the second part.

1.3 Related Work

The search for physics beyond the SM is ongoing worldwide with different experiments. The LHC at CERN provides proton collisions with the currently highest energies. One of the purposes of the LHC is to discover the Higgs particle and answer the question why elementary particles are massive. In addition, the energies of the LHC are high enough to observe supersymmetric particles. The discovery of such particles would prove that physics beyond the SM exists. The search for new physics with high energies is called the “high energy frontier” of particle physics.

An alternative way to search for new physics is the so-called “high precision frontier”. Experiments at this frontier try to find small deviations from the SM, which requires extremely precise measurements. One experiment at this frontier is the nEDM experiment [26] at the PSI. This experiment is trying to measure the electric dipole moment of the neutron using a new ultra cold neutron source [27]. The measurement of a non-zero electric dipole moment could explain the matter-antimatter asymmetry in the universe.

Other experiments at the high precision frontier are searching for “forbidden” particle decays, that is, decays that are suppressed in the SM. An observation of such a decay at branching ratios larger than the SM expectations would be a proof for new physics. Lepton flavor violating decays of muons and tau particles are particularly well suited for such new physics searches as their final states are very simple. An overview of current and future charged lepton flavor violation experiments and the corresponding theoretical background is given in [28] and [29]. In the following, some of those experiments are introduced.

The most recent result in this field is provided by the MEG experiment in the channel $\mu^+ \rightarrow e^+ + \gamma$ as described in this thesis. In addition, a letter of intent for a new experiment, called Mu3e, searching for $\mu^+ \rightarrow e^+ + e^- + e^+$ was submitted to the PSI in January 2012 [30]. The goal of the Mu3e experiment is to reach a sensitivity of 10^{-16} for the branching ratio $\mathcal{B}(\mu^+ \rightarrow e^+ + e^- + e^+)$. Therefore, the Mu3e experiment would lower the current experimental upper limit of $1.0 \cdot 10^{-12}$ at 90 % C.L. found by the SINDRUM experiment [31] by four orders of magnitude. After developing and testing prototypes, the Mu3e experiment will be performed in two phases. In the first phase (2014-2017), the Mu3e experiment will use the existing beamlines of the PSI and reach with the provided stopping rate of $10^8 \mu^+/\text{s}$ a sensitivity of approximately 10^{-15} . For the second phase (after 2017), a new muon beam line has to be built at PSI to ensure stopping rates of $2 \cdot 10^9 \mu^+/\text{s}$. With this stopping rate, the

Mu3e experiment will be able to measure the branching ratio $\mathcal{B}(\mu^+ \rightarrow e^+ + e^- + e^+)$ with a sensitivity of 10^{-16} .

The $\mu \rightarrow e$ conversion on elements such as aluminium or titanium is another lepton flavor violating process that is used to search for new physics beyond the SM. There are two different experiments that submitted their letters of intend in 2007: the Mu2e experiment [32] at the Fermi National Accelerator Laboratory (Fermilab, [33]) and COMET (“COherent Muon to Electron Transition”, [34]) at the Japan Proton Accelerator Research Complex (J-PARC, [35]). Both experiments are going to measure the branching ratio $\mathcal{B}(\mu^- + Al \rightarrow e^- + Al)$ with a sensitivity better than 10^{-16} . There exist also plans for a future project called PRISM/PRIME (“Phase Rotated Intense Slow Muon Source” and “PRISM Mu E”, [36]) at the J-PARC that aims to measure the branching ratio $\mathcal{B}(\mu^- + Ti \rightarrow e^- + Ti)$ with a unprecedented sensitivity of 10^{-18} . The currently best experimental limit for $\mu \rightarrow e$ conversion was found by the SINDRUM II experiment and is given by $\mathcal{B}(\mu^- + Au \rightarrow e^- + Au) < 7 \cdot 10^{-13}$ at 90 % C.L. [37]. Therefore, the planned experiments would lower the experimental limit by four or six orders of magnitude.

The searches for lepton flavor violating processes with charged leptons in the channels $\mu^+ \rightarrow e^+ + \gamma$, $\mu^+ \rightarrow e^+ + e^- + e^+$, and $\mu \rightarrow e$ are testing a wide parameter space of theoretical models about new physics beyond the SM and are therefore complementary with the search for new physics at the LHC.

1.4 Thesis Outline

This thesis is divided into two parts: Part 1 covers the experimental apparatus and Part 2 includes physics analysis. The results presented in this thesis are based on data collected by the MEG experiment during the data taking runs of 2009 and 2010.

In Chapter 2, the MEG experiment is explained in general. After an introduction about the detector setup and the used coordinate systems, the features of the beamline and the target are highlighted. The innovative positron spectrometer is introduced and the liquid xenon photon detector is described. In addition, details about the electronics and data acquisition systems and the used simulation and analysis software are presented. Furthermore, calibration and monitoring tools are explained in detail. Finally, the chapter gives an overview of the physics data taking periods and the detector performances of the MEG experiment during the last few years.

Some aspects of the MEG drift chamber system are detailed in Chapter 3. In particular, the features of the automated pressure control system and the sophisticated high voltage system are highlighted. In addition, the optical survey of the drift chamber system and the target is explained and the newly adopted measuring method with corner cube reflectors is presented along with the achieved improvements.

In Chapter 4, a measuring method to determine the timing resolution of the DRS4 chip is proposed and the obtained results are presented. Furthermore, the impact of clock cables on the timing measurement of the MEG experiment is estimated.

The experimental setup of a liquid xenon monitoring tool using a neutron generator is described in Chapter 5. The data analysis techniques are detailed and the obtained results are presented. In addition, the neutron generator method is used to verify that the dead channel recovery algorithm to compensate broken photomultiplier tubes works as expected.

In Chapter 6, the $\mu^+ \rightarrow e^+ + \gamma$ search analysis of the MEG collaboration is detailed. In particular, the maximum likelihood analysis is explained, the probability density functions are introduced, and the calculation procedure to obtain the confidence interval is detailed. In addition, the methods for the normalization and sensitivity calculation are described and the results of the analysis of the data collected during 2009 and 2010 are presented. Finally, systematic uncertainties are discussed.

Goodness of fit tests are performed in Chapter 7 to verify that the used background probability density functions and the event distributions measured by the MEG experiment are consistent. In addition, the event distributions are studied to confirm that the detection and reconstruction processes are well understood. In particular, the focus is on events with a high likelihood to be a $\mu^+ \rightarrow e^+ + \gamma$ decay.

In Chapter 8, the definition of the relative signal likelihood is introduced, the corresponding probability density functions are presented, and goodness of fit checks are performed. A cut analysis based on the relative signal likelihood is proposed to calculate the confidence interval limits of the branching ratio $\mathcal{B}(\mu^+ \rightarrow e^+ + \gamma)$ and the obtained results are presented. In addition, an alternative analysis method is proposed that is also based on the relative signal likelihood. The goal of this analysis is to determine the confidence interval limits of the branching ratio $\mathcal{B}(\mu^+ \rightarrow e^+ + \gamma)$ and to confirm the results of the official analysis method of the MEG collaboration. The basic idea of the alternative analysis method is detailed and the expected background is estimated. The details of the alternative analysis are described and the expected sensitivity is calculated. Furthermore, the statistical and systematic uncertainties are discussed. The results of the alternative analysis method applied to the data collected in 2009 and 2010 are presented and compared with the results of the MEG collaboration. Finally, sensitivities that can be reached by the MEG experiment in the next few years are estimated.

Chapter 9 summarizes the obtained results and completes this thesis with some concluding remarks.

Part I

Experimental Apparatus

Chapter 2

The MEG Experiment

The search for the lepton flavor violating decay $\mu^+ \rightarrow e^+ + \gamma$ requires a continuous and high intense muon beam to suppress accidental background and to collect enough muon decays to be sensitive for the rare decay $\mu^+ \rightarrow e^+ + \gamma$. In addition, very precise measurements of the kinematic variables of both the positron and the photon are necessary. This chapter describes the experimental apparatus of the MEG experiment, which achieves sensitivities in the range of 10^{-13} for the branching ratio $\mathcal{B}(\mu^+ \rightarrow e^+ + \gamma)$.

Section 2.1 gives an overview of the MEG detector and introduces the used coordinate systems. The beamline and the target are explained in Section 2.2. The positron spectrometer and the photon detector are introduced in Section 2.3 and Section 2.4, respectively. Section 2.5 explains the data acquisition system, the trigger, the waveform digitizer, and the slow control used by the MEG experiment. The simulation and analysis software is detailed in Section 2.6. Calibration and monitoring tools are presented in Section 2.7. Finally, Section 2.8 gives an overview of the data taking periods during the last few years. The discussed techniques and specifications presented in this chapter originate from the MEG collaboration. The photographs shown in this chapter are provided by several collaborators.

2.1 Detector Overview

The MEG experiment is located at the Paul Scherrer Institute (PSI) in Villigen, Switzerland [3]. The PSI is an interdisciplinary research center, which provides the world's most intense continuous muon beams. After passing the MEG beam transport system, the muons are stopped in a thin target where they decay at rest. The emitted photons are detected with the world's largest liquid xenon scintillation detector and the kinematic variables of the positrons are measured with an innovative positron spectrometer. It consists of a special superconducting magnet called COBRA, a low-mass drift chamber system, and fast timing counters. Figure 2.1 shows a schema of the MEG detector with all important components.

The global MEG coordinate system (x, y, z) is also drawn in this figure. Its origin is defined as the center of the COBRA magnet. The z -axis corresponds to the beamline and the y -axis

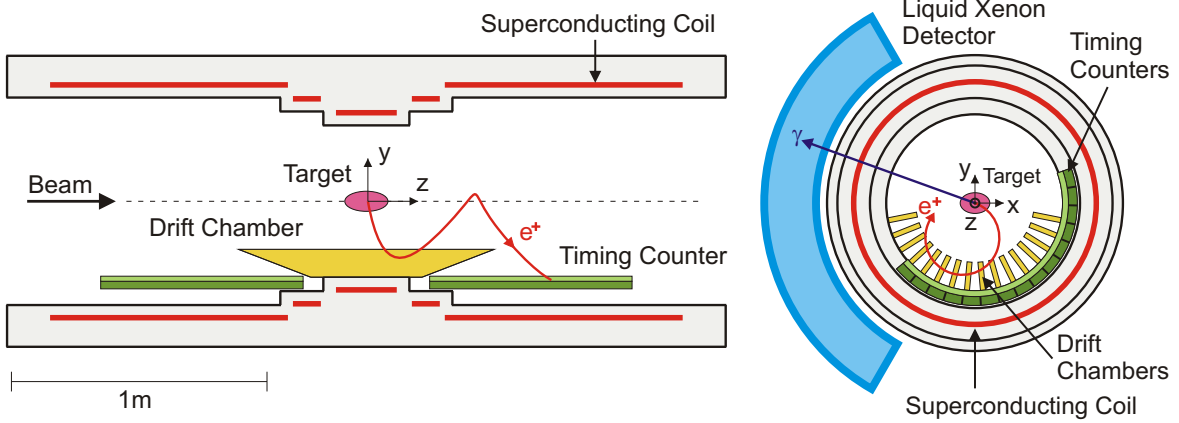


Figure 2.1: Schema of the MEG detector with the superconducting magnet COBRA, the drift chamber system, the timing counters, and the liquid xenon detector.

is the vertical axis describing the height. The x -axis is the missing axis of a right-handed rectangular coordinate system composed of y - and z -axis. In this coordinate system, θ and ϕ denote the polar and azimuthal angle, respectively.

An additional local coordinate system (u, v, w) is defined for the liquid xenon detector. The u -axis is identical to the z -axis, that is, the beam direction with origin at the center of the COBRA magnet. The v -axis corresponds to the inverted ϕ coordinate along the inner face¹ with origin at $y = 0$. The w -axis describes the depth in the liquid xenon detector. It corresponds to the radial direction in cylindrical coordinates with origin at the inner face.

2.2 Beam and Target

A high intense muon beam is required to search for the rare decay $\mu^+ \rightarrow e^+ + \gamma$ as the sensitivity increases with the number of observed muons. The consequence of a high intensity beam is an increased number of accidental coincidences. This is the reason why a continuous muon beam is better suited for the $\mu^+ \rightarrow e^+ + \gamma$ search than a pulsed one. As the PSI provides the world's most intense continuous muon beam, the MEG experiment is located there.

The proton ring cyclotron facility of the PSI produces a 590 MeV proton beam with a current of 2.2 mA. The proton beam is guided through two targets and the produced pions and muons are steered in several secondary beamlines. The MEG experiment uses the $\pi E5$ beam channel [38], which provides surface muons of 28 MeV/c. Those muons are produced by pions decaying at rest on the production target surface.

To ensure that the muon beam is stopped in the target with the desired stopping rate, the MEG collaboration developed a beam transport system. Figure 2.2 shows a schema of this system. A triplet of quadrupoles (Triplet I) focuses the beam to a Wien filter, which reduces

¹The inner face denotes the surface of the liquid xenon detector that is the closest to the COBRA magnet as explained in Section 2.4.

the positron contamination in the muon beam. A second quadrupole triplet (Triplet II) refocuses the beam to the collimator system and the so-called beam transport solenoid (BTS), which ensures a small beam spot size at the MEG target position. A momentum degrader made of $300\ \mu\text{m}$ mylar is installed inside the BTS to reduce the muon momentum. This degrader ensures that the muon beam is stopped in the target with a stopping rate of $3 \cdot 10^7\ \mu^+/\text{s}$.

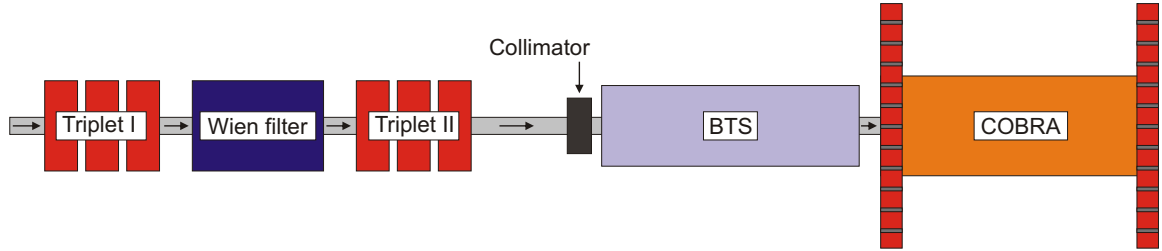


Figure 2.2: Schema of the MEG beam transport system with quadrupole triplet, Wien filter, second quadrupole triplet, collimator, and BTS. In addition, the COBRA magnet and the compensation coils are shown.

The MEG target consists of an ellipsoidal polyethylene foil with a major axis of 200.5 mm, a minor axis of 79.8 mm, and a thickness of $205\ \mu\text{m}$. The target foil is mounted inside the COBRA magnet in a ROHACELL frame. It has a slanted angle of 20.5° with respect to the beam axis. This mounting reduces the background produced by positron annihilation and minimizes multiple scattering. A picture of the MEG target before the installation in the detector is shown in Fig. 2.3. The holes in the target foil are used to check the vertex reconstruction and to align the target position with particle tracks. The drawn crosses are necessary to determine the target position with optical survey methods as described in Section 3.3.

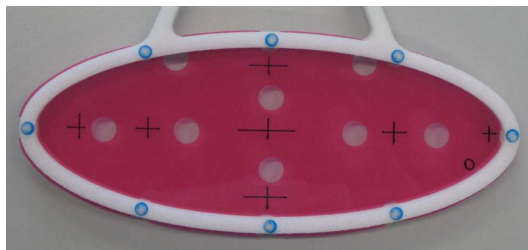


Figure 2.3: Picture of the MEG target before installation in the detector.

2.3 Positron Spectrometer

The MEG collaboration developed an innovative positron spectrometer [39] to measure the momentum, the direction, and the timing of the emitted positrons with high resolution.

The positron spectrometer consists of the superconducting magnet COBRA, a drift chamber system, and timing counters, which are detailed in the following.

2.3.1 COBRA Magnet

COBRA (COntant Bending RAdius) is a specially designed superconducting magnet composed of five coils with three different radii [40]. Figure 2.4 shows a picture of the COBRA magnet before detector assembly and a schema of the magnet design. The step structure of the coils produce a gradient magnetic field of 1.27 T at the center and 0.49 T at the edge of the magnet.

The use of COBRA instead of a normal uniform magnet has important advantages for the MEG experiment. First, positrons emitted close to 90° are swept away very quickly from the sensitive detector volume by the COBRA field. In a solenoid magnet, such positrons undergo many turns inside the detector, which causes worse resolutions due to reconstruction difficulties. Second, positrons with the same momentum but different emission angles follow tracks with constant projected bending radii. In a uniform magnet, the bending radii of monochromatic positrons depend on the emission angles. The advantages of COBRA are illustrated in Fig. 2.5.

To ensure a high performance of the photomultiplier tubes (PMTs) of the liquid xenon detector, which is described in Section 2.4, two normal conducting compensation coils are necessary. They are shown in Fig. 2.4. The task of those compensation coils is to reduce the stray field of the main magnet to 50 Gauss around the position of the liquid xenon detector.

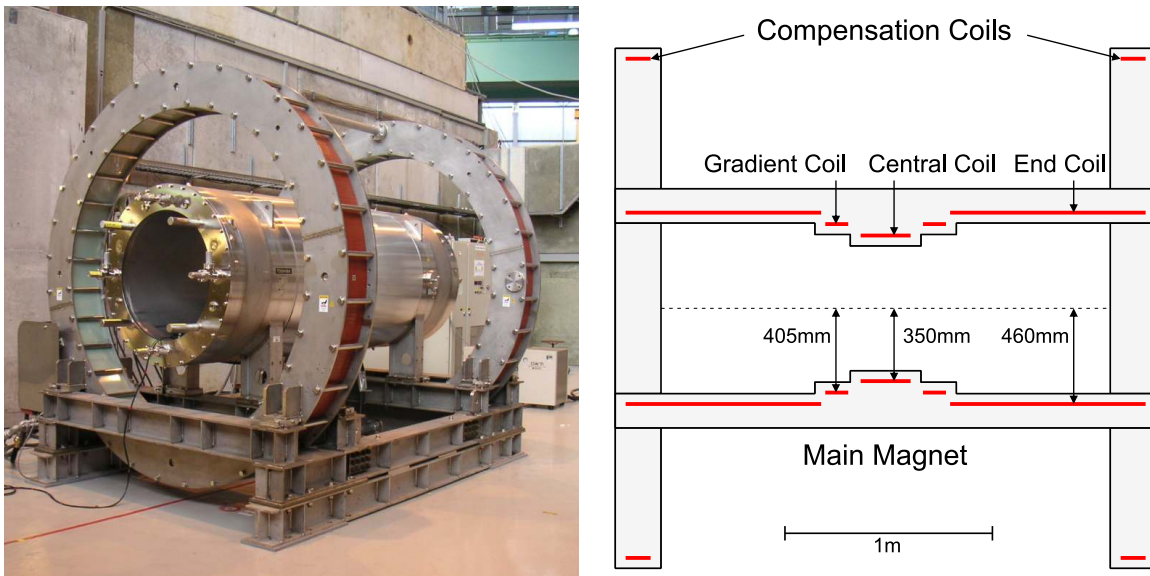


Figure 2.4: Picture and schema of the superconducting main magnet and the two normal conducting compensation coils.

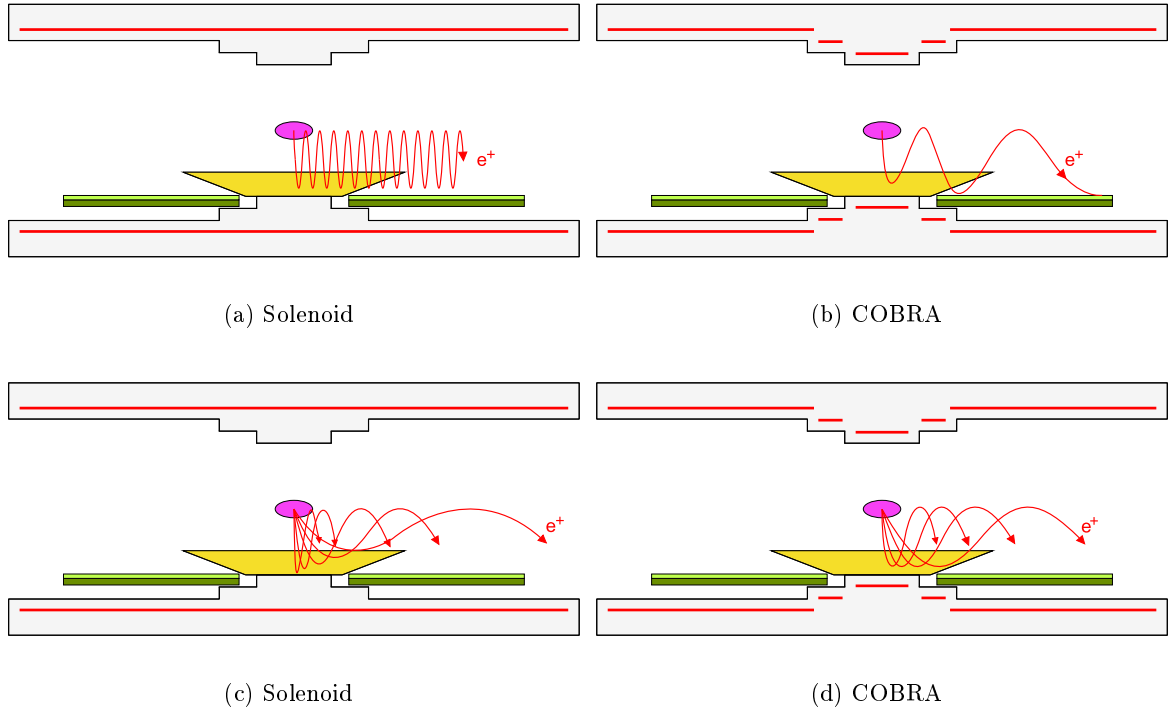
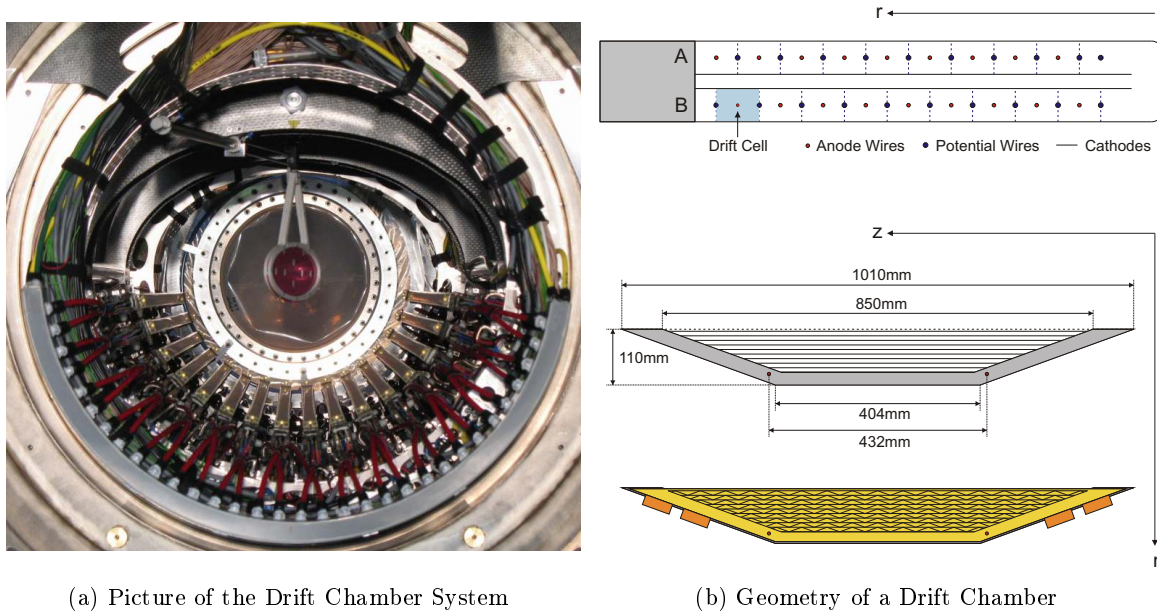


Figure 2.5: Illustrations of the advantages of COBRA compared to a solenoid magnet. In (a) and (b), it is shown how positrons emitted close to 90° are swept away from the sensitive volume of the drift chambers in different magnetic fields. The bending radii of monochromatic positrons in a solenoid magnetic field depend on the emission angles as illustrated in (c). Monochromatic positrons follow tracks with constant projected bending radii in the COBRA field as shown in (d).

2.3.2 Drift Chamber System

The MEG collaboration uses a drift chamber system [41] to measure the trajectories of the emitted positrons. The drift chamber system should be able to operate with a high counting rate as the desired muon stopping rate is $3 \cdot 10^7 \mu^+/\text{s}$. Due to the great advantages of the COBRA magnet, most of the low energy Michel positrons never reach the drift chamber system, which dramatically suppresses the counting rate. Nevertheless, the counting rate is still quite high especially in the innermost drift chamber region. As Coulomb scattering worsens the resolution of the particle track measurement, it is necessary to minimize the spectrometer material. The reduction of detector material has also the advantage that photon background is suppressed.

To address these requirements, the MEG drift chamber system consists of 16 drift chamber modules that are radially aligned to the beam axis. The drift chambers are separated by an angle of 10.5° . The drift chamber system is placed in the lower half of the COBRA interior as shown in Fig. 2.1. In radial direction r , the sensitive volume of the drift chamber system is



(a) Picture of the Drift Chamber System

(b) Geometry of a Drift Chamber

Figure 2.6: Picture of the drift chamber system and the target mounted inside the COBRA magnet (a) and schemas of one drift chamber module with geometrical details (b). The cross-sectional schema shows the two drift planes each with nine drift cells shifted against each other. The longitudinal schemas show the alignment of the anode wires and the Vernier pattern, respectively.

between $r = 190$ mm and $r = 300$ mm from the beam axis. With this configuration, the drift chamber system is sensitive to positrons with a momentum larger than 35 MeV/c. A picture of the drift chamber system and the target mounted inside COBRA is shown in Fig. 2.6a.

Each drift chamber module consists of two drift planes each with nine drift cells. The two planes are shifted radially against each other by half a drift cell to solve the left-right-ambiguity. Each drift cell has a rectangular cross-section of 7 mm \times 9 mm. In the center of each drift cell is an anode wire with a diameter of 25 μ m to which a high voltage of approximately 1800 V is applied. The applied high voltage is controlled by an autonomous and sophisticated high voltage control system with a special trip recovery procedure and safety features to prevent the chambers from damage. More information about the high voltage control system is presented in Section 3.2.

The drift cells are confined by ultrathin cathode foils (12.5 μ m polyimide foil deposited with 250 nm aluminium) and potential wires with a diameter of 50 μ m. Both, cathode foils and potential wires are grounded. To measure the z position of the positron transition, the cathode foils have a Vernier pattern [42,43] with a period of 5 cm. Figure 2.6b shows the schema of one drift chamber module with geometrical details. As shown in the figure, the drift chambers have an open frame construction, that is, the top of each drift chamber does not consist of massive material. This is necessary as the highest counting rate is expected at the innermost region of the drift chamber system. Therefore, this design allows to suppress Coulomb scattering

and photon generation but complicates the construction of the drift chambers. A detailed description of the chamber production and the different calibration methods is given in [44] and [45], respectively.

A gas mixture of helium (50%) and ethane (50%) is used as counting gas in the drift chambers. To reduce the amount of material in the interior of COBRA, it is filled with a helium atmosphere. Both, drift chambers and COBRA are therefore filled and flushed with gases. To prevent the ultrathin cathode foils from damage, a pressure control system is necessary to keep the pressure differences between drift chambers, COBRA, and environment constant. A detailed discussion about the pressure control system is given in Section 3.1.

The drift chamber modules and the target are mounted on a support structure made of carbon fiber. This structure is extracted during every winter shutdown² for maintenance work and hardware modifications. After finishing these actions, the support structure is again inserted into the COBRA magnet. Before starting a new data taking period, an optical survey of the target and the drift chambers is therefore necessary to calculate the alignment. The optical survey is detailed in Section 3.3.

2.3.3 Timing Counters

After passing the drift chamber system, the positron hits the timing counters, which measure the timing of the positron very precisely. The MEG collaboration uses two sets of timing counters each one at the upstream and downstream side of the detector as shown in Fig. 2.1. Each timing counter set consists of a ϕ and a z timing counter. The ϕ timing counter consists of 15 plastic scintillator bars aligned parallel to the beam axis and read out by PMTs at each end. The z timing counter consists of 256 scintillating fibers aligned orthogonally to the bars of the ϕ timing counter. The fibers are read out by avalanche photodiodes. A picture of one timing counter is shown in Fig. 2.7 and [46–48] give a detailed description about development, functional principle, and calibration of the timing counters.

2.4 Photon Detector

The emitted photons are detected in a liquid xenon scintillation detector [49] to measure their kinematics. With 900 liter of liquid xenon, the MEG photon detector is currently the world's largest liquid xenon detector. The photons interact with the liquid xenon and produce scintillation light [25], which is picked up by 846 PMTs surrounding the sensitive volume of the detector. The energy and the timing of the photons as well as the position of their first interaction with the liquid xenon is determined with signals from these PMTs.

Liquid xenon has many advantages such as high density of $\rho = 2.95$ g/cm, short radiation length of $X_0 = 2.77$ cm, fast response of 45 ns for gamma rays, and no scintillation light

²Further information about the run schedules are presented in Section 2.8.

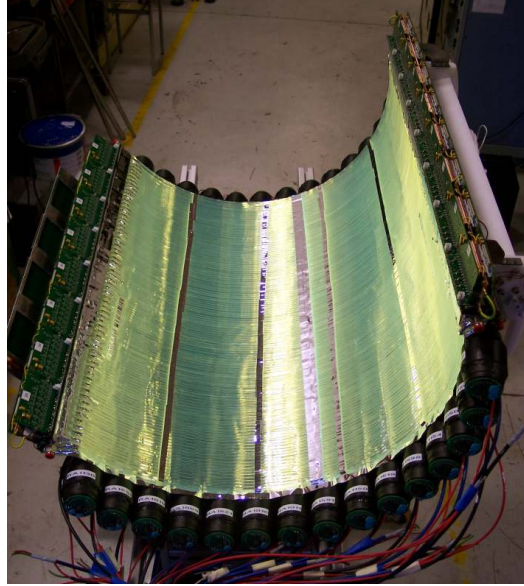


Figure 2.7: Picture of one timing counter extracted from the MEG detector.

absorption. Liquid xenon is therefore perfectly suited as scintillator material. On the other hand, liquid xenon is extremely expensive, needs a cooling system to keep the whole sensitive volume in a stable liquid phase, and requires a purification system to avoid scintillation light absorption due to impurities. As the photon detector of the MEG experiment is the first liquid xenon detector of this size, careful studies with prototypes [50] had been necessary before successfully constructing the final photon detector.

The MEG photon detector is C-shaped and is placed outside the COBRA magnet between the compensation coils. The inner and outer radius of the C-shape is $r = 67.85$ cm and $r = 106.35$ cm, respectively. The six faces of the liquid xenon detector are called top, bottom, upstream, downstream, inner, and outer and are equipped with 54, 54, 144, 144, 216, and 234 PMTs, respectively. The faces and their geometries are shown in Fig. 2.8. With this geometry, the MEG photon detector covers 10 % of the whole solid angle. The MEG experiment uses the PMT R9869, which was developed in collaboration with Hamamatsu Photonics. Figure 2.9 shows pictures of the liquid xenon detector and the PMT holder frame.

To keep the xenon in a stable liquid phase, a cryogenic system with a pulse-tube refrigerator [51] is necessary to keep the temperature between 161 K and 165 K. In addition to the liquid xenon detector, the MEG collaboration constructed two kinds of storage systems [52]. One is a dewar that can hold the whole xenon used by the MEG experiment in liquid phase, the other system consists of eight high-pressure tanks that can store the xenon in gas phase. The MEG collaboration developed also a purification system [53,54] that consists of purification cartridges for liquid xenon and heated getter filters for gaseous xenon.

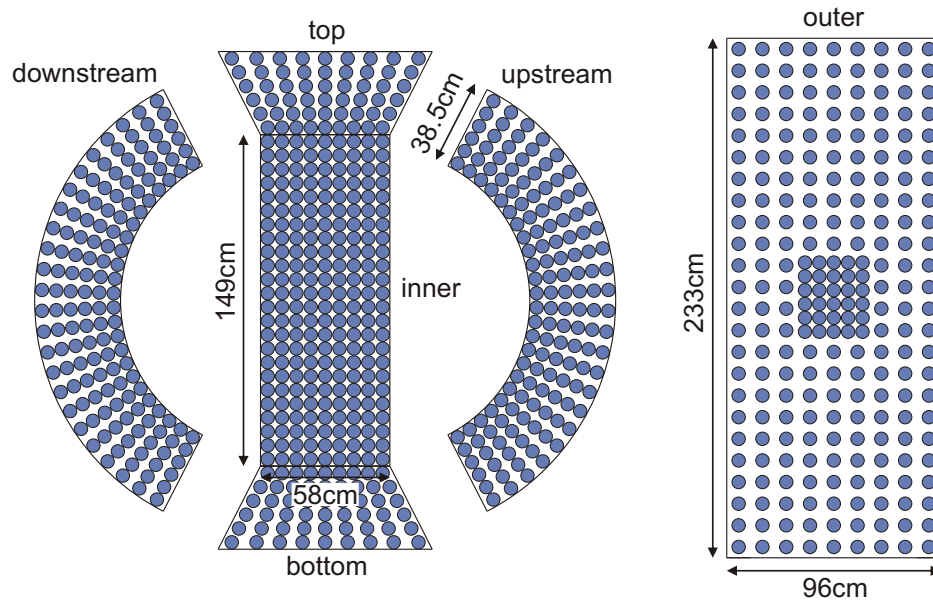


Figure 2.8: Schema of the six faces of the liquid xenon detector with geometrical details. In addition, the assembly of the PMTs is shown.

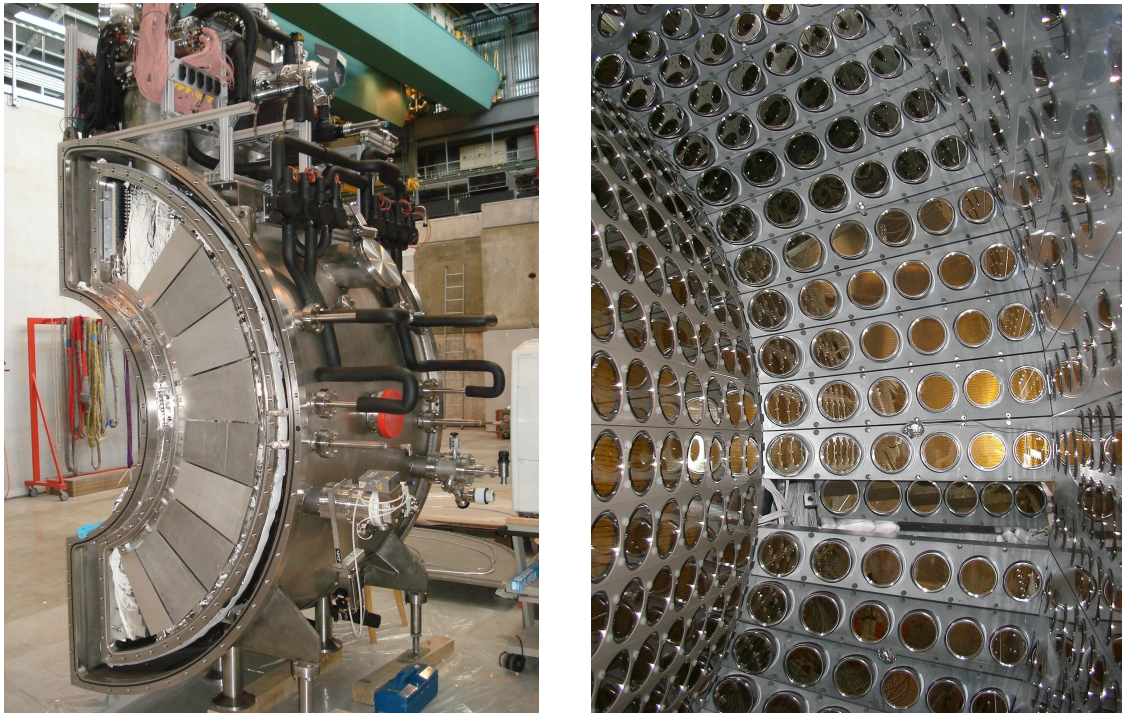


Figure 2.9: Pictures of the liquid xenon detector and the PMT holder frame with implemented PMTs.

2.5 Electronics and Data Acquisition

The electronic signals from liquid xenon detector, timing counters, and drift chambers have to be collected, stored, and analyzed to determine the kinematics of photon and positron. For that purpose, signals from the different sub-detectors are split to use them as trigger signals and to digitize the waveforms. The data acquisition system MIDAS is described in Section 2.5.1 and the trigger conditions are presented in Section 2.5.2. The domino ring sampler chip which digitizes the waveforms is introduced in Section 2.5.3. Finally, the slow control system of the MEG experiment is explained in Section 2.5.4.

2.5.1 Data Acquisition System

The data acquisition system of the MEG experiment is based on the MIDAS (Maximum Integration Data Acquisition System) package [55]. It was developed at PSI and TRIUMF [56] as a general purpose data acquisition system. The whole MEG experiment is remotely controllable by MIDAS. It allows to start and stop data taking runs with different settings and manages the coordination of trigger and waveform digitalization for each event. All required settings are written in an online data base (ODB). Furthermore, MIDAS provides an alarm system which automatically contacts the corresponding experts in case of communication problems, changed event rates, unexpected measuring values, or crashed programs. MIDAS also provides various tools for the slow control of the MEG experiment. They are discussed later in Section 2.5.4.

2.5.2 Trigger

The trigger system of the MEG experiment is based on 100 MHz 10-bit pipeline analog to digital converters (ADCs) that sample the signals from the sub-detectors and field programmable gate arrays (FPGAs) that analyze the digitized information to fire the trigger in case of a positive match. The trigger for $\mu^+ \rightarrow e^+ + \gamma$ signal candidates (MEG trigger) is based on three conditions:

Photon Energy The pulse height of the sum waveform of all photon detector PMTs corresponds to the energy of the detected photon.

Timing The time difference between the PMT signals from the photon detector and the ϕ timing counter is obtained by analyzing the leading edge of the waveforms.

Direction Match The photon direction is estimated from the position of the inner face PMT that measures the most light and the direction of the positron is obtained from the index (azimuthal angle ϕ) and the charge ratio (polar angle θ) of the ϕ timing counter PMTs.

All three conditions are implemented in the trigger system by fast reconstruction algorithms executed on the FPGAs. Signals from the drift chambers are not used for the MEG trigger due to the long drift time. With a muon stopping rate of $3 \cdot 10^7 \mu^+/\text{s}$, the typical trigger

rate of the MEG trigger is approximately 5 Hz. The MEG collaboration developed additional trigger settings for calibration runs and background studies. A detailed discussion about the MEG trigger system is given in [57].

2.5.3 Domino Ring Sampler

The MEG experiment needs a waveform digitizer to identify and reject pile-up events and to extract precise timing and energy information from the sub-detector signals. Therefore, the so-called Domino Ring Sampler (DRS) chip has been developed at the PSI starting in 2001 [58]. The DRS chip is also used by other experiments such as MAGIC [59]. Currently, the MEG experiment uses the most recent version of this chip, DRS4 [60].

DRS4 is produced in a $0.25\ \mu\text{m}$ CMOS process and digitizes waveforms with a sampling rate between 0.7 and 6 Giga samples per second (GSPS). It can sample 9 different input channels each having a switched capacitor array with 1024 cells. A so-called domino wave propagates continuously with the chosen sampling rate through an inverter ring. This enables the analog sampling in the capacitors by deleting the signal stored during the previous turn of the domino wave. The domino wave is stopped by an external trigger and the sampling capacitors are read out and digitized. Figure 2.10 shows the simplified schema of the DRS chip. A mezzanine board is composed of two DRS4 chips and two mezzanine boards are mounted on a VME board. The synchronization between the different boards is guaranteed by an external reference clock. The signals from the liquid xenon detector and the ϕ timing counter are digitized with a sampling rate of 1.6 GSPS while the drift chamber signals are sampled with 0.7 GSPS. Studies about the timing resolutions achievable with the DRS4 chip are presented in Chapter 4.

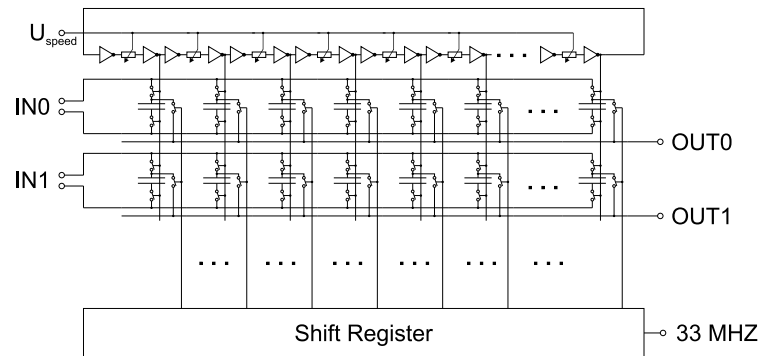


Figure 2.10: Simplified schema of the DRS chip. [61]

2.5.4 Slow Control

To remotely control and monitor all hardware devices (high voltage modules, liquid xenon storage and purification system, temperature sensors, etc.), the MEG collaboration uses a slow control system based on the Midas Slow Control Bus (MSCB) developed at PSI [62]. The PSI

developed also various slow control devices such as the slow control system SCS2001. It is equipped with 8 slots for I/O cards each with maximal 8 channels. The SCS is programmable, that is, it can be used as control unit independent of graphical user interface programs such as LabVIEW [63]. Another slow control device is the high voltage regulator HVR200 which controls the output voltage. Both SCS2001 and HVR200 are remotely accessible via MSCB.

To combine all information about the MEG experiment on one platform, all slow control units are embedded in the MEG DAQ system MIDAS. All settings and measuring values such as high voltage, gas concentrations, or temperatures are written in the ODB and are remotely accessible. MIDAS provides additional slow control tools such as a history that graphically displays the progress of measuring values. To display the overall status of a sub-system and to control it, MIDAS also provides the possibility to set up a custom page. A custom page is a web page which acts as graphical user interface and is connected with the ODB. Although MIDAS already implements various tools like displaying the current measuring values or coloring certain areas depending on the measured values, the user can create his own tools for the custom page. A detailed discussion about the slow control system of the drift chambers is given in Chapter 3.

2.6 Simulation and Analysis Software

The MEG software is divided into two parts, namely an online and an offline component. The online component of the MEG software is provided by MIDAS. It ensures the data acquisition from the MEG detector and provides the raw data. The offline component of the MEG software consists of MEGMC, MEGBartender, and MEGAnalyzer. The structure of the MEG software is schematically shown in Fig. 2.11.

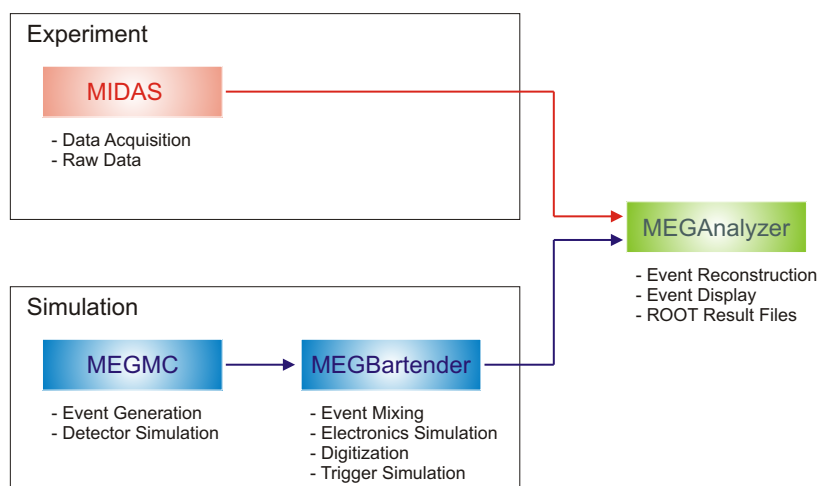


Figure 2.11: Structure of the MEG software.

MEGMC is the Monte Carlo (MC) simulation of the MEG detector. It is based on GEANT3.21 [64] and performs event generation and detector simulation. The event generation includes not only signal and background events but also several calibration events. The detector simulation implements detailed geometry and material information about the detector.

To get a realistic picture of an event in the detector, it is necessary to simulate the accidental overlap of different generated events (accidental coincidences, pile-up), that is, the simulation software has to mix generated events. Furthermore, it is necessary to simulate the electronic chain as signals from the sub-detectors pass several devices such as cables, splitter, or connectors and finally, they are digitized in the DRS4 chip. Last but not least, the MEG trigger system must be simulated. All these tasks are implemented in MEGBartender.

The MEGAnalyzer includes event reconstruction algorithms to determine the kinematics of positrons and photons. In addition, it provides an event display that allows to check waveforms and reconstructed parameters of each event. The MEGAnalyzer can read either raw data from the online MIDAS system or the simulated data from MEGMC and MEGBartender. The result files of the MEGAnalyzer are in ROOT [65] format. The MEG simulation and analysis software is detailed in [66].

2.7 Calibration and Monitoring Hardware

The MEG collaboration adopted various calibration and monitoring tools for the different sub-detector systems. In this section, a selection of the used calibration and monitoring hardware is presented. More details about the individual calibration methods are given in [67]. Section 2.7.1 describes the LEDs and alpha sources that are mounted inside the liquid xenon detector. The Cockcroft-Walton proton accelerator and the corresponding calibration possibilities are explained in Section 2.7.2. The charge exchange calibration apparatus is detailed in Section 2.7.3. Finally, Section 2.7.4 gives an overview of a new monitoring method based on neutrons that was applied in 2010 for the first time.

2.7.1 Stationary Calibration Devices inside the Liquid Xenon Detector

To calibrate and monitor the PMTs of the liquid xenon detector, 12 blue LEDs are placed inside the photon detector. The LEDs can be flushed with different intensities, which allows to calibrate the gain of each PMT. As the LED light has a different wavelength than the liquid xenon scintillation light, the LEDs cannot be used to calibrate the quantum efficiency of the PMTs.

For that purpose, the MEG collaboration developed a calibration method based on a lattice of 25 point-like radioactive sources [68]. Always five americium ^{241}Am sources are attached on five tungsten wires that have diameters of $100\ \mu\text{m}$. The tungstate wires are mounted inside the liquid xenon detector. Figure 2.12 shows the PMT holder frame with implemented PMTs, two LEDs, and one wire with alpha sources. The calibration of the PMT gain and quantum efficiency takes approximately one hour and is performed two or three times per week.

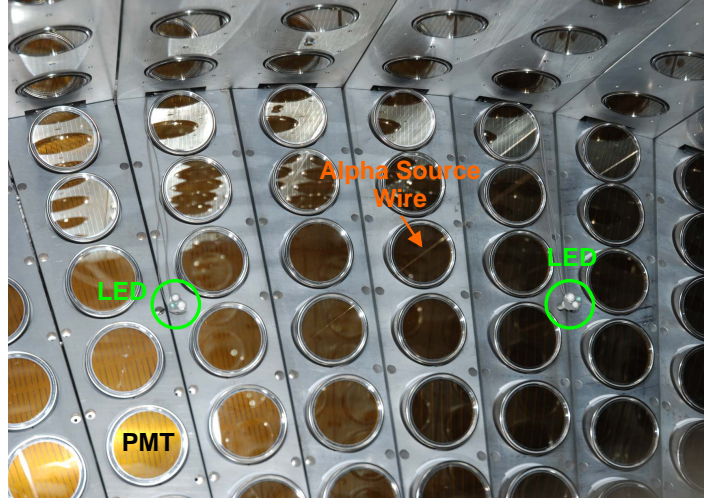


Figure 2.12: PMT holder frame of the liquid xenon detector with implemented PMTs. Two LEDs and one alpha source wire are highlighted.

2.7.2 Cockcroft-Walton Proton Accelerator

The MEG collaboration uses a 1 MeV Cockcroft-Walton (CW) proton accelerator to calibrate the liquid xenon detector and the relative timing of photon detector and ϕ timing counter. The CW accelerator is placed at the downstream side of the MEG detector. As a lithium tetraborate ($\text{Li}_2\text{B}_4\text{O}_7$) target is inserted in the MEG detector for this calibration method, the usually used muon beam must be blocked. The proton beam interacts with the target and induces the reaction ${}^7_3\text{Li}(p, \gamma){}^8_4\text{Be}$, which produces a photon with an energy of 17.6 MeV. Those gamma rays are used to calibrate and monitor the liquid xenon detector. The proton beam also induces the reaction ${}^{11}_5\text{B}(p, \gamma){}^{12}_6\text{C}$, which produces two photons of 11.67 MeV and 4.4 MeV that are coincident in time. The MEG collaboration uses this reaction to measure the relative timing of the photon detector and the ϕ timing counter. The CW calibration methods are detailed in [69]. The MEG collaboration performs the CW calibration two or three times per week when the PMTs are calibrated. One CW calibration takes approximately two hours.

2.7.3 Charge Exchange Calibration Apparatus

The CW calibration method provides photons with a maximal energy of 17.6 MeV to calibrate the liquid xenon detector. As photons from $\mu^+ \rightarrow e^+ + \gamma$ decays have an energy of 52.8 MeV, a calibration method with photons of the same energy range is desirable. For that purpose, the MEG collaboration uses the so-called charge exchange (CEX) calibration method. This method uses a negative pion (π^-) beam instead of the usual muon beam. Therefore, the whole beamline must be reconfigured. A liquid hydrogen (LH) target is inserted in the MEG detector where the pion beam induces the charge exchange reaction $\pi^- + p \rightarrow \pi^0 + n$. The neutral pion decays into two photons $\pi^0 \rightarrow \gamma + \gamma$ with almost 100 % branching ratio. The spectrum of the

two photons is continuous and ranges from 54.9 MeV to 82.9 MeV. The correlation between energy E_γ of one of the photons and the relative opening angle $\Theta_{\gamma\gamma}$ between the two photons is given by [67]

$$\Theta_{\gamma\gamma} = \arccos\left(1 - \frac{m_{\pi^0}^2}{2E_\gamma(E_{\pi^0} - E_\gamma)}\right) \quad (2.1)$$

with $m_{\pi^0} = 135.0 \text{ MeV}/c^2$ the mass and $E_{\pi^0} = 137.8 \text{ MeV}$ the energy of the neutral pion. This relation is also shown in Fig. 2.13a. By selecting events with back-to-back photons from $\pi^0 \rightarrow \gamma + \gamma$ decays, monochromatic gamma rays with an energy of 54.9 MeV and 82.9 MeV are obtained. The MEG collaboration uses a NaI detector with a cross section of approximately $20 \text{ cm} \times 20 \text{ cm}$. The NaI detector is mounted on a movable stage, which is placed at the opposite site of the liquid xenon detector as schematically shown in Fig. 2.13b. With this construction, back-to-back photon events can be detected by scanning the whole active volume of the liquid xenon with the NaI detector. For run 2011, the NaI detector was replaced with a BGO detector. As the reconfiguration of the beamline and the installation of the LH target takes approximately five days, the CEX calibration cannot take place every week. The MEG collaboration decided to perform the CEX calibration once or twice per year.

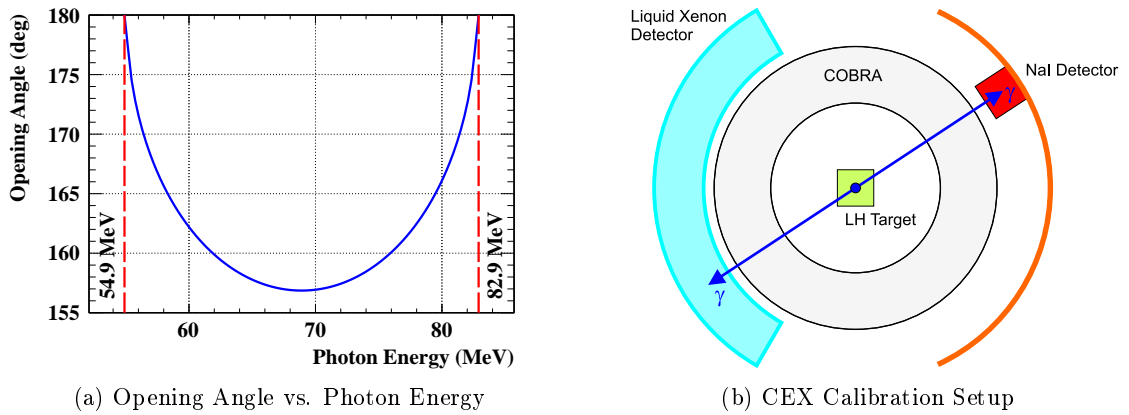


Figure 2.13: The correlation between the energy of one of the photons from the decay $\pi^0 \rightarrow \gamma + \gamma$ and the opening angle between the two photons (a) and a schema of the CEX calibration setup with the NaI detector on the movable stage (b).

2.7.4 Neutron Generator

The calibration methods with CW and CEX can only be performed if the usual muon beam is blocked. Therefore, the MEG collaboration adopted an additional monitoring method that checks the stability of the liquid xenon detector during variable muon beam conditions. It is based on a neutron generator which produces 2.5 MeV neutrons. It is placed at the opposite site of the liquid xenon detector, that is, at the same position as the NaI stage used for CEX calibrations. The neutron generator is surrounded with a shield of polyethylene which

acts as moderator to slow down the neutrons. After passing the polyethylene, the neutrons are captured in a nickel absorber. The thermal neutron captured in nickel produces several gamma lines [67]. The process with the largest cross section produces a photon with an energy of 9 MeV, which is detected in the liquid xenon detector. The calibration with the neutron generator was applied for the first time in 2010. It is performed two to three times per week together with the PMT and CW calibrations and takes approximately one hour. A neutron generator calibration includes one data sample without and one data sample with muon beam to monitor beam related effects. A more detailed description of the neutron generator monitoring method and the results of the neutron generator data analysis of run 2010 are presented in Chapter 5.

2.8 Data Taking

In 2008, the MEG collaboration started physics data taking with the MEG trigger. Section 2.8.1 explains the basic conditions for the data taking at PSI while Section 2.8.2 gives an overview of the different runs performed during the last years. Finally, Section 2.8.3 presents the performance of the MEG detector during the data taking periods.

2.8.1 Data Taking at the Paul Scherrer Institute

As the MEG detector is located at PSI in Switzerland, the MEG data taking depends on the PSI beam schedule [70]. This means, there is a long beam shutdown every winter from December to April (winter shutdown) and there are approximately 8 short shutdowns of roughly 3 days during the beam time for maintenance and beam development work. The MEG collaboration cannot take data based on muon, positron, or pion beams during those shutdowns. These interruptions are usually used for calibrations with the CW, the neutron generator, or cosmic rays. In addition, hardware modifications and maintenance work for the MEG detector are performed during these shutdowns.

2.8.2 Data Taking Periods

This section gives an overview of the data taking runs between 2008 and 2011 performed by the MEG collaboration. The physics data taking, the performed calibrations, and the appeared and solved problems will be briefly discussed for each run. The number of DAQ days with the MEG trigger and the number of muons stopped in the target are presented in Table 2.1.

2008

The first physics data taking period of the MEG experiment started in September 2008 and stopped in December 2008. The total MEG DAQ time with the MEG trigger was 51 days and $9.5 \cdot 10^{13}$ muons were stopped in the target. During physics data taking, the MEG collaboration

Table 2.1: Overview of the MEG data taking periods from 2008 to 2011. The DAQ time with the MEG trigger and the number of muons stopped in the target are presented. The values for run 2011 are realistic estimates.

| Year | DAQ Time (days) | Stopped Muons |
|-------|-----------------|---------------------|
| 2008 | 51 | $9.5 \cdot 10^{13}$ |
| 2009 | 35 | $6.5 \cdot 10^{13}$ |
| 2010 | 56 | $1.1 \cdot 10^{14}$ |
| 2011* | 81 | $1.9 \cdot 10^{14}$ |

* = estimates

performed calibrations for the liquid xenon detector three times per week with LED, alpha, cosmic rays, and CW. The MEG collaboration did one CEX calibration before the physics data taking period in August and one later in December. During this first run, the drift chambers had a discharge problem that was caused by printed circuit boards in combination with helium diffusion. In addition, the light yield of the liquid xenon detector decreased faster than expected due to impurities. Both problems were fixed during winter shutdown 2008/2009. The MEG collaboration analyzed the data collected in 2008 and published in [71] the obtained upper limit for the branching ratio

$$\mathcal{B}(\mu^+ \rightarrow e^+ + \gamma) < 2.8 \cdot 10^{-11} \text{ at } 90\% \text{ C.L.} \quad (2.2)$$

This result confirms the upper limit of $1.2 \cdot 10^{-11}$ at 90% C.L. obtained by the MEGA experiment [1]. The sensitivity of run 2008 was calculated to be $1.3 \cdot 10^{-11}$ in branching ratio. Run 2008 and its result are not part of this thesis.

2009

In 2009, the MEG collaboration collected physics data with total 35 MEG DAQ days and $6.5 \cdot 10^{13}$ stopped muons in the target. The liquid xenon detector was calibrated three times per week and one CEX calibration was performed before physics data taking started. Time resolution problems appeared during run 2009 that were caused by the read-out electronics. The problem was fixed during winter shutdown 2009/2010 by hardware modifications on the mezzanine boards. The obtained results of the 2009 data analysis are presented in Chapter 6.

2010

The MEG collaboration was able to collect twice the statistics of 2009 during physics data taking run 2010. The total MEG DAQ time was 56 days and $1.1 \cdot 10^{14}$ muons were stopped in the target. Due to stable performance of the liquid xenon detector in 2009, the MEG collaboration decided to reduce the number of weekly calibrations to two photon detector calibrations per week. Compared to run 2008 and 2009, the weekly calibrations of 2010 included also neutron monitoring. One CEX calibration was performed during the physics data taking period. Compared to 2009, the positron resolutions were worse in 2010 due to

electronic noise on the drift chamber signals. Investigations showed that they were caused by the high voltage system of the drift chambers. The high voltage system was therefore replaced during winter shutdown 2010/2011. The obtained results of the 2010 data analysis are presented in Chapter 6.

2011

Data collected during run 2011 are not yet analyzed and are therefore not part of this thesis. Nevertheless, the total DAQ time with the MEG trigger was approximately 81 days and roughly $1.9 \cdot 10^{14}$ muons were stopped in the target. The MEG collaboration was therefore able to collect the same statistics as during run 2009 and 2010 together.

2.8.3 Detector Performance

Table 2.2 presents the MEG detector performance during run 2009 and 2010. The timing resolutions could be improved in 2010 compared to 2009 due to hardware modifications on the DRS mezzanine boards. The positron resolutions are slightly worse in 2010, which were caused by electronic noise on the drift chamber signals. This problem was fixed for run 2011 by replacing the high voltage power supply of the drift chambers.

2.9 Summary

The MEG experiment is located at the Paul Scherrer Institute in Switzerland where it uses a continuous and high intense muon beam. The MEG collaboration developed a beamline which ensures that a high quality muon beam is stopped in the MEG target with a stopping rate of $3 \cdot 10^7 \mu^+/\text{s}$. The kinematics of the emitted positrons are measured with a spectrometer consisting of the superconducting magnet COBRA, a low-mass drift chamber system, and fast timing counters. Photons are detected with the world's largest liquid xenon scintillation detector. The MEG collaboration uses MIDAS as data acquisition system which allows a remote control of the whole experiment. The sub-detector signals are digitized with the DRS chip and the stored waveforms are analyzed with the MEGAnalyzer to obtain the kinematics of positrons and photons. To ensure a high performance detector, the MEG collaboration adopted various calibration methods by using for example LEDs, alpha sources, a Cockcroft-Walton proton accelerator, or a neutron generator. The MEG collaboration started physics data taking in 2008 followed by data taking periods in 2009, 2010, and 2011.

Table 2.2: Performance of the MEG detector during run 2009 and 2010.

| | 2009 | 2010 |
|-------------------------|---------------------------|---------------------------|
| Photon Energy (%) | 1.9 | 1.9 |
| Photon Timing (ps) | 96 | 67 |
| Photon Position (mm) | 5 (u, v) / 6 (w) | 5 (u, v) / 6 (w) |
| Photon Efficiency (%) | 58 | 59 |
| Positron Timing (ps) | 107 | 107 |
| Positron Energy (MeV) | 0.31 | 0.32 |
| Positron Theta (mrad) | 9.4 | 11 |
| Positron Phi (mrad) | 6.7 | 7.2 |
| Positron Vertex (mm) | 1.5 (z) / 1.1 (y) | 2.0 (z) / 1.1 (y) |
| Positron Efficiency (%) | 40 | 34 |
| Relative Timing (ps) | 146 | 122 |
| Trigger Efficiency (%) | 91 | 92 |

Chapter 3

Drift Chamber System

The positron spectrometer of the MEG experiment consists of the superconducting magnet COBRA, a drift chamber system, and timing counters as described in Chapter 2. The spectrometer is used to determine the kinematic variables of positrons coming from muons decaying in the target. The drift chamber system measures the positron track as a precisely reconstructed track is essential to obtain energy and direction of the positron. A deliberate chamber design, carefully chosen materials, powerful reconstruction algorithms, and accurate calibration methods are necessary to ensure a high performance drift chamber system. In addition, slow control systems are needed to guarantee stable detector performances.

This chapter focuses on only a few aspects of the drift chamber system, namely the pressure control system, the high voltage system, and the optical survey of the drift chambers and the MEG target. Detailed discussions about chamber production, event reconstruction, calibrations, and achieved resolutions are given in [44, 45, 72, 73]. The remainder of this chapter is structured as follows: The pressure control system of the drift chamber system is explained in Section 3.1. It regulates the gas flows inside the chambers and the interior of COBRA. Section 3.2 introduces the high voltage system, which controls the voltage applied to the anode wires of the drift chambers. Finally, Section 3.3 gives an overview of the optical survey of the drift chamber system and the target.

3.1 Pressure Control System

The drift chambers are filled and flushed with a counting gas that is a mixture of 50 % helium and 50 % ethane. To reduce the amount of material, a helium atmosphere fills the interior of the COBRA magnet. Due to the open frame construction and the ultra-thin cathode foils of the drift chambers, a small and constant pressure difference between drift chambers and COBRA volume is essential to avoid foil deformations. A pressure stability of 1 Pa corresponds to approximately 100 μm deformation of the cell-spacing, which is the maximum allowed deformation [44]. Therefore, a powerful pressure control system (PCS) that regulates the different gas flows through drift chambers and COBRA is required to ensure stable detector performances.

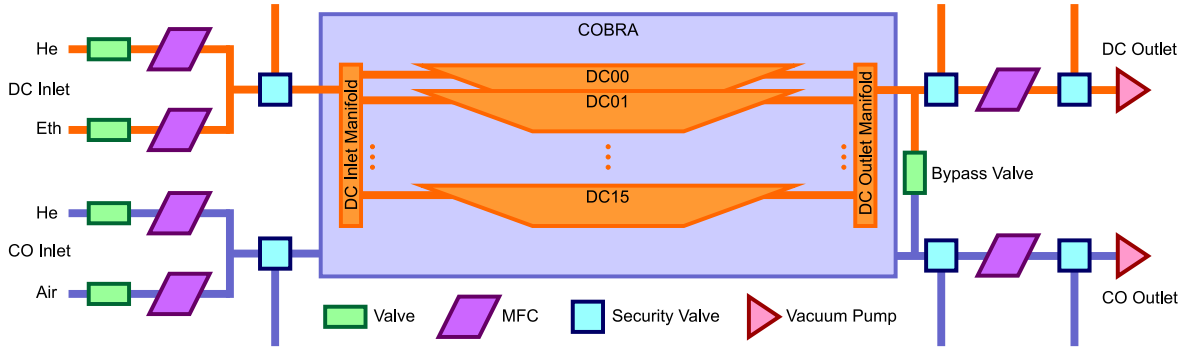


Figure 3.1: Schema of the PCS used for the MEG drift chambers (DCs) and COBRA (CO). The schema shows all important components such as valves, mass flow controllers, security valves, and vacuum pumps.

The basic functional principle of the PCS used for the MEG drift chamber system is shown in Fig. 3.1. If the system is running, the inlet valves for helium and ethane for the drift chambers and helium for COBRA are open. For each kind of inlet gas, mass flow controllers (MFCs) regulate the gas flows flushing into the detector. When the system is starting, the inlet flows slowly ramp up to the desired values and remain constant. Differential pressure sensors measure the pressure difference between drift chambers and COBRA and between COBRA and environment. A proportional-integral-derivative (PID) control algorithm [74] calculates from the deviation between measured and desired pressure difference the required amount of gas that has to be exhausted from the drift chambers and COBRA. Vacuum pumps ensure that the inserted gas is exhausted and for each line, a MFC controls the outlet flow. This means, the pressures between drift chambers, COBRA, and environment are regulated via the outlet MFCs. In case of overpressure, the gas is relieved to the environment through several security valves. In addition, there is a bypass valve combining the normally separated gas lines of drift chambers and COBRA. This valve is closed during normal operation but is opened in case of too large pressure differences to allow a fast pressure equalization. Several temperature and gas concentration sensors monitor permanently the current conditions in the gas system.

As shown in Fig. 3.1, COBRA has an additional gas inlet line for air. Experience has shown that the drift chamber high voltage performance is more stable with a small air admixture to the COBRA helium atmosphere. Not shown in this figure is the “high rate” system, which is necessary due to the weekly Cockcroft-Walton (CW) calibrations described in Chapter 2. For those calibrations, a $\text{Li}_2\text{B}_4\text{O}_7$ target has to be inserted into COBRA that is done with a bellow system. This insertion and the followed extraction cause dramatic pressure changes in COBRA that cannot be compensated with the normal MFCs. To prevent overpressures, a huge amount of helium has to be flushed out of (into) COBRA during insertion (extraction) of the $\text{Li}_2\text{B}_4\text{O}_7$ target. The “high rate” system is controlled with an additional MFC that can handle high gas flows.

Besides the PCS of the MEG detector, the MEG collaboration has a second PCS used for drift chamber studies in the so-called “Aquarium”. A picture of the “Aquarium” is shown in

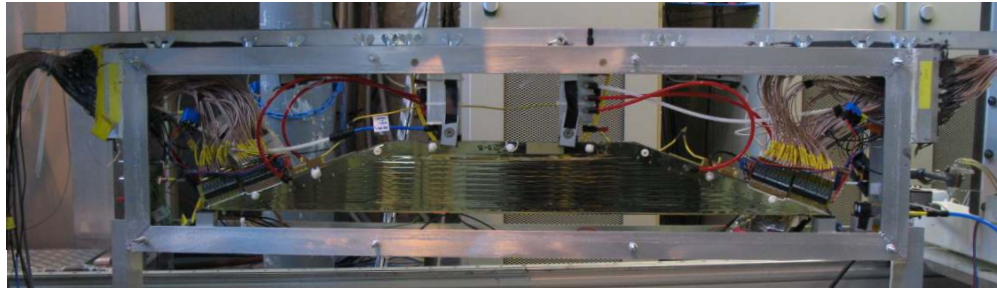


Figure 3.2: Picture of the “Aquarium” with drift chamber. The optically transparent lateral faces are not yet mounted.

Fig. 3.2. It is a box with dimensions of approximately $120\text{ cm} \times 30\text{ cm} \times 10\text{ cm}$ and optically transparent lateral faces. It provides space and connectors for two drift chambers to study them under real experimental conditions.

The temperature, gas concentration, and pressure sensors of the PCS are read out by a slow control system SCS2001, which was introduced in Chapter 2. In addition, the SCS2001 operates valves and MFCs. The SCS2001 is connected to MIDAS, which provides a history displaying the transient evolution of the measuring values. Originally, the SCS2001 was controlled by the graphical user interface program LabVIEW [63]. This had the disadvantage that starting or stopping the PCS and changing parameters such as gas flows could only be done via the computer on which LabVIEW was running. In addition, communication problems occurred sometimes between LabVIEW program and SCS2001. To avoid these problems, all system algorithms such as the PID calculation or safety algorithms have been implemented directly in the SCS2001. As a consequence, the PCS is now remotely controllable via the SCS2001 without using LabVIEW. A MIDAS custom page has been designed that displays the current status of the PCS. The custom page uses HTML 5 and JavaScript to interactively control the whole PCS through any web browser. It displays measuring values such as gas flows or pressures and it illustrates which valves are opened or closed. With the custom page, the system can be started or stopped and the different gas inlet lines can be activated. Furthermore, the desired values for gas flows, differential pressures, and PID parameters can be changed.

During the last data taking periods, the desired pressure difference between drift chambers and COBRA is usually set to 1.2 Pa while the regulation value for the pressure difference between COBRA and environment is chosen to be 7 Pa . A helium inlet flow of $2'000\text{ cm}^3/\text{min}$ with an air admixture of $50\text{ cm}^3/\text{min}$ is defined for COBRA. For the drift chamber system, the inlet flow of helium is chosen to be $65\text{ cm}^3/\text{min}$ and ethane is flushed into the drift chambers with $72\text{ cm}^3/\text{min}$. Due to helium permeation through the thin cathode foils from COBRA into the drift chambers, the inlet gas flow of helium is smaller than the one of ethane so that the desired counting gas mixture is achieved.

With those settings, the PCS of the MEG drift chamber system performed stable during the last data taking periods. Figure 3.3a shows the history of the pressure difference between drift chambers and COBRA during run 2010. Figure 3.3b shows the measured values as histogram.

Even though the pressure difference is measured and stored every second, Fig. 3.3 shows only one measurement per hour to reduce the amount of data. The spikes in Fig. 3.3a are caused by the CW calibrations. As the drift chambers do not contribute to the data taking during those calibrations and as the pressure difference spikes are small, the spikes neither influence the calibration nor cause any damage to the drift chambers. During run 2010, the PCS provided a pressure difference stability of 0.002 Pa in RMS. Therefore, the stability is two orders of magnitude better than the required 1 Pa precision.

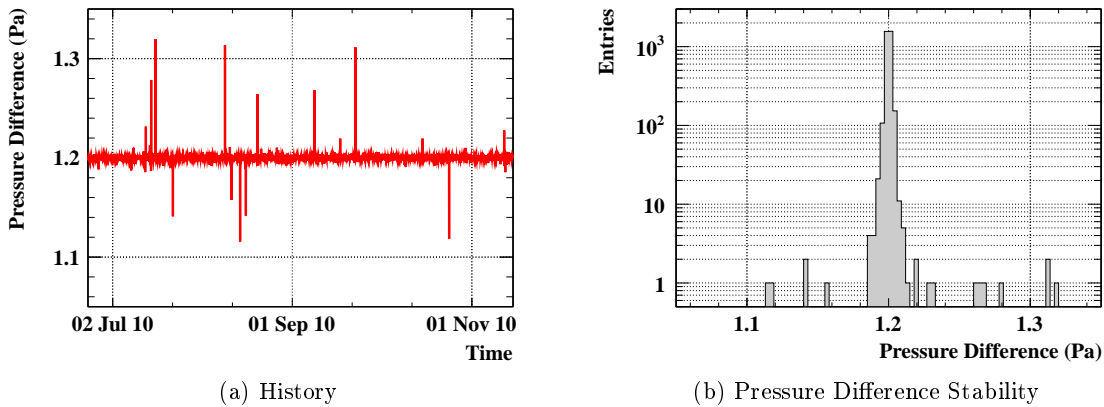


Figure 3.3: History of the pressure difference between drift chambers and COBRA during run 2010 (a) and histogram of the measured values (b).

3.2 High Voltage System

A high voltage of approximately 1800 V is applied to the anode wires of the drift chambers. The voltage of each drift plane is separately controlled, that is, a high voltage system (HV system) with 32 channels is required (16 drift chambers each with 2 planes). The drift chamber HV system consists of a commercial primary high voltage supply and 16 high voltage regulators HVR200, which were developed at the PSI. Each HVR200 module has two channels individually regulating the high voltage of one drift chamber plane. In addition, the HVR200 modules measure the actually applied high voltage and the anode current. Figure 3.4a shows the measured voltage of one drift chamber plane in 2010. The history does not include the complete run 2010 as the applied voltage was sometimes reduced before and after the shown time line due to maintenance work. The measured values are shown in Fig. 3.4b as histogram. Even though the voltage and current are measured every second, Fig. 3.4 shows only one measurement per hour to reduce the amount of data. The described HV system provides a voltage stability of 0.02 V in RMS for 1840 V applied to the drift planes.

Originally, the HV system was controlled by the graphical user interface program LabVIEW [63]. As a consequence, the applied voltages could only be changed via the computer on which LabVIEW was running. To avoid this problem, an automated and sophisticated high voltage control algorithm has been implemented in the HVR200 modules. It includes a step-by-step

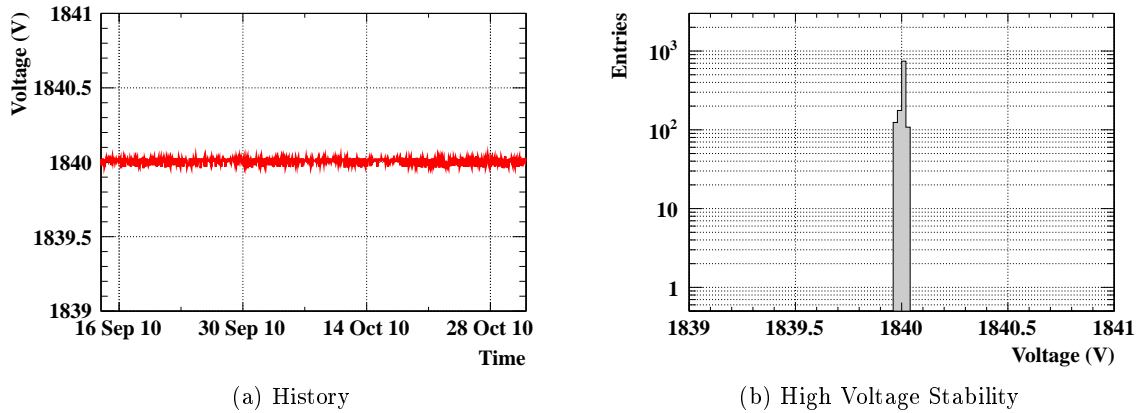


Figure 3.4: History of the measured voltage applied to one drift plane during run 2010 (a). The history does not include the complete run 2010 as the applied voltage was sometimes reduced before and after the shown time line due to maintenance work. The measured values are shown as histogram in (b).

ramping procedure, a fast trip recovery, and several safety algorithms that are explained in the following.

When starting up the HV system, that is, ramping the applied voltage from zero to approximately 1800 V, current spikes can occur. Those spikes can be caused by the high voltage regulation circuit or charging currents. Therefore, an automated step-by-step ramping procedure is implemented in the HVR200 modules. With this procedure, the voltage is ramped up by typically 100 V with a ramping speed of 0.1 V/s followed by a relaxing time of usually 30 minutes. The applied voltage remains constant during the relaxing period.

It can happen that current spikes cause hardware trips of the high voltage channel if they are too large. Ramping up the voltage back to the nominal value after such a trip with the step-by-step procedure would take approximately 13 hours with the typical settings. During this time, the drift plane does not contribute to data taking. This is the reason why a fast trip recovery, which starts automatically after a trip, is implemented in the HVR200 modules. The voltage is fast ramped up to a certain value to keep the polarization of dielectric materials in the chambers. This value is usually 500 V below the voltage that was applied just before the trip. After reaching this value and a certain relaxing time, the step-by-step ramping starts. With this trip recovery method, the dead time of a tripped drift chamber plane is reduced to approximately 4.5 hours which corresponds to a reduction of 65 %. Figure 3.5 shows a realistic illustration of the applied voltage during trip recovery and step-by-step ramping procedures. The curves are obtained by using typical settings of the MEG drift chamber HV system. The measured voltage and current during a real trip are shown in Fig. 3.6a and Fig. 3.6c, respectively. The current of $8 \mu\text{A}$ at nominal voltage corresponds to the usual current load due to Michel positrons traversing the drift chambers when the muon beam is stopped in the target with $3 \cdot 10^7 \mu^+/\text{s}$.

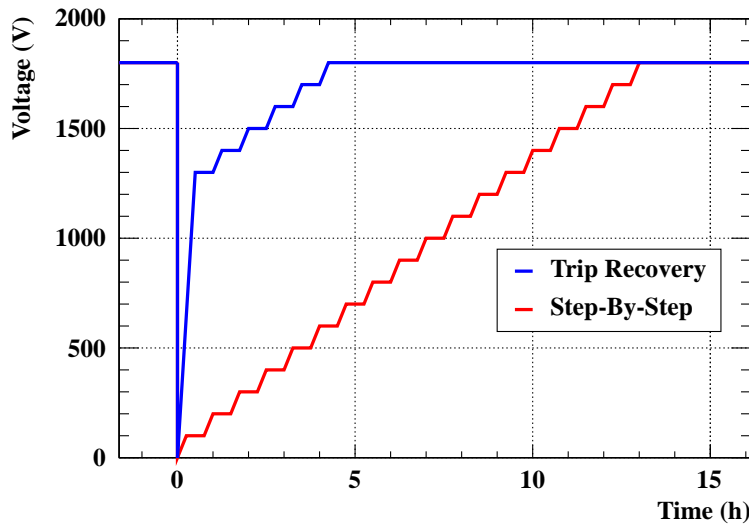


Figure 3.5: Illustration of the applied voltage during trip recovery and step-by-step ramping procedures. The shown curves are obtained by using typical settings of the MEG drift chamber HV system.

The HVR200 modules also provide several safety algorithms. In case of current spikes or dark currents, those algorithms automatically stop the ramping process. If the current is too large, the safety algorithms ramp down the voltage. The measured voltage and current during such a current spike are shown in Fig. 3.6b and Fig. 3.6d, respectively. The safety algorithms ramp down the voltage by a certain value, typically 100 V, and wait for several minutes before restarting the ramp up process.

The HVR200 modules are remotely accessible and connected to MIDAS. A custom page allows the shift crew of the MEG experiment to ramp down the high voltage in case of an emergency. With the step-by-step ramping, the trip recovery, and the safety algorithms, the HV system of the drift chambers provide a fully automated and sophisticated high voltage control.

During run 2010, studies showed that the previously described HV system causes electrical noise on the drift chamber signals. As a consequence, the HV system was replaced with a low noise commercial high voltage device for run 2011. It consists of 32 channels each with individually controllable high voltage. Compared to the HVR200 modules, this device is not programmable. Therefore, the step-by-step ramping, trip recovery, and safety procedures cannot be directly implemented. As those tools are essential to ensure a stable and safe operation of the drift chamber system, the algorithms are now implemented in MIDAS, which controls the new high voltage device. First analyses of run 2011 show an improved noise situation but the data of this run were not fully analyzed at the time of writing this thesis.

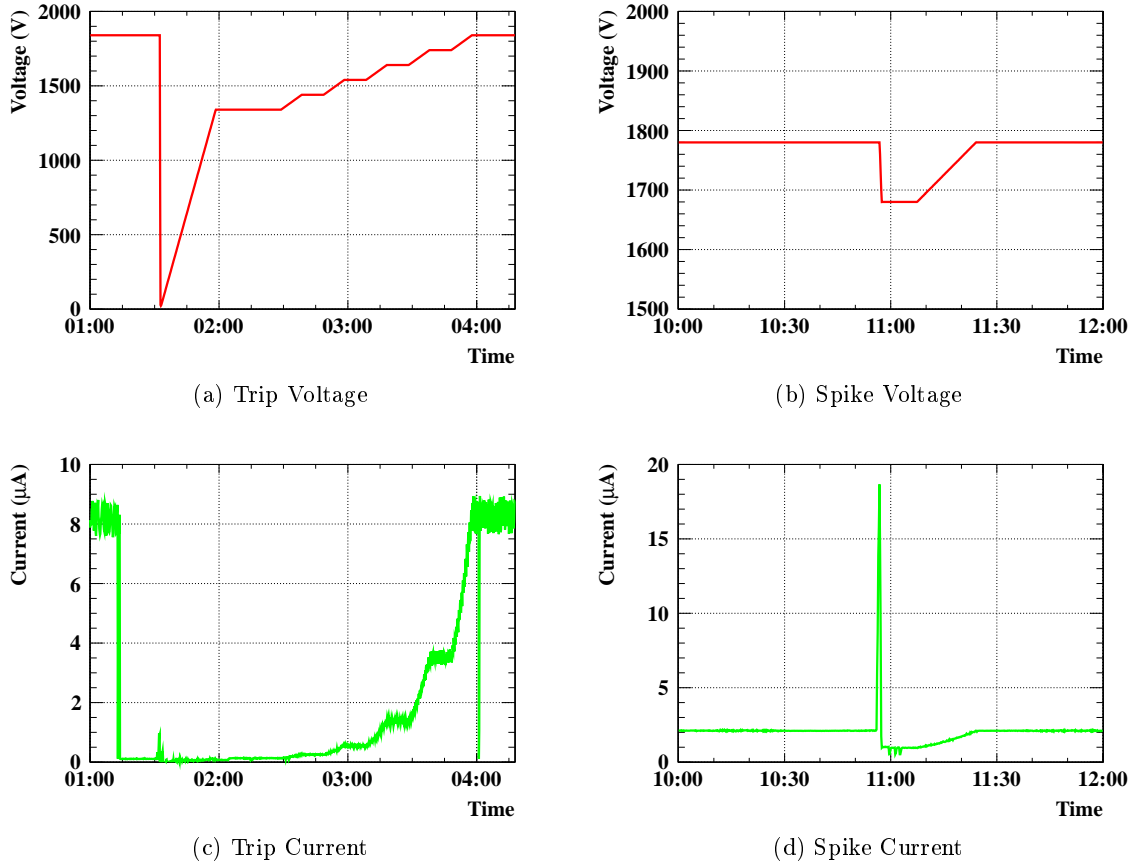


Figure 3.6: The measured voltage (a) and current (c) of a real trip. The current of $8 \mu\text{A}$ at nominal voltage corresponds to the usual current load due to Michel positrons traversing the drift chambers when the muon beam is stopped in the target with $3 \cdot 10^7 \mu^+/\text{s}$. The trip itself occurred when the muon beam was blocked. Figures (b) and (d) show the measured voltage and current during a current spike. The safety algorithms ramp down the voltage by 100 V and wait for a certain time before restarting the ramp up process.

3.3 Optical Survey

The support structure with drift chambers and MEG target is extracted every winter shutdown from the MEG detector for maintenance work. An optical survey of the drift chambers and target is performed after the reinsertion of the support structure into COBRA, that is, at the beginning of every data taking period. The goal of the optical survey is to confirm that the support structure is placed at the right position and that the drift chambers are mounted correctly. Furthermore, the optical survey provides the geometrical alignment of the drift chamber system. The geometrical alignment is used as starting point for the data alignment using particle tracks. The outcome of the tracking alignment algorithms depends strongly on the starting point of the initial alignment. Therefore, a very precise geometrical alignment

including all known geometrical effects such as twisted chambers is essential. Finally, the optical survey provides the exact position of the MEG target inside COBRA.

There are several measuring points mounted, glued, or drawn on the support structure, drift chambers, and MEG target serving as identification marks for the optical survey:

Support Structure Pins with optically recognizable center are mounted at the upstream and downstream end of the support structure (17 pins upstream, 17 pins downstream). A picture of such a pin is shown in Fig. 3.7a.

Drift Chambers Small printed circuit boards with crosshairs are glued at the upstream and downstream end of each drift chamber (16 crosshairs upstream, 16 crosshairs downstream). Figure 3.7b shows a picture of the drift chambers mounted on the support structure with highlighted printed circuit boards and crosshairs.

MEG Target Crosses are drawn on the target foil with well known relation to each other and to the holes in the foil (7 crosses). A picture of the target with crosses and holes is shown in Fig. 2.3.

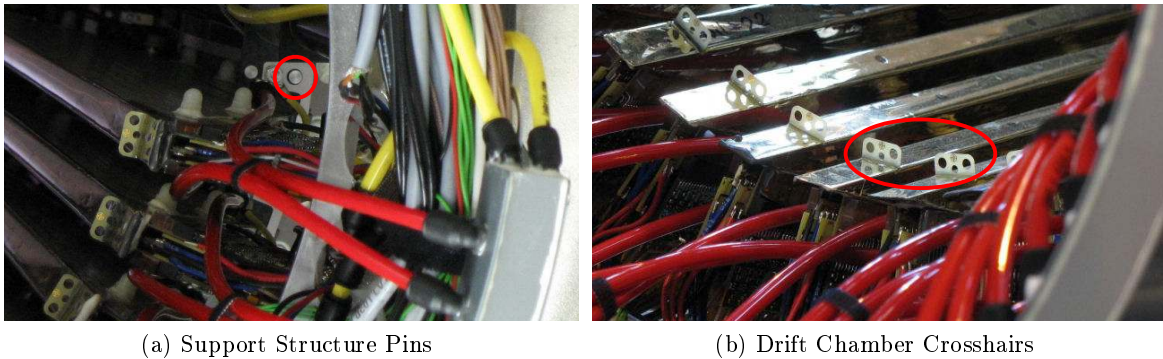


Figure 3.7: Pictures of the MEG drift chamber system with highlighted support structure pins and drift chamber crosshairs.

The drift chamber crosshairs and target crosses are measured with a theodolite from different angles. The three-dimensional coordinates (x, y, z) of those survey points are calculated by using the method of forward intersection. This method is not applicable to the support structure pins, as they are only visible from one theodolite position. To obtain the x and y coordinates of the pins, the z position has to be assumed. The resolution of the forward intersection method is approximately 0.3 mm for x and y coordinates and between 0.5 mm and 2 mm (depending on the forward intersection calculation software) for z coordinates.

The position and direction of all anode wires, hence the geometrical alignment of the drift chamber system, is calculated by using the measured coordinates of the support structure pins and drift chamber crosshairs and by applying some geometrical considerations. The position of the target is determined by calculating the target plane from the drawn crosses. A detailed discussion about the optical survey method and the calculation methods for geometrical alignment and target plane is presented in [75].

The previously described optical survey and the calculation of the geometrical alignment was performed from 2008 to 2010. Every year, unexpected effects concerning the z measurement of the drift chamber crosshairs occurred. By comparing the measured z coordinates of the upstream and downstream crosshairs, the drift chambers seemed to be either squeezed or stretched by up to 1 mm which is physically impossible. In addition, the measured z coordinates indicate that the whole support structure is shifted towards downstream by more than 2 mm. Those observations were most probable caused by underestimated systematic effects due to the small intersection angles of the theodolite measurements. Enlarging those intersection angles is geometrically impossible due to the limited space in COBRA.

To resolve those problems, the MEG collaboration decided to use a more precise optical survey method for run 2011 to determine the z position of the drift chambers. Corner cube reflectors were mounted on the drift chamber survey marks in a way that the original crosshairs are still visible. This allows to perform the original and new optical survey method simultaneously and to compare the obtained results. The coordinates of the drift chamber crosshairs are still measured with a theodolite and forward intersection while the x , y , and z coordinates of the corner cube reflectors are determined with a laser tracker system. The resolution of the laser method is 0.015 mm for all coordinates. Figure 3.8 shows a picture of the drift chamber system equipped with corner cube reflectors and it shows at the top right a schema of a corner cube mounted on a drift chamber survey mark.

The z coordinates in 2011 obtained with the original optical survey method using drift chamber crosshairs induce that the upstream crosshairs are shifted by 2.4 mm while the downstream crosshairs are shifted by 1.8 mm towards downstream with respect to their expected position. This means that the drift chambers seem to be squeezed by 0.6 mm. Figure 3.9a shows for each chamber the difference between the chamber length measured by the original optical

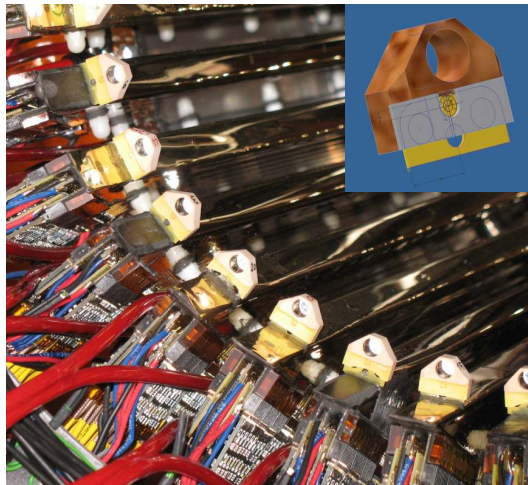


Figure 3.8: Picture of the drift chamber system equipped with corner cube reflectors and at the top right a schema of a corner cube mounted on a drift chamber survey mark. The corner cube reflectors are mounted in a way that the crosshairs are still visible as shown in both the picture and the schema.

survey and the real chamber length, which was precisely measured with a touch sensor. This plot shows that chamber 12 is squeezed by 1.3 mm, which is physically impossible.

On the other hand, the results of the optical survey with corner cube reflectors induce that both upstream and downstream reflectors are shifted towards downstream by 1.2 mm compared to their expected position. The measurements of upstream and downstream reflectors are therefore consistent. The discrepancy of 1.2 mm compared to the expected position is caused by deformations of the support structure due to the weight of the read out cables. Figure 3.9b shows the difference between the chamber length measured by the new optical survey and the real chamber length. The plot shows maximum deviations of 0.4 mm for chamber 9, which can be explained by mechanical accuracy in the corner cube mounting on the drift chambers.

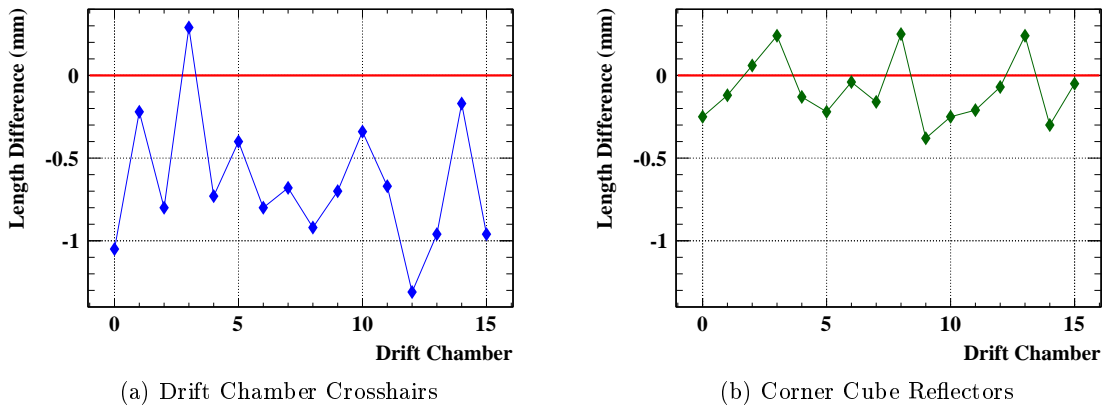


Figure 3.9: Difference between the chamber length measured with the optical survey and the real chamber length precisely measured with a touch sensor. The plots show the results obtained with drift chamber crosshairs and forward intersection (a) and corner cube reflectors and laser tracker system (b).

Comparing the measurements of x and y coordinates obtained with crosshairs and corner cube reflectors, the observed deviations are within 0.1 mm, which corresponds to the uncertainty of the forward intersection. As conclusion, the x and y measurements of the drift chamber crosshairs with theodolite and forward intersection are consistent with the results obtained with the corner cube reflectors and the laser tracker system. Furthermore, the corner cube reflector measurements show consistent shifts of upstream and downstream reflectors, therefore, they do not induce squeezed drift chambers. The inconsistent z measurements of the crosshairs with the theodolite are most probable caused by systematic effects due to small intersection angles.

3.4 Summary

The pressure difference between drift chambers and COBRA must be constant to ensure a stable performance of the MEG drift chamber system. A pressure control system with constant inlet gas flows and regulated outlet flows achieves a pressure stability of 0.002 Pa in RMS. The performance of the pressure control system is therefore two orders of magnitude better than the required 1 Pa precision. The drift chambers only contribute to the data taking with full efficiency when a high voltage of approximately 1800 V is applied to the anode wires. The high voltage system of the drift chambers ensures a stable power supply of 0.02 V in RMS for applied 1840 V. A step-by-step ramping procedure is implemented to ensure a safe ramp up from zero to nominal high voltage. Furthermore, a special trip recovery procedure minimizes the dead time of a drift plane after a trip and safety algorithms ramp down the voltage in case of current spikes or dark current. After every winter shutdown, an optical survey of the drift chambers and the target is necessary. It checks if the support structure is placed at the right position, provides the geometrical alignment of the drift chamber system, and determines the exact position of the MEG target inside COBRA. For run 2011, a new optical survey method using corner cube reflectors was introduced. With this method, the z position of the drift chambers is measured with high accuracy.

Chapter 4

DRS4 Chip

The signal channels of the MEG experiment are read out by a high frequency waveform digitizer, namely the so-called Domino Ring Sampler (DRS) chip [58] that was developed at the PSI. The functional principle of this chip was already described in Chapter 2. For run 2009, the newest generation of this chip, DRS4 [60], was implemented in the MEG experiment to read out signals from the liquid xenon scintillation detector and the drift chambers. The resolution of the photon timing measurement during run 2009 was measured to be 96 ps. This result is worse than the expected resolution estimated from the detector performance in 2008 and the DRS4 specifications. The timing measurement of the positron was not affected by this effect as the timing counter channels were not read out by the DRS4 chip in 2009. The MEG collaboration has undertaken substantial efforts to improve the photon timing resolution. Section 4.1 describes timing resolution measurements with the DRS4 chip that are independent of the MEG electronics system. Those measurements give an indication about the timing resolutions reachable with the DRS4 chip. Section 4.2 studies the influence of clock cables on the timing measurement. Such clock cables ensure the synchronization between the DRS4 chips.

4.1 Timing Resolution Measurements

The goal of the measurements described in this section is to determine the timing resolution of the DRS4 chip. Those measurements are not done with the DRS chips implemented in the MEG detector as the electronic chain may influence the timing resolution. Section 4.1.1 argues why a timing calibration of the DRS4 chip is required. The measurement setup and the analysis methods to determine the timing resolution are described in Section 4.1.2. Finally, the results of the timing resolution measurements are presented in Section 4.1.3.

4.1.1 Timing Calibration

The functional principle of the DRS chip is based on a domino wave that propagates continuously through an array of 1024 inverters. The propagation speed of the wave depends on

external factors such as the temperature. To address this problem, the propagation speed is locked to a reference clock via a phase-locked loop (PLL) that ensures constant sampling rates [60]. However, due to transistor variations in the inverter chain, the 1024 time bins of the sampled time window have not equal bin widths. Each time bin i has a slightly different bin width Δt_i which varies from the theoretical bin width Δt . The theoretical bin width is given by $\Delta t = 1/f$ with f the sampling rate. The integrated nonlinearity I_j is defined as the integral over the differences between theoretical and real bin widths up to a certain bin j :

$$I_j = \sum_{i=0}^j (\Delta t - \Delta t_i). \quad (4.1)$$

Figure 4.1 shows the distribution of the real bin widths and the resulting integrated nonlinearity for a sampling rate of 1.617 Giga Samples Per Second (GSPS). The plots show that deviations from the theoretical bin width of up to 40 ps occur and that the integrated nonlinearity reaches up to 2.7 ns. To reach timing resolutions of a few picoseconds, a timing calibration of the DRS4 chip is therefore required to determine the real bin widths.

The MEG collaboration uses an external square wave with known frequency but random phase to calibrate the bin widths. The measured time difference between two rising zero-crossings is compared with the theoretical value and all bins within that period are scaled to fit to the theoretical period. This procedure is repeated iteratively for many events until the bin widths stabilize.

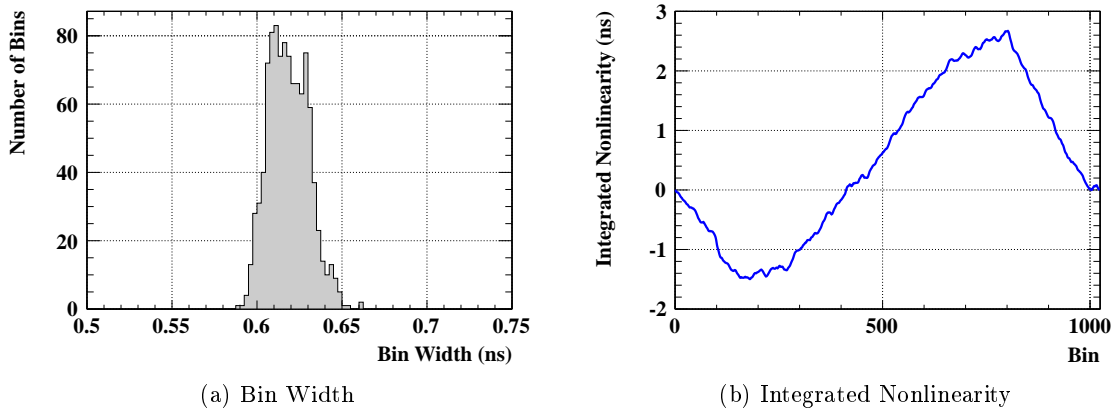


Figure 4.1: Distribution of the real widths of all 1024 bins of a DRS4 chip (a) and the resulting integrated nonlinearity (b). Both plots are obtained with a sampling rate of 1.617 GSPS, the theoretical bin width is therefore given by 0.619 ns.

4.1.2 Measuring Principle

The setup for the timing resolution measurements is shown in Fig. 4.2. A pulse generator produces a triangular pulse with a certain height, leading edge, and trailing edge, each individually adjustable. The generated pulses are split into two signals where the first signal is

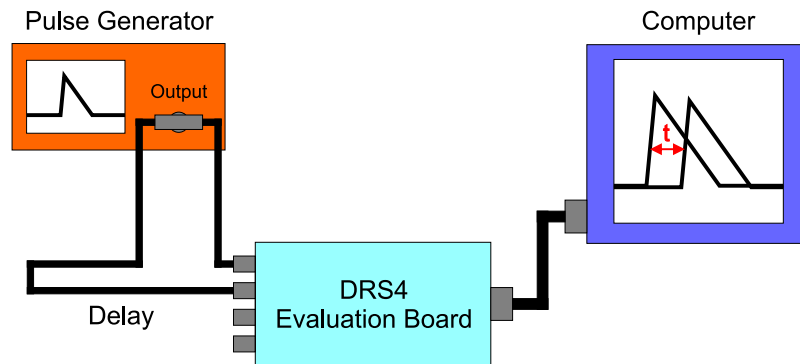


Figure 4.2: Measuring principle to determine the timing resolution of a DRS4 chip.

directly connected to a DRS4 evaluation board [76]. The second signal is delayed with cables before it is read out by the second input channel of the evaluation board. This evaluation board contains one DRS4 chip with four input channels. The incoming signals are digitized and the waveforms are read out via an USB 2.0 interface. This interface also powers the evaluation board so that no additional power supply is necessary. An example of a signal read out with 1.617 GSPS is shown in Fig. 4.3a.

The evaluation board contains a reference clock of 132 MHz which is used to perform timing calibrations of the DRS4 chip. The waveform of this clock signal read out with 1.617 GSPS is shown in Fig. 4.3b. The timing of each zero-crossing of the clock signal is measured with linear interpolation. The time differences between two rising or falling zero-crossings are compared with the theoretical period and the widths of the bins within that period are scaled to fit

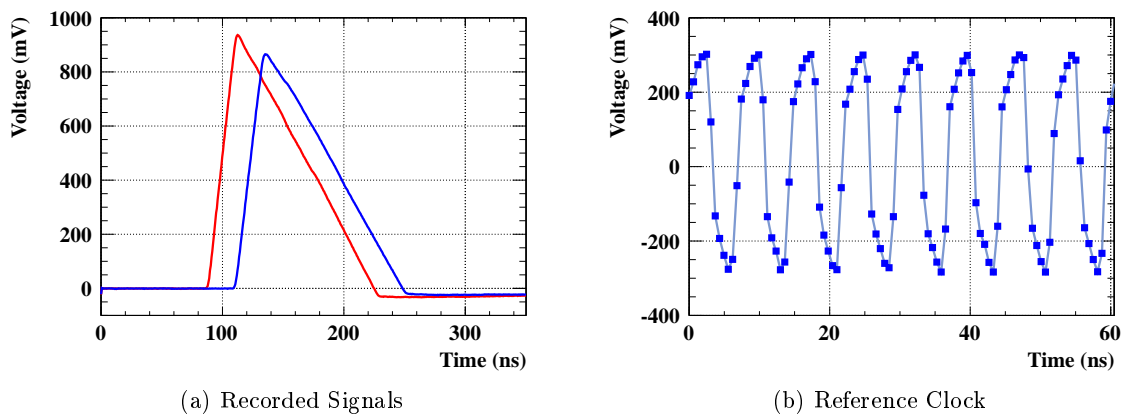


Figure 4.3: An example of a signal digitized by the DRS4 chip where the second signal is delayed by 24 ns (a) and the 132 MHz reference clock used for the DRS4 timing calibration (b). A sampling rate of 1.617 GSPS was chosen to obtain those plots and both plots show only parts of the sampled time window.

to this value. This procedure is repeated iteratively for many events until the bin widths stabilize. The information about the obtained timing calibration, that is, the real bin width of each of the 1024 bins, is stored in a EEPROM on the evaluation board. Therefore, no external clock signals are necessary to perform the timing calibration of the evaluation board.

The recorded waveforms from the pulse generator and the corresponding timing calibration information are analyzed with two different methods to determine the time difference between the first and the delayed signal.

The first analysis method determines the timing of the signals with linear interpolation. A threshold value is chosen and the two timing bins of the leading edge whose bin contents are just below and above this threshold are identified. The exact timing of the threshold crossing is calculated with linear interpolation. The time difference between the two signals is obtained by comparing the timing of the threshold crossings of both signals.

As this analysis method strongly depends on noise, a second analysis method is applied to determine the timing resolution of the DRS4 chip. This analysis method uses a template of the generated pulse that is obtained by recording 5'000 signals¹. Each timing bin has a different bin width due to timing calibration and the signal trigger fires arbitrary in one of the timing bins. As a consequence, the signals cannot be shifted together while keeping the original signal waveform as this would lead to a loss of the timing calibration information. To address this challenge, an equidistant timing grid is superimposed over the signal waveform and the signal values at the timing grid are calculated with linear interpolation. By shifting together the recorded signals and averaging them, a template array is calculated for the 1024 timing bins. To obtain an unbinned template function, a natural cubic spline curve is evaluated that goes through the template array points. The signals recorded for the timing resolution determination are fitted with this template function using the Levenberg-Marquardt algorithm [77] to obtain the timing of the signals. By comparing the timing of the first and the delayed signal, the time difference is evaluated.

Repeating these analysis procedures for 5'000 recorded signals results in a distribution of measured time delays. The distribution is fitted with a Gaussian function and the obtained value for sigma denotes the timing resolution.

4.1.3 Results

In the following, the most important results of the timing resolution measurements are presented. First, the effect of the timing calibration is demonstrated. For that purpose, triangular pulses with a height of 1450 mV, a leading edge of 18.5 ns, and a trailing edge of 93.5 ns are generated with the pulse generator². The generated pulses are split into two signals and are digitized by a DRS4 evaluation board with a sampling rate of 1.617 GSPS. The time delay between the two signals is chosen to be 0 ns for the first test and 200 ns for the second test. The stored waveforms are analyzed with the template analysis method, which is described in

¹Those signals are only used to calculate the template and are not used to determine the timing resolution of the DRS4 chip.

²The specified pulse height of 1450 mV is the pulse generator setting. After splitting the signals, the pulse height at the DRS4 input is approximately 940 mV.

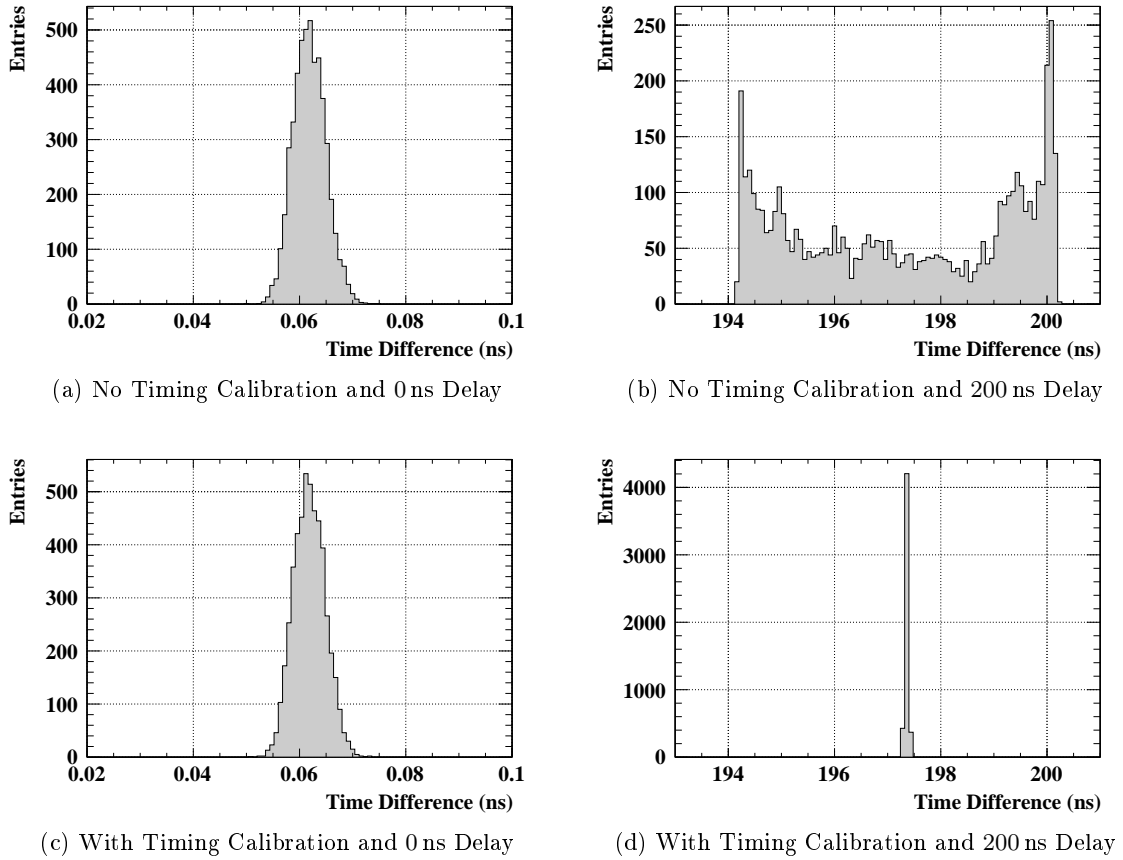


Figure 4.4: Calculated time differences between two signals separated by 0 ns if the timing calibration information is ignored (a) or used (c) for the analysis and the calculated time differences between two signal separated by 200 ns if the timing calibration information is ignored (b) or used (d) for the analysis.

the previous section. Figures 4.4a and 4.4b show the calculated time differences between the two pulses for both tests if the timing calibration information is not used for the analysis. In case of a 0 ns delay between the pulses, the timing resolution is 3 ps. With a time delay of 200 ns, the time resolution is worse than the width of a timing bin that is given by 619 ps. In contrast, Figs. 4.4c and 4.4d show the time differences between the two pulses for both tests if the timing calibration information is used for the analysis. The timing resolution calculation results in 3 ps for 0 ns delay and 28 ps for 200 ns delay. Those examples show that a timing calibration of the DRS4 chip is necessary to reach reasonable timing resolutions. However, the fact that the timing resolution is worse for longer time delays shows that the timing calibration is not perfect.

The electronic noise on the DRS4 evaluation board input channels is approximately 0.32 mV in RMS. This noise causes time jitter that worsens the timing resolution. To estimate the influence of noise on the timing resolution, triangular pulses with a leading edge of 18.5 ns

and a trailing edge of 93.5 ns are generated with the pulse generator. The generated pulses are split into two signals and are digitized by a DRS4 evaluation board with a sampling rate of 1.617 GSPS. The time delay between the two signals is chosen to be 0 ns. Four different measurements are done each with different pulse heights, namely 550 mV, 850 mV, 1150 mV, and 1450 mV. The recorded signals are analyzed with the linear and the template method, both using the timing calibration information. The results of this analysis are presented in Fig. 4.5a, which shows the timing resolution as a function of the chosen pulse height and the analysis method. The plot shows that the timing resolution becomes worse with decreased pulse height as the influence of the noise gets stronger. In addition, the results show that the template analysis method provides more accurate results and is more noise independent than the linear analysis method. As a consequence, the remaining analyses in this section are done with the template analysis method.

If the timing bins are not perfectly calibrated, the timing resolution is expected to become worse with larger time delays between the two signals. To describe the relation between delay and resolution, triangular pulses with a height of 1450 mV, a leading edge of 18.5 ns, and a trailing edge of 93.5 ns are generated with the pulse generator and then split into two signals. Both signals are connected to the DRS4 evaluation board and are digitized with a sampling rate of 1.617 GSPS. The first signal is directly connected and the second one is delayed with cables of different lengths. The recorded signals are analyzed with the template analysis method. The resulting correlation between time delay and resolution is shown in Fig. 4.5b. The plot shows that the resolution is 3 ps for 0 ns delay and 37 ps for 283 ns delay and becomes therefore worse with increased time delay between the two signals. In addition, the curve shows an unexpected improved timing resolution for a time delay of 34 ns.

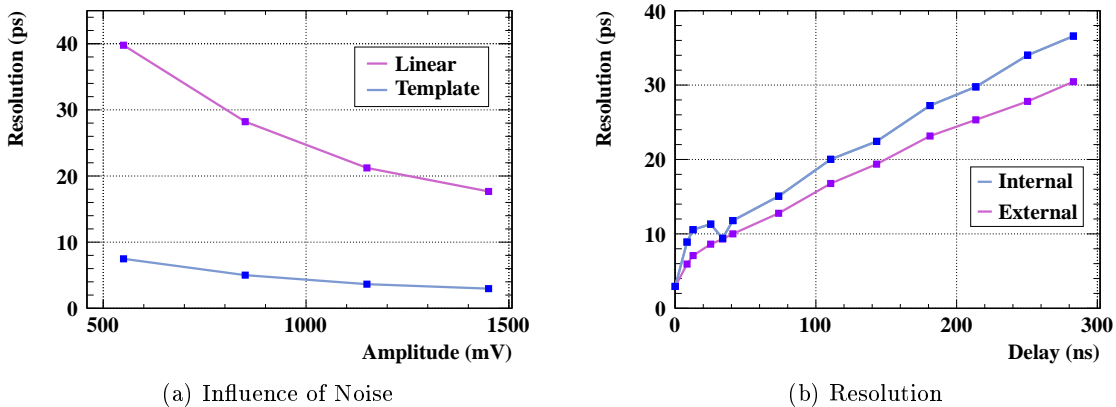


Figure 4.5: The relation between pulse height and timing resolution is shown in (a). The results obtained with linear interpolation and natural cubic spline template are shown to compare the two analysis methods. The timing resolution as a function of the time delay between the two pulses is shown in (b). The plot shows the results obtained with two different calibration clocks, namely the internal clock on the evaluation board and an external sine wave.

In order to find the reason for the improved timing resolution for 34 ns time delay, a special measurement is performed. The timing of the DRS4 chip on the evaluation board is calibrated as usual with the on board clock. A square pulse with a frequency of 19.44 MHz is connected to the DRS evaluation board and the waveform is digitized with a sampling rate of 1.617 GSPS. The timing of the leading and falling edges are determined by using a template. The template is calculated with the same method as used for the triangular shaped pulses described before. With this method, the time length of each period is determined and it is stored as a function of the corresponding time bin. Repeating this measurement 5'000 times and averaging over the measured periods in each time bin results in the plot shown in Fig. 4.6a. In principle, a random fluctuation around the theoretical period length of 51.44 ns would be expected but the plot shows a periodic pattern. The Fourier transform of this distribution is presented in Fig. 4.6c and shows a clear excess at approximately 30 MHz. The timing calibration is redone with the same calibration algorithm but with an external 132 MHz sine wave instead

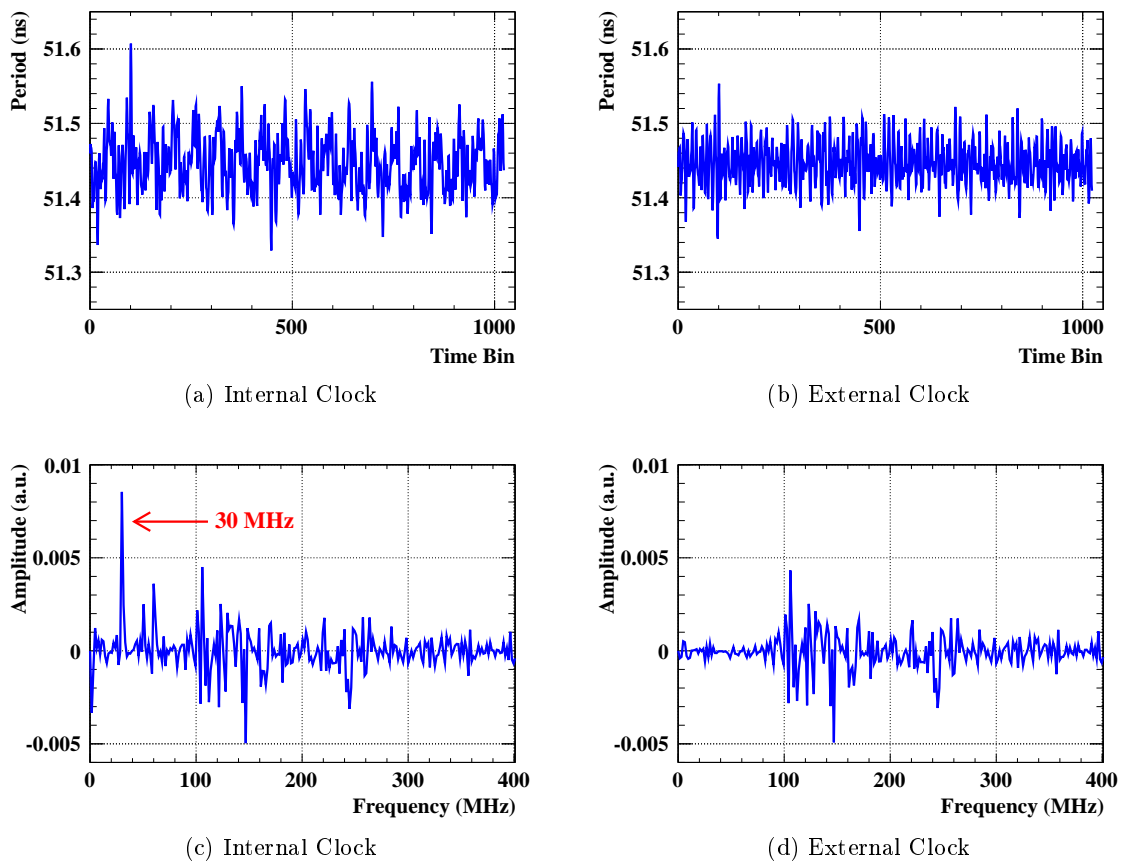


Figure 4.6: The measured periods of a square signal as a function of the corresponding time bin is shown in (a) and (b) for a timing calibration using the internal clock on the evaluation board and an external sine wave, respectively. The corresponding Fourier transforms of the obtained distributions are shown in (c) and (d).

of the on board clock. The previously described measurement is repeated and the resulting distribution is shown in Fig. 4.6b. The plot shows no pattern which is also proven by the Fourier transform of the distribution shown in Fig. 4.6d. The excess at 30 MHz vanishes if an external clock is used for the timing calibration.

To check if the timing calibration with an external clock improves the timing resolution, the resolution measurements with the delayed second signal are repeated. The obtained timing resolutions as a function of the delay between the two signals are shown in Fig. 4.5b. The plot shows that the resolution is 3 ps for 0 ns delay and 30 ps for 283 ns delay. The timing resolution with the timing calibration using the external clock is therefore always better than the resolution obtained with the timing calibration using the internal clock.

In conclusion, the timing resolution measurements showed that the timing calibration of the DRS4 chip is necessary to ensure timing resolutions of less than 100 ps. Furthermore, it was shown that the electrical noise has non-negligible impact on the timing resolution. It is therefore recommended to use analysis methods that are almost independent of noise and, if possible, to digitize signals with large pulse heights. Finally, it was shown that the internal clock on the evaluation board causes a periodic interference that worsens the timing resolution. This deficit can be eliminated by using an external sine wave with the same frequency as the internal clock. Note that this effect has no impact on timing measurements of the MEG detector as the timing calibration is performed with an external clock signal.

During the studies with the evaluation board, it turned out that optimizing the PLL parameters of the DRS4 mezzanine boards improve the timing resolution of the MEG experiment dramatically. After hardware modifications of the mezzanine boards, the timing resolution of the photon detection is improved to 67 ps. Nevertheless, the knowledge gained from the studies presented in this section contributes to future detector upgrades. For example, a new generation of waveform digitizers, the DRS5 chip, is currently being developed at the PSI [78].

4.2 Influence of Clock Cables

To synchronize the DRS chips of the MEG experiment, they are connected to a 19.44 MHz external global clock via clock cables. All DRS chips are calibrated before the physics data taking period starts. If problems with the synchronization occurs during the run, the affected clock cables are exchanged by new ones. Such synchronization problems can be caused, for example, by broken clock cable connectors. Until run 2011, no additional timing calibration was performed after a clock cable exchange as it was assumed that those exchanges do not affect the timing measurement. After run 2010, short test runs were performed to confirm this assumption or to estimate the impact of clock cable exchanges.

The clock cable tests are performed with the photomultiplier tube (PMT) signals of the liquid xenon detector. An LED calibration run³ with approximately 3'000 triggered events is recorded with the present detector configuration to have a reference measurement (“reference”).

³Details about LED calibrations are presented in Chapter 2.

Then, the clock cables of 14 VME boards are swapped according to the following schema:

$$\begin{aligned}
 4-4-1 &\leftrightarrow 4-5-1 \\
 4-6-1 &\leftrightarrow 4-7-1 \\
 4-8-1 &\leftrightarrow 4-9-1 \\
 4-10-1 &\leftrightarrow 4-11-1 \\
 4-12-1 &\leftrightarrow 4-13-1 \\
 4-14-1 &\leftrightarrow 4-15-1 \\
 4-16-1 &\leftrightarrow 4-17-1
 \end{aligned} \tag{4.2}$$

The numbers 4-4-1 to 4-17-1 are the identification codes of the boards. Each VME board hosts four DRS4 chips and can therefore digitize 16 signals as described in Chapter 2. In total 219 PMTs are affected by the cable swapping as some of the DRS input channels are not assigned. The LED calibration is repeated with this clock cable configuration (“swapped”). Finally, all cables are reconnected to their origin boards and the LED calibration run is redone to have a control measurement (“control”).

To check the influence of the cable swapping, the timing t_k of each PMT k ($k = 0, \dots, 845$) is calculated for each event. The time measurement t_j of one PMT j that is not affected by the cable swapping is defined as reference time. The relative timing $t(i) = t_i - t_j$ of all other PMTs i ($i = 0, \dots, 845 \wedge i \neq j$) to this particular reference PMT is calculated for each event. For each PMT, the obtained distribution is fitted with a single Gaussian function. The obtained result for the mean value is used as the relative time between analyzed and reference PMT. This procedure is repeated for the reference, the swapped, and the control measurement resulting in the relative times $t_R(i)$, $t_S(i)$, and $t_C(i)$, respectively. For each PMT, the following time differences are calculated:

$$\begin{aligned}
 \Delta t_{RS}(i) &= t_R(i) - t_S(i) \\
 \Delta t_{RC}(i) &= t_R(i) - t_C(i).
 \end{aligned} \tag{4.3}$$

For PMTs that are not affected by the cable swapping, it is expected that both Δt_{RS} and Δt_{RC} do not show anomalies. The same applies to PMTs on the affected VME boards if the cable swapping has no influence. But if the clock cable swapping influences the timing measurement, it is expected that the corresponding PMTs have a Δt_{RC} value that is comparable with the ones of the not affected PMTs while the value of Δt_{RS} shows significant deviations.

Figure 4.7 shows the result of this analysis with PMT 845 as reference PMT. The measured values of Δt_{RC} are shown in Fig. 4.7a and the corresponding results for Δt_{RS} are presented in Fig. 4.7b. The PMTs affected and not affected by the cable swapping are visually highlighted with different colors. Figure 4.7c and Fig. 4.7d show the same results than Fig. 4.7a and Fig. 4.7b but the curves for the affected PMTs are normalized to the number of not affected PMTs to enhance the visual comparability of the plots. The normalized curves are not used for the following discussion. The RMS of the Δt_{RC} distribution is 23 ps and differentiating between PMTs results in 24 ps for affected PMTs and 23 ps for not affected PMTs. Therefore, no significant deviations between affected and not affected PMTs can be identified. Looking at the Δt_{RS} distribution results in a completely different conclusion, namely 32 ps for all PMTs, 43 ps for affected PMTs, and 26 ps for not affected PMTs. This means that not affected PMTs

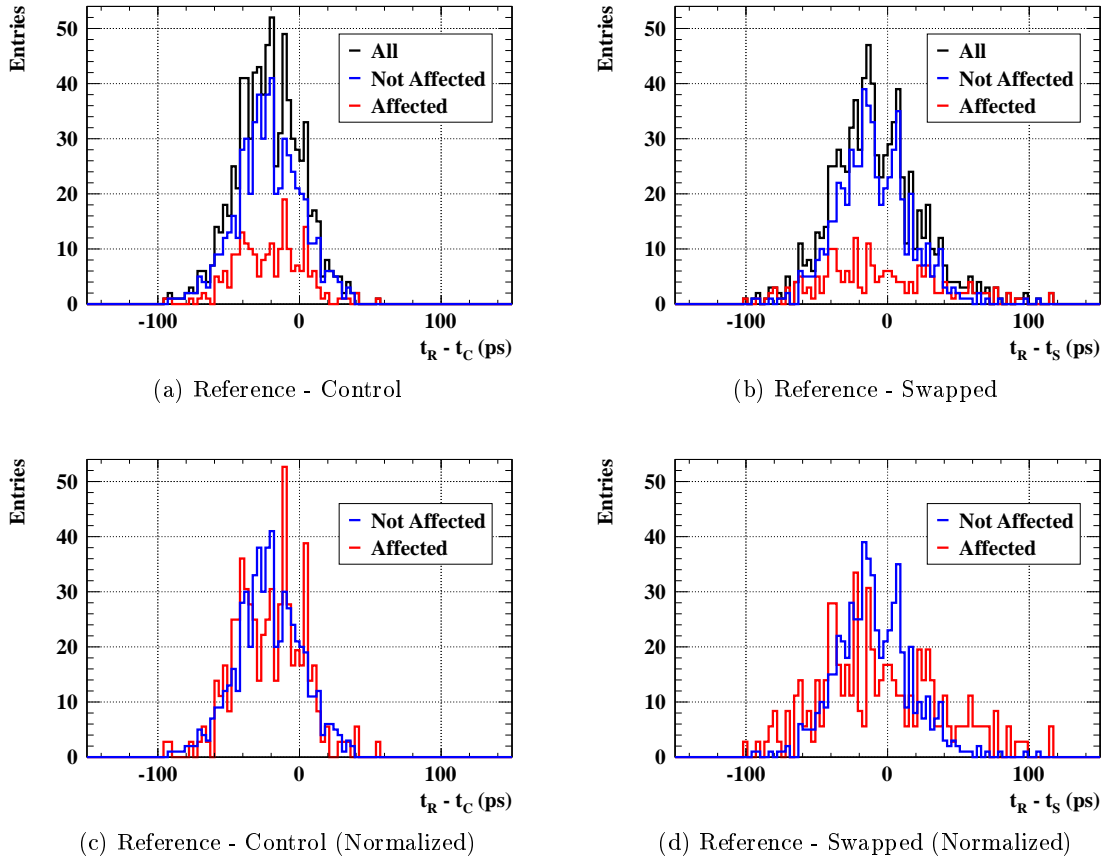


Figure 4.7: Obtained values for Δt_{RC} , that is, the relative time differences between the reference and the control measurement (a) and the obtained values for Δt_{RS} , that is, the relative time differences between the reference measurement and the measurement with the swapped clock cables (b). The affected and not affected PMTs are visually highlighted. Figures (c) and (d) show the same results than (a) and (b) but the curves for the affected PMTs are normalized to the number of not affected PMTs to enhance the visual comparability of the plots.

have an RMS value that is in the same range as the ones obtained from the Δt_{RC} distributions but the affected PMTs have a significantly higher RMS value. As conclusion, swapping the clock cables seems to influence the timing measurement of the affected PMTs.

To improve the previously described analysis, the timing of an entire VME board instead of the timing of single PMTs is analyzed. For that purpose, the arithmetic mean T_I of the time measurements of all DRS chips on a VME board I is calculated for each event. The time measurement T_J of one VME board J that is not affected by the cable swapping is defined as reference time. For this analysis, the reference board is defined to be the board with the identification code 5-12-1. The relative timing $T(I) = T_I - T_J$ of all other VME boards to this particular reference board is calculated for each event and the obtained distributions are

fitted with a single Gaussian function. The obtained result for the mean value is used as the relative time between the analyzed and the reference board. This procedure is repeated for the reference, the swapped, and the control run resulting in the relative times $T_R(I)$, $T_S(I)$, and $T_C(I)$, respectively. For each VME board, the following time differences are calculated:

$$\begin{aligned}\Delta T_{RS}(I) &= T_R(I) - T_S(I) \\ \Delta T_{RC}(I) &= T_R(I) - T_C(I).\end{aligned}\tag{4.4}$$

Similar to the previous test, it is expected that the difference between reference and control measurement shows no anomalies neither for affected nor for not affected VME boards. The same is expected for the difference between reference measurement and measurement with swapped clock cables by only looking at not affected VME boards.

The resulting time differences between the three recorded LED runs for 14 VME boards that are not affected by the clock cable swapping are shown in Table 4.1a. Both time differences ΔT_{RC} and ΔT_{RS} are in the range of approximately 10 ps and meet therefore the expectations. The corresponding results of the VME boards affected by the cable swapping are presented in Table 4.1b. The time differences ΔT_{RC} between reference and control measurement are approximately 10 ps and are therefore comparable with the results of the not affected VME boards. However, by looking at the time differences between reference measurement and measurement with swapped cables, time differences of up to 65 ps occur. In addition, the results show that the two VME boards with swapped clock cable show always similar deviations with opposite sign. Therefore, this analysis proves that changing the clock cable can have a significant influence on the timing measurement of up to 65 ps. After exchanging a clock cable due to synchronization problems, it is therefore necessary to redo the timing calibration or to estimate the impact with calibration runs as described in this section.

4.3 Summary

Timing resolution measurements were performed with the DRS4 evaluation board to determine the timing resolution of the DRS4 chip independent of the MEG electronics system. Those measurements showed that timing calibration of the DRS4 chip is necessary to ensure timing resolutions less than 100 ps. Furthermore, it was proven that the electrical noise has non-negligible impact on the timing resolution. Finally, it was shown that the internal clock on the evaluation board causes a periodic interference that worsens the timing resolution. By using an external sine wave with the same frequency as the internal clock for the timing calibration, the interference vanishes. In addition, the impact of swapping clock cables on the timing measurement was studied. The clock cables are used to synchronize the DRS chips of the MEG experiment. By performing special calibration runs with different clock cable configurations, it was proven that an exchanged clock cable can influence the timing measurement by up to 65 ps. It is therefore necessary to redo the timing calibration after clock cable exchanges.

Table 4.1: Results of the clock cable analysis of 14 VME boards that are not affected by the cable swapping (a) and 14 VME boards that are affected (b). The board identification code is listed together with the obtained time difference between reference and control measurement ΔT_{RC} and the time difference between the reference measurement and the measurement with swapped clock cables ΔT_{RS} . For the affected VME boards, the associated boards with exchanged clock cables are highlighted with different shades of gray.

| (a) Not Affected VME Boards | | | (b) Affected VME Boards | | |
|-----------------------------|----------------------|----------------------|-------------------------|----------------------|----------------------|
| Board | ΔT_{RC} (ps) | ΔT_{RS} (ps) | Board | ΔT_{RC} (ps) | ΔT_{RS} (ps) |
| 4-4-2 | 14 | -9 | 4-4-1 | 11 | -46 |
| 4-5-2 | -2 | -8 | 4-5-1 | -1 | 38 |
| 4-6-2 | 5 | 1 | 4-6-1 | 4 | -49 |
| 4-7-2 | -1 | -19 | 4-7-1 | 1 | 62 |
| 4-10-2 | 8 | -14 | 4-8-1 | 0 | -3 |
| 4-11-2 | -6 | -11 | 4-9-1 | 13 | 8 |
| 4-14-2 | 11 | -1 | 4-10-1 | -2 | -15 |
| 4-15-2 | 6 | -5 | 4-11-1 | 2 | 11 |
| 5-2-1 | 0 | -11 | 4-12-1 | -4 | 37 |
| 5-2-2 | 16 | 5 | 4-13-1 | 8 | -39 |
| 5-3-1 | 2 | -9 | 4-14-1 | -9 | -17 |
| 5-3-2 | 2 | -1 | 4-15-1 | 8 | 9 |
| 5-5-1 | 0 | -14 | 4-16-1 | 2 | -46 |
| 5-5-2 | 6 | -10 | 4-17-1 | 18 | 65 |

Chapter 5

Liquid Xenon Monitoring with a Neutron Generator

The liquid xenon scintillation detector of the MEG experiment measures the kinematic variables of photons. To ensure high performance measurements, it is necessary to monitor and calibrate the detector frequently and precisely. The gain and quantum efficiency of the photomultiplier tubes (PMTs) are calibrated with LEDs and alpha sources. In addition, a Cockcroft-Walton (CW) proton accelerator is used to monitor the detector stability, to calibrate the energy scale, and to check the detector uniformity. Once per year, the MEG collaboration performs the pion charge exchange (CEX) calibration to calibrate the energy scale of the calorimeter and to measure the energy and timing resolutions at 54.9 MeV. The liquid xenon detector and all those calibration and monitoring methods are described in Chapter 2.

Both the CW and the CEX methods cannot be performed in parallel with the muon beam stopping in the MEG target as they require different particle beams and different targets. Therefore, an additional monitoring tool is desired that checks the detector performance in the presence of the muon beam. The MEG collaboration adopted a monitoring method based on a pulsed neutron generator. A detailed description of the method and preparatory studies are presented in [67]. During run 2010, the neutron generator monitoring tool was added to the usual calibration procedure, which is performed two or three times per week during the physics data taking period. The experimental setup is described in Section 5.1 and the neutron generator data collected during run 2010 is analyzed in Section 5.2. Finally, Section 5.3 illustrates the effect of the dead channel recovery.

5.1 Experimental Setup

A pulsed neutron generator is used by the MEG collaboration to produce neutrons with energies of 2.5 MeV by means of the nuclear reaction $D + D \rightarrow {}^3\text{He} + n$. The pulsed operation allows a good signal-to-noise ratio and therefore a good performance of this monitoring

method even if the muon beam is stopped in the target with $3 \cdot 10^7 \mu^+/\text{s}$. The neutron generator produces $2.5 \cdot 10^4$ neutrons per pulse with a frequency of 30 Hz and a pulse length of approximately $10 \mu\text{s}$. The generated neutrons are thermalized in a polyethylene moderator to ensure an effective capture in nickel plates. Nickel is chosen because of its unique characteristic to emit a single photon at an energy of 9 MeV with a relatively large probability of approximately 34%. Neutron generator, moderator, and nickel plates are mounted outside the COBRA magnet at the opposite site than the liquid xenon detector as shown in Fig. 5.1a. A picture of the neutron generator is shown in Fig. 5.1b.

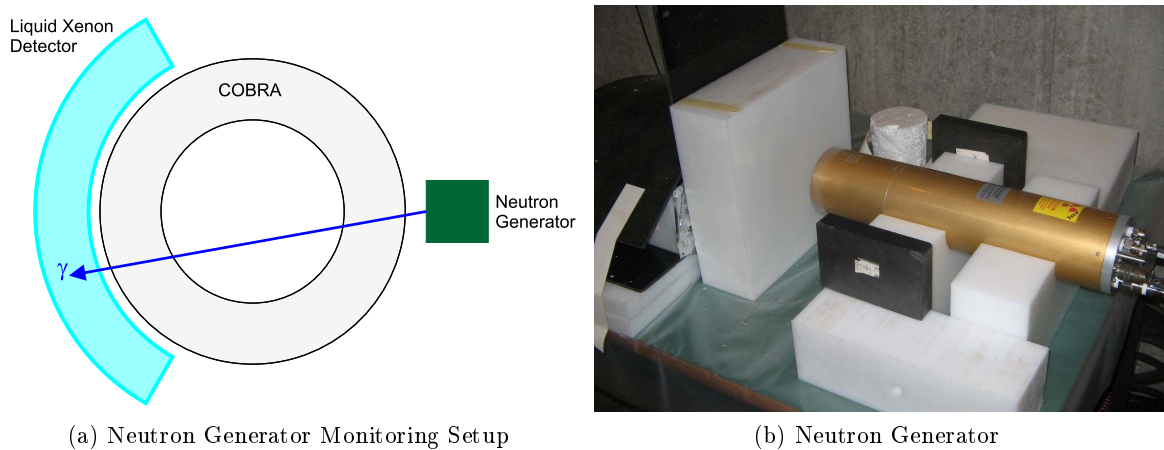


Figure 5.1: The experimental setup of the neutron generator monitoring method (a) and a picture of the neutron generator [79] (b).

Two different trigger types are used to collect neutron generator data. Trigger #15 is correlated with the neutron generator pulse to record photons of the neutron capture in nickel. The trigger selects a certain photon energy range and a time window of 100 ns delayed by $15 \mu\text{s}$ with respect to the neutron pulse. Trigger #29 selects the same photon energy range and has the same time window length of 100 ns but trigger #29 is not correlated to the neutron pulse. Therefore, trigger #29 is used to analyze the background spectrum.

One neutron monitoring includes three data sets: one set with blocked muon beam, one set during which the beam blocker is opened, and one set with the muon beam stopped in the target with $3 \cdot 10^7 \mu^+/\text{s}$. One data set is composed of six runs each with 5'000 triggered events and takes approximately 18 minutes. The pre-scaling factors for trigger #15 and #29 are chosen to be different for runs with or without muon beam.

5.2 Data Analysis

The energy spectra of neutron generator data sets with and without muon beam are shown in Fig. 5.2. The plotted event distributions show data collected with trigger #15. To remove background events, the following cuts are applied to the data sets:

- Alpha events from the alpha sources mounted inside the liquid xenon detector are removed by applying the cut $(\text{waveform height})/(\text{waveform charge}) > 6.4$.
- Cosmic ray events are removed with the cut $(\text{number of PMTs inner face})/(\text{number of PMTs outer face}) > 0.3$.

To select events with a good reconstruction quality, the following cuts are also applied to the data sets:

- The cut $2 \text{ cm} < w < 30 \text{ cm}$, with w the photon detection depth within the liquid xenon detector, removes shallow events.
- The cut $|v| < 65 \text{ cm}$ removes events at the top and the bottom face of the liquid xenon detector.

Applying these cuts to data sets collected with and without muon beam results in the event distributions shown in Fig. 5.2. The cuts remove approximately 55 % of all events of the data sets. The large peak corresponds to the 9 MeV photon line from neutron capture in nickel. The lower energy lines from the nickel capture are visible on the left of the energy spectrum. Events with lower energy are suppressed by the trigger condition. The 9 MeV peak and the contributions from the lower energy lines are fitted with two Gaussian functions to obtain the position of the 9 MeV peak and monitor its temporal development.

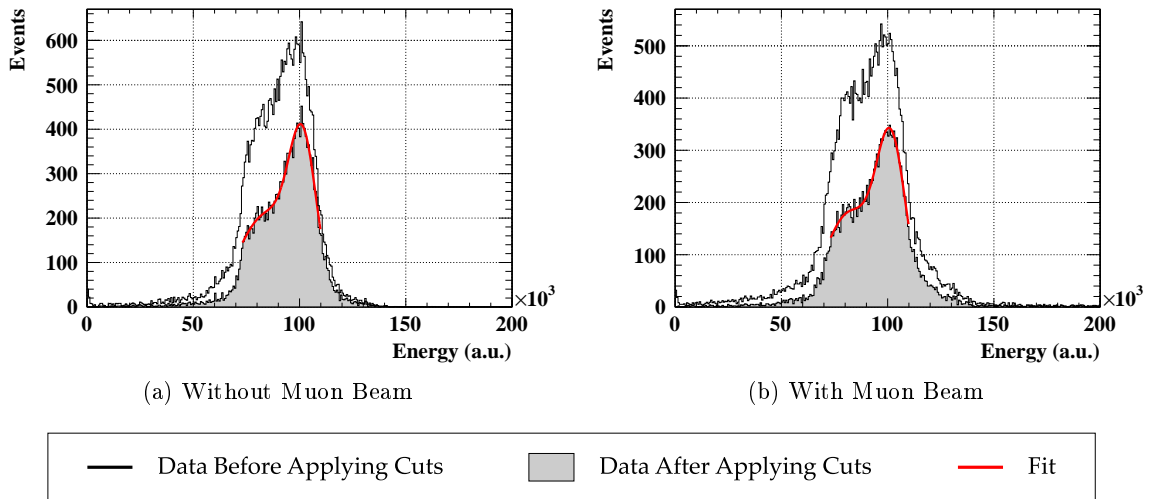


Figure 5.2: Energy spectra of the neutron generator data collected during periods when the muon beam was blocked (a) or when the muon beam was stopped in the target with $3 \cdot 10^7 \mu^+ / \text{s}$ (b). The curves show the data collected with trigger #15 and the filled areas show the same data after applying the cuts described in this chapter. In addition, the fit function consisting of two Gaussian functions is shown.

The energy spectra of the data collected during periods with and without muon beam look very similar except of small differences at the higher energy edge. By analyzing data collected with trigger #29 it should be possible to produce templates that describe the background, which is not induced by the neutron generator. The background template can be subtracted from the energy spectra obtained with trigger #15 data. Looking at data collected with trigger #29 and applying the cuts described in this chapter results in almost empty data sets for periods without muon beam while the data sets contain events if the muon beam is stopped in the target. Thus, the stopped muon beam generates background events for the neutron generator data. Unfortunately, the chosen pre-scaling factors for the neutron generator runs in 2010 were not optimized so that the data sets collected with trigger #29 do not contain enough events to produce a template. However, at the beginning of run 2010, some neutron generator test runs were performed with modified pre-scaling factors. One of these runs is used to generate a template to describe the background induced by the muon beam. This template is shown in Fig. 5.3a. For each neutron monitoring data set collected with muon beam, the template has to be normalized with the corresponding pre-scaling factors and the number of collected events. The normalized template is then subtracted from the data set as shown in Fig. 5.3b. The resulting event distribution is fitted with two Gaussian functions to obtain the 9 MeV peak position.

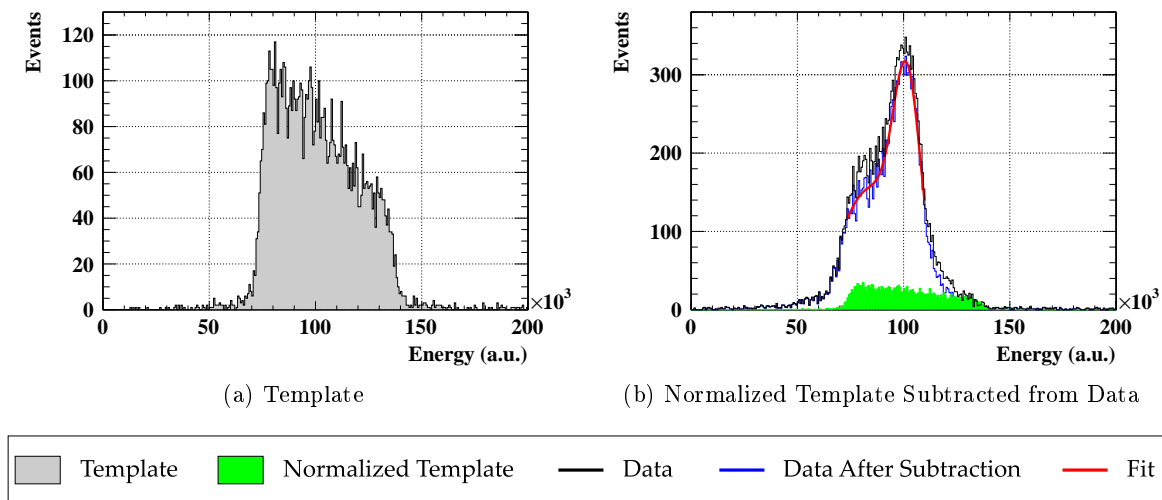


Figure 5.3: The template for the muon beam induced background (a) and the collected data before and after template subtraction as well as the normalized template (b). In addition, the fit function consisting of two Gaussian functions is shown.

After subtracting the background template from the data sets collected when the muon beam was present, the energy spectra with and without blocked muon beam look almost identical. Especially, there is no offset between the positions of the 9 MeV peak which indicates that the energy scale is constant even with variable beam conditions. This is only possible if the gains of the photomultiplier tubes (PMTs) are calibrated correctly as they depend on the beam intensity. Figure 5.4a shows the temporal development of the energy measurements during

a neutron generator monitoring run if constant gain values are used for all runs. The beam blocker is closed at the beginning of the data taking and it is opened at the time indicated by a vertical line. A clear change in the energy response is visible in this plot. By applying calibrated PMT gains, the difference between energy measurements with and without blocked muon beam is reduced as shown in Fig. 5.4b. The neutron generator data is therefore used to check if the PMT gains are calibrated correctly for the different beam intensities.

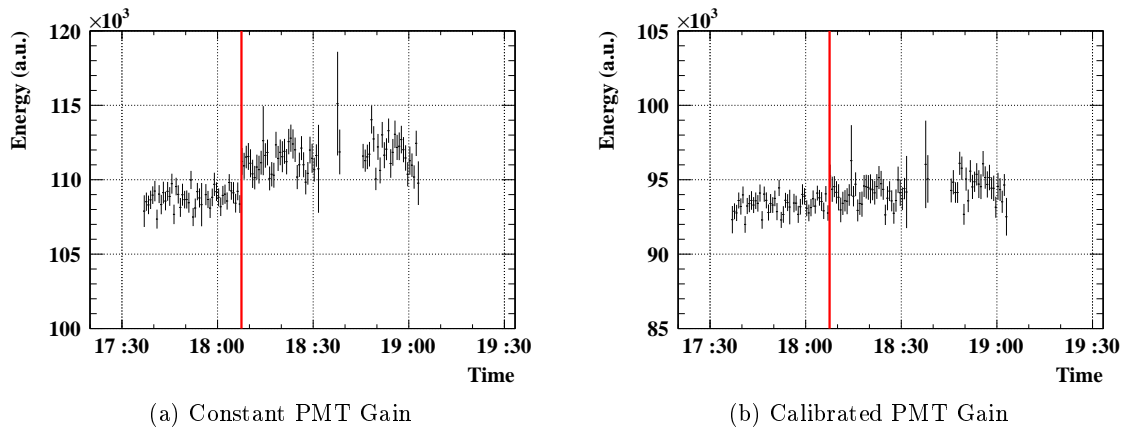


Figure 5.4: Temporal development of the energy measurement during a neutron generator monitoring run. The beam blocker is closed at the beginning and it is opened at the time indicated by the vertical line. The plots show the measured energy in case of constant (a) or calibrated (b) PMT gain values. Muon beam induced background is not subtracted.

Analyzing all neutron generator runs performed in 2010 and plotting the obtained 9 MeV peak positions results in the graph shown in Fig. 5.5. The error bars correspond to the fitting errors. The neutron generator method has a stable performance and is used in run 2011 as standard monitoring tool. To improve the performance and to understand the muon beam induced background better, it is requested to adjust the pre-scaling factors so that enough events are collected with trigger #29. As a consequence, the data taking time for one data set will increase but should be still at an acceptable level (few minutes more than in 2010). In addition, special test runs with different experimental setups (with/without nickel, with/without moderator) and different trigger settings (lower energy threshold) are planned for the future to better understand the performance of this monitoring tool. Furthermore, efforts will be made to use the neutron generator data not only for monitoring but also for calibration purposes such as corrections of non-uniformities in the energy response.

5.3 Dead Channel Recovery

During run 2010, total 8 out of 846 PMTs of the liquid xenon detector were not working. To avoid that the outage of one PMT lowers the energy scale of the scintillation detector, the MEG collaboration implemented the so-called “dead channel recovery” method [80]. The light that would be measured by a broken PMT is estimated by the amount of light measured by

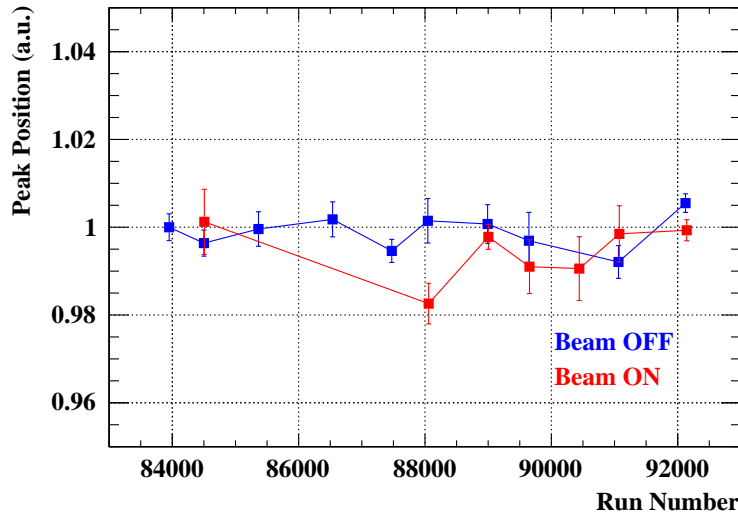


Figure 5.5: Performance of the neutron generator monitoring method during run 2010. The plot shows the relative 9 MeV peak positions obtained from data sets with and without blocked muon beam. Muon beam induced background is subtracted.

the adjacent PMTs. The neutron generator data provides a tool to check how powerful this recovery is. By disabling some PMTs for the analysis, the effect of several missing PMTs on the measured energy is estimated. The analysis is done with four different sets of missing PMTs, namely 8 (original setting), 11, 15, and 22 missing PMTs. The missing PMTs are arbitrarily selected and only the set with 22 missing PMTs contains five PMTs from the inner face of the liquid xenon detector. Figure 5.6 shows the obtained 9 MeV peak positions if the dead channel recovery is used or not. Only five data sets collected without muon beam are used for this study and the fitting errors are skipped to increase the readability of the plots. The plots show that the 9 MeV peak position decreases by up to 2% if the dead channel recovery is not applied. On the other hand, the 9 MeV peak position is stable within 0.5% if the missing PMTs are corrected with the dead channel recovery algorithm. Therefore, the dead channel recovery works satisfactorily even with five missing PMTs in the inner face of the liquid xenon detector and additional 17 missing PMTs on the other faces.

5.4 Summary

To check the performance of the liquid xenon detector in the presence of the muon beam, the MEG collaboration adopted a monitoring method based on a pulsed neutron generator. The neutrons are thermalized and captured in nickel which produces a photon with an energy of 9 MeV. Muon beam induced background is subtracted from the collected data by producing a background template with data collected with a special trigger. After subtracting the background, energy spectra from data collected with and without muon beam are similar. With the neutron generator data, the stability of the liquid xenon detector, the correctness

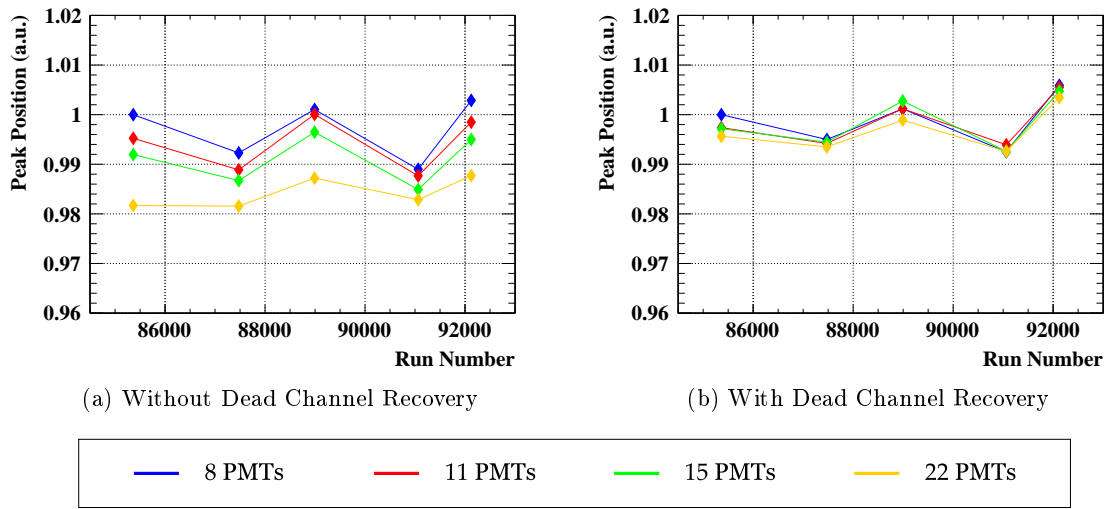


Figure 5.6: Relative 9 MeV peak position for five data sets collected without muon beam. The plots show the results if 8, 11, 15, and 22 PMTs are missing and if the analysis is performed without (a) and with (b) applied dead channel recovery.

of the PMT gain calibrations, and the efficiency of the dead channel recovery is checked. The neutron generator method showed a stable performance during run 2010 and is used as standard monitoring tool during run 2011.

Part II

Physics Analysis

Chapter 6

$\mu^+ \rightarrow e^+ + \gamma$ Search Analysis

The official analysis method of the MEG collaboration to determine the branching ratio of the lepton flavor violating decay $\mu^+ \rightarrow e^+ + \gamma$ is explained in this chapter. In addition, the results of this analysis applied to the data sets collected in 2009 and 2010 are presented. The discussed analysis techniques and all results originate from the MEG collaboration and are partially published in [81].

To prevent the results from any bias, the MEG collaboration applies a blind box analysis technique. Events around the signal region are hidden and are not used for calibrations, background studies, and analysis optimizations. Due to finite detector resolutions, radiative muon decays and accidental background events are expected to be within the $\mu^+ \rightarrow e^+ + \gamma$ signal region. To address this challenge, a maximum likelihood analysis is performed to obtain the number of signal events. The analysis window is chosen to be wide enough to not lose signal efficiency and to allow a simultaneous fitting of both signal and background events. The confidence interval for the branching ratio is obtained by using the Feldman-Cousins unified approach with profile likelihood ordering.

The remainder of this chapter is structured as follows: First, the definitions of the kinematic variables, the blind box, and the analysis window are presented in Section 6.1. The maximum likelihood analysis and the definition of the likelihood function are described in Section 6.2. The required probability density functions are shown in Section 6.3. The confidence level calculation procedure and the required normalization factor are explained in Sections 6.4 and 6.5, respectively. The sensitivity reached by the MEG experiment is presented in Section 6.6 and the results of the maximum likelihood analysis and the confidence level calculation are presented in Section 6.7. Finally, the systematic uncertainties are estimated in Section 6.8.

6.1 Definitions

The used kinematic variables and the analyzed data sets are defined in Section 6.1.1 and Section 6.1.2, respectively. The pre-selection cuts to reduce the amount of data are specified in Section 6.1.3. Section 6.1.4 describes the principle of blind analyses and defines the blind

box used by the MEG collaboration. The analysis window in which the analysis is performed is defined in Section 6.1.5. Finally, the number of background events expected to be within the analysis window is estimated in Section 6.1.6.

6.1.1 Kinematic Variables

Signal events of the decay $\mu^+ \rightarrow e^+ + \gamma$ are characterized by a photon and a positron each carrying an energy of 52.8 MeV, positron and photon must be emitted coincident in time, and they must be emitted back-to-back from the same vertex as described in Chapter 1. To distinguish $\mu^+ \rightarrow e^+ + \gamma$ signals from background events, namely radiative muon decays and accidental coincidences, the MEG collaboration uses five kinematic parameters:

- Photon energy E_γ .
- Positron energy E_e .
- Relative azimuthal angle between positron and photon $\phi_{e\gamma}$ that is defined as $\phi_{e\gamma} = (\pi + \phi_e) - \phi_\gamma$ with ϕ_e and ϕ_γ the azimuthal angles of positron and photon, respectively. The beam axis is taken as z -axis.
- Relative polar angle between positron and photon $\theta_{e\gamma}$ that is defined as $\theta_{e\gamma} = (\pi - \theta_e) - \theta_\gamma$ with θ_e and θ_γ the polar angles of positron and photon, respectively. The beam axis is taken as z -axis.
- Relative timing between positron and photon $t_{e\gamma}$ obtained from the photon timing measurement in the liquid xenon detector, the positron timing measurement in the timing counters, and timing corrections due to particle track lengths.

6.1.2 Data Sets

Data collected by the MEG detector in 2009 and 2010 are analyzed in this and the following chapters. The following data sets are defined:

- 2009 data set: Data collected during physics data taking run 2009.
- 2010 data set: Data collected during physics data taking run 2010.
- Combined data set: Data set containing data collected during physics data taking runs 2009 and 2010.

A detailed description of the physics data taking runs 2009 and 2010 of the MEG experiment and a summary of the corresponding detector resolutions are presented in Chapter 2. It is important to note that the analysis methods described in this and the following chapters are separately applied to all three data sets defined before. This means that the results of the combined data set are not obtained by combining the results of the 2009 and 2010 data analysis.

6.1.3 Pre-Selection

Full reconstruction of all collected events is time consuming as all five kinematic variables must be determined for each event. A fast pre-selection to reduce the amount of data is therefore desirable. The pre-selection cuts are defined as:

$$\begin{aligned} \text{Liquid Xenon / Timing Counter Coincidence:} & \quad -6.9 \text{ ns} \leq t_\gamma - t_{\text{TC}} \leq 4.4 \text{ ns} \\ \text{Drift Chamber / Timing Counter Coincidence:} & \quad |t_{\text{track}} - t_{\text{TC}}| \leq 50 \text{ ns} \end{aligned} \quad (6.1)$$

In this formula, t_γ is the timing of the photon emission assuming the emission point is at the center of the target, t_{TC} is the timing of the timing counter bar hit, and t_{track} is the timing of the positron track in the drift chambers. The window of the liquid xenon and timing counter coincidence is chosen to be asymmetric to not reject signal events with two turn positrons. That are positrons following tracks with two turns in the sensitive volume of the drift chambers before hitting the timing counter. The pre-selection is not based on fully reconstructed kinematics but the cuts are chosen to be loose enough to not discard any signal events. Using these pre-selection cuts reduces the amount of data and makes therefore the analysis faster and more effective.

6.1.4 Blind Box

It is well known that the outcome of an experiment can be biased by the scientist's expectation of the result. This is why blind analysis techniques become increasingly important for scientific experiments, in particular for particle physics experiments. There exist different blind analysis methods as using a hidden signal box, adding or removing events in the signal region, pre-scaling the data set or adding an arbitrary and unknown offset to some observables. An overview of different blind analysis methods used in nuclear and particle physics with some examples is given in [82]. The ANTARES neutrino telescope experiment, for example, searched for relativistic magnetic monopoles [83] by optimizing the analysis with a fraction of 15 % of the whole data set. After fixing the analysis procedure, the remaining 85 % were unblinded and analyzed. For lifetime measurements in particle physics, the usual blind analysis method is to blind the frequency of the reference clock used for the time measurement. Examples for this kind of blind analysis are the MuCap experiment, which determined the muon capture rate in hydrogen gas [84], or the MuLan experiment, which measured the muon lifetime [85]. To search for rare particle decays, a blind box analysis method is well suited as the signature of the corresponding rare decay is usually well known. The E791 collaboration, for example, defined a blind box to search for the decay $K_L^0 \rightarrow \mu^\pm e^\pm$ [86] and the D0 collaboration hid the signal mass region to search for $B_s^0 \rightarrow \mu^+ \mu^-$ [87]. A recent example of an experiment using blind box analysis techniques is the LHCb experiment (CERN) which searches, amongst others, for rare decays as $B_s^0 \rightarrow \mu^+ \mu^-$ and $B^0 \rightarrow \mu^+ \mu^-$ [88]. The MEG collaboration also uses the blind box analysis technique to hide $\mu^+ \rightarrow e^+ + \gamma$ signal events. The blind box is defined as follows:

$$\begin{aligned} \text{Photon Energy:} & \quad |E_\gamma - m_\mu/2| < 4.8 \text{ MeV} \\ \text{Timing:} & \quad |t_{e\gamma}| \leq 1 \text{ ns} \end{aligned} \quad (6.2)$$

In this formula, $m_\mu = 105.6 \text{ MeV}$ is the muon mass. The blind box in the $(E_\gamma, t_{e\gamma})$ plane is shown in Fig. 6.1. The plot shows events of the combined data set with positron energy, azimuthal angle, and polar angle constrained to be within the analysis window, which is defined in the next section. All events falling into the blind box are written to separated and locked data files. Only events outside the blind box are used for calibrations, background studies, and optimization of the analysis. As calibrations might not be fully completed during data taking, the blind box is chosen to be wide enough to cover the signal region in either case. As soon as all calibrations are done and the analysis procedure is fixed, the blinding box is opened and the contained data are analyzed.

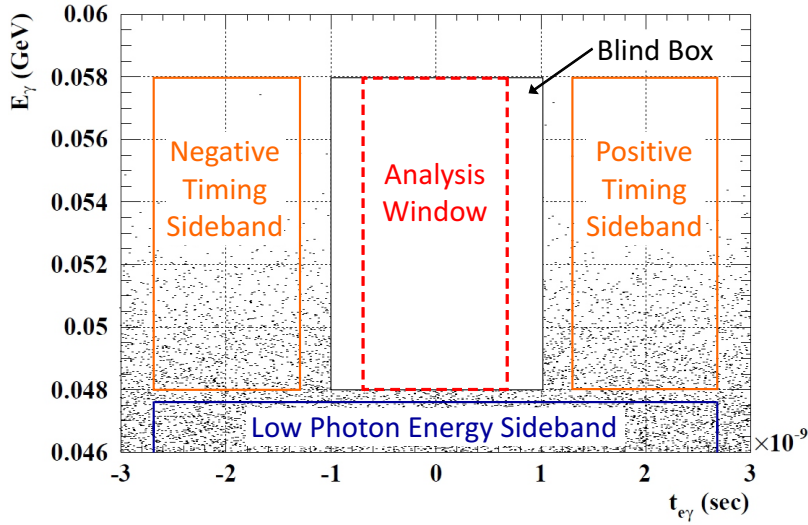


Figure 6.1: The blind box, the analysis window, both timing sidebands, and the low photon energy sideband used by the MEG collaboration are shown in the $(E_\gamma, t_{e\gamma})$ plane. The plot shows events of the combined data set with positron energy, azimuthal angle, and polar angle constrained to be within the analysis window.

6.1.5 Analysis Window

After opening the blind box, a maximum likelihood analysis is performed in the following five-dimensional analysis window:

$$\begin{aligned}
 \text{Photon Energy:} & \quad 48 \text{ MeV} \leq E_\gamma \leq 58 \text{ MeV} \\
 \text{Positron Energy:} & \quad 50 \text{ MeV} \leq E_e \leq 56 \text{ MeV} \\
 \text{Azimuthal Angle:} & \quad |\phi_{e\gamma}| \leq 50 \text{ mrad} \\
 \text{Polar Angle:} & \quad |\theta_{e\gamma}| \leq 50 \text{ mrad} \\
 \text{Timing:} & \quad |t_{e\gamma}| \leq 0.7 \text{ ns}
 \end{aligned} \tag{6.3}$$

The analysis window is shown in Fig. 6.1. It is much wider than a simple signal window to also include enough background events. As a consequence, the number of signal events,

the number of radiative muon decays, and the number of accidental coincidences can be determined simultaneously by the maximum likelihood fit.

6.1.6 Estimations from Sideband Data

So-called sidebands are used to calibrate the detector, to study the background, and to optimize the analysis procedure. This term refers to a well defined region in the kinematic space. The important point is that the sidebands do not include the blind box, that is, the events within the sideband are not hidden. For the MEG experiment, the background distributions in certain sidebands are well known. Therefore, sidebands are used to study the number of background events expected to be within the analysis window and to cross check the analysis procedure by applying it to sideband data instead of events within the analysis window.

Because the distribution of the accidental background is naturally constant over time, it is evident to define timing sidebands. The negative and positive timing sidebands are almost identical with the analysis region except of the timing window which has a positive or negative offset of $\Delta t = 2$ ns. With such a time difference between photon and positron emission, neither signal events nor radiative muon decays are expected to be within the timing sidebands. The definitions of the negative and positive timing sidebands are as follows:

| | Negative Timing Sideband | Positive Timing Sideband | |
|------------------|---------------------------------------------------------|-------------------------------------------------------|-------|
| Photon Energy: | $48 \text{ MeV} \leq E_\gamma \leq 58 \text{ MeV}$ | $48 \text{ MeV} \leq E_\gamma \leq 58 \text{ MeV}$ | |
| Positron Energy: | $50 \text{ MeV} \leq E_e \leq 56 \text{ MeV}$ | $50 \text{ MeV} \leq E_e \leq 56 \text{ MeV}$ | |
| Azimuthal Angle: | $ \phi_{e\gamma} \leq 50 \text{ mrad}$ | $ \phi_{e\gamma} \leq 50 \text{ mrad}$ | (6.4) |
| Polar Angle: | $ \theta_{e\gamma} \leq 50 \text{ mrad}$ | $ \theta_{e\gamma} \leq 50 \text{ mrad}$ | |
| Timing: | $-2.7 \text{ ns} \leq t_{e\gamma} \leq -1.3 \text{ ns}$ | $1.3 \text{ ns} \leq t_{e\gamma} \leq 2.7 \text{ ns}$ | |

The MEG collaboration defined also extended timing sidebands with wider windows for the timing, the photon energy, or the relative angles. Those timing sidebands are used to calculate the probability density functions for accidental background events as described in Section 6.3.

To analyze the radiative muon decay background, a low photon energy sideband is defined. With this sideband, photons with energies in the range of $40 \text{ MeV} < E_\gamma < 47 \text{ MeV}$ are analyzed. The negative and positive timing sidebands and the low photon energy sideband are shown in Fig. 6.1. Additional angular sidebands are defined to check if there are coincidences of photons and positrons that are not predicted from the expected radiative muon decays and accidental coincidences. As this thesis does not deal with those angular sidebands, the results of this analysis are neither presented nor discussed.

The sidebands are also used to estimate the number of radiative muon decays and accidental background events expected to be within the analysis window. Table 6.1 shows the obtained numbers for the 2009, 2010, and combined data sets. The calculation of the expected number of background events is done before opening the blind box. As the blind box is defined in only two kinematic variables, namely the photon energy E_γ and the timing $t_{e\gamma}$, the analysis of a hidden event might show that it is a background event. This is the reason why the obtained expected number of background events has to be updated after opening the blind

box. The numbers presented in Table 6.1 already contain those updates. The number of expected background is needed for the maximum likelihood analysis, which is described in Section 6.2. The likelihood function is constrained to the expected number of background events by Gaussian distributed functions with mean and sigma values corresponding to the numbers shown in Table 6.1.

Table 6.1: Expected number of radiative muon decays (RMD) and accidental background events (ABG) within the analysis window for the 2009, 2010, and combined data sets.

| Data Set | RMD | ABG |
|----------|----------------|------------------|
| 2009 | 27.2 ± 2.8 | 270.9 ± 8.3 |
| 2010 | 52.2 ± 6.0 | 610.8 ± 12.6 |
| combined | 79.4 ± 7.9 | 881.7 ± 15.1 |

6.2 Maximum Likelihood Analysis

Due to finite detector resolutions, radiative muon decays and accidental coincidences are expected to be within the $\mu^+ \rightarrow e^+ + \gamma$ signal region. Consequently, it is not recommended to obtain the number of signal events by defining strong signal cuts as the efficiency of such a cut analysis decreases by optimizing the sensitivity of the chosen cuts. To address this challenge, a maximum likelihood analysis is performed to obtain the number of observed signal events. By applying a maximum likelihood analysis, full information of all events is used for the analysis. This is a useful advantage over the cut analysis which only needs the information whether the event passes the cuts or not. The analysis window defined in Eq. (6.3) is chosen to be wider than the signal region to not lose signal efficiency and to include enough background events. This enables a simultaneous fitting of signal events, radiative muon decays, and accidental background events. Furthermore, performing a maximum likelihood analysis has the advantage that the result is almost independent of the size of the analysis window, edge effects are therefore negligible.

The result of the maximum likelihood analysis should include the number of signal events N_{sig} , the number of radiative muon decays N_{RMD} , and the number of accidental background events N_{ABG} where the sum $N = N_{\text{sig}} + N_{\text{RMD}} + N_{\text{ABG}}$ is not constrained to be equal to the number of observed events N_{obs} . Therefore, the MEG collaboration uses the following extended likelihood function \mathcal{L} with three free parameters:

$$\mathcal{L}(N_{\text{sig}}, N_{\text{RMD}}, N_{\text{ABG}}) = \frac{e^{-N}}{N_{\text{obs}}!} \cdot e^{-\frac{(N_{\text{RMD}} - \langle N_{\text{RMD}} \rangle)^2}{2\sigma_{\text{RMD}}^2}} \cdot e^{-\frac{(N_{\text{ABG}} - \langle N_{\text{ABG}} \rangle)^2}{2\sigma_{\text{ABG}}^2}} \times \prod_{i=1}^{N_{\text{obs}}} (N_{\text{sig}} \cdot S(\vec{x}_i) + N_{\text{RMD}} \cdot R(\vec{x}_i) + N_{\text{ABG}} \cdot A(\vec{x}_i)). \quad (6.5)$$

The five-dimensional vector $\vec{x}_i = (E_\gamma, E_e, \phi_{e\gamma}, \theta_{e\gamma}, t_{e\gamma})_i$ describes the kinematics of the i th event. S , R , and A are the probability density functions for signal events, radiative muon decays, and accidental background events, respectively. The likelihood function is constrained to the expected number of radiative muon decays ($\langle N_{\text{RMD}} \rangle, \sigma_{\text{RMD}}$) and accidental background events ($\langle N_{\text{ABG}} \rangle, \sigma_{\text{ABG}}$). Those values are obtained from sideband data and are listed in Table 6.1. Rather than maximizing the likelihood function shown in Eq. (6.5), the parameters N_{sig} , N_{RMD} , and N_{ABG} are determined by minimizing the negative-log-likelihood (NLL) function using the MINUIT package [89].

6.3 Probability Density Functions

The maximum likelihood analysis requires the probability density functions (PDFs) for signal events S , radiative muon decays R , and accidental background events A . The MEG collaboration uses event-by-event PDFs. This means that different PDFs are prepared for different detector regions and different quality categories. The quality of the positron track reconstruction, for example, depends on the number of fully efficient drift chambers passed by the positron. Therefore, the corresponding PDFs of each event are used for its analysis. The sensitivity (defined in Section 6.6) of the 2010 data set obtained with event-by-event PDFs is about 20 % better than the sensitivity calculated with constant PDFs. Using event-by-event PDFs has also the advantage that the combination of data sets recorded in different years with different detector resolutions is straightforward. The PDFs are obtained from sideband data, data from dedicated calibration runs, Monte Carlo studies, and theoretical considerations. Therefore, the derivation of the PDFs is not based on data within the blind box.

In the following, the PDFs for signal events, radiative muon decays, and accidental coincidences are described. The averaged PDFs of the combined data set are shown in Fig. 6.2.

6.3.1 Signal

In theory, no correlations exist between the observables E_γ , E_e , $\phi_{e\gamma}$, $\theta_{e\gamma}$, and $t_{e\gamma}$ of a signal event. But as the positron kinematics are obtained by fitting a track and extrapolating it to the intersection with the target, the observables are correlated between each other. Those correlations are included in the signal PDF. Due to position dependent detector responses, the PDF depends additionally on the vertex location (x, y, z) , the photon detection point (u, v, w) , and the positron emission angle (ϕ_e) , which are defined in Chapter 2. The total signal PDF is given by:

$$\begin{aligned}
 S(E_\gamma, E_e, \phi_{e\gamma}, \theta_{e\gamma}, t_{e\gamma} | u, v, w, x, y, z, \phi_e) = & \\
 & S(t_{e\gamma} | E_\gamma, E_e) \times \\
 & S(E_\gamma | u, v, w) \times \\
 & S(\phi_{e\gamma} | u, v, w, x, y, z, \theta_{e\gamma}, E_e, \phi_e) \times \\
 & S(\theta_{e\gamma} | u, v, w, x, y, z, E_e) \times \\
 & S(E_e | \phi_e).
 \end{aligned} \tag{6.6}$$

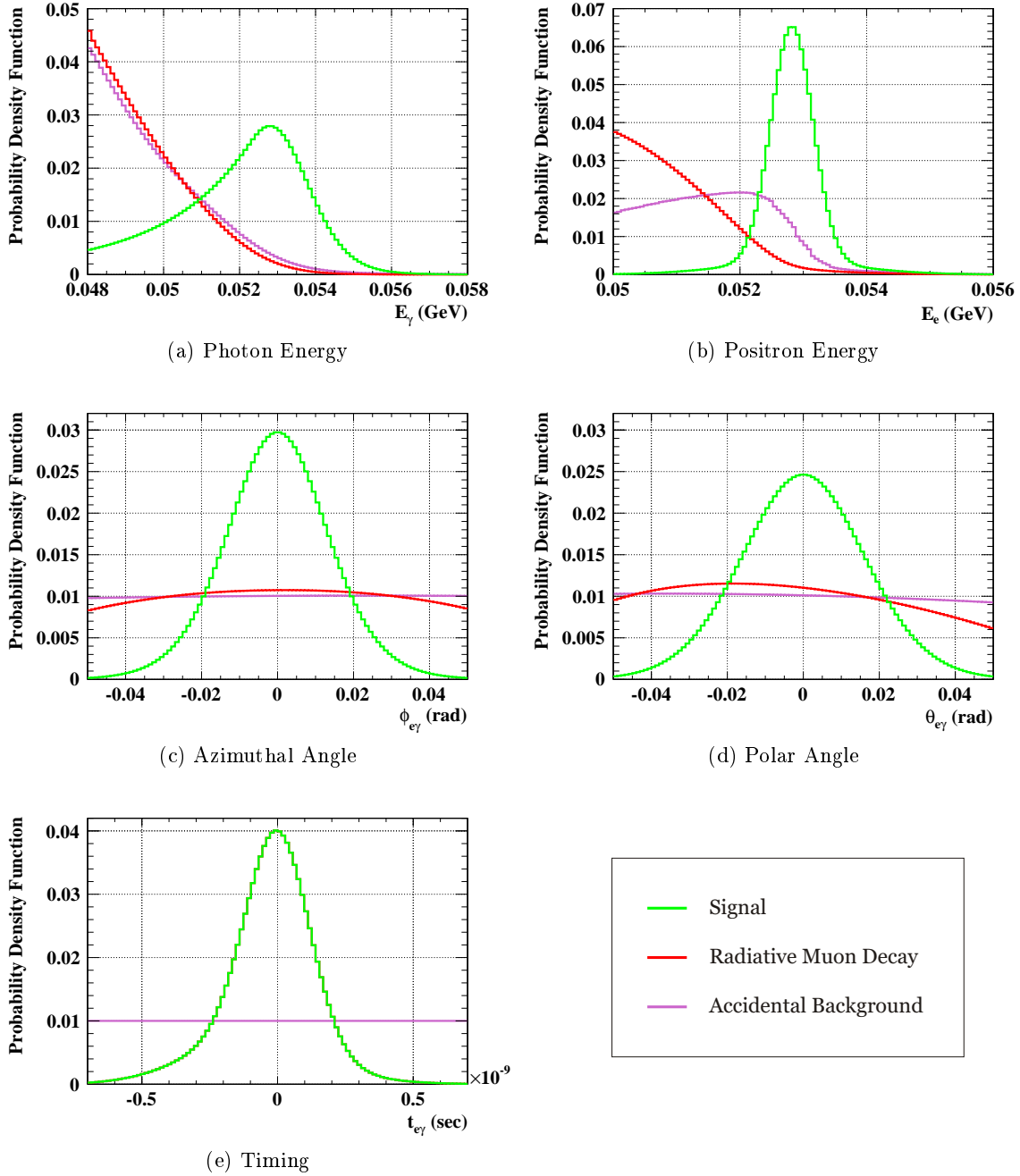


Figure 6.2: PDFs for signal events, radiative muon decays, and accidental background events of each observable (E_γ , E_e , $\phi_{e\gamma}$, $\theta_{e\gamma}$, $t_{e\gamma}$) averaged over all events within the analysis window of the combined data set. The averaged timing PDFs for signal events and radiative muon decays are identical.

The timing PDF $S(t_{e\gamma}|E_\gamma, E_e)$ is obtained by using the radiative muon decay peak in the low photon energy sideband. The energy dependence of the photon time resolution is taken into account and is extracted from CEX data (the CEX calibration and its purpose are described in Chapter 2). The position dependent photon energy PDF $S(E_\gamma|u, v, w)$ is also extracted from CEX data. The relative angle PDFs $S(\phi_{e\gamma}|u, v, w, x, y, z, \theta_{e\gamma}, E_e, \phi_e)$ and $S(\theta_{e\gamma}|u, v, w, x, y, z, E_e)$ are defined as sums of several Gaussian functions whose parameters are obtained by taking into account the photon position resolutions, the muon vertex resolutions, and the positron angle resolutions. The emission angle dependent positron energy PDF $S(E_e|\phi_e)$ is obtained by fitting the kinematic edge of the Michel spectrum.

6.3.2 Radiative Muon Decay

For the radiative muon decay, the kinematic observables E_γ , E_e , $\phi_{e\gamma}$, and $\theta_{e\gamma}$ are correlated while $t_{e\gamma}$ is independent. Therefore, a separated treatment of PDFs of each observable, as done previously for signal events, is not applicable for radiative muon decays. The PDF for those kind of events is defined as:

$$\begin{aligned} R(E_\gamma, E_e, \phi_{e\gamma}, \theta_{e\gamma}, t_{e\gamma}|u, v, w, \phi_e, \theta_e) = & \\ & R(E_\gamma, E_e, \phi_{e\gamma}, \theta_{e\gamma}|u, v, w, \phi_e, \theta_e) \times \\ & R(t_{e\gamma}|E_\gamma, E_e). \end{aligned} \quad (6.7)$$

The first term is obtained by folding the theoretical four-dimensional spectrum [90] with the detector response. The second term is extracted from the low photon energy sideband.

6.3.3 Accidental Background

The PDF of accidental background events has no correlations among the different observables, thus the PDF is given by:

$$\begin{aligned} A(E_\gamma, E_e, \phi_{e\gamma}, \theta_{e\gamma}, t_{e\gamma}|u, v, w, \phi_e) = & \\ & A(t_{e\gamma}) \times \\ & A(E_\gamma|u, v, w) \times \\ & A(\phi_{e\gamma}|v) \times \\ & A(\theta_{e\gamma}|u) \times \\ & A(E_e|\phi_e). \end{aligned} \quad (6.8)$$

The timing PDF $A(t_{e\gamma})$ is assumed to be a constant function. All other terms in the formula are obtained by using extended timing sidebands. It is important to note that events within the negative and positive timing sidebands defined in Eq. (6.4) are not used to calculate the accidental background PDFs. The photon energy PDF $A(E_\gamma|u, v, w)$ is extracted by fitting the sideband data with a function obtained by folding Monte Carlo distributions (radiative muon decay and annihilation in flight) with the detector response. Additionally, cosmic rays

and pile-up effects are taken into account. The relative angle PDFs $A(\phi_{e\gamma}|v)$ and $A(\theta_{e\gamma}|u)$ are described by a third degree polynomial function. The positron energy PDF $A(E_e|\phi_e)$ is obtained by fitting the Michel edge with a fitting function derived from the theoretical Michel spectrum, an acceptance function, and a response function composed of a sum of two Gaussian functions.

6.4 Confidence Interval

To calculate the upper and a possible lower limit of the confidence interval of the branching ratio $\mathcal{B}(\mu^+ \rightarrow e^+ + \gamma)$, a frequentist approach is used, namely the Feldman-Cousins unified approach [91]. Even though the maximum likelihood analysis described in Section 6.2 provides the best fit values for the number of radiative muon decays N_{RMD} and the number of accidental background events N_{ABG} , the final result of the MEG experiment will be a confidence interval in number of signal events N_{sig} . That means, upper or lower limits for the parameters N_{RMD} and N_{ABG} are not of any interest. Therefore, N_{RMD} and N_{ABG} are so-called nuisance parameters. For an analysis including nuisance parameters, a profile likelihood ratio can be used to determine the confidence interval including the systematic uncertainty from the number of background events [9]. For the MEG experiment, the profile likelihood ratio is defined as:

$$\lambda_p(N_{\text{sig}}) = \frac{\mathcal{L}(N_{\text{sig}}, \hat{N}_{\text{RMD}}(N_{\text{sig}}), \hat{N}_{\text{ABG}}(N_{\text{sig}}))}{\mathcal{L}(\hat{N}_{\text{sig}}, \hat{N}_{\text{RMD}}, \hat{N}_{\text{ABG}})}. \quad (6.9)$$

In this formula, \hat{N}_{sig} , \hat{N}_{RMD} , and \hat{N}_{ABG} are the best fit values obtained from the maximum likelihood analysis, that is, the triplet $(\hat{N}_{\text{sig}}, \hat{N}_{\text{RMD}}, \hat{N}_{\text{ABG}})$ maximizes the likelihood function \mathcal{L} defined in Eq. (6.5). The values of $\hat{N}_{\text{RMD}}(N_{\text{sig}})$ and $\hat{N}_{\text{ABG}}(N_{\text{sig}})$ maximize the likelihood function \mathcal{L} for fixed N_{sig} . For the confidence interval calculation, the MEG collaboration defines the following test statistics:

$$q(N_{\text{sig}}) = -2 \ln(\lambda_p(N_{\text{sig}})). \quad (6.10)$$

With this test statistics, the confidence interval is determined by means of the following procedure:

1. A set of different values for N_{sig} is defined, for example $\{N_{\text{sig}}\} = \{0, 1, 2, \dots, 19, 20\}$.
2. A large number (typically around $N_{\text{toy}}(N_{\text{sig}}) = 10'000$) of toy Monte Carlo (toyMC) experiments are generated for each element of the set $\{N_{\text{sig}}\}$. The toyMC experiments are generated by using PDFs as defined in Section 6.3 with the expected number of background events (N_{RMD} and N_{ABG}) obtained from sideband data and the chosen number of signal events N_{sig} .

3. The following is done for each toyMC experiment of each $\{N_{\text{sig}}\}$ element:
 - The maximum likelihood fit is performed to find the best fit values $(\hat{N}_{\text{sig}}, \hat{N}_{\text{RMD}}, \hat{N}_{\text{ABG}})$ and $\mathcal{L}_{\text{toy}}(\hat{N}_{\text{sig}}, \hat{N}_{\text{RMD}}, \hat{N}_{\text{ABG}})$ is calculated.
 - N_{sig} is fixed to the chosen $\{N_{\text{sig}}\}$ element and the maximum likelihood fit is performed to find the best fit values for $\hat{N}_{\text{RMD}}(N_{\text{sig}})$ and $\hat{N}_{\text{ABG}}(N_{\text{sig}})$. Finally, $\mathcal{L}_{\text{toy}}(N_{\text{sig}}, \hat{N}_{\text{RMD}}(N_{\text{sig}}), \hat{N}_{\text{ABG}}(N_{\text{sig}}))$ is determined.
 - The value of $q_{\text{toy}}(N_{\text{sig}})$ is calculated.
4. Now, the data is analyzed:
 - The maximum likelihood fit is performed to find the best fit values $(\hat{N}_{\text{sig}}, \hat{N}_{\text{RMD}}, \hat{N}_{\text{ABG}})$ and $\mathcal{L}_{\text{data}}(\hat{N}_{\text{sig}}, \hat{N}_{\text{RMD}}, \hat{N}_{\text{ABG}})$ is calculated.
 - N_{sig} is successively fixed to each element of $\{N_{\text{sig}}\}$ and the maximum likelihood fit is performed to find the best fit values for $\hat{N}_{\text{RMD}}(N_{\text{sig}})$ and $\hat{N}_{\text{ABG}}(N_{\text{sig}})$. Finally, $\mathcal{L}_{\text{data}}(N_{\text{sig}}, \hat{N}_{\text{RMD}}(N_{\text{sig}}), \hat{N}_{\text{ABG}}(N_{\text{sig}}))$ is determined.
 - The value of $q_{\text{data}}(N_{\text{sig}})$ is calculated for each element of $\{N_{\text{sig}}\}$.
5. To calculate the confidence level (C.L.) for each element of $\{N_{\text{sig}}\}$, the number of toyMC experiments $N_{\text{count}}(N_{\text{sig}})$ with $q_{\text{data}}(N_{\text{sig}}) > q_{\text{toy}}(N_{\text{sig}})$ is counted and it is normalized by the number of toyMC experiments $N_{\text{toy}}(N_{\text{sig}})$ generated for that specific N_{sig} . The confidence level is therefore calculated with $\text{C.L.}(N_{\text{sig}}) = N_{\text{count}}(N_{\text{sig}})/N_{\text{toy}}(N_{\text{sig}})$. The obtained values of $\text{C.L.}(N_{\text{sig}})$ are plotted as a function of N_{sig} resulting in a so-called confidence level curve. An example of such a confidence level curve is shown in Fig. 6.3.
6. The upper and a possible lower limit at 90 % C.L. are extracted from the confidence level curve by cutting it with the C.L. = 0.9 level.

To avoid unphysical confidence intervals, the number of signal events is constrained to be positive ($N_{\text{sig}} > 0$) for the calculation of the confidence level curve. This is almost equivalent to define the test statistics q as in Eq. (6.10) for $N_{\text{sig}} > 0$ and set $q = 0$ for $N_{\text{sig}} \leq 0$. A small anomaly arises only if the maximum likelihood analysis of the data results in a best fit value of $\hat{N}_{\text{sig}} \leq 0$. Nevertheless, this anomaly affects only the value of the confidence level curve at $N_{\text{sig}} = 0$. No lower limit of the confidence interval is expected in this case, the anomaly is therefore irrelevant for the result of the MEG analysis.

The accuracy of the MEG analysis method can be improved by choosing a denser grid for $\{N_{\text{sig}}\}$ but the computing time increases with the number of points on the confidence level curve. With the currently available computing power of the MEG experiment, the generation and fitting of 1'000 toyMC experiments for the combined data set takes typically 35 minutes.

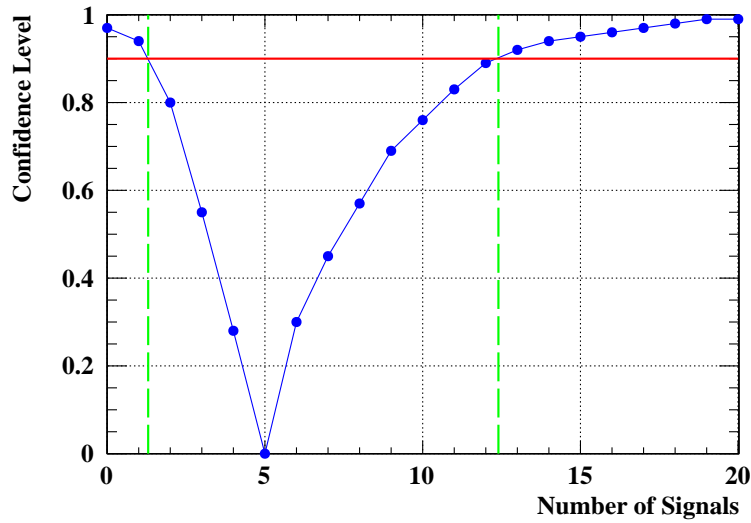


Figure 6.3: Example of a confidence level curve with 21 points corresponding to the set $\{N_{\text{sig}}\} = \{0, 1, 2, \dots, 19, 20\}$ together with the 90 % C.L. line. For this example, the lower limit is at approximately 1.3 and the upper limit is at roughly 12.4 signal events. This plot shows a fictive confidence level curve and is not based on data collected by the MEG experiment.

6.5 Normalization

The confidence interval calculation described in Section 6.4 provides an upper and, if it exists, a lower confidence interval limit at 90 % C.L. in number of signal events N_{sig} . Those limits have to be normalized to get the confidence interval of the branching ratio. The branching ratio $\mathcal{B}(\mu^+ \rightarrow e^+ + \gamma)$ is defined as the fraction of muons decaying into a positron and a photon with respect to the total number of muon decays. But as shown in Table 1.1, the total muon rate is highly dominated by the rate of Michel decays. Therefore, the MEG collaboration normalizes the number of signal events with the number of Michel decays:

$$\mathcal{B}(\mu^+ \rightarrow e^+ + \gamma) = \frac{\Gamma(\mu^+ \rightarrow e^+ + \gamma)}{\Gamma(\mu^+ \rightarrow e^+ + \bar{\nu}_u + \nu_e)}. \quad (6.11)$$

The MEG experiment developed two methods to find the number of Michel decays. First, the number is obtained by using a Michel trigger which is implemented in the normal MEG trigger and by calculating the efficiencies and acceptances for both Michel decays and signal events. The final formula is given in [71] and all contributing factors are detailed in [25]. The other possibility to obtain the number of Michel decays is to count the radiative muon decay events in the low photon energy sideband. The number of Michel decays is extracted by considering the theoretical radiative muon decay branching ratio. Both methods are used for cross checking and the results, weighted with the corresponding uncertainties, are combined to get the final number of Michel decays. After determining all contributing factors, the formula

for the branching ratio $\mathcal{B}(\mu^+ \rightarrow e^+ + \gamma)$ can be rewritten as:

$$\mathcal{B}(\mu^+ \rightarrow e^+ + \gamma) = \frac{N_{\text{sig}}}{k}. \quad (6.12)$$

The normalization factor k includes all information about number of Michel decays, efficiencies, and acceptances. The obtained normalization factors for the 2009, 2010, and combined data sets are summarized in Table 6.2. The results of the confidence interval calculation described in Section 6.4, which are given in number of signals, are inserted into Eq. (6.12) to obtain the corresponding limits of the branching ratio.

Table 6.2: Normalization factors for the 2009, 2010, and combined data sets.

| Data Set | Normalization Factor k |
|----------|---------------------------------|
| 2009 | $(1.08 \pm 0.07) \cdot 10^{12}$ |
| 2010 | $(2.23 \pm 0.16) \cdot 10^{12}$ |
| combined | $(3.31 \pm 0.22) \cdot 10^{12}$ |

6.6 Sensitivity

For each data set, the MEG collaboration estimates the expected upper limit of the confidence interval. This is done by calculating the expected upper confidence interval limit of generated toyMC experiments. To cross check the obtained sensitivities, the MEG analysis method is applied to the negative and positive timing sidebands instead the analysis window. Section 6.6.1 explains the sensitivity calculation method and presents the obtained sensitivities. Section 6.6.2 presents the results of the timing sideband analysis.

6.6.1 Expected Confidence Interval Limit

The expected upper limit of the confidence interval is obtained by generating toyMC experiments assuming the background-only hypothesis. For each data set (2009, 2010, and combined), 1'000 toyMC experiments are generated. By taking into account the corresponding PDFs and the corresponding expected number of background events for each data set, the sensitivity includes information about both resolutions and statistics. The upper confidence interval limit at 90% C.L. is calculated for each generated experiment by applying the MEG analysis method. The sensitivity is then determined by calculating the median value of the obtained distribution of upper limits. The median value is calculated because it has the advantage to be less sensitive to outliers than the mean value. Figure 6.4 shows the distributions of the upper limits in number of signal events and branching ratio for the 2009, 2010, and combined data sets. The obtained sensitivities¹ are summarized in Table 6.3. Those

¹The sensitivity is calculated before opening the blind box with the number of expected background events obtained from sideband data. As the number of expected background events is updated after opening the blind box (Section 8.3.2), the sensitivity is recalculated after opening the blind box. The results shown in Table 6.3 are the numbers obtained with the updated number of expected background events.

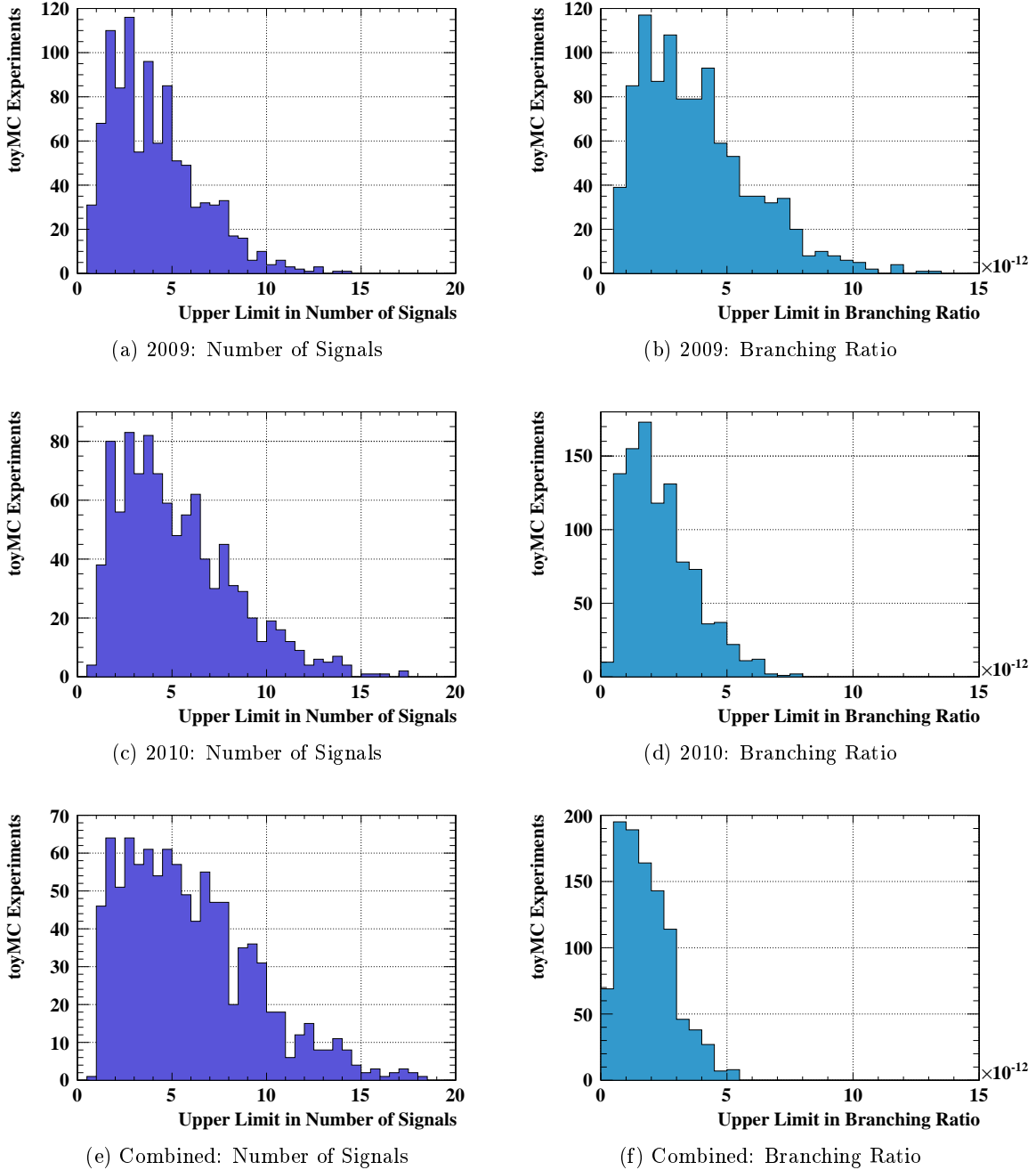


Figure 6.4: Distributions of the upper limits obtained from toyMC experiments assuming the background-only hypothesis. The plots show the distributions in number of signal events (left) and in branching ratio (right) for the statistics and resolutions of the 2009 (top), 2010 (middle), and combined (bottom) data sets. These plots show results obtained by the MEG collaboration.

numbers show that the expected upper confidence interval limit of the MEG experiment is up to 7.5 times better than the upper limit of $1.2 \cdot 10^{-11}$ at 90 % C.L. reached by the MEGA experiment [1].

Table 6.3: Expected upper limits at 90 % C.L. obtained from toyMC experiments assuming the background-only hypothesis in number of signals and branching ratio for the 2009, 2010, and combined data sets.

| Data Set | Expected Upper Limit | |
|----------|----------------------|----------------------|
| | Number of Signals | Branching Ratio |
| 2009 | 3.6 | $3.3 \cdot 10^{-12}$ |
| 2010 | 4.8 | $2.2 \cdot 10^{-12}$ |
| combined | 5.2 | $1.6 \cdot 10^{-12}$ |

6.6.2 Results of the Timing Sideband Analysis

For testing purposes, the MEG analysis procedure is applied to events within the negative and positive timing sidebands which are defined in Eq. (6.4). Neither signal nor radiative muon decays are expected in those sidebands. For timing sideband analyses, the likelihood function defined in Eq. (6.5) is therefore not constrained in the number of radiative muon decays N_{RMD} . The results of the sideband analysis are used to verify the maximum likelihood fit and the confidence level curve calculation before opening the blind box². In addition, the obtained upper limits for the branching ratio are estimations for the sensitivity.

The number of analyzed events, the best fit values for the number of signal events, and the corresponding 1.645σ MINOS errors are summarized in Table 6.4. The asymmetric 1.645σ MINOS errors obtained from MINUIT [92] are only asymptotically valid and might be wrong in case of small data samples [93]. As a consequence, the MEG collaboration calculates the confidence interval limits with the Feldman-Cousins unified approach instead of using MINOS errors. The obtained upper limits³ at 90 % C.L. both in number of signals and branching ratio are also summarized in Table 6.4. No lower limits are presented because the analyses of the timing sidebands of all data sets do not result in lower limits for the confidence interval.

The results show that the maximum likelihood fit as well as the confidence level calculation works as expected and no unanticipated effects appear. Additionally, the upper limits in branching ratio obtained from timing sideband data and the sensitivities presented in Table 6.3 are consistent. In summary, the analysis of the timing sidebands is a useful tool to check the analysis procedures and to estimate the sensitivity.

²The timing sidebands are analyzed before opening the blind box by using the number of expected accidental background events obtained from sideband data. As the number of expected background events is updated after opening the blind box (Section 8.3.2), the timing sideband analysis is redone after opening the blind box. The results shown in Table 6.4 are the numbers obtained with the updated number of expected background events.

³Systematic uncertainties are not included in the upper limits obtained from the timing sideband analysis.

Table 6.4: Results of the analysis of the negative and positive timing sidebands of the 2009, 2010, and combined data sets. The number of analyzed events N_{obs} , the best fit values for the number of signal events N_{sig} obtained with the maximum likelihood fit, and the upper limits at 90 % C.L. in number of signal events and branching ratio \mathcal{B} are listed. The errors for the best fit values are 1.645σ MINOS errors.

| | Data Set | N_{obs} | N_{sig} Best Fit | UL in N_{sig} | UL in \mathcal{B} |
|----------|----------|------------------|---------------------------|------------------------|----------------------|
| positive | 2009 | 266 | $-7.4^{+5.0}_{-2.8}$ | 3.0 | $2.8 \cdot 10^{-12}$ |
| | 2010 | 614 | $-4.3^{+5.5}_{-2.1}$ | 3.5 | $1.6 \cdot 10^{-12}$ |
| | combined | 880 | $-7.0^{+5.7}_{-2.2}$ | 3.67 | $1.1 \cdot 10^{-12}$ |
| negative | 2009 | 277 | $-2.1^{+4.5}_{-2.1}$ | 3.8 | $3.5 \cdot 10^{-12}$ |
| | 2010 | 593 | $2.4^{+7.7}_{-4.8}$ | 10.1 | $4.5 \cdot 10^{-12}$ |
| | combined | 870 | $0.8^{+8.2}_{-5.2}$ | 9.06 | $2.7 \cdot 10^{-12}$ |

6.7 Results of the 2009 and 2010 Data Analysis

This section presents the results of the 2009 and 2010 data analysis. The data analysis is based on events with kinematics within the analysis window defined in Eq. (6.3). The total number of observed events N_{obs} within this window are $N_{\text{obs}} = 311$ (645) for the 2009 (2010) data set. The number of expected background events is estimated using sideband data and the obtained values are listed in Table 6.1. The number of observed events and the number of expected background events are consistent within uncertainties. Section 6.7.1 summarizes the results of the maximum likelihood analysis and Section 6.7.2 presents the obtained confidence interval limits.

6.7.1 Results of the Maximum Likelihood Analysis

The maximum likelihood analysis described in Section 6.2 is applied to the data within the analysis window to find the best fit values for the number of signal events \hat{N}_{sig} , the number of radiative muon decays \hat{N}_{RMD} , and the number of accidental background events \hat{N}_{ABG} . The results of this analysis and the corresponding asymmetric 1.645σ MINOS errors are summarized in Table 6.5. The distributions of the events within the analysis window for all observables E_γ , E_e , $\phi_{e\gamma}$, $\theta_{e\gamma}$, and $t_{e\gamma}$ together with the PDFs weighted with the corresponding best fit values for the 2009, 2010, and combined data sets are shown in Figs. 6.5 to 6.7. For this analysis, N_{sig} is not constrained to the physics region, negative values are therefore allowed.

The maximum likelihood fit of the 2009 data finds $\hat{N}_{\text{sig}} = 3.4$ while the analysis of the 2010 data set yields a result of $\hat{N}_{\text{sig}} = -2.2$. The reason for those opposed results are statistical fluctuations. By considering the large errors and the result of the likelihood fit of $\hat{N}_{\text{sig}} = -0.5$ for the combined data set, which contains more statistics, it is evident that the data collected by the MEG experiment is consistent with the no-signal hypothesis.

Table 6.5: Results of the maximum likelihood analysis for the 2009, 2010, and combined data sets. The number of observed events N_{obs} in the analysis window as well as the best fit values for the number of signal events \hat{N}_{sig} , the radiative muon decays \hat{N}_{RMD} , and accidental background events \hat{N}_{ABG} are listed. The errors are given in 1.645σ MINOS errors.

| Data Set | N_{obs} | \hat{N}_{sig} | \hat{N}_{RMD} | \hat{N}_{ABG} |
|----------|------------------|------------------------|------------------------|-------------------------|
| 2009 | 311 | $3.4^{+6.6}_{-4.4}$ | $26.9^{+4.5}_{-4.5}$ | $273.1^{+12.3}_{-12.3}$ |
| 2010 | 645 | $-2.2^{+5.0}_{-1.9}$ | $50.2^{+9.2}_{-9.2}$ | $608.5^{+18.7}_{-18.6}$ |
| combined | 956 | $-0.5^{+7.9}_{-4.7}$ | $76.5^{+12.0}_{-12.0}$ | $882.1^{+22.4}_{-22.3}$ |

6.7.2 Results of the Confidence Level Calculation

The confidence interval is determined using the procedure described in Section 6.4. The obtained confidence level curves as a function of the number of signal events as well as the normalized curves as a function of the branching ratio are shown in Fig. 6.8. The plots show that both an upper and a lower limit at 90 % C.L. are found for the 2009 data set while only an upper limit is found for the 2010 and the combined data set. The obtained upper and lower limits in number of signals and branching ratio are summarized in Table 6.6. Even though the 2009 data set leads to a lower limit of the confidence interval, it is consistent with the hypothesis $\mathcal{B}(\mu^+ \rightarrow e^+ + \gamma) = 0$ with 8 % probability. Therefore, the lower limit at 90 % C.L. found with the 2009 data set might be caused by a statistical fluctuation.

The results show that even with the separated data sets collected in 2009 and 2010, the previous valid upper limit in branching ratio of $1.2 \cdot 10^{-11}$ found by the MEGA experiment [1] is lowered. Before opening the blind boxes, the MEG collaboration decided to publish in either case the result of the analysis of the combined data set. Therefore, the MEG collaboration presents [81] a new upper limit for the branching ratio of the lepton flavor violating decay $\mu^+ \rightarrow e^+ + \gamma$ of

$$\mathcal{B}(\mu^+ \rightarrow e^+ + \gamma) < 2.4 \cdot 10^{-12} \text{ at } 90\% \text{ C.L.} \quad (6.13)$$

New physics beyond the Standard Model of particle physics is now constrained by a five times tighter upper limit than with the result of MEGA.

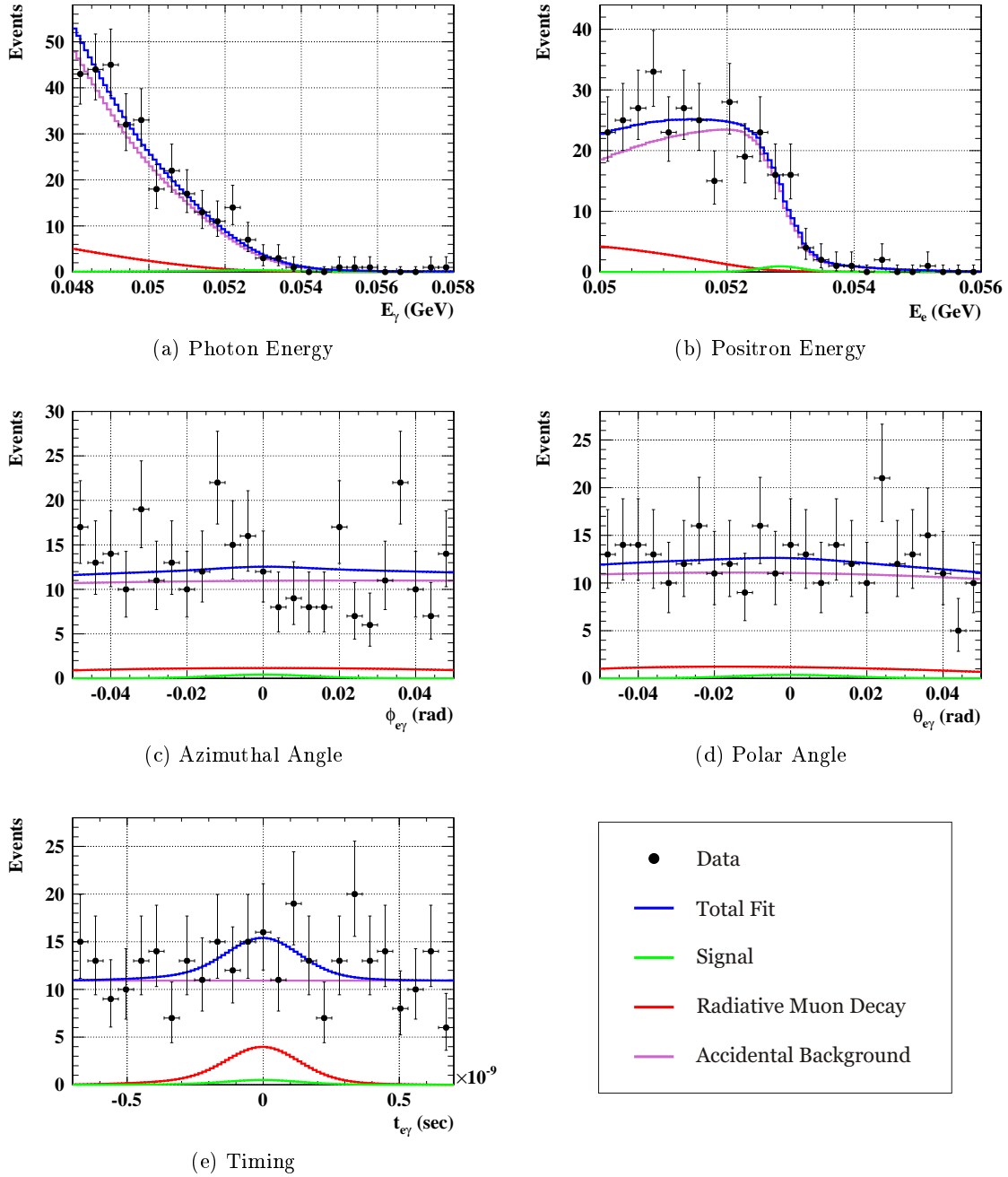


Figure 6.5: Distribution of all events within the analysis window of the 2009 data set for all observables together with the maximum likelihood fit result. The total fit, the contributions of the signal events, the radiative muon decays, and accidental background events weighted with the corresponding best fit values are shown. These plots show results obtained by the MEG collaboration.

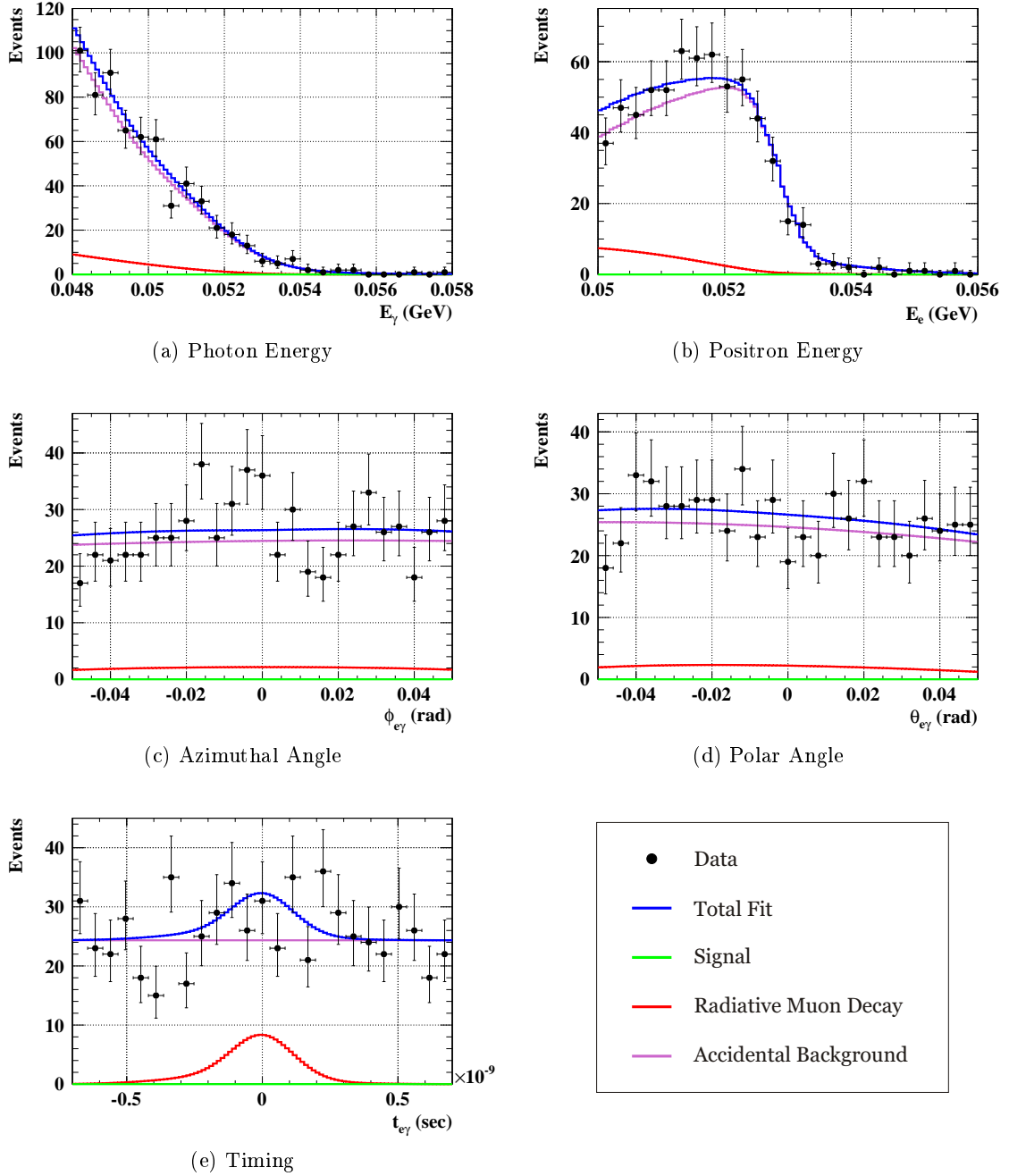


Figure 6.6: Distribution of all events within the analysis window of the 2010 data set for all observables together with the maximum likelihood fit result. The total fit, the contributions of the signal events, the radiative muon decays, and accidental background events weighted with the corresponding best fit values are shown. These plots show results obtained by the MEG collaboration.

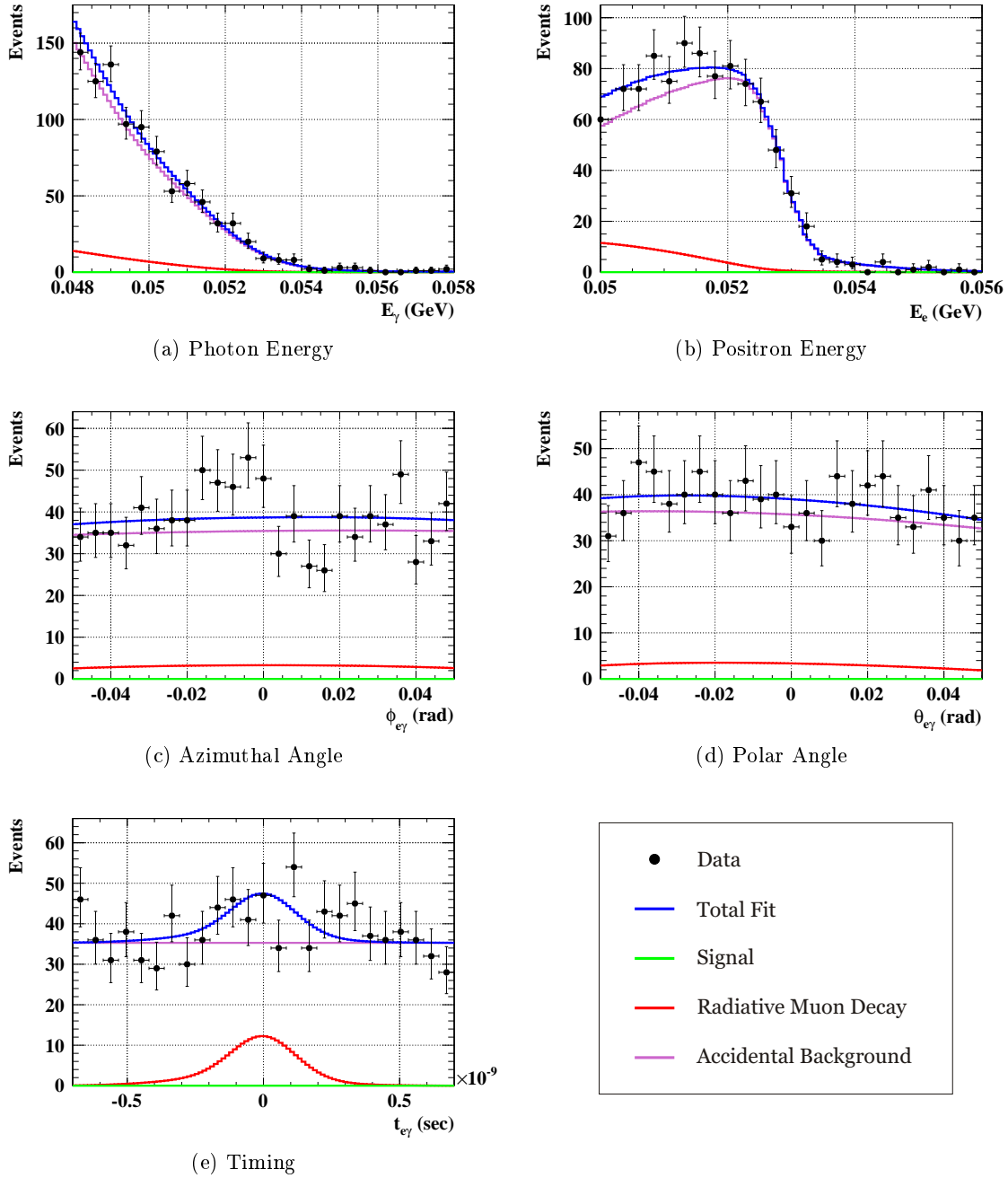


Figure 6.7: Distribution of all events within the analysis window of the combined data set for all observables together with the maximum likelihood fit result. The total fit, the contributions of the signal events, the radiative muon decays, and accidental background events weighted with the corresponding best fit values are shown. These plots show results obtained by the MEG collaboration.

Table 6.6: Results of the confidence level calculation for the 2009, 2010, and combined data sets. The obtained upper limits (UL) and lower limits (LL) are given in number of signals (a) and in branching ratio (b).

| (a) Upper and Lower Limits in Number of Signals | | | |
|-------------------------------------------------|----------------|----------------|----------------|
| Data Set | LL (90 % C.L.) | UL (90 % C.L.) | UL (95 % C.L.) |
| 2009 | 0.2 | 10.4 | 11.9 |
| 2010 | - | 3.8 | 5.0 |
| combined | - | 7.8 | 9.8 |

| (b) Upper and Lower Limits in Branching Ratio | | | |
|-----------------------------------------------|-----------------------|----------------------|-----------------------|
| Data Set | LL (90 % C.L.) | UL (90 % C.L.) | UL (95 % C.L.) |
| 2009 | $0.17 \cdot 10^{-12}$ | $9.6 \cdot 10^{-12}$ | $11.0 \cdot 10^{-12}$ |
| 2010 | - | $1.7 \cdot 10^{-12}$ | $2.3 \cdot 10^{-12}$ |
| combined | - | $2.4 \cdot 10^{-12}$ | $2.9 \cdot 10^{-12}$ |

6.8 Systematic Uncertainties

Systematic uncertainties are already included in steps (2) to (4) of the confidence level calculation described in Section 6.4 by the following procedure:

1. The toyMC experiments are generated by using alternative PDFs, that is, PDFs with all parameters randomized simultaneously according to their uncertainties (systematical uncertainties and statistical fluctuations). Correlations between the errors of variables are taken into account for the randomization.
2. The generated toyMC experiments and the data sets are then analyzed with the original PDFs.

Therefore, all confidence level limits presented in this chapter (except of the timing sideband results) already include systematic uncertainties. For the combined data set, the total effect of systematic uncertainties on the upper limit is roughly 2%. It is therefore significantly smaller than the statistical uncertainty of the likelihood fit. The relative contributions of each possible source of systematic uncertainties on the total impact of 2% are determined with the following procedure:

1. First, toyMC experiments are generated using the original PDFs and $N_{\text{sig}} = \text{Poisson}(7.8)$ where 7.8 corresponds to the upper confidence interval limit at 90% C.L. obtained from the combined data set.

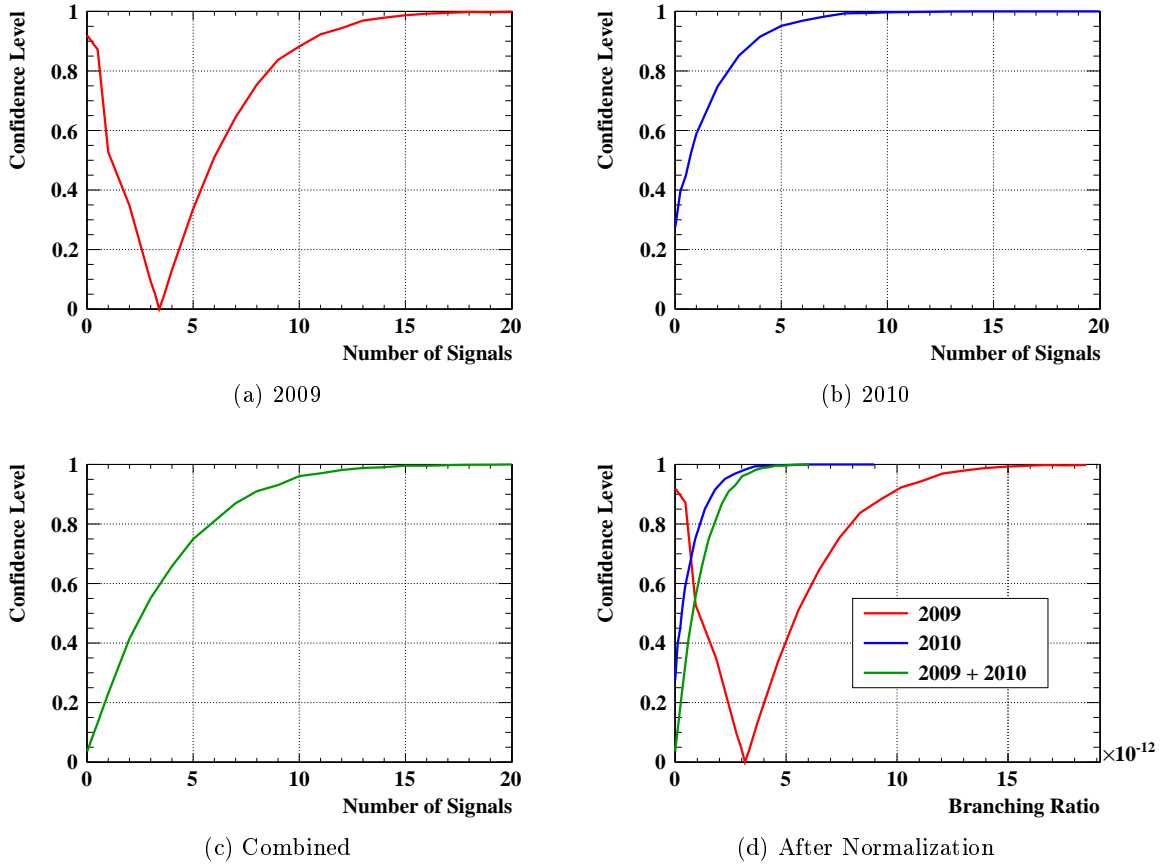


Figure 6.8: Confidence level curves of 2009 (a), 2010 (b), and combined (c) data sets as a function of the number of signals along with the comparison of all confidence level curves after normalization (d). These plots show results obtained by the MEG collaboration.

2. The generated toyMC experiments are analyzed with the original PDFs and the likelihood is calculated for the best fit value and for fixed $N_{\text{sig}} = 7.8$. Finally, the negative-log-likelihood-ratio $\Delta NLL_{\text{original}}$ is determined.
3. For each source of systematic uncertainties the following is done:
 - (a) The same toyMC experiments are analyzed using alternative PDFs with parameters randomized according to the corresponding uncertainty. The likelihood is calculated for the best fit value as well as for fixed $N_{\text{sig}} = 7.8$ and the negative-log-likelihood-ratio $\Delta NLL_{\text{alternative}}$ is determined.
 - (b) The RMS value of the distribution of the differences between the negative-log-likelihood ratios obtained in step (2) and (3a) $\Delta\Delta NLL$ is then used to compare the contribution of the different sources of systematic uncertainties.

The obtained relative contributions of the systematic uncertainties on the upper limit in branching ratio are shown in Table 6.7. Therefore, the most dominant contributions are

uncertainties in relative angles $\phi_{e\gamma}$ and $\theta_{e\gamma}$. They are caused by uncertainties in the alignment, namely between liquid xenon calorimeter and positron spectrometer, between the magnetic field of COBRA and the drift chamber system, and between MEG target and drift chamber system. This is one of the reasons why the MEG collaboration introduced a new optical survey method to determine the z position of the drift chamber system very precisely. The optical survey of the drift chamber system is discussed in Chapter 3.

Table 6.7: Relative contributions of the most important sources of systematic uncertainties. The values shown in this table are the obtained RMS values of the $\Delta\Delta NLL$ distributions in units of $\Delta\Delta NLL$ and are used to compare the relative contributions of the different sources of systematic uncertainties.

| RMS | Uncertainty |
|------|---------------------------------------------------|
| 0.18 | Center of $\phi_{e\gamma}$ and $\theta_{e\gamma}$ |
| 0.16 | Positron correlations |
| 0.1 | $\phi_{e\gamma} : \theta_{e\gamma}$ correlation |
| 0.05 | $\phi_e : E_e$ anomaly |
| 0.05 | correlation due to E_e bias |
| 0.13 | Normalization |
| 0.07 | E_γ scale |
| 0.06 | E_e bias |
| 0.06 | $t_{e\gamma}$ center |

6.9 Summary

The MEG collaboration uses a blind box analysis technique to prevent the results from any bias. All calibrations, the determination of the probability density functions, and the background studies are performed by means of data from sidebands or data collected during dedicated calibration runs. After completing all calibrations and fixing the analysis procedure, the blind box is opened and a maximum likelihood analysis is applied to get the best fit value for the number of signal events. The Feldman-Cousins unified approach with profile likelihood ordering is applied to find the upper and a possible lower limit of the confidence interval. The analysis of the combined data set of run 2009 and 2010 results in a new upper limit of the branching ratio of $\mathcal{B}(\mu^+ \rightarrow e^+ + \gamma) < 2.4 \cdot 10^{-12}$ at 90 % C.L., which lowers the best limit known so far found by the MEGA collaboration. New physics beyond the Standard Model is now constrained by a five times tighter upper limit.

Chapter 7

Event and Background Distribution Checks

To calculate the confidence interval of the branching ratio $\mathcal{B}(\mu^+ \rightarrow e^+ + \gamma)$ with the official MEG analysis, probability density functions (PDFs) for signal events, radiative muon decays, and accidental background events are required. Those PDFs are obtained without using events within the analysis window defined in Eq. (6.3) or the timing sidebands defined in Eq. (6.4). Therefore, goodness of fit checks can be performed to verify that the PDFs are consistent with the background distributions in the analysis window and the timing sidebands. Section 7.1 gives an overview of the used goodness of fit methods, presents the results of the background PDF checks with sideband data, and verifies the agreement of the background PDFs with the event distributions within the analysis window. Section 7.2 defines so-called high ranked events and checks the distribution of those events to identify unexpected dependencies between observables or the appearance of event clusters. The consistency checks presented in this chapter are essential to verify that the detection and analysis processes of the MEG experiment behave as expected. Therefore, such checks enhance the authenticity of the collected data and the results based on these data.

7.1 Background Distributions

The basic idea of the goodness of fit checks presented in this section is to compare a data set \mathcal{D} with the corresponding null hypothesis \mathcal{H}_0 that is defined by the a priori knowledge about the expected background distributions. Two methods are used in this chapter to perform the goodness of fit checks, namely Pearson's χ^2 test and the Kolmogorov-Smirnov test, which are both described in Section 7.1.1. The goodness of fit checks are applied to two significant application domains. First, the events within the negative and positive timing sidebands are tested if they are consistent with the hypothesis that all events observed in those sidebands are accidental coincidences. This null hypothesis is reasonable as neither signal events nor radiative muon decays are expected to be within the timing sidebands due to the large time difference between positron and photon. The purpose of this goodness of fit check is to validate

the accidental background PDFs. The results are presented in Section 7.1.2. Second, it is tested if the events within the analysis window are compatible with the hypothesis that all events within that window are background events. Therefore, the null hypothesis states that the events within the analysis window are composed of 10 % radiative muon decays and 90 % accidental coincidences. These percentages are rough estimations of the fractions of number of radiative muon decays and accidental coincidences expected to be within the analysis window. The results of this goodness of fit check are presented in Section 7.1.3.

In the remainder of this section, the goodness of fit checks of the negative and positive timing sidebands are identified as Test A1 and A2, respectively. The check of the analysis window is labeled as Test B. All performed goodness of fit checks with the corresponding data sets and null hypotheses are summarized in Table 7.1. The checks are separately applied to the 2009 and the 2010 data set.

Table 7.1: Summary of the performed goodness of fit checks including data sets \mathcal{D} and corresponding null hypotheses \mathcal{H}_0 that describe the expected composition of radiative muon decays (RMS) and accidental background events (ABG).

| Test | Data Set \mathcal{D} | Null Hypothesis \mathcal{H}_0 |
|------|--------------------------|---------------------------------|
| A1 | Negative Timing Sideband | 100 % ABG |
| A2 | Positive Timing Sideband | 100 % ABG |
| B | Analysis Window | 90 % ABG + 10 % RMD |

7.1.1 Goodness of Fit Methods

The goodness of fit checks are done with two different methods, namely with Paerson's χ^2 test and with the Kolmogorov-Smirnov test. Both are explained in the following.

Paerson's χ^2 Test

Paerson's χ^2 test [94] is one of the most famous methods to check the goodness of fit between an observed event distribution and a theoretical distribution. For the analysis presented in this chapter, Paerson's χ^2 test is done separately for each observable E_γ , E_e , $\phi_{e\gamma}$, $\theta_{e\gamma}$, and $t_{e\gamma}$ with the same histogram binning as the one used for Figs. 6.5 to 6.7 to plot the maximum likelihood analysis results in Section 6.7. Therefore, the number of bins N_{bin} of the histograms is set to $N_{\text{bin}} = 25$. The number of events in bin i is given by n_i and the expected value of the bin content is E_i . The test statistic χ^2 is then defined as:

$$\chi^2 = \sum_{i=1}^{N_{\text{bin}}} \frac{(n_i - E_i)^2}{E_i}. \quad (7.1)$$

The crucial point is to calculate the values of E_i . As the PDFs for radiative muon decays and accidental background events are well defined, the PDFs for the theoretical distributions can

be calculated separately for each null hypothesis. In case of Test A1 and A2, the hypothesis PDF is given by the one for accidental coincidences and for Test B, it is a combination of 10 % radiative muon decay PDF and 90 % accidental background PDF. The calculated hypothesis PDF determines the normalized probability p_i to find an event in bin i so that $\sum_{i=1}^{N_{\text{bin}}} p_i = 1$. With the number of observed events N_{obs} in the data set \mathcal{D} , the test statistic can be rewritten as:

$$\chi^2 = \sum_{i=1}^{N_{\text{bin}}} \frac{(n_i - p_i N_{\text{obs}})^2}{p_i N_{\text{obs}}}. \quad (7.2)$$

Assuming a large enough number of events in each bin, this test statistic follows approximately a χ^2 distribution with $N_{\text{bin}} - 1 = 24$ degrees of freedom. The result of the goodness of fit checks is given by the so-called p -value. It describes the probability to observe a data distribution with larger or equal value of χ^2 than the one of the analyzed data set under the assumption that the null hypothesis is true. If the calculated p -value is less than the significant value, which is often defined as 0.01 or 0.001, the null hypothesis is rejected.

For Paerson's χ^2 test, it is necessary to have enough events within each bin as the approximation of a χ^2 distribution is only valid in this case [94]. For the combined data set, there are less than 1'000 events within the analysis window and each timing sideband. Paerson's χ^2 test is therefore not the most suitable method to perform goodness of fit checks. The problem of bins with small content can be addressed by using Monte Carlo methods [94] but the result will still depend on the chosen binning. This is the reason why the goodness of fit checks are also done with the Kolmogorov-Smirnov test that is applied to continuous data sets, binning is therefore not necessary.

Kolmogorov-Smirnov Test

The Kolmogorov-Smirnov test [95] is applied to one-dimensional data samples to test if a certain data set is consistent with a given probability distribution function. No binning of the data set is necessary, which has the advantage that no information is lost due to large bins and that the test can be applied to small data samples.

Assuming a data set \mathcal{D} with size N and a one-dimensional observable x with $x_1 \leq x_2 \leq \dots \leq x_N$, the cumulative distribution function $F_N(x)$ is defined as

$$F_N(x) = \frac{n(x)}{N} = \begin{cases} 0 & \text{if } x < x_1 \\ \frac{i}{N} & \text{if } x_1 \leq x \leq x_N \\ 1 & \text{if } x_N < x \end{cases} \quad (7.3)$$

where $n(x)$ is the number of observed events with $x_i \leq x$. In other words, F_N is a step function which can be compared with the cumulative distribution function $F(x)$ of a certain null hypothesis \mathcal{H}_0 . The test statistic D_N is the maximal vertical difference between $F(x)$ and $F_N(x)$:

$$D_N = \max_x \{|F_N(x) - F(x)|\}. \quad (7.4)$$

As this test statistic strongly depends on the number of events N , the following modified test statistic is used in practice [96]:

$$d_{KS} = D_N \cdot \sqrt{N}. \quad (7.5)$$

Small values of d_{KS} are equivalent to a good agreement between data set \mathcal{D} and null hypothesis \mathcal{H}_0 . The p -value describes the probability that an event distribution with a larger or equal d_{KS} as the one of the analyzed data set is observed assuming the null hypothesis \mathcal{H}_0 is true. It is calculated by using the test statistics d_{KS} and the Kolmogorov distribution [95].

7.1.2 Accidental Background Probability Density Function Validation using Timing Sideband Data

The previously described goodness of fit methods are applied to the negative and positive timing sidebands (Test A1 and A2) to validate the accidental background PDFs. Table 7.2 summarizes the p -values obtained with Paerson's χ^2 test and the Kolmogorov-Smirnov test. The distributions of the measured azimuthal angles $\phi_{e\gamma}$ of the 2009 and the 2010 data set with the corresponding null hypotheses are shown in Fig. 7.1. The event distributions and null hypotheses for the other observables E_γ , E_e , $\theta_{e\gamma}$, and $t_{e\gamma}$ are shown in Figs. A.1 to A.4 in Appendix A. Those plots are used for Paerson's χ^2 test. Figure 7.2 shows the cumulative distribution functions of the measured azimuthal angle $\phi_{e\gamma}$ and the corresponding null hypotheses, which are used for the Kolmogorov-Smirnov test. The cumulative distribution functions for the other observables E_γ , E_e , $\theta_{e\gamma}$, and $t_{e\gamma}$ are shown in Figs. A.5 to A.8 in Appendix A.

The Kolmogorov-Smirnov test results in small p -values for the $\phi_{e\gamma}$, $\theta_{e\gamma}$, and $t_{e\gamma}$ distribution of the 2009 positive timing sideband. However, by checking the event distributions shown in Fig. 7.1, Fig. A.3, and Fig. A.4, it is evident that all these deviations are caused by large statistical fluctuations. In conclusion, the event distributions in the timing sidebands show no significant deviations from the expected accidental background distributions, the accidental background PDFs are therefore validated.

Table 7.2: Results of the goodness of fit checks with the negative and positive timing sidebands (Test A1 and A2). The p -values obtained with Paerson's χ^2 test and the Kolmogorov-Smirnov (KS) test are listed for all observables.

| Observable | A1 2009 | | A1 2010 | | A2 2009 | | A2 2010 | |
|--------------------|----------|-------|----------|-------|----------|-------|----------|-------|
| | χ^2 | KS | χ^2 | KS | χ^2 | KS | χ^2 | KS |
| E_γ | 0.951 | 0.481 | 0.712 | 0.983 | 0.868 | 0.834 | 0.986 | 0.470 |
| E_e | 0.779 | 0.913 | 0.877 | 0.638 | 0.788 | 0.694 | 0.811 | 0.884 |
| $\phi_{e\gamma}$ | 0.956 | 0.658 | 0.861 | 0.997 | 0.626 | 0.018 | 0.241 | 0.718 |
| $\theta_{e\gamma}$ | 0.287 | 0.141 | 0.130 | 0.990 | 0.199 | 0.024 | 0.205 | 0.130 |
| $t_{e\gamma}$ | 0.672 | 0.361 | 0.906 | 0.728 | 0.361 | 0.052 | 0.360 | 0.429 |

7.1.3 Background Distribution in the Analysis Window

After validating the accidental background PDFs, the goodness of fit checks are also applied to the analysis window (Test B). The purpose of this test is to check if the event distribution is consistent with the expected background. Table 7.3 summarizes the p -values obtained with Paerson's χ^2 test and the Kolmogorov-Smirnov test. The event distributions with corresponding null hypotheses used for Paerson's χ^2 test are shown in Fig. 7.1 and Figs. A.1 to A.4 in Appendix A. The cumulative distribution functions used for the Kolmogorov-Smirnov test are shown in Fig. 7.2 and Figs. A.5 to A.8.

The results of Test B show that the events within the analysis window fit to the expected background distribution for almost all observables. The only exception is the distribution of the azimuthal angle $\phi_{e\gamma}$ of the 2009 data set which results in a p -value of 2.2%. By visually checking Fig. 8.4e, it is evident that the event distribution shows large statistical fluctuations but no significant angular dependencies. In conclusion, the events of the analysis window for 2009 and 2010 are in good agreement with the expected background distribution and no evidence was found to reject the null hypotheses for neither 2009 nor 2010 data.

In summary, both Paerson's χ^2 test and the Kolmogorov-Smirnov test show that the events within the negative and positive timing sidebands fit to the expected accidental background distributions and the events within the analysis window are consistent with the predicted background composed of accidental background events and radiative muon decays. Some of the event distributions of 2009 show small p -values. However, by visually checking the corresponding event distributions it is evident that they are caused by statistical fluctuations. Paerson's χ^2 test and the Kolmogorov-Smirnov test are useful tools to verify the goodness of fit of the observed events to the expected background distributions and to validate the background PDFs.

Table 7.3: Results of the goodness of fit checks with the analysis window (Test B). The p -values obtained with Paerson's χ^2 test and the Kolmogorov-Smirnov (KS) test are listed for all observables.

| Observable | B 2009 | | B 2010 | |
|--------------------|----------|-------|----------|-------|
| | χ^2 | KS | χ^2 | KS |
| E_γ | 0.095 | 0.268 | 0.507 | 0.368 |
| E_e | 0.644 | 0.946 | 0.894 | 0.373 |
| $\phi_{e\gamma}$ | 0.022 | 0.020 | 0.173 | 0.243 |
| $\theta_{e\gamma}$ | 0.859 | 0.794 | 0.840 | 0.879 |
| $t_{e\gamma}$ | 0.566 | 0.976 | 0.125 | 0.556 |

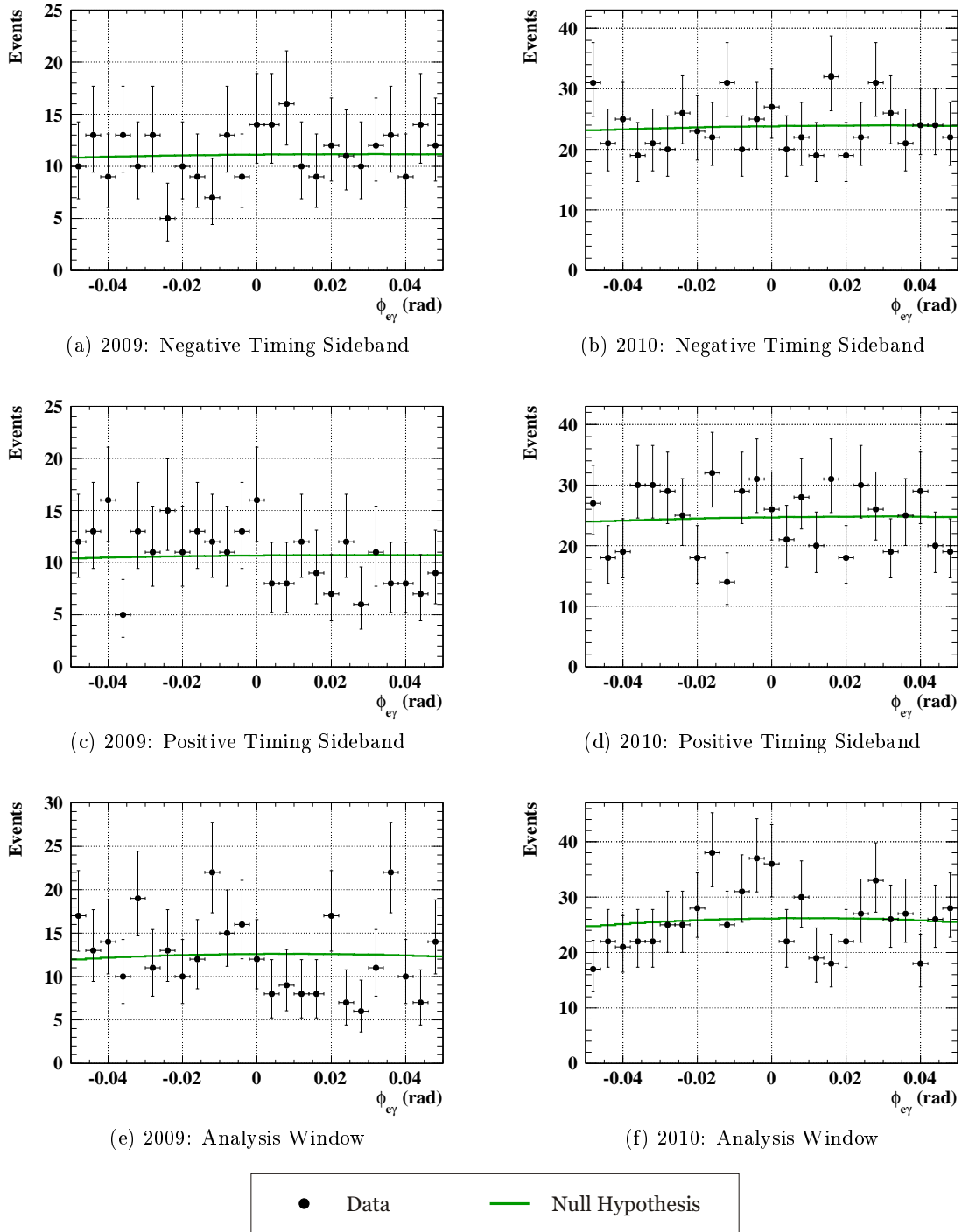


Figure 7.1: Distributions of the measured azimuthal angles $\phi_{e\gamma}$ within the negative and positive timing sidebands and within the analysis window separately plotted for the 2009 and the 2010 data set. In addition, the corresponding null hypotheses are shown. These plots are used for Paerson's χ^2 test.

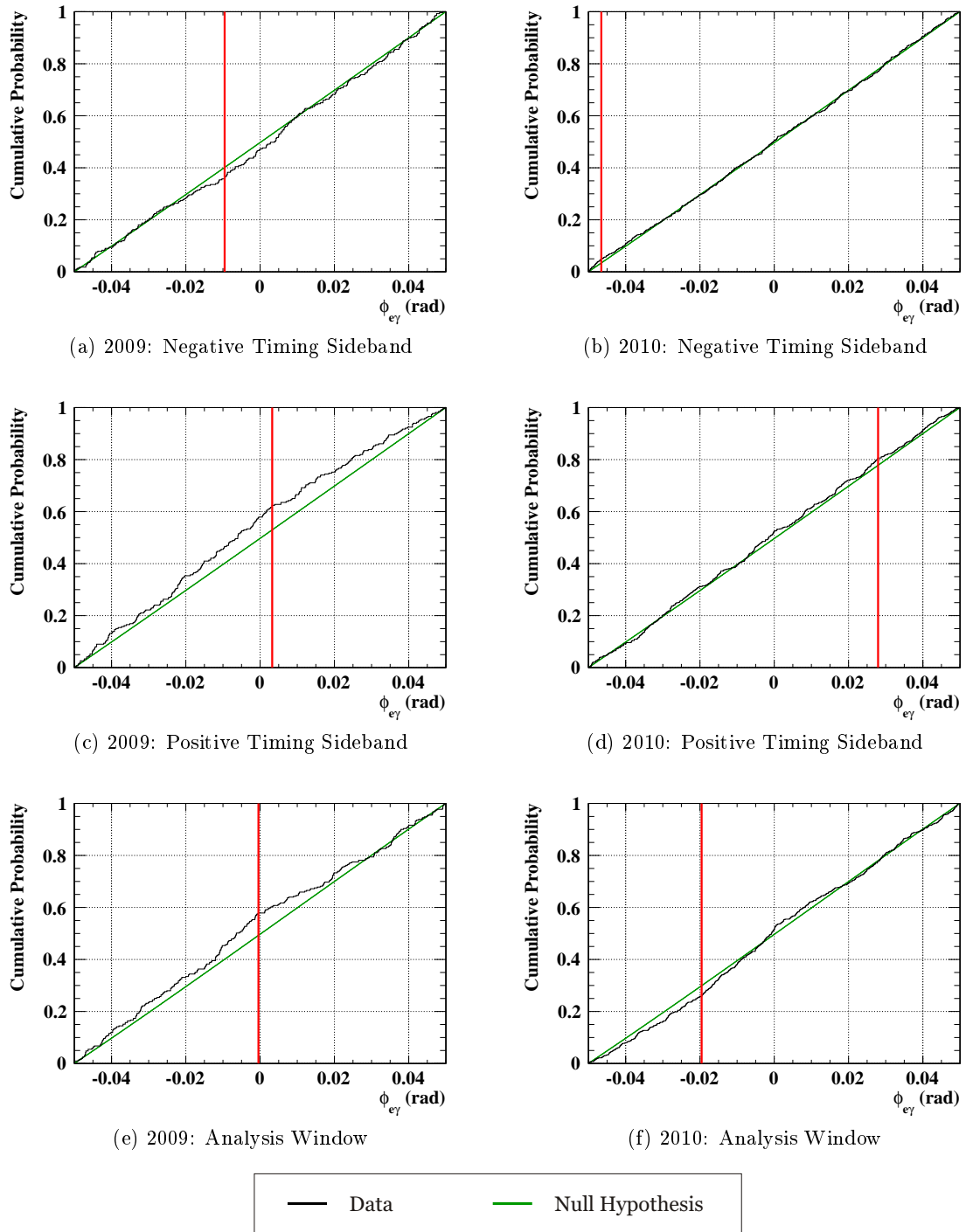


Figure 7.2: Cumulative distribution functions of the measured azimuthal angles $\phi_{e\gamma}$ and the corresponding null hypotheses within the negative and positive timing sidebands and within the analysis window separately plotted for the 2009 and the 2010 data set. These plots are used for the Kolmogorov-Smirnov test. The position of the largest deviation between data and null hypothesis is highlighted with a vertical line.

7.2 Event Distributions

For the event distribution checks, all events within the analysis window are studied to identify anomalous event clusters or unexpected dependencies. Those checks show if the detection and reconstruction processes are well understood. In particular, the focus is on “high ranked” events (events with high likelihood to be a $\mu^+ \rightarrow e^+ + \gamma$ decay) to check if their properties are conspicuous or not. Section 7.2.1 explains how high ranked events are defined and Section 7.2.2 checks the distributions of those events within the analysis window.

7.2.1 Definition of High Ranked Events

For the MEG experiment, the best suited discriminant variable to determine the rank of an event is the relative signal likelihood R_{sig} , which is defined as

$$\begin{aligned} R_{\text{sig}} &= \log_{10} \left(\frac{S}{f_{\text{R}} \cdot R + f_{\text{A}} \cdot A} \right) \\ &= \log_{10} \left(\frac{S}{0.1 \cdot R + 0.9 \cdot A} \right) \end{aligned} \tag{7.6}$$

where S , R , and A are the signal, radiative muon decay, and accidental background likelihoods, respectively. The numbers $f_{\text{R}} = 0.1$ and $f_{\text{A}} = 0.9$ are rough estimations of the fractions of number of radiative muon decays and accidental coincidences expected to be within the analysis window. The value of R_{sig} is calculated for each event within the analysis window of the 2009 and the 2010 data set. The higher this value the higher is the likelihood that this event is a $\mu^+ \rightarrow e^+ + \gamma$ decay and the higher is its rank. However, a high R_{sig} value does not necessarily mean that the corresponding event is a $\mu^+ \rightarrow e^+ + \gamma$ decay as the likelihood that this event is a radiative muon decay or an accidental coincidence is not zero. The PDFs of the relative signal likelihood for signal events, radiative muon decays, and accidental coincidences are shown and discussed in Section 8.3.

In total, the 2009 (2010) data set contains 9 (11) high ranked events with $R_{\text{sig}} > 0.7$ including 3 (1) events with a very high relative signal likelihood of $R_{\text{sig}} > 1.7$. Table 7.4 shows the properties of those high ranked events with the calculated value of R_{sig} and the observables E_{γ} , E_e , $\phi_{e\gamma}$, $\theta_{e\gamma}$, and $t_{e\gamma}$ of each event.

7.2.2 Event Distributions of the 2009 and 2010 Data Sets

In addition to check the properties of individual high ranked events, it is also informative to study the distribution of the events within the analysis window. Such distribution plots can provide useful hints about time dependencies or non-uniformities in the detector response. For example, an observed time dependency of the photon energy would indicate a non-constant detector performance or problems with the photomultiplier tube calibrations, which are detailed in Chapter 2. It is also interesting to compare event distributions from different runs as the drift chamber system is extracted and reinserted in every shutdown as described in

Table 7.4: Properties of the most high ranked events of 2009 and 2010 with $R_{\text{sig}} > 0.7$. The rank, the detecting year, the run and event number, the value of R_{sig} , and the observables E_γ , E_e , $\phi_{e\gamma}$, $\theta_{e\gamma}$, and $t_{e\gamma}$ are listed in this table. The four most high ranked events have a very high relative signal likelihood of $R_{\text{sig}} > 1.7$.

| Rank | Year | Run | Event | R_{sig} | E_γ (MeV) | E_e (MeV) | $\phi_{e\gamma}$ (mrad) | $\theta_{e\gamma}$ (mrad) | $t_{e\gamma}$ (ns) |
|------|------|-------|-------|------------------|---------------------|----------------|----------------------------|------------------------------|-----------------------|
| 1 | 2010 | 77431 | 1715 | 2.19 | 53.86 | 52.82 | 9.17 | -34.70 | 0.142 |
| 2 | 2009 | 56081 | 35 | 1.96 | 52.38 | 52.43 | 19.88 | -15.92 | -0.060 |
| 3 | 2009 | 54396 | 1820 | 1.85 | 52.43 | 52.76 | 9.78 | -13.43 | 0.253 |
| 4 | 2009 | 56787 | 1606 | 1.78 | 51.75 | 53.05 | -10.34 | 20.45 | -0.196 |
| 5 | 2010 | 77442 | 1978 | 1.69 | 50.22 | 53.32 | 21.20 | -16.82 | -0.131 |
| 6 | 2010 | 73947 | 1617 | 1.68 | 52.21 | 53.29 | -45.14 | 43.37 | 0.065 |
| 7 | 2009 | 62069 | 107 | 1.66 | 48.18 | 52.94 | -10.41 | 4.47 | 0.100 |
| 8 | 2009 | 64388 | 65 | 1.64 | 55.26 | 52.65 | 19.06 | -20.89 | -0.385 |
| 9 | 2009 | 59731 | 1212 | 1.59 | 52.05 | 52.43 | 23.52 | -23.17 | 0.002 |
| 10 | 2010 | 75547 | 1635 | 1.50 | 52.49 | 52.41 | -7.06 | 24.35 | -0.118 |
| 11 | 2009 | 59016 | 611 | 1.49 | 51.99 | 52.67 | 16.27 | -21.56 | 0.249 |
| 12 | 2010 | 74577 | 678 | 1.43 | 53.56 | 52.56 | 45.18 | 4.71 | 0.096 |
| 13 | 2010 | 83404 | 66 | 1.36 | 52.62 | 52.59 | 25.10 | 24.02 | 0.136 |
| 14 | 2010 | 89450 | 457 | 1.25 | 50.01 | 52.75 | 7.61 | -17.80 | 0.142 |
| 15 | 2010 | 81282 | 933 | 1.23 | 54.83 | 52.36 | 25.68 | -43.35 | -0.100 |
| 16 | 2009 | 58162 | 1820 | 1.22 | 50.62 | 52.56 | -14.59 | 25.29 | -0.052 |
| 17 | 2009 | 63468 | 735 | 1.22 | 51.51 | 52.76 | 2.11 | 0.84 | 0.313 |
| 18 | 2010 | 83509 | 1360 | 1.04 | 49.22 | 52.96 | -21.91 | 13.04 | -0.169 |
| 19 | 2010 | 76900 | 695 | 0.92 | 50.11 | 53.33 | -23.38 | 35.22 | -0.040 |
| 20 | 2010 | 91679 | 1389 | 0.77 | 51.90 | 52.08 | -0.60 | -19.89 | -0.058 |

Chapter 3. Additionally, the event distributions before and after the charge exchange (CEX) calibration in 2010 are checked. The CEX calibration is described in Chapter 2.

Figure 7.3 shows the distributions of the measured observables (E_γ , E_e , $\phi_{e\gamma}$, $\theta_{e\gamma}$, $t_{e\gamma}$) and R_{sig} for all events within the analysis window of the 2009 and the 2010 data set as a function of their run number. In these plots, the four most high ranked events are identified with diamonds and the other high ranked events listed in Table 7.4 are highlighted with squares. Events with a run number less than 70'000 were recorded in 2009 while all other events were collected in 2010. The data break around run number 80'000 is caused by the 2010 CEX run. By visually comparing the event distributions in Fig. 7.3, no significant differences between data collected in 2009 and 2010 are recognizable and the interruption for the CEX run 2010 has no visible effect. Therefore, it can be concluded that the calibration methods work well and the detector performance behaves as expected during run 2009 and 2010.

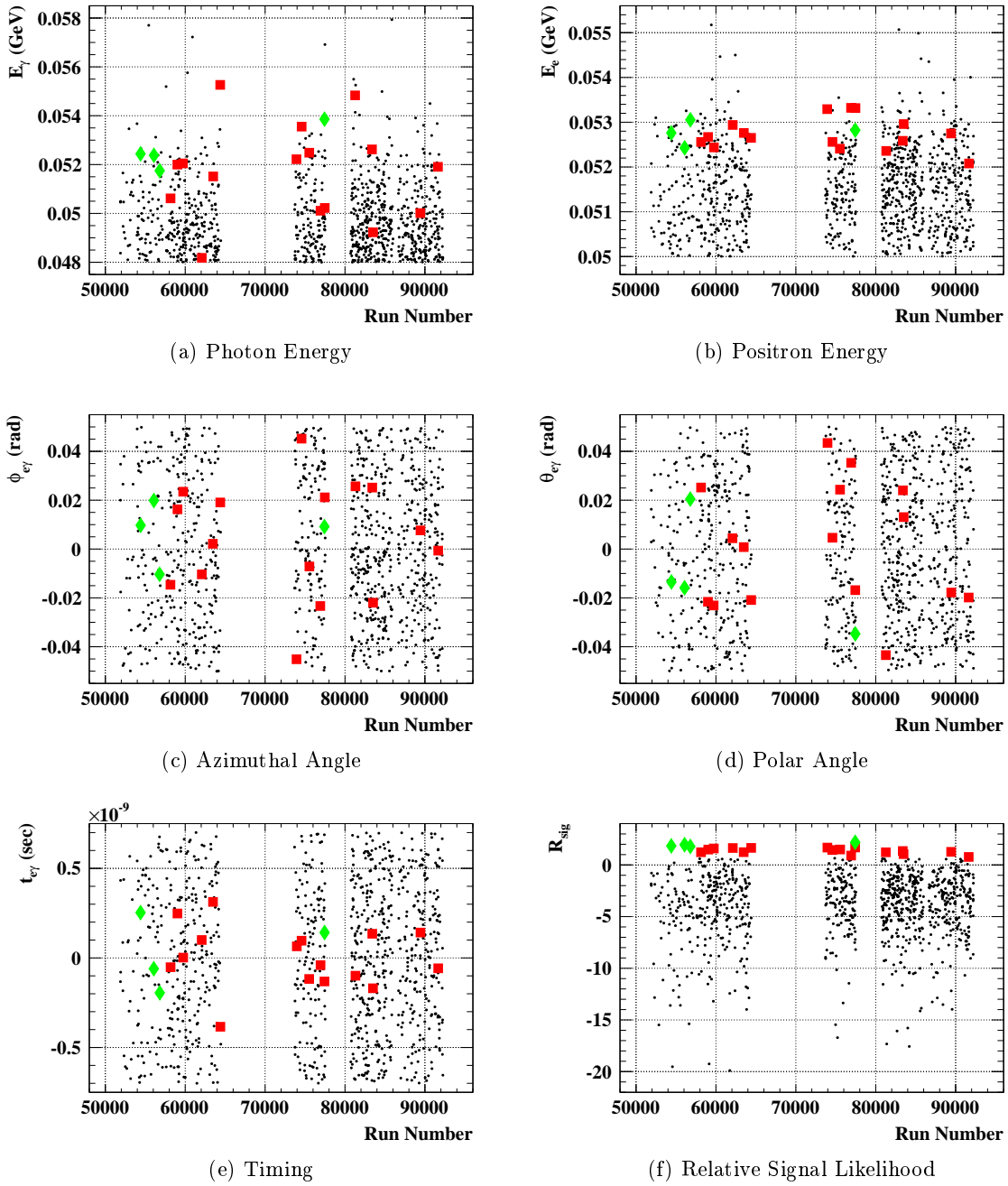


Figure 7.3: Event distributions of all events within the analysis window collected in 2009 and 2010. The plots show the measured values of the five observables (E_γ , E_e , $\phi_{e\gamma}$, $\theta_{e\gamma}$, $t_{e\gamma}$) and the calculated relative signal likelihood (R_{sig}) as a function of the run number. Events with a run number less than 70'000 were recorded in 2009 while all other events were collected in 2010. The four most high ranked events are identified with diamonds and the other high ranked events presented in Table 7.4 are highlighted with squares.

The muon decay position (vertex) and the location of the photon detection point are also studied. The corresponding coordinate systems are described in Chapter 2. Such studies are used to check if the decay points on the MEG target and the photon detection points are distributed as expected. The corresponding distributions as a function of the run number are shown in Fig. A.9 in Appendix A. Again, the distributions show no time dependencies and there are also no event clusters visible.

Instead of analyzing those coordinates as a function of the run number, it is also possible to plot the vertex and the photon detection point in two spatial coordinates. Such plots provide possible hints about spatially dependent effects. The distributions of the vertex coordinates are shown in Fig. 7.4. The events are plotted in always two spatial coordinates and, to distinguish properly between 2009 and 2010 data, there are separated graphs for the two data sets. By visually checking these plots, neither event clustering nor spacial dependencies are recognizable. Only Figs. 7.4e and 7.4f indicate that the target is not at the same position in 2009 and 2010. This is caused by the extraction and reinsertion of the support structure with the drift chambers and the target during every shutdown. As described in Chapter 3, the position of the target is measured with optical survey methods and is included in the analysis. The distributions of the photon detection coordinates are shown in Fig. A.10 in Appendix A. By visually checking the individual plots, neither unexpected spacial dependencies nor event clustering are recognizable. In conclusion, the event distributions of the vertex and photon detection positions do not show any anomalies.

Knowing the best fit values for the number of signal events \hat{N}_{sig} obtained by the maximum likelihood analysis described in Chapter 6, a closer look at the signal region of the five-dimensional observable space $\vec{x} = (E_\gamma, E_e, \phi_{e\gamma}, \theta_{e\gamma}, t_{e\gamma})$ for the 2009 and 2010 data set is desirable. Figures 7.5a and 7.5b show the events in the (E_γ, E_e) plane for run 2009 and 2010, respectively. Figures 7.5c and 7.5d show the events in the $(t_{e\gamma}, \Theta_{e\gamma})$ plane for run 2009 and 2010, respectively. The opening angle $\Theta_{e\gamma}$ is defined as

$$\begin{aligned} \Theta_{e\gamma} = & \sin(\theta_\gamma) \cos(\phi_\gamma) \sin(\theta_e) \cos(\phi_e) \\ & + \sin(\theta_\gamma) \sin(\phi_\gamma) \sin(\theta_e) \sin(\phi_e) \\ & + \cos(\theta_\gamma) \cos(\theta_e) \end{aligned} \quad (7.7)$$

with θ_γ and ϕ_γ (θ_e and ϕ_e) being the polar and azimuthal angles of the photon (positron). The plots show that the three most high ranked events of the 2009 data set are close to the signal region in all dimensions while the event with the highest R_{sig} value of the 2010 data set is outside of the signal region. This observation is consistent with the best fit values of the maximum likelihood analysis with $\hat{N}_{\text{sig}} = 3.4$ for 2009 and $\hat{N}_{\text{sig}} = -2.2$ for 2010 presented in Chapter 6.

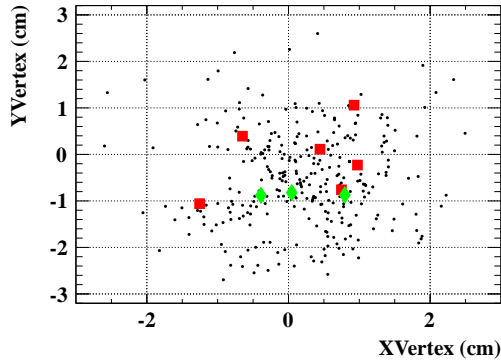
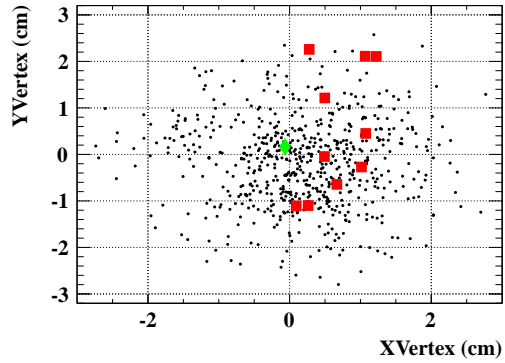
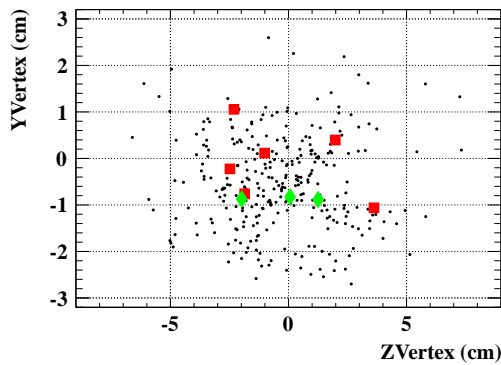
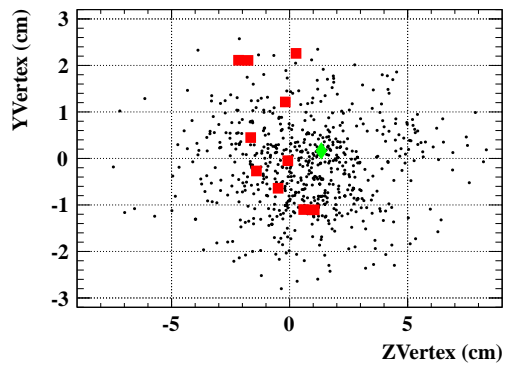
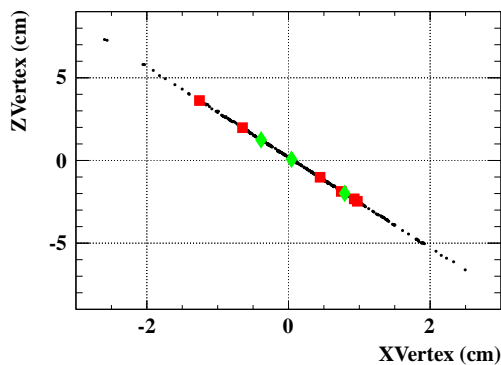
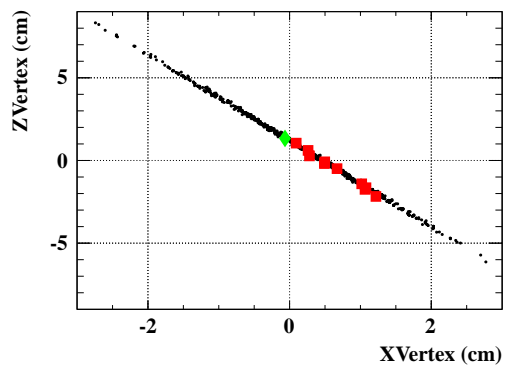
(a) 2009: yx Coordinates Vertex(b) 2010: yx Coordinates Vertex(c) 2009: yz Coordinates Vertex(d) 2010: yz Coordinates Vertex(e) 2009: zx Coordinates Vertex(f) 2010: zx Coordinates Vertex

Figure 7.4: Event distributions of the muon decay vertex coordinates (x , y , z) separately plotted for the 2009 and 2010 data set. The events are plotted in always two spatial coordinates. The four most high ranked events are identified with diamonds and the other high ranked events presented in Table 7.4 are highlighted with squares.

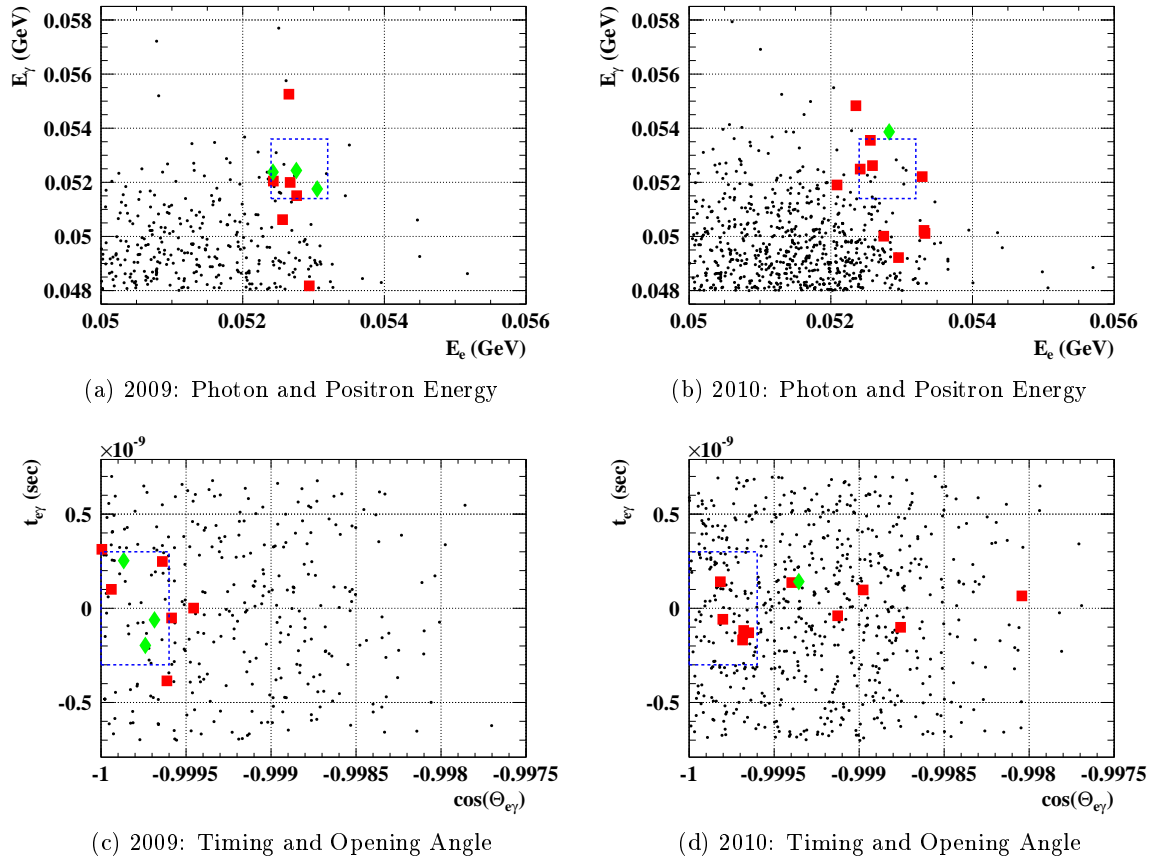


Figure 7.5: Event distributions separately plotted for the 2009 and 2010 data set. The (E_γ, E_e) plane is plotted in (a) and (b) and the $(t_{e\gamma}, \Theta_{e\gamma})$ plane is plotted in (c) and (d). An additional dashed box is drawn to visually indicate the signal region even if it is not used in the $\mu^+ \rightarrow e^+ + \gamma$ search analysis. The four most high ranked events are identified with diamonds and the other high ranked events presented in Table 7.4 are highlighted with squares.

7.3 Summary

This chapter described several tools to check the consistency of the data collected by the MEG detector. First, two goodness of fit methods were introduced, namely Pearson's χ^2 test and the Kolmogorov-Smirnov test. Those goodness of fit checks were applied to the negative and positive timing sideband and the analysis window of the 2009 and the 2010 data set to validate the accidental background probability density functions and to confirm the consistency between the event distribution and the expected background. To exclude unexpected event clusters or dependencies between observables, the event distributions of the analysis window of the 2009 and the 2010 data set were plotted. In particular, the focus was placed on events with high relative signal likelihood. The results of all tests did not show any significant deviations from the expectation.

Chapter 8

Relative Signal Likelihood Analysis

The analysis procedure described in Chapter 6 to determine the confidence interval of the branching ratio $\mathcal{B}(\mu^+ \rightarrow e^+ + \gamma)$ is the official analysis method of the MEG collaboration to analyze the collected data. This analysis method is extremely time-consuming as the calculation of the confidence level curve requires the generation and analysis of many toyMC experiments in all five dimensions of the kinematic space $(E_\gamma, E_e, \phi_{e\gamma}, \theta_{e\gamma}, t_{e\gamma})$. Therefore, alternative analysis methods that allow a faster estimation of the confidence interval limits are desired. Those estimations should be as accurate as possible such that they can be used to verify the results of the official MEG analysis. In particular, the computing time can be reduced by transforming the information about the events from the five-dimensional kinematic space into the one-dimensional space of a discriminant variable. This chapter describes two analysis methods based on such a discriminant variable, namely the relative signal likelihood R_{sig} . The definition of R_{sig} and the corresponding probability density functions for signal events, radiative muon decays, and accidental coincidences are introduced in Section 8.1. In addition, the event distributions of the 2009 and 2010 data sets as a function of R_{sig} are presented, the R_{sig} condition is introduced, and goodness of fit checks are performed. A cut analysis method that is performed in the one-dimensional R_{sig} space to calculate the confidence interval limits and the achieved results are presented in Section 8.2. Finally, an alternative analysis method based on the relative signal likelihood to calculate the confidence interval for the branching ratio $\mathcal{B}(\mu^+ \rightarrow e^+ + \gamma)$ is detailed in Section 8.3. It includes a maximum likelihood analysis and the Feldman-Cousins unified approach.

The cut analysis and the alternative analysis method were developed and optimized with the opened blind box of run 2009. After defining the analysis procedure and fixing all parameters, the analysis methods have been applied to the opened blind box of run 2010 and the combined data set.

8.1 The Relative Signal Likelihood R_{sig}

Each event collected by the MEG detector is completely characterized by the photon and the positron energy, the azimuthal and the polar angle, and the timing. This means that

all information about an event is specified in the five-dimensional space of the observable $\vec{x} = (E_\gamma, E_e, \phi_{e\gamma}, \theta_{e\gamma}, t_{e\gamma})$ which makes the generation and analysis of toyMC events time-consuming. To reduce computing time, the information about the events is transformed into a one-dimensional discriminant variable. The best suited discriminant variable for the MEG experiment is the relative signal likelihood R_{sig} . For each event, the value of R_{sig} is calculated with the formula

$$\begin{aligned} R_{\text{sig}} &= \log_{10} \left(\frac{S}{f_{\text{R}} \cdot R + f_{\text{A}} \cdot A} \right) \\ &= \log_{10} \left(\frac{S}{0.1 \cdot R + 0.9 \cdot A} \right) \end{aligned} \quad (8.1)$$

where S , R , and A are the event specific signal, radiative muon decay, and accidental background likelihoods, respectively. The values $f_{\text{R}} = 0.1$ and $f_{\text{A}} = 0.9$ are rough estimations of the fractions of the number of radiative muon decays and accidental coincidences expected to be within the analysis window, which is defined in Eq. (6.3). The relative signal likelihood and its definition were already introduced in Chapter 7 to identify high ranked events.

For any kind of analysis performed with the relative signal likelihood, the probability density functions of R_{sig} for signal events, radiative muon decays, and accidental coincidences are required. The probability density functions of R_{sig} are described in Section 8.1.1. In Section 8.1.2, the event distributions as a function of R_{sig} are presented and the R_{sig} condition is introduced. Finally, goodness of fit checks are performed in Section 8.1.3.

8.1.1 Probability Density Functions of R_{sig}

Unfortunately, well defined functions do not exist for the probability density functions (PDFs) of R_{sig} for signal events $S(R_{\text{sig}})$, radiative muon decays $R(R_{\text{sig}})$, and accidental coincidences $A(R_{\text{sig}})$ as they cannot be extracted from sideband data or dedicated calibration runs. Nevertheless, it is possible to generate many toyMC events for each kind of event by using the PDFs of the five observables E_γ , E_e , $\phi_{e\gamma}$, $\theta_{e\gamma}$, and $t_{e\gamma}$, which were presented in Section 6.3. The value of R_{sig} is calculated for each generated event and the obtained distributions are used as PDFs of R_{sig} . As those PDFs are not well defined functions but distributions of generated toyMC events, all analyses based on the relative signal likelihood are performed with binned histograms.

Figure 8.1 shows the arbitrary normalized PDFs of R_{sig} for signal events, radiative muon decays, and accidental coincidences, each obtained by generating 25'000'000 toyMC events using the kinematic PDFs of the combined data set. The corresponding PDFs of the separated data sets 2009 and 2010 are almost identical to the ones shown in Fig. 8.1 and are therefore omitted. Generating those PDFs takes approximately 6 hours per kind of event (signal, radiative muon decay, and accidental coincidence) and data set (2009, 2010, and combined) with the currently available computing power of the MEG experiment.

The plotted histograms in Fig. 8.1 illustrate that the PDF for signal events is clearly distinguishable from the ones of the background events while the PDFs for radiative muon decays and accidental coincidences are almost identical.

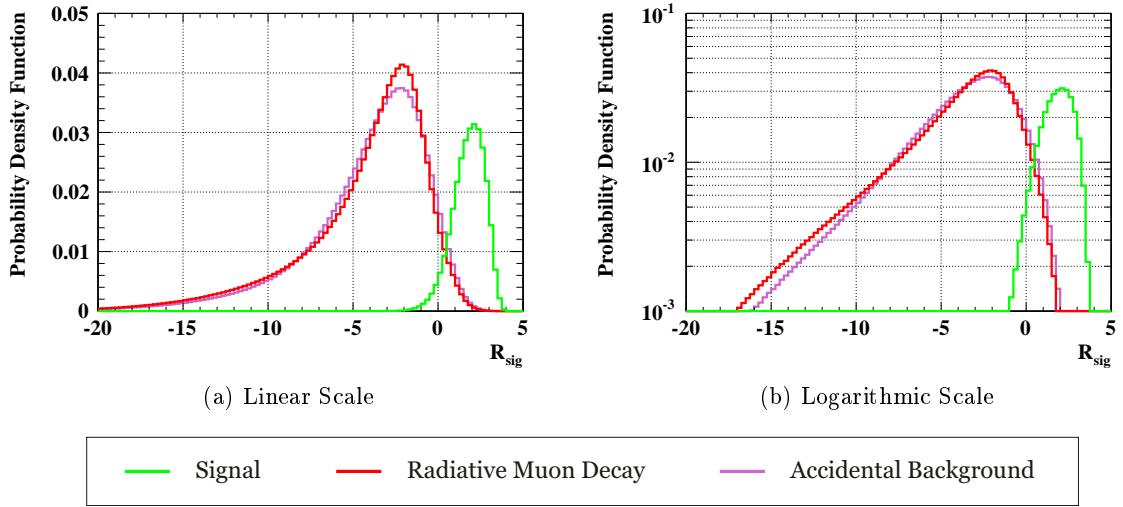


Figure 8.1: Arbitrary normalized PDFs of R_{sig} for signal events, radiative muon decays, and accidental coincidences. The PDFs are obtained by producing 25'000'000 toyMC events for each kind of event using the kinematic PDFs of the combined data set. The PDFs are plotted on a linear (a) and a logarithmic scale (b).

8.1.2 The R_{sig} Condition

The distribution of the calculated R_{sig} values of all events within the analysis window of the combined data set is plotted in Fig. 8.2. The plots show that events were collected that have small relative signal likelihoods of down to $R_{\text{sig}} = -20$. By visually checking the PDFs shown in Fig. 8.1, it is evident that events with $R_{\text{sig}} < -10$ are background events with high probability, that is, radiative muon decays or accidental coincidences. Therefore, a reduced analysis window is used for analyses based on the relative signal likelihood which is defined by the R_{sig} condition:

$$-10 \leq R_{\text{sig}} \leq 5. \quad (8.2)$$

By applying this stronger R_{sig} condition, the number of observed events N_{obs} is reduced and the R_{sig} PDFs for radiative muon decays and accidental background events are cut off by approximately 10 % while the R_{sig} PDF for signal events is not affected. The effects on the number of observed events and the PDFs by using the R_{sig} condition are summarized in Table 8.1. The distributions of the calculated R_{sig} values of events that are within the analysis window and fulfill the R_{sig} condition are shown in Fig. 8.3. In addition, the PDFs for signal events, radiative muon decays, and accidental background events are plotted. They are normalized by the best fit values of the official MEG maximum likelihood analysis, which are listed in Table 6.5. Unless stated otherwise, the R_{sig} condition is applied to all analyzed events for the remainder of this chapter.

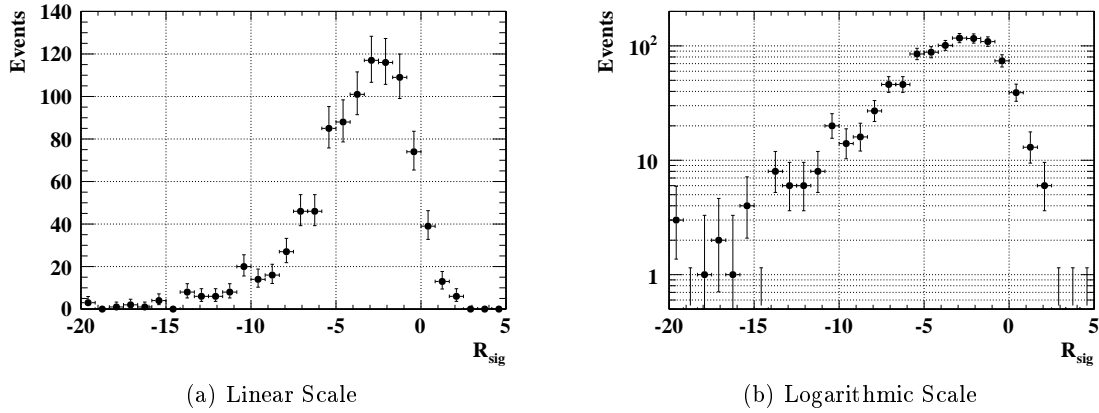


Figure 8.2: Distribution of the calculated R_{sig} values of all events within the analysis window of the combined data set plotted on a linear (a) and a logarithmic scale (b).

Table 8.1: Effects of applying the R_{sig} condition. The number of events passing this condition and the corresponding relative reduction compared to the number of observed events within the original analysis window are listed. In addition, the fractions of the PDFs for signal events, radiative muon decays (RMD), and accidental background events (ABG) that are cut off by using the R_{sig} condition are presented.

| Data Set | Events | Reduction of N_{obs} (%) | PDF Cut Off (%) | | |
|----------|--------|--------------------------------------|-----------------|------|-----|
| | | | Signal | RMD | ABG |
| 2009 | 281 | 9.6 | 0 | 11.9 | 9.0 |
| 2010 | 616 | 4.5 | 0 | 7.7 | 6.8 |
| Combined | 897 | 6.2 | 0 | 9.1 | 7.5 |

8.1.3 Goodness of Fit Checks

In Chapter 7, goodness of fit checks were performed to verify that the measured event distributions fit to the expected background distributions for all observables E_γ , E_e , $\phi_{e\gamma}$, $\theta_{e\gamma}$, and $t_{e\gamma}$. For that purpose, Paerson's χ^2 test and the Kolmogorov-Smirnov test were applied to events within the negative and positive timing sidebands and the analysis window. The same methods are used to check if the distributions of the calculated R_{sig} values are consistent with the corresponding expected background distributions.

The data sets and null hypotheses listed in Table 7.1 are used for the goodness of fit checks of the relative signal likelihood, that is, the same tests as in Section 7.1 are performed. First, the event distributions of the negative and positive timing sidebands are verified to be consistent with the accidental background hypothesis (Test A1 and A2). These tests validate the accidental background PDF. Second, the events within the analysis window are checked to fit to the expected background distribution that is composed of 10% radiative muon decays

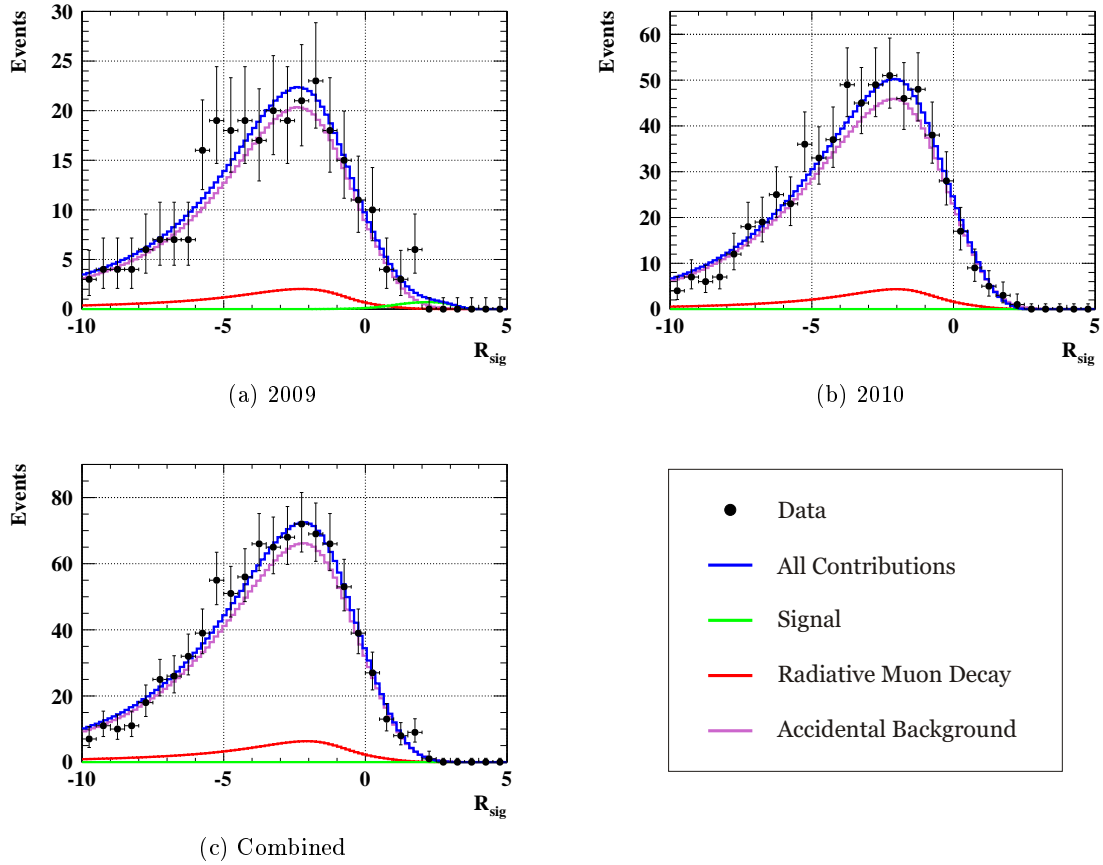


Figure 8.3: Event distributions as a function of R_{sig} for the 2009 (a), 2010 (b), and combined (c) data sets. The events shown in these plots are within the analysis window and fulfill the R_{sig} condition. In addition, the PDFs of R_{sig} for signal events, radiative muon decays, and accidental background events are plotted. They are normalized by the best fit values of the official MEG maximum likelihood analysis (listed in Table 6.5).

and 90 % accidental coincidences (Test B). All tests are separately performed for the 2009 and the 2010 data set.

The distributions of the calculated R_{sig} values of events within the negative and positive timing sidebands and within the analysis window with the corresponding null hypotheses are shown in Fig. 8.4. These plots are used for Paerson's χ^2 test. The bin width of those histograms is chosen to be $\Delta R_{\text{sig}} = 0.5$. As the expected number of events within the two bins with the largest value of R_{sig} is zero, those two bins are ignored for Paerson's χ^2 test. Furthermore, the Kolmogorov-Smirnov test is performed. The cumulative distribution functions of the calculated R_{sig} values and the corresponding null hypotheses are shown in Fig. 8.5. The number of events passing the R_{sig} condition, the p -values obtained with Paerson's χ^2 test, and the p -values obtained with the Kolmogorov-Smirnov test are summarized in Table 8.2.

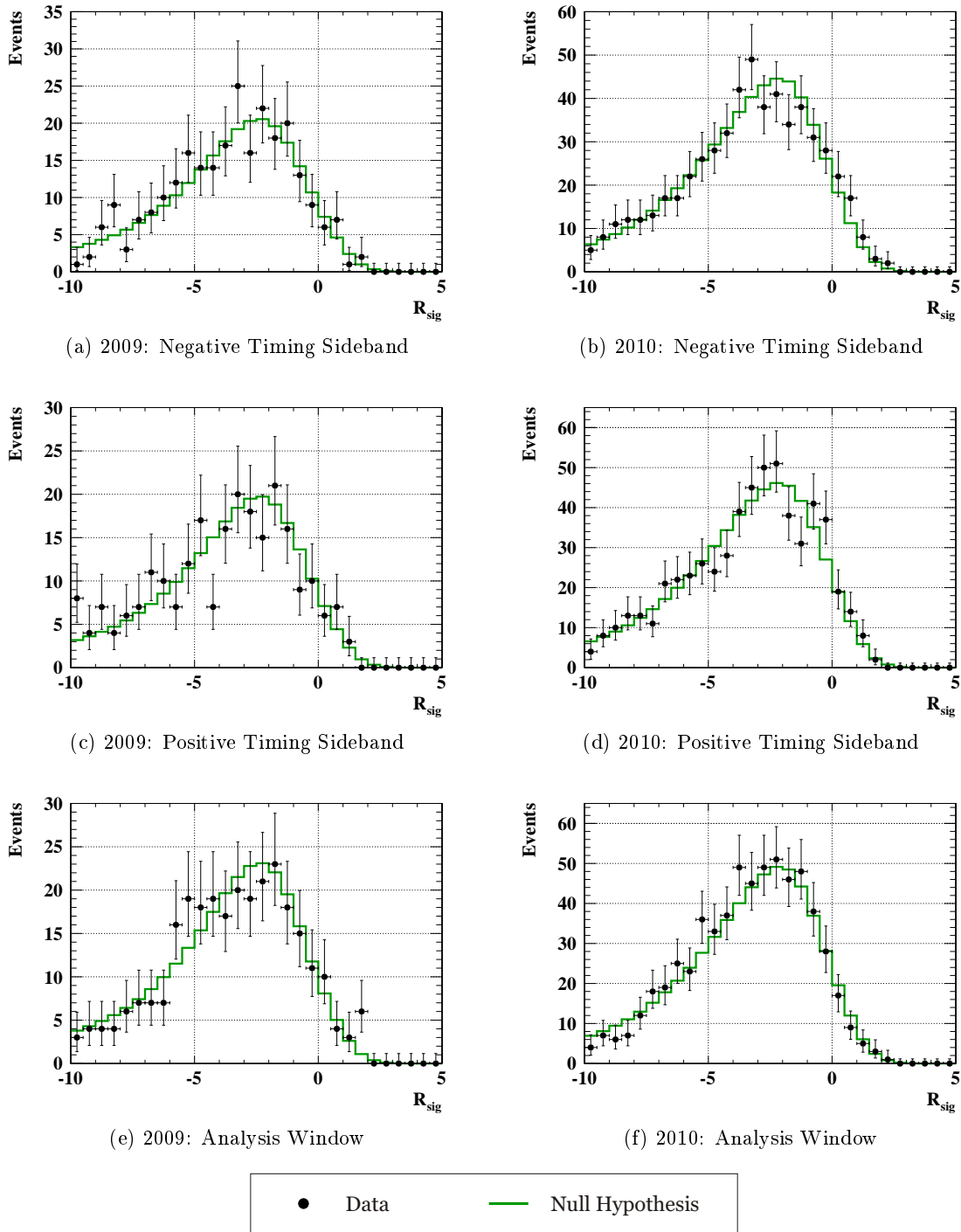


Figure 8.4: Distributions of the calculated R_{sig} values within the negative and positive timing sidebands and within the analysis window separately plotted for the 2009 and the 2010 data set. In addition, the corresponding null hypotheses are shown. These plots are used for Paerson's χ^2 test.

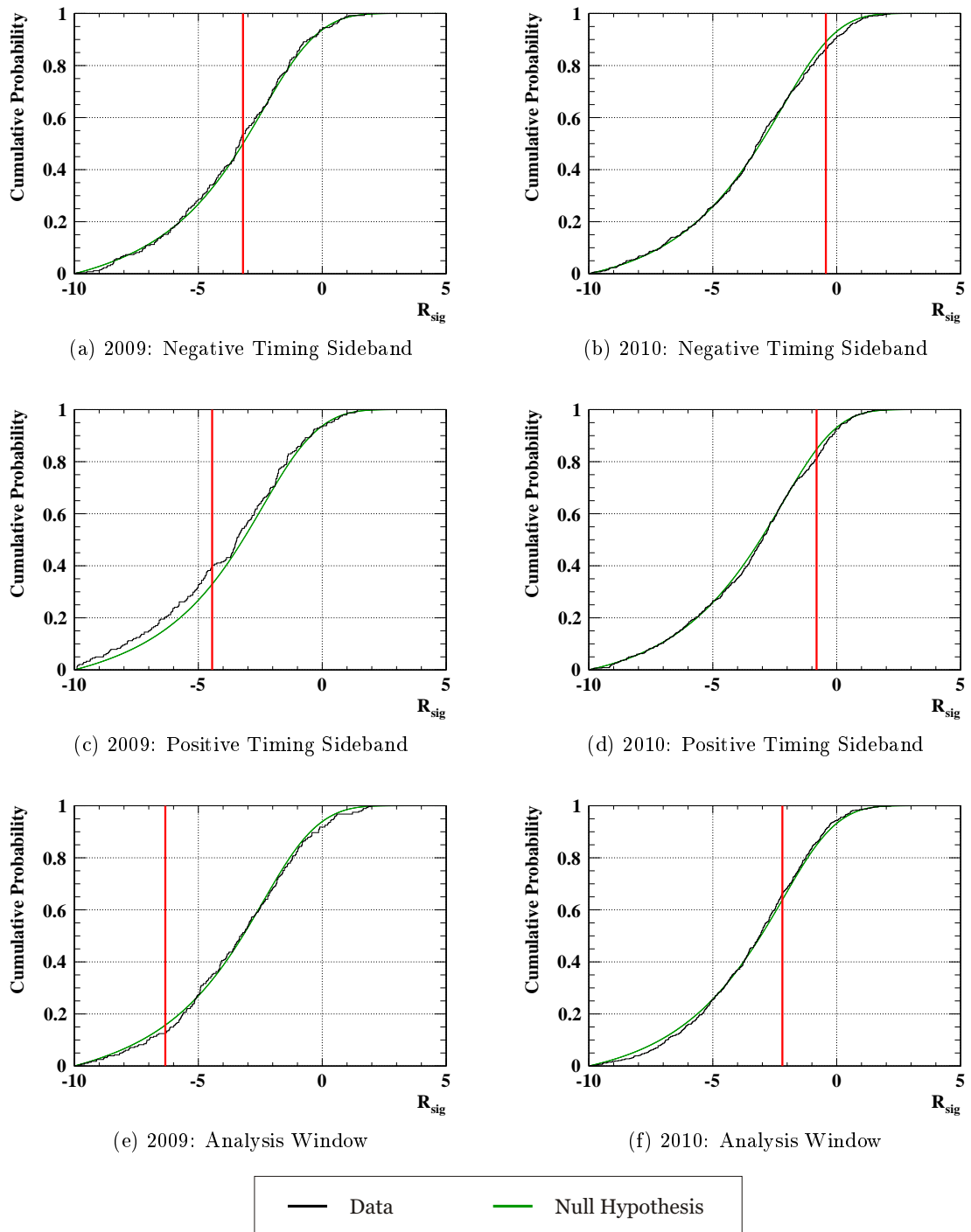


Figure 8.5: Cumulative distribution functions of the calculated R_{sig} values and the corresponding null hypotheses within the negative and positive timing sidebands and within the analysis window separately plotted for the 2009 and the 2010 data set. These plots are used for the Kolmogorov-Smirnov test. The position of the largest deviation between data and null hypothesis is highlighted with a vertical line.

The p -values obtained with Paerson's χ^2 test and the Kolmogorov-Smirnov test do not show any significant anomaly, thus, it is verified that the events distributions fit to the expected background and the accidental background PDFs are validated. This result is consistent with the conclusions of Chapter 7.

Table 8.2: Results of the R_{sig} goodness of fit checks. The number of events passing the R_{sig} condition, the p -values obtained with Paerson's χ^2 test, and the p -values obtained with the Kolmogorov-Smirnov (KS) test are listed for all test configurations.

| | Test | Events | p -Value | |
|------|------|--------|------------|-------|
| | | | χ^2 | KS |
| 2009 | A1 | 258 | 0.925 | 0.801 |
| | A2 | 241 | 0.606 | 0.116 |
| | B | 281 | 0.243 | 0.899 |
| 2010 | A1 | 556 | 0.968 | 0.618 |
| | A2 | 578 | 0.884 | 0.296 |
| | B | 616 | 0.991 | 0.733 |

8.2 The R_{sig} Cut Analysis

The purpose of the R_{sig} cut analysis is to verify the results of the official MEG analysis using an alternative statistical method. As the official MEG analysis method described in Chapter 6 is time-consuming, the cut analysis should be performed faster than the MEG analysis to allow a quick estimation of the confidence interval limits. The basic idea of this analysis is to find an optimal cut for R_{sig} that optimizes both the signal efficiency and the background rejection. By counting the number of observed events and calculating the number of expected background events with R_{sig} values larger than the cut, the upper limit for the branching ratio $\mathcal{B}(\mu^+ \rightarrow e^+ + \gamma)$ is calculated using the Feldman-Cousins method [91]. In the following, the cut analysis method is detailed in Section 8.2.1 and the results of the 2009, 2010, and combined data sets are presented in Section 8.2.2.

8.2.1 Cut Analysis Method

As described in the previous section, the information about all events is reduced to a one-dimensional discriminant variable R_{sig} . By looking at the PDFs shown in Fig. 8.1, it is evident that signal and background events are expected to have different R_{sig} values. Nevertheless, the plots also show that the PDFs for signal and background events overlap between $-2 \lesssim R_{\text{sig}} \lesssim 3$. The crucial task is to find the optimal cut \tilde{c}_R for R_{sig} that maximizes the signal efficiency ϵ_S and the background rejection $1 - \epsilon_B$ simultaneously. As the R_{sig} PDFs are not well defined functions, the cut analysis is performed with binned histograms. The signal efficiency and the

background rejection are therefore defined as:

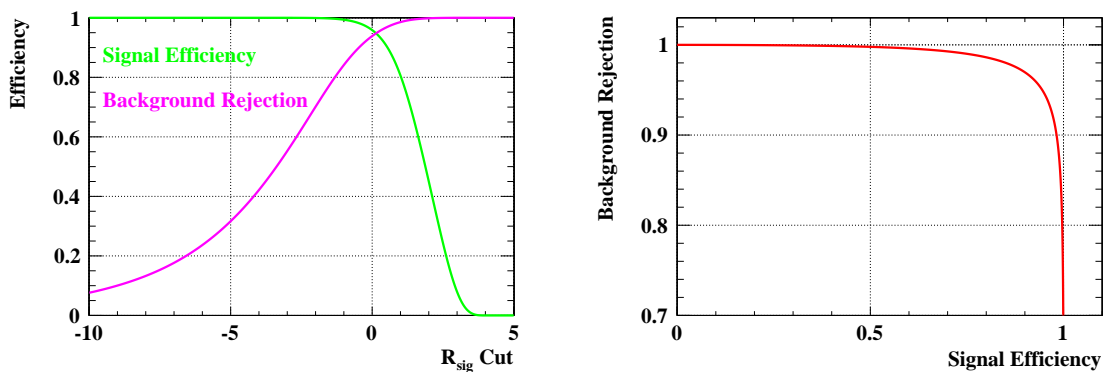
$$\epsilon_S(c_R) = \frac{\sum_{i=n(c_R)}^{n_{max}} S(R_{sig}(i))}{\sum_{i=0}^{n_{max}} S(R_{sig}(i))}, \quad (8.3)$$

$$1 - \epsilon_B(c_R) = 1 - \frac{\sum_{i=n(c_R)}^{n_{max}} B(R_{sig}(i))}{\sum_{i=0}^{n_{max}} B(R_{sig}(i))}. \quad (8.4)$$

In this formula, bin $i = 0$ corresponds to the underflow bin which is required to guarantee correctly normalized signal efficiencies and background rejections. For this analysis, bin $i = 1$ corresponds to $R_{sig}(i = 1) = -10$ while the last bin n_{max} corresponds to $R_{sig}(n_{max}) = 5$. Consequently, $R_{sig}(i)$ is defined as $R_{sig}(i) = R_{sig}(n_{min}) + (i - 1) \cdot \Delta R_{sig}$ with ΔR_{sig} the chosen bin width. The bin $n(c_R)$ denotes the bin which includes the chosen cut c_R for R_{sig} . $S(R_{sig})$ and $B(R_{sig})$ are the PDFs of R_{sig} for signals and the total background. The total background PDF $B(R_{sig})$ is the sum of the PDFs of radiative muon decays $R(R_{sig})$ and accidental coincidences $A(R_{sig})$ normalized by the number of expected radiative muon decays $\langle N_{RMD} \rangle$ and accidental coincidences $\langle N_{ABG} \rangle$, which were introduced in Chapter 6 and are listed in Table 6.1. The total background PDF is therefore defined as:

$$B(R_{sig}) = \frac{\langle N_{RMD} \rangle \cdot R(R_{sig}) + \langle N_{ABG} \rangle \cdot A(R_{sig})}{\langle N_{RMD} \rangle + \langle N_{ABG} \rangle}. \quad (8.5)$$

The signal efficiency and background rejection obtained with the PDFs of the combined data set are shown in Fig. 8.6. The plots show that an increased signal efficiency worsens the



(a) Signal Efficiency and Background Rejection

(b) Background Rejection vs. Signal Efficiency

Figure 8.6: Signal efficiency and background rejection as a function of the chosen cut c_R for R_{sig} (a) and the resulting dependency between signal efficiency and background rejection (b). Both plots are obtained by using the PDFs and the expected background events of the combined data set.

background rejection and vice versa. To find the optimal cut, Punzi [97] proposed to define the quantity

$$\mathcal{N}(c_R) = \frac{a^2}{8} + \frac{9b^2}{13} + a\sqrt{\langle N_B(c_R) \rangle} + \frac{b}{2}\sqrt{b^2 + 4a\sqrt{\langle N_B(c_R) \rangle} + 4\langle N_B(c_R) \rangle} \quad (8.6)$$

where the significance a is chosen to be 5σ and the power b is chosen to be 90%. $\langle N_B(c_R) \rangle$ is the total number of background events that are expected to be above the cut c_R . It is calculated by using the expected number of background events in the analysis window together with the background PDFs of R_{sig} :

$$\langle N_B(c_R) \rangle = (\langle N_{\text{RMD}} \rangle + \langle N_{\text{ABG}} \rangle) \cdot \sum_{i=n(c_R)}^{n_{\text{max}}} B(R_{\text{sig}}(i)). \quad (8.7)$$

To normalize the quantity $\mathcal{N}(c_R)$ correctly, it is divided by the product of the signal efficiency $\epsilon_S(c_R)$, which depends on the cut c_R and the normalization factor k , which is defined in Section 6.5. The obtained quantity $\mathcal{S}(c_R)$ is therefore defined by

$$\mathcal{S}(c_R) = \frac{\mathcal{N}(c_R)}{k \cdot \epsilon_S(c_R)} \quad (8.8)$$

and is called ‘‘Punzi sensitivity’’ for the remainder of this thesis. The optimal cut \tilde{c}_R for R_{sig} minimizes the Punzi sensitivity:

$$\mathcal{S}(\tilde{c}_R) = \min_{c_R} \{\mathcal{S}(c_R)\}. \quad (8.9)$$

After fixing the optimal cut \tilde{c}_R for R_{sig} , the number of observed events $N_O(\tilde{c}_R)$ with an R_{sig} value larger than this cut are counted

$$N_O(\tilde{c}_R) = \sum_{i=n(\tilde{c}_R)}^{n_{\text{max}}} N(i) \quad (8.10)$$

with $N(i)$ the number of observed events in bin i and $n(\tilde{c}_R)$ denotes the bin which includes the optimal cut \tilde{c}_R . Based on the number $N_O(\tilde{c}_R)$ and the number of expected background events above the cut $\langle N_B(\tilde{c}_R) \rangle$, the confidence interval at 90% C.L. is calculated with the Feldman-Cousins method [91]. To obtain the upper and possible lower limit of the branching ratio $\mathcal{B}(\mu^+ \rightarrow e^+ + \gamma)$, the results have to be normalized with the corresponding product $k \cdot \epsilon_S(\tilde{c}_R)$ as described before. Note that systematic uncertainties are not included in this cut analysis.

8.2.2 Results of the Cut Analysis

The R_{sig} cut analysis is applied to the events within the analysis windows of the 2009, 2010, and combined data sets. To reach an accuracy which is as good as possible, a very small binning of $\Delta R_{\text{sig}} = 0.01$ is chosen. For each data set, the optimal cut \tilde{c}_R for R_{sig} was

Table 8.3: Results of the R_{sig} cut analysis of the 2009, 2010, and combined data sets. The cut \tilde{c}_R , the corresponding signal efficiency ϵ_S , the background rejection $1 - \epsilon_B$, the number of observed events N_O , the number of expected background events $\langle N_B \rangle$, and the obtained lower limits (LL) and upper limits (UL) of the branching ratio $\mathcal{B}(\mu^+ \rightarrow e^+ + \gamma)$ at 90 % C.L. are listed.

| Data Set | \tilde{c}_R | ϵ_S (%) | $1 - \epsilon_B$ (%) | N_O | $\langle N_B \rangle$ | LL (90 % C.L.) | UL (90 % C.L.) |
|----------|---------------|---------------------|-------------------------|-------|-----------------------|-----------------------|----------------------|
| 2009 | 1.68 | 61.13 | 99.65 | 3 | 1.03 | $0.11 \cdot 10^{-12}$ | $9.7 \cdot 10^{-12}$ |
| 2010 | 1.73 | 54.50 | 99.68 | 1 | 2.09 | - | $2.0 \cdot 10^{-12}$ |
| combined | 1.82 | 52.43 | 99.75 | 3 | 2.44 | - | $2.9 \cdot 10^{-12}$ |

identified and the upper and lower confidence interval limits were calculated. The results of the cut analysis are listed in Table 8.3. Figure 8.7a shows the Punzi sensitivity $\mathcal{S}(c_R)$ for the combined data set as a function of the cut c_R . The position of the minimum of the Punzi sensitivity is highlighted with a vertical line. In addition, the corresponding number of observed events $N_O(c_R)$ and expected number of background events $\langle N_B(c_R) \rangle$ as a function of the cut c_R are plotted in Fig. 8.7b.

The results listed in Table 8.3 show that the optimal cuts \tilde{c}_R are approximately 1.7 for all data sets. With those cuts, the signal efficiency ϵ_S is given by values between 50 % and 60 % and the background rejection is higher than 99.6 %. As background events are not totally rejected, some of them are expected to have R_{sig} values larger than the cut \tilde{c}_R , namely 1.0, 2.1, and 2.4 events for the 2009, 2010, and combined data sets. The number of actually observed events

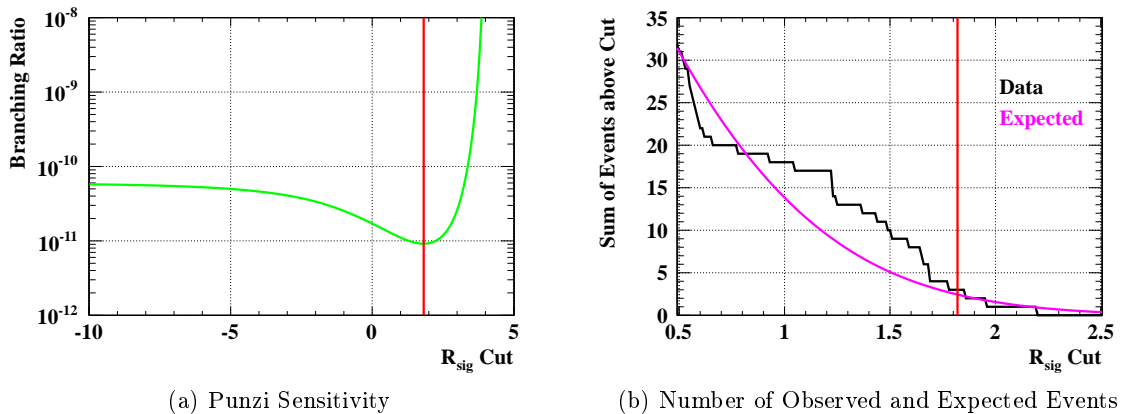


Figure 8.7: Punzi sensitivity as a function of the cut c_R (a) and the number of observed events $N_O(c_R)$ and the expected number of background events $\langle N_B(c_R) \rangle$ with a R_{sig} value larger than the cut c_R (b). The position of the minimum of the Punzi sensitivity is highlighted with a vertical line. Both plots are obtained with the PDFs, expected background events, and data of the combined data set.

above the cut is $N_O = 3$ for 2009 and $N_O = 1$ for 2010 which is consistent with the number of highest rank events presented in Chapter 7. The obtained upper and lower limits for the 2009 data set are in good agreement with the results of the official MEG analysis presented in Table 6.6 while slightly higher upper limits for the 2010 and combined data sets are achieved. The upper limit for the combined data set obtained with the cut analysis is $2.9 \cdot 10^{-12}$ at 90 % C.L. while the official MEG analysis found an upper limit of $2.4 \cdot 10^{-12}$ [81]. The R_{sig} cut analysis confirms therefore the results of the MEG collaboration.

With the currently available computing power, it takes roughly 35 minutes to generate and analyze 1'000 toyMC experiments for the combined data set. As described in Section 6.4, the confidence level curve is obtained by calculating in total 21 points on the curve each with 10'000 toyMC experiments. The total computing time for the upper limit at 90 % takes therefore roughly 120 hours. The cut analysis of the combined data set takes only 30 minutes and is therefore 240 times faster than the official MEG analysis.

The cut analysis is also applied to the negative and positive timing sidebands, which are defined in Eq. (6.4). Due to the large time difference between photon and positron, neither signal events nor radiative muon decays are expected to be within those sidebands. Thus, the number of expected background events $\langle N_B(c_R) \rangle$ above a certain cut c_R is calculated by using the PDF of R_{sig} for accidental coincidences $A(R_{\text{sig}})$ and the number of expected accidental coincidences $\langle N_A \rangle$. The obtained results of the cut analysis of each data set and each timing sideband are summarized in Table 8.4. As in the case of the official MEG analysis, no lower limits of the branching ratio $\mathcal{B}(\mu^+ \rightarrow e^+ + \gamma)$ at 90 % C.L. were found. By comparing the obtained upper limits with the results presented in Table 6.4, it is obvious that the results from the cut analysis tend to slightly higher upper confidence interval limits.

In conclusion, the R_{sig} cut analysis provides confidence interval limits, which tend to be slightly wider than the ones obtained with the MEG analysis. However, the cut analysis method is a fast tool to estimate the order of magnitude of the expected confidence interval limits and to verify the obtained results of the official MEG analysis.

Table 8.4: Results of the R_{sig} cut analysis of the negative and positive timing sidebands of the 2009, 2010, and combined data sets. The cut \tilde{c}_R in R_{sig} , the corresponding signal efficiency ϵ_S , the background rejection $1 - \epsilon_B$, the number of observed events N_O , the number of expected background events $\langle N_B \rangle$, and the upper limits (UL) of the branching ratio $\mathcal{B}(\mu^+ \rightarrow e^+ + \gamma)$ at 90 % C.L. are listed.

| | Data Set | \tilde{c}_R | ϵ_S (%) | $1 - \epsilon_B$ (%) | N_O | $\langle N_B \rangle$ | UL (90 % C.L.) |
|----------|----------|---------------|---------------------|-------------------------|-------|-----------------------|----------------------|
| positive | 2009 | 1.67 | 61.51 | 99.63 | 0 | 1.00 | $2.4 \cdot 10^{-12}$ |
| | 2010 | 1.71 | 55.30 | 99.66 | 1 | 2.07 | $2.0 \cdot 10^{-12}$ |
| | combined | 1.82 | 52.43 | 99.74 | 1 | 2.30 | $1.3 \cdot 10^{-12}$ |
| negative | 2009 | 1.67 | 61.51 | 99.63 | 2 | 1.00 | $7.4 \cdot 10^{-12}$ |
| | 2010 | 1.71 | 55.30 | 99.66 | 4 | 2.07 | $5.3 \cdot 10^{-12}$ |
| | combined | 1.82 | 52.43 | 99.74 | 4 | 2.30 | $3.6 \cdot 10^{-12}$ |

8.3 The R_{sig} Alternative Analysis

The official analysis method of the MEG collaboration to obtain the confidence interval limits at 90 % C.L. is time-consuming as the analysis is performed in the five-dimensional kinematic space $(E_\gamma, E_e, \phi_{e\gamma}, \theta_{e\gamma}, t_{e\gamma})$. To reduce computing time, a cut analysis based on the relative signal likelihood R_{sig} was introduced in Section 8.2. The obtained confidence interval limits tend to be wider than the results of the official MEG analysis. Therefore, an alternative analysis method with a computing time similar to the cut analysis and a precision of the confidence interval limits similar to the MEG analysis is desirable.

This section describes an alternative analysis method based on the relative signal likelihood R_{sig} to calculate the confidence interval limits of the branching ratio $\mathcal{B}(\mu^+ \rightarrow e^+ + \gamma)$. It includes a maximum likelihood analysis and Feldman-Cousins unified approach with profile likelihood ordering. Section 8.3.1 describes the basic idea of this analysis method and the expected background is calculated in Section 8.3.2. A detailed discussion about the analysis method, that is the maximum likelihood analysis and the confidence interval calculation, is given in Section 8.3.3. The sensitivity of this method and the impact of uncertainties are estimated in Section 8.3.4 and Section 8.3.5, respectively. The results of the alternative analysis method for the 2009, 2010, and combined data sets are presented in Section 8.3.6 and they are compared with the results of the official MEG analysis in Section 8.3.7. Finally, sensitivities reachable by the MEG experiment in the next few years are estimated in Section 8.3.8.

8.3.1 Basic Idea

The relative signal likelihood R_{sig} , which was introduced in Section 8.1, is calculated for each event collected by the MEG detector in 2009 and 2010. As described in Section 8.1.1, the PDFs of R_{sig} for signal events $S(R_{\text{sig}})$, radiative muon decays $R(R_{\text{sig}})$, and accidental coincidences $A(R_{\text{sig}})$ are available as binned histograms. Therefore, it is possible to perform a maximum likelihood analysis in the one-dimensional space of the relative signal likelihood.

The maximum likelihood analysis used for the official MEG analysis is described in Section 6.2. It provides the number of signal events N_{sig} , radiative muon decays N_{RMD} , and accidental background events N_{ABG} simultaneously. By looking at the PDFs of R_{sig} shown in Fig. 8.1, it is evident that the PDFs for radiative muon decays and accidental coincidences are almost identical. With such similar PDFs, it is not possible to determine the number of radiative muon decays and accidental coincidences simultaneously. Nevertheless, the expected fraction between those two kinds of events within the analysis window is roughly known. Therefore, a new PDF $B(R_{\text{sig}})$ can be derived from the PDFs of radiative muon decays and accidental coincidences by normalizing them by the fixed fraction between the two kind of events. This new PDF describes the total background composed of radiative muon decays and accidental background events. For analyses with the timing sidebands defined in Eq. (6.4), the total background is composed of accidental coincidences as no radiative muon decays are expected to be within those sidebands. The following PDFs are therefore used for the maximum likelihood analysis described in this chapter:

- $S(R_{\text{sig}})$: Relative signal likelihood PDF for signal events
- $B(R_{\text{sig}})$: Relative signal likelihood PDF for background events
 - Analysis Window: $B(R_{\text{sig}}) = 0.1 \cdot R(R_{\text{sig}}) + 0.9 \cdot A(R_{\text{sig}})$
 - Timing Sidebands: $B(R_{\text{sig}}) = A(R_{\text{sig}})$

Figure 8.8a shows the PDFs of R_{sig} for signal and background events used for the maximum likelihood analysis of the analysis window of the combined data set. The PDFs for signal and background events used for the timing sideband analysis of the combined data set are shown in Fig. 8.8b. By comparing the PDFs for background events, it is evident that they are almost identical for analyses in the analysis window and the timing sidebands.

For the R_{sig} cut analysis described in Section 8.2, radiative muon decays and accidental coincidences were treated separately by using the respective PDFs and the corresponding numbers of expected background events, which are obtained with sideband data. For the R_{sig} analysis described in this chapter, an individual treatment of radiative muon decays and accidental coincidences is not longer possible as the fraction between the two kind of events is fixed. Due to this fixation, a systematic effect is introduced into the analysis whose consequences are estimated later in this section.

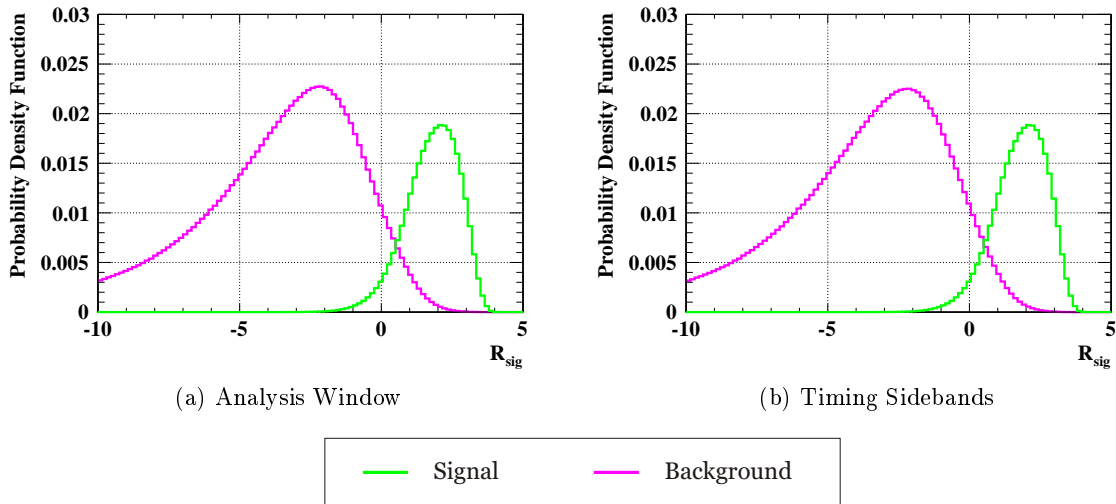


Figure 8.8: Arbitrary normalized PDFs of R_{sig} for signal and background events used for the maximum likelihood analysis of the combined data set. The PDFs used for events within the analysis window are shown in (a) while the PDFs used for timing sideband analyses are shown in (b).

8.3.2 Expected Background

The maximum likelihood analysis based on the relative signal likelihood R_{sig} is applied to events that are within the analysis window defined in Eq. (6.3) and fulfill the R_{sig} condition defined in Eq. (8.2). This means that only events within the analysis window that have a relative signal likelihood between -10 and 5 are allowed. For timing sideband studies, events that are within the time sidebands defined in Eq. (6.4) and fulfill the R_{sig} condition are analyzed.

As shown in Section 8.1.2, roughly 10 % of the background events are cut away by applying the R_{sig} condition while signal events are unaffected. The expected number of background events passing the R_{sig} condition has to be estimated to perform the maximum likelihood analysis correctly. This value is calculated from the number of radiative muon decays and accidental coincidences expected to be within the analysis window (listed in Table 6.1) and the percentage of the corresponding PDFs that is cut off by applying the R_{sig} condition (listed in Table 8.1). The obtained numbers for radiative muon decays, accidental coincidence, and the sum of them are listed in Table 8.5 together with their uncertainties. The latter are composed of the uncertainties of the expected number of background events from the sideband data. As the PDFs are obtained by generating 25'000'000 toyMC events for each kind of event, statistical uncertainties coming from the PDFs are negligible.

As shown in Table 8.1, the percentages of the PDFs which are cut away by using the R_{sig} condition are slightly different for radiative muon decays and accidental coincidences. Nevertheless, this effect has no significant consequences on the fraction between the expected number of radiative muon decays and accidental background events. Unless stated otherwise, the R_{sig} condition is applied to all analyzed events for the remainder of this chapter.

Table 8.5: Expected number of radiative muon decays (RMD) and accidental background events (ABG) that are within the analysis window and fulfill the R_{sig} condition. The sum of those numbers, that is, the total number of expected background (B) is used for the maximum likelihood analysis based on R_{sig} .

| Data Set | RMD | ABG | B |
|----------|----------------|------------------|------------------|
| 2009 | 24.0 ± 2.5 | 246.5 ± 7.6 | 270.5 ± 7.9 |
| 2010 | 48.2 ± 5.5 | 569.3 ± 11.7 | 617.4 ± 13.0 |
| Combined | 72.2 ± 7.2 | 815.6 ± 14.0 | 887.7 ± 15.7 |

8.3.3 Analysis Method

The analysis method used for R_{sig} is similar to the official MEG analysis method presented in Chapter 6. This means that a maximum likelihood analysis is applied to the events within the analysis window to find the number of signal events. The confidence interval limits of the branching ratio $\mathcal{B}(\mu^+ \rightarrow e^+ + \gamma)$ are obtained by using the Feldman-Cousins unified approach with profile likelihood ordering. Compared to the official MEG analysis, the R_{sig} analysis is performed in only one dimension, it is based on binned histograms, and it is applied to events

passing the R_{sig} condition. An independent treatment of radiative muon decays and accidental coincidences is not possible, that is, only the total background is analyzed.

In the following, the maximum likelihood analysis in R_{sig} is explained, the chosen binning is discussed, and the method to calculate the confidence level limits for the branching ratio is presented.

Maximum Likelihood Analysis

The maximum likelihood analysis based on R_{sig} is applied to a number of observed events N_{O} that are within the analysis window Eq. (6.3) and fulfill the R_{sig} condition Eq. (8.2). The advantages of using a maximum likelihood analysis instead of a simple signal box cut analysis were already discussed in Section 6.2. The maximum likelihood analysis provides the number of signal events N_{S} and the total number of background events N_{B} . A simultaneous determination of the number of radiative muon decays and accidental coincidences is not possible as the PDFs for those two kind of events are too similar. The sum of N_{S} and N_{B} is not constrained to be equal to the number of observed events N_{O} . The following extended likelihood function \mathcal{L} with two free parameters is therefore used for this analysis:

$$\mathcal{L}(N_{\text{S}}, N_{\text{B}}) = \frac{e^{-(N_{\text{S}}+N_{\text{B}})} e^{-\frac{(N_{\text{B}}-\langle N_{\text{B}} \rangle)^2}{2\sigma_{\text{B}}^2}}}{N_{\text{O}}!} \times \prod_{i=1}^{N_{\text{O}}} (N_{\text{S}} \cdot S(R_{\text{sig}}) + N_{\text{B}} \cdot B(R_{\text{sig}})). \quad (8.11)$$

In this formula, $S(R_{\text{sig}})$ and $B(R_{\text{sig}})$ describe the PDFs of R_{sig} for signal and background events, respectively. The likelihood function \mathcal{L} is constrained to the total number of expected background events $(\langle N_{\text{B}} \rangle, \sigma_{\text{B}})$ listed in Table 8.5. The parameters N_{S} and N_{B} are determined by minimizing the negative logarithm of the likelihood function using the MINUIT package [89].

Binning

As the PDFs of R_{sig} are obtained by generating many toyMC events using the kinematic PDFs, the previous described maximum likelihood analysis is performed with binned histograms. As a consequence, the result of this analysis depends on the chosen binning. Due to the fact that a lot of toyMC events were generated to produce the R_{sig} PDFs, it is possible to choose small bin widths of down to $\Delta R_{\text{sig}} = 0.009$. Figure 8.9 shows the best fit of the number of signals obtained with the maximum likelihood analysis applied to the 2009 data set as a function of the chosen number of bins in the range $-10 \leq R_{\text{sig}} \leq 5$.

This plot shows that the maximum likelihood analysis becomes insensitive to signal events if larger bin widths are used for the analysis. On the other hand, the smaller the bin widths the less depends the outcome of the maximum likelihood analysis on the chosen binning. By choosing 500 bins or more, the observed fluctuations of the obtained number of signals are much smaller than the statistical uncertainty of the likelihood fit as presented later in this

chapter. For the remainder of this chapter, the range $-10 \leq R_{\text{sig}} \leq 5$ is divided into 900 bins which corresponds to a bin width of $\Delta R_{\text{sig}} = 0.017$.

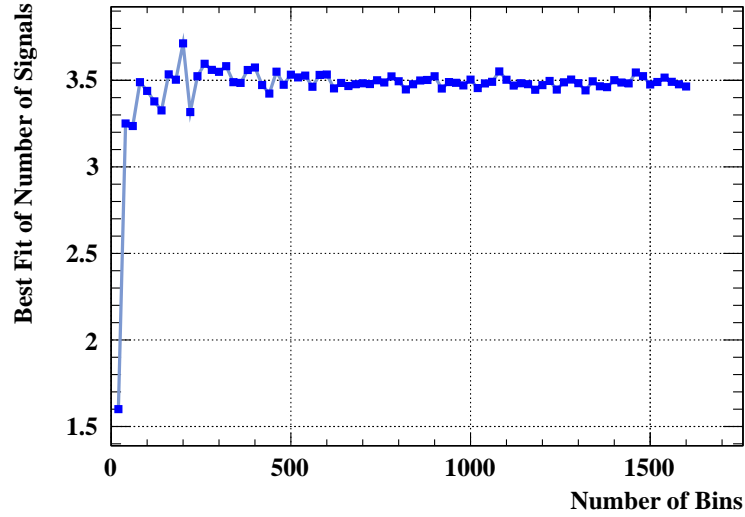


Figure 8.9: Best fit of the number of signals obtained with the R_{sig} maximum likelihood analysis applied to the 2009 data set as a function of the number of bins. To calculate the corresponding bin width, the range $-10 \leq R_{\text{sig}} \leq 5$ has to be divided by the number of bins.

Confidence Interval Calculation

To calculate the upper and possible lower limit of the confidence interval of the branching ratio $\mathcal{B}(\mu^+ \rightarrow e^+ + \gamma)$, the Feldman-Cousins unified approach [91] with profile likelihood ordering [90] is used. The number of background events N_{B} acts as nuisance parameter. The test statistics q used for this analysis is given by

$$q(N_{\text{S}}) = -2 \ln \left(\frac{\mathcal{L}(N_{\text{S}}, \hat{N}_{\text{B}}(N_{\text{S}}))}{\mathcal{L}(\hat{N}_{\text{S}}, \hat{N}_{\text{B}})} \right) \quad (8.12)$$

where \hat{N}_{S} and \hat{N}_{B} are the best fit values for signal and background events obtained from the maximum likelihood analysis. The value $\hat{N}_{\text{B}}(N_{\text{S}})$ maximizes the likelihood function \mathcal{L} defined in Eq. (8.11) for a fixed number of signals N_{S} . A description of the analysis procedure to determine the lower and upper limits of the confidence interval is given in Section 6.4 for the case of two kind of background events (radiative muon decays and accidental coincidences). It can be easily translated to the case with the total background and is therefore not rewritten here. With this analysis procedure, the confidence level curve is calculated. The upper and possible lower limit of the confidence interval in number signal events are determined by cutting the curve with the 90 % confidence level. The obtained limits are normalized with the

normalization factor k introduced in Section 6.5 to get the confidence interval limits of the branching ratio $\mathcal{B}(\mu^+ \rightarrow e^+ + \gamma)$.

As described in Section 6.4, the MEG analysis uses the set $N_{\text{sig}} = \{0, 1, 2, 3, \dots, 19, 20\}$ to obtain the confidence level curve. Each of the 21 points on the curve is calculated by generating and analyzing 10'000 toyMC experiments. In order to increase the accuracy of the R_{sig} analysis compared to the MEG analysis, a denser N_S grid with 41 points is chosen to obtain the confidence level curve, namely $N_S = \{0, 0.5, 1, 1.5, \dots, 19.5, 20\}$. For each point, 10'000 toyMC experiments are generated and analyzed with the R_{sig} alternative analysis.

8.3.4 Sensitivity

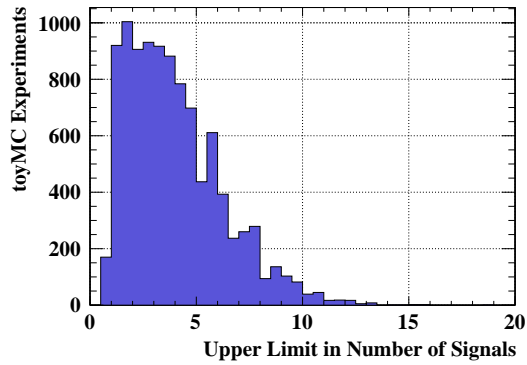
The expected upper limit of the confidence interval was estimated in Section 6.6 for each data set by generating and analyzing many toyMC experiments with the official MEG analysis. In addition, the official MEG analysis was applied to the negative and positive timing sidebands instead of the analysis window. The obtained results are used to cross check the calculated sensitivity. The same idea is used to calculate the sensitivity of the R_{sig} alternative analysis method. In the following, the expected upper limit of the confidence interval is calculated and the timing sidebands are analyzed with the R_{sig} alternative analysis.

Expected Confidence Interval Limit

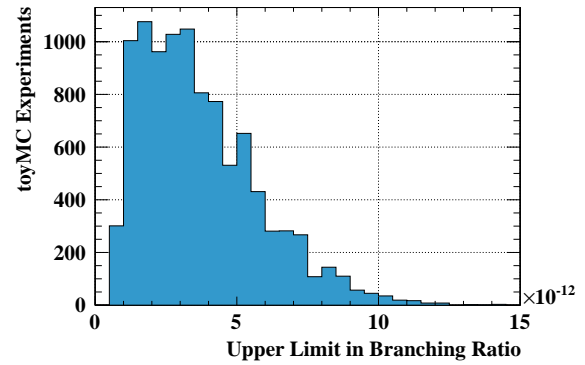
Many toyMC experiments are generated by using the expected number of background events listed in Table 8.5 and the PDFs of R_{sig} for background events. This means that toyMC experiments with the prevailing statistics and detector resolutions are generated for each data set (2009, 2010, and combined) using the background-only hypothesis. Each toyMC experiment is analyzed and the upper limit at 90 % C.L. is calculated. The sensitivity is defined to be the median value of the obtained distribution.

Compared to the MEG sensitivity calculation described in Section 6.6, the computing time of the R_{sig} sensitivity is much shorter as discussed later in this section. Therefore, it is possible to generate ten times more toyMC experiments for each data set (10'000 instead of 1'000) and to choose a denser grid for the confidence level curve ($N_S = \{0, 0.5, 1, 1.5, \dots, 19.5, 20\}$ instead of $N_{\text{sig}} = \{0, 1, 2, 3, \dots, 19, 20\}$). Even though the number of toyMC experiments is increased, the computing time for the sensitivity calculation is still less than one hour with the currently available computing power of the MEG experiment.

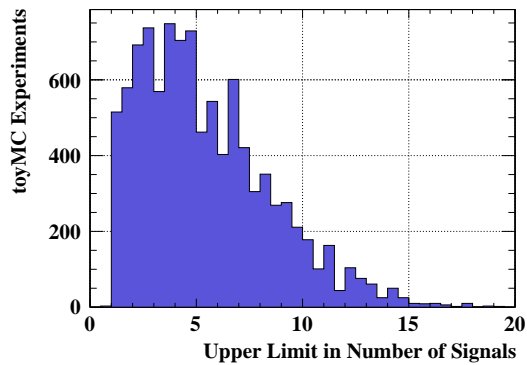
The obtained distributions of the upper limits at 90 % C.L. in number of signals and branching ratio for each data set are shown in Fig. 8.10 and the resulting expected upper limits of the confidence interval are summarized in Table 8.6. By comparing those numbers with the corresponding sensitivities obtained with the official MEG analysis (listed in Table 6.3), it is evident that they are almost identical. The sensitivity reached by the R_{sig} alternative analysis is therefore as accurate as the one of the official MEG analysis.



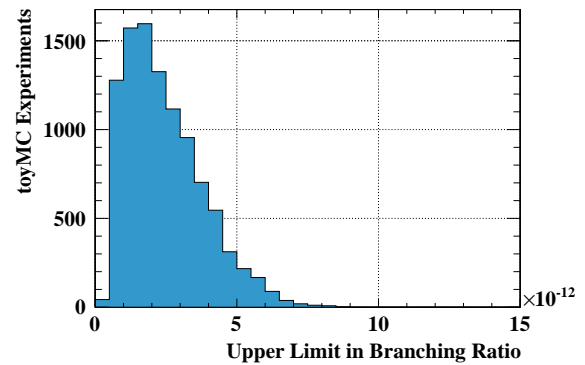
(a) 2009: Number of Signals



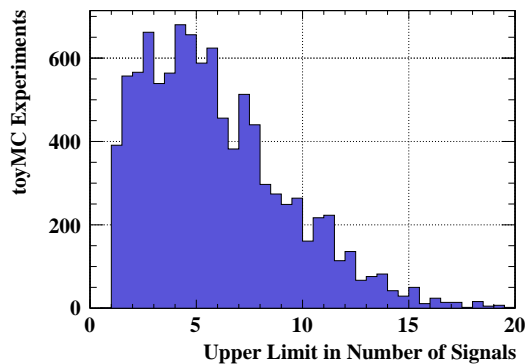
(b) 2009: Branching Ratio



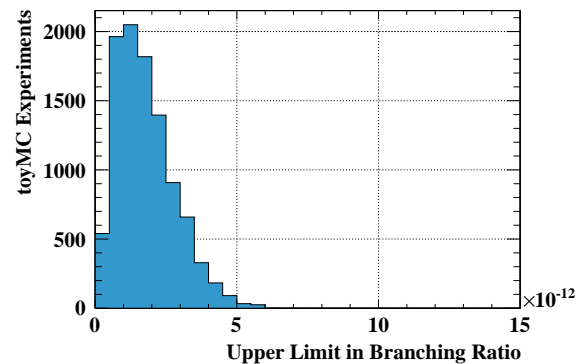
(c) 2010: Number of Signals



(d) 2010: Branching Ratio



(e) Combined: Number of Signals



(f) Combined: Branching Ratio

Figure 8.10: Distributions of the upper limits obtained from toyMC experiments assuming the background-only hypothesis. The plots show the distributions in number of signal events (left) and in branching ratio (right) for the statistics and resolutions of the 2009 (top), 2010 (middle), and combined (bottom) data sets. For each data set, 10'000 toyMC experiments are generated and analyzed with the R_{sig} alternative analysis.

Table 8.6: Expected upper confidence interval limits at 90 % C.L. obtained from toyMC experiments assuming the background-only hypothesis. The results are obtained with the R_{sig} alternative analysis and are given in number of signals and branching ratio for the 2009, 2010, and combined data sets.

| Data Set | Expected Upper Limit | |
|----------|----------------------|----------------------|
| | Number of Signals | Branching Ratio |
| 2009 | 3.6 | $3.3 \cdot 10^{-12}$ |
| 2010 | 4.8 | $2.2 \cdot 10^{-12}$ |
| combined | 5.4 | $1.6 \cdot 10^{-12}$ |

Results of the Timing Sideband Analysis

For testing purposes, the R_{sig} alternative analysis is also applied to events within the negative and positive timing sidebands defined in Eq. (6.4). Due to the large time difference between positron and photon, neither signal events nor radiative muon decays are expected to be within those sidebands. The likelihood function defined in Eq. (8.11) is therefore only constrained to the expected number of accidental coincidences. The number of analyzed events, the best fit values for the number of signals, and the calculated upper limits at 90 % C.L. of the 2009, 2010, and combined data sets are listed in Table 8.7. Similar to the sideband analysis with the official MEG analysis, the R_{sig} alternative analysis provides no lower limits at 90 % C.L. of the branching ratio. The results are in good agreement with the numbers obtained with the official MEG analysis, which are listed in Table 6.4. This means that the maximum likelihood fit and the confidence level calculation work as expected and the obtained upper limits of the branching ratio $\mathcal{B}(\mu^+ \rightarrow e^+ + \gamma)$ are consistent with the sensitivities summarized in Table 8.6.

Table 8.7: Results of the R_{sig} alternative analysis of the negative and positive timing sidebands of the 2009, 2010, and combined data sets. The number of analyzed events N_{O} , the best fit values for the number of signal events N_{S} obtained with the maximum likelihood fit, and the upper limits at 90 % C.L. in number of signal events and branching ratio \mathcal{B} are listed. The errors for the best fit values are 1.645σ MINOS errors.

| | Data Set | N_{O} | N_{S} Best Fit | UL in N_{S} | UL in \mathcal{B} |
|----------|----------|----------------|-------------------------|----------------------|----------------------|
| positive | 2009 | 241 | $-6.8^{+5.0}_{-2.7}$ | 2.8 | $2.6 \cdot 10^{-12}$ |
| | 2010 | 578 | $-4.5^{+5.4}_{-2.1}$ | 3.6 | $1.6 \cdot 10^{-12}$ |
| | combined | 819 | $-7.1^{+5.6}_{-2.1}$ | 3.1 | $0.9 \cdot 10^{-12}$ |
| negative | 2009 | 258 | $-2.3^{+4.5}_{-2.1}$ | 3.5 | $3.2 \cdot 10^{-12}$ |
| | 2010 | 556 | $2.2^{+7.7}_{-4.8}$ | 9.9 | $4.5 \cdot 10^{-12}$ |
| | combined | 814 | $0.5^{+8.1}_{-5.1}$ | 9.0 | $2.7 \cdot 10^{-12}$ |

8.3.5 Uncertainties

The impact of different sources of systematic and statistical uncertainties on the best fit values and the confidence interval limits obtained with the R_{sig} alternative analysis are estimated in this section. The systematic effect of the fixed fraction between radiative muon decays and accidental coincidences, the influence of systematic uncertainties in the PDFs, and the impact of the chosen bin width are analyzed. The uncertainties are estimated using the combined data set.

Fixed Fraction between Radiative Muon Decays and Accidental Coincidences

An independent treatment of radiative muon decays and accidental coincidences is not possible with the R_{sig} alternative analysis because the PDFs of R_{sig} for those two backgrounds are too similar. By fixing the fraction between the two kind of events, it is possible to perform a maximum likelihood analysis and to calculate the confidence level curve as described in Section 8.3.3. However, this fixation introduces a systematic uncertainty to the analysis procedure.

Figure 8.11 shows the correlation between the best fit value of the number of signals obtained with the R_{sig} maximum likelihood analysis and the chosen percentage of radiative muon decays in the total background. The deviations are much smaller than the statistical error of the fitting.

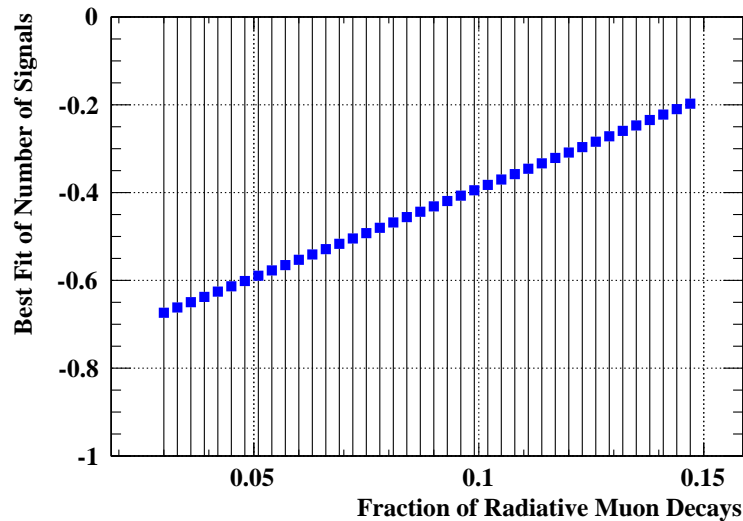


Figure 8.11: Best fit values of the number of signals obtained with the R_{sig} maximum likelihood analysis applied to the combined data set as a function of the chosen percentage of radiative muon decays in the total background. The obtained 1.645σ MINOS errors exceed the shown scale and are in the range of $(-4.7 / +7.9)$.

By looking closely at the expected number of background events obtained from sideband analyses (Table 6.1 used for the official MEG analysis and Table 8.5 for the R_{sig} alternative analysis), it is evident that the fraction of radiative muon decays in the total background is not exactly 10 % but varies between 7.8 % and 9.1 %. An interval of [7 %, 10 %] for the fraction of radiative muon decays is chosen for further investigations. In this interval, the best fit values vary by approximately 0.12 in number of signals which corresponds to 1 % of the 1.645σ MINOS fitting errors, which are in the range of $(-4.7/+7.9)$. The confidence level curve for the combined data set was calculated for 7 % and 10 % radiative muon decays. By comparing the resulting upper limits at 90 % C.L. the systematic effect of fixing the fraction between the two backgrounds is estimated to be 0.6 % of the upper limit.

Systematics

To estimate the total effect of systematic uncertainties of the PDFs, the upper limit of the branching ratio is calculated for the combined data set by including systematic uncertainties. For this purpose, 12'000'000 toyMC events for each kind of event (signal, radiative muon decay, and accidental coincidence) are generated by using alternative kinematic PDFs to produce alternative R_{sig} PDFs. The alternative kinematic PDFs are the PDFs presented in Section 6.3 with all parameters randomized simultaneously according to their uncertainties (statistical and systematic). To calculate the confidence level curve, the required toyMC experiments are generated by using the alternative R_{sig} PDFs. The generated toyMC experiments and the data set are then analyzed with the original R_{sig} PDFs. This means, the same method is applied as it is used for the official MEG analysis to include systematic uncertainties (Section 6.8). For the combined data set, the total effect of systematic uncertainties on the upper limit is calculated to be 1.5 %, which is consistent with the obtained result of the official MEG analysis. The systematic effects are therefore significantly smaller than the statistical uncertainty of the R_{sig} maximum likelihood fit.

Statistical Effects

The R_{sig} PDFs for signal events, radiative muon decays, and accidental coincidences are produced by generating many toyMC events with the kinematic PDFs. In total 25'000'000 toyMC events were produced for each data set (2009, 2010, and combined) and each kind of event. The R_{sig} alternative analysis is based on binned histograms and depends therefore on the chosen binning. A binning of 900 bins in the range of $-10 \leq R_{\text{sig}} \leq 5$ was chosen for the R_{sig} alternative analysis.

In this section, the impact of the finite number of toyMC events used for the PDFs and the chosen binning is estimated. For this purpose, the best fit value \hat{N}_{S} is calculated for the combined data set by using different binnings. Figure 8.12 shows the resulting \hat{N}_{S} as a function of the number of bins within the range $-10 \leq R_{\text{sig}} \leq 5$. For the estimation of the statistical effects, only the values on the right-hand side of the vertical line are used, that is, best fit values obtained with a binning with more than 900 bins. The systematic uncertainty from the binning is defined to be the difference between the maximum and the minimum best

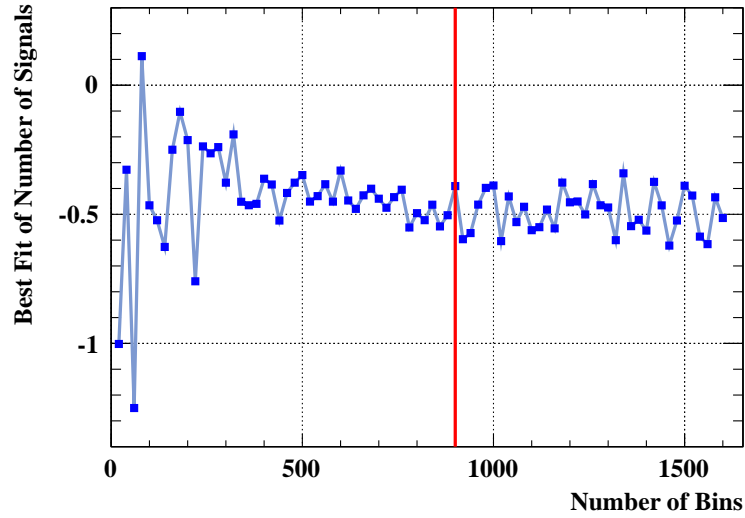


Figure 8.12: Best fit values of the number of signals obtained with the R_{sig} maximum likelihood analysis applied to the combined data set as a function of the chosen number of bins within the range $-10 \leq R_{\text{sig}} \leq 5$. The vertical line denotes the setting (900 bins) used for the analyses presented in this section.

fit values and is therefore a criterion for the occurrent fluctuations. It is compared with the 1.645σ MINOS errors of the fitting, which are in the range of $(-4.7/+7.9)$. For the combined data set, the fluctuations cover a range of $\Delta N_S = 0.23$, which corresponds to 2.2% of the MINOS errors. The impact of the statistical effects is therefore more than twice the impact due to fixing the fraction between radiative muon decays and accidental coincidences.

The estimations of the uncertainties described in this section show that they are small compared to the statistical uncertainties of the maximum likelihood fit so that they are neglected in the following sections.

8.3.6 Results of the R_{sig} Alternative Analysis

This section presents the results of the R_{sig} alternative analysis applied to the 2009, 2010, and combined data sets. The number of analyzed events N_O , the resulting best fit values (\hat{N}_S , \hat{N}_B), and the corresponding asymmetric 1.645σ MINOS errors obtained with MINUIT [89] are summarized in Table 8.8. For this analysis, \hat{N}_S is not constrained to the physics region so that negative values are allowed. The event distributions as a function of R_{sig} for the 2009, 2010, and combined data sets are shown in Fig. 8.13. Additionally, the total fit as well as the contributions of signal and background events weighted with the corresponding best fit values are plotted. As mentioned in Section 8.3.3, a very small binning was chosen for this analysis. To increase the readability, a rougher binning of $\Delta R_{\text{sig}} = 0.5$ is used to create the plots.

Table 8.8: Results of the R_{sig} maximum likelihood analysis of the 2009, 2010, and combined data sets. The number of observed events N_O that are within the analysis window and fulfill the R_{sig} condition as well as the best fit values of the number of signal events \hat{N}_S and the total number of background events \hat{N}_B are listed. The errors are given in 1.645σ MINOS errors.

| Data Set | N_O | \hat{N}_S | \hat{N}_B |
|----------|-------|----------------------|-------------------------|
| 2009 | 281 | $3.5^{+6.6}_{-4.4}$ | $271.8^{+11.8}_{-11.7}$ |
| 2010 | 616 | $-2.2^{+5.0}_{-1.9}$ | $617.6^{+19.0}_{-18.9}$ |
| combined | 897 | $-0.4^{+7.9}_{-4.7}$ | $889.8^{+22.9}_{-22.8}$ |

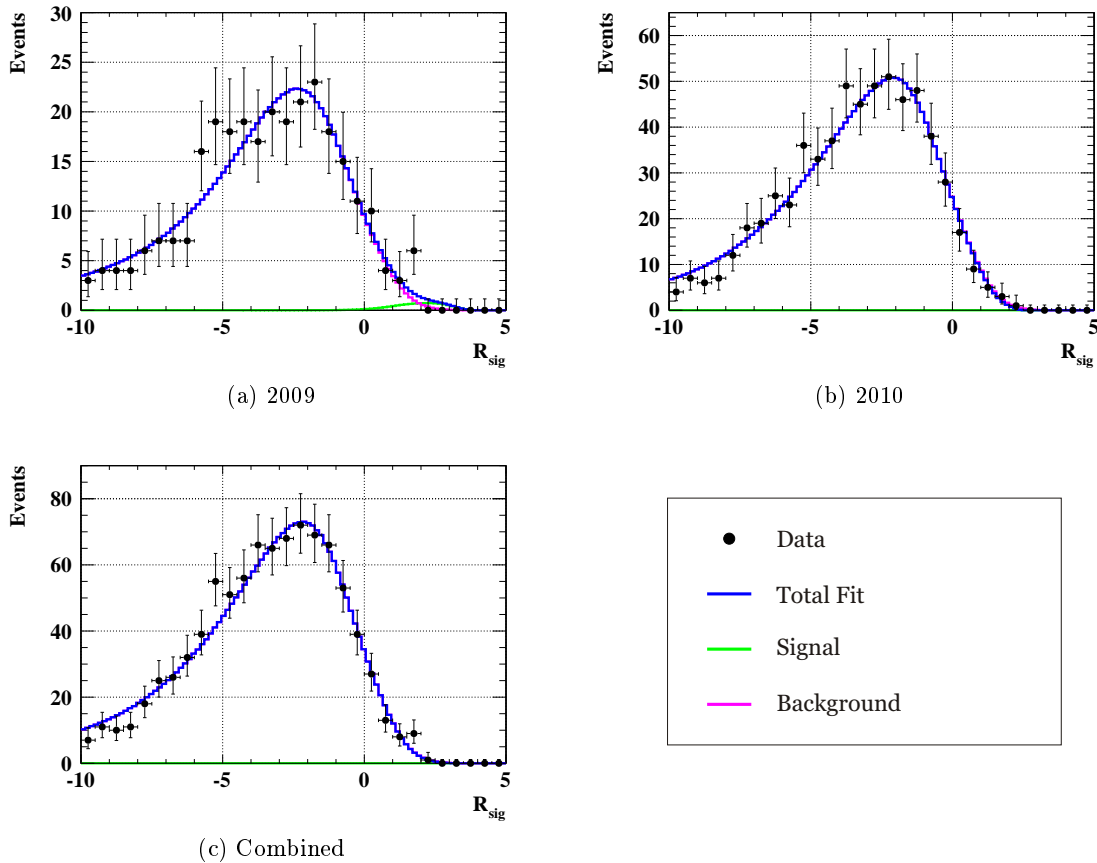


Figure 8.13: Event distribution of the calculated R_{sig} values of the 2009 (a), 2010 (b), and combined (c) data sets. The events are within the analysis window and fulfill the R_{sig} condition. In addition, the total fit as well as the contributions of signal and background events weighted with the corresponding best fit values obtained with the R_{sig} alternative analysis are shown.

Similar to the official MEG analysis, the R_{sig} alternative analysis of the 2009 data set results in $\hat{N}_S = 3.5$ number of signal events, the analysis of the 2010 data set yields to a result of $\hat{N}_S = -2.2$, and the analysis of the combined data set finds $\hat{N}_S = -0.4$. This means that the R_{sig} alternative analysis confirms the no-signal hypothesis and the obtained best fit values of the number of signals are consistent with the official MEG results presented in Table 6.5.

After determining the best fit values for the number of signal and background events, the confidence interval is determined using Feldman-Cousins unified approach with profile likelihood ordering. The calculated confidence level curves for each data set as a function of the number of signals as well as the normalized curves as a function of the branching ratio are shown in Fig. 8.14. The corresponding upper and lower limits of the confidence interval are summarized in Table 8.9. It is important to note that the number of signal events is constrained to be positive to calculate the confidence level curves (a more detailed discussion about the consequences of this constrain is given in Section 6.4).

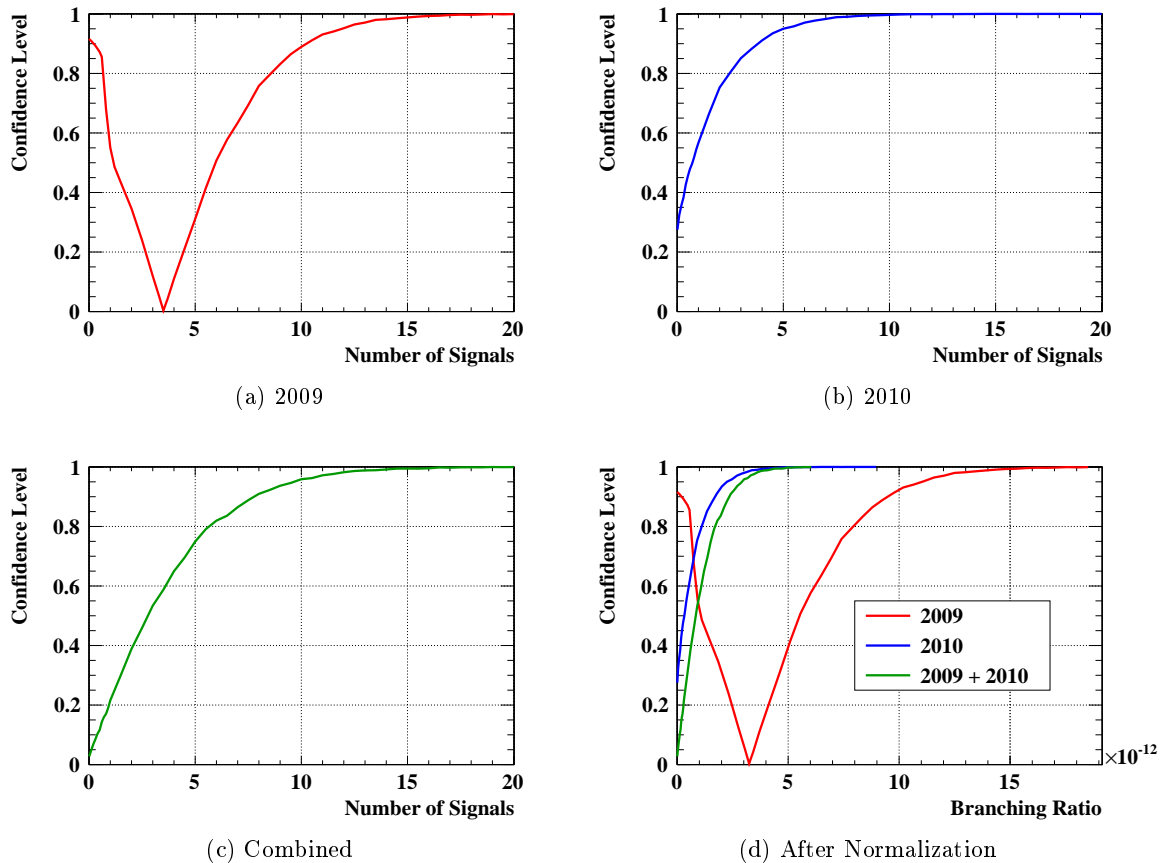


Figure 8.14: Confidence level curves of 2009 (a), 2010 (b), and combined (c) data sets as a function of the number of signal events along with the comparison of all confidence level curves after normalization (d) obtained with the R_{sig} alternative analysis.

The comparison of the obtained numbers with the results of the official MEG analysis presented in Table 6.6 clearly shows that the two analyses provide consistent confidence level limits. Similar to the official MEG analysis, the R_{sig} alternative analysis finds for the 2009 data set both a lower and an upper confidence interval limit at 90 % C.L. while the analysis of the 2010 and combined data sets yields only an upper limit. Finally, also the R_{sig} alternative analysis obtains an upper limit of $2.4 \cdot 10^{-12}$ at 90 % C.L. for the branching ratio $\mathcal{B}(\mu^+ \rightarrow e^+ + \gamma)$ which lowers the result found by the MEGA experiment by a factor of five. The results obtained with the official MEG analysis, the R_{sig} cut analysis, and the R_{sig} alternative analysis are compared in Section 8.3.7.

With the official MEG analysis and the currently available computing power of the MEG experiment, it takes roughly 35 minutes to generate and analyze 1'000 toyMC experiments for the combined data set. This means, to calculate a confidence level curve with 41 points ($N_S = \{0, 0.5, 1, 1.5, \dots, 19.5, 20\}$) each with 10'000 toyMC experiments, as it is done for the R_{sig} alternative analysis, would take in total 10 days. As the R_{sig} alternative analysis is performed in only one dimension, the generation and analysis of toyMC experiments is much faster. For the statistics of the combined data set, the confidence level curve and therefore the confidence interval limits are calculated within 30 minutes which lowers the computing time of the official MEG analysis by a factor of 480.

In conclusion, the R_{sig} alternative analysis provides confidence interval limits that are comparable with the results of the official MEG analysis. The R_{sig} alternative analysis finds for the combined data set an upper limit of $2.4 \cdot 10^{-12}$ at 90 % C.L. of the branching ratio $\mathcal{B}(\mu^+ \rightarrow e^+ + \gamma)$, which is the same result as presented by the MEG collaboration [81]. A disadvantage of the R_{sig} alternative analysis is that an independent treatment of radiative

Table 8.9: Results of the confidence level calculation for the 2009, 2010, and combined data sets obtained with the R_{sig} analysis. The obtained upper limits (UL) and lower limits (LL) are given in number of signals (a) and in branching ratio (b).

| (a) Upper and Lower Limits in Number of Signals | | | |
|-------------------------------------------------|----------------|----------------|----------------|
| Data Set | LL (90 % C.L.) | UL (90 % C.L.) | UL (95 % C.L.) |
| 2009 | 0.2 | 10.2 | 11.9 |
| 2010 | - | 3.8 | 5.0 |
| combined | - | 7.8 | 9.7 |

| (b) Upper and Lower Limits in Branching Ratio | | | |
|-----------------------------------------------|-----------------------|----------------------|-----------------------|
| Data Set | LL (90 % C.L.) | UL (90 % C.L.) | UL (95 % C.L.) |
| 2009 | $0.20 \cdot 10^{-12}$ | $9.5 \cdot 10^{-12}$ | $11.0 \cdot 10^{-12}$ |
| 2010 | - | $1.7 \cdot 10^{-12}$ | $2.2 \cdot 10^{-12}$ |
| combined | - | $2.4 \cdot 10^{-12}$ | $2.9 \cdot 10^{-12}$ |

muon decays and accidental coincidences is not possible. The fraction between those two kind of background events is fixed by hand which introduces a small systematic uncertainty. On the other hand, the relative signal likelihood analysis is performed very fast. Once the PDFs of R_{sig} are generated, the R_{sig} analysis is performed 480 times faster than the MEG analysis. The newly proposed analysis method is therefore a fast alternative to the official MEG analysis.

8.3.7 Comparison of Results

In this section, the confidence interval limits obtained with the R_{sig} cut analysis and the R_{sig} alternative analysis are compared with the results of the official MEG analysis. The obtained upper and lower limits of the confidence intervals at 90 % C.L. of the branching ratio $\mathcal{B}(\mu^+ \rightarrow e^+ + \gamma)$ are summarized in Table 8.10. The table shows that both the cut analysis and the alternative analysis confirm the results obtained with the official MEG analysis. The cut analysis tends to result in confidence intervals that are wider than the ones obtained with the official MEG analysis and the alternative analysis. The R_{sig} alternative analysis results in almost identical confidence interval limits than the official MEG analysis.

Table 8.10: Upper (a) and lower (b) confidence interval limits at 90 % C.L. of the branching ratio $\mathcal{B}(\mu^+ \rightarrow e^+ + \gamma)$ obtained with the official MEG analysis, the R_{sig} cut analysis, and the R_{sig} alternative analysis.

| (a) Upper Confidence Interval Limits of $\mathcal{B}(\mu^+ \rightarrow e^+ + \gamma)$ at 90 % C.L. | | | |
|----------------------------------------------------------------------------------------------------|----------------------|----------------------|----------------------|
| Data Set | MEG Analysis | Cut Analysis | Alternative Analysis |
| 2009 | $9.6 \cdot 10^{-12}$ | $9.7 \cdot 10^{-12}$ | $9.5 \cdot 10^{-12}$ |
| 2010 | $1.7 \cdot 10^{-12}$ | $2.0 \cdot 10^{-12}$ | $1.7 \cdot 10^{-12}$ |
| combined | $2.4 \cdot 10^{-12}$ | $2.9 \cdot 10^{-12}$ | $2.4 \cdot 10^{-12}$ |

| (b) Lower Confidence Interval Limits of $\mathcal{B}(\mu^+ \rightarrow e^+ + \gamma)$ at 90 % C.L. | | | |
|----------------------------------------------------------------------------------------------------|-----------------------|-----------------------|-----------------------|
| Data Set | MEG Analysis | Cut Analysis | Alternative Analysis |
| 2009 | $0.17 \cdot 10^{-12}$ | $0.11 \cdot 10^{-12}$ | $0.20 \cdot 10^{-12}$ |
| 2010 | - | - | - |
| combined | - | - | - |

8.3.8 Prospects

As described in Chapter 2, the MEG experiment performed another physics data taking run in 2011 and a further run is planned to take place in 2012. The amount of data collected during these runs are roughly estimated by using the run schedules and subtracting the time needed for calibrations. No significant hardware upgrades are planned for run 2011

and 2012 so that the detector resolutions will be comparable with the performances in 2009 and 2010. Theoretically, the expected upper limits at the 90 % C.L. for $\mathcal{B}(\mu^+ \rightarrow e^+ + \gamma)$ can be estimated by calculating the sensitivity with the official MEG analysis method. But in practice, those sensitivities were never calculated with this analysis method as it is too time-consuming especially due to the increased statistics. Therefore, the MEG collaboration calculated the sensitivities using the R_{sig} cut analysis and the results were scaled to take into account the differences between cut analysis and the official MEG analysis. The proposed R_{sig} alternative analysis method provides a fast calculation tool, which provides similar results as the official MEG analysis, a scaling factor becomes therefore unnecessary.

The number of data acquisition (DAQ) days with the MEG trigger, the normalization factor k , and the expected total number of background events B (radiative muon decays and accidental coincidences) for each run are listed in Table 8.11. The numbers for run 2009 and 2010 correspond to the results presented in this thesis while the numbers for 2011, 2012, and 2013 are realistic estimates. For this analysis, the expected upper limit with an additional run performed in 2013 is also estimated even though such a physics data taking run is not planned.

Table 8.11: Specifications used to calculate the sensitivities for data taking runs until 2013. The number of DAQ days with the MEG trigger, the normalization factor k , and the expected total number of background events B (radiative muon decays and accidental coincidences) are listed for each run. The numbers for run 2009 and 2010 correspond to the results presented in this thesis while the numbers for 2011, 2012, and 2013 are realistic estimates.

| Data Set | DAQ Days | Normalization Factor k | Expected Background B |
|----------|----------|--------------------------|-------------------------|
| 2009 | 35 | $1.08 \cdot 10^{12}$ | 270.5 ± 7.9 |
| 2010 | 56 | $2.23 \cdot 10^{12}$ | 617.4 ± 13.0 |
| 2011* | 81 | $3.36 \cdot 10^{12}$ | 926.1 ± 15.2 |
| 2012* | 122 | $5.04 \cdot 10^{12}$ | 1389.2 ± 20.0 |
| 2013* | 122 | $5.04 \cdot 10^{12}$ | 1389.2 ± 20.0 |

* = estimates

For the following analysis, the statistics of each run beginning with 2009 are added together to get the total amount of data after each run. The sensitivities of 2009 and 2009-2010 (combined data set) were already calculated and are listed in Table 8.6. To calculate the expected upper limit of 2009-2011, 2009-2012, and 2009-2013 the method described in Section 8.3.4 is used together with the combined R_{sig} PDFs and the specifications listed in Table 8.11. The window for the number of signals to calculate the confidence level curves is expanded to $N_S = \{0, 1, 2, 3, \dots, 38, 39\}$ to take into account the increased statistics. The obtained sensitivities are listed in Table 8.12 together with the sensitivity of 2008 presented in Chapter 2. The 2008 statistics is not included in the analysis of the following runs. The sensitivities are also plotted in Fig. 8.15 as a function of the number of DAQ days. The error area covers 68 % of the toyMC experiments that were generated to calculate the expected upper limit. In addition, the actually obtained upper limits at 90 % C.L. for the 2008, 2009, and 2009-2010 data taking periods are shown.

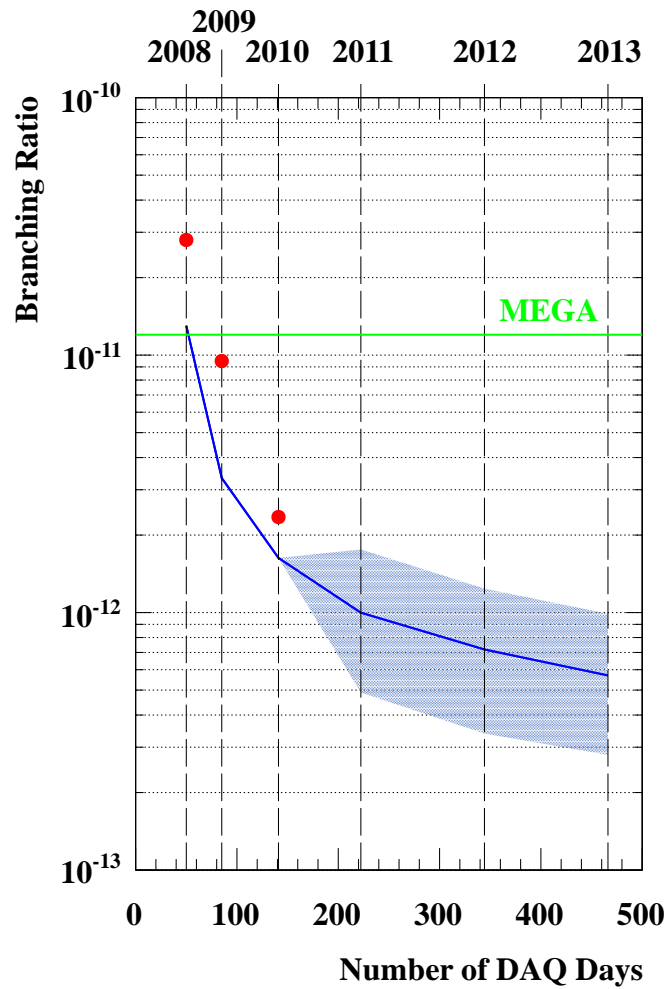


Figure 8.15: Expected upper limits of the branching ratio $\mathcal{B}(\mu^+ \rightarrow e^+ + \gamma)$ for the physics data taking periods from 2008 to 2013 obtained with the R_{sig} alternative analysis plotted as a function of the number of DAQ days. The error area covers 68 % of the toyMC experiments that were generated to calculate the expected upper limit. In addition, the actually obtained upper limits at 90 % C.L. for the 2008, 2009, and 2009-2010 data taking periods (dots) and the result of the MEGA experiment (horizontal line) are shown in this plot. The dates refer to the end of the corresponding run.

Table 8.12: Results of the sensitivity calculations for the physics data taking periods from 2008 to 2013 obtained with the R_{sig} alternative analysis. The sensitivities of 2008, 2009, and 2009-2010 were already presented in Chapter 2 and Section 8.3.4.

| Periods | Sensitivity |
|-----------|----------------------|
| 2008 | $1.3 \cdot 10^{-11}$ |
| 2009 | $3.3 \cdot 10^{-12}$ |
| 2009-2010 | $1.6 \cdot 10^{-12}$ |
| 2009-2011 | $1.0 \cdot 10^{-12}$ |
| 2009-2012 | $7.2 \cdot 10^{-13}$ |
| 2009-2013 | $5.7 \cdot 10^{-13}$ |

The result of the prospect calculations show that the MEG experiment can achieve a sensitivity of $7.2 \cdot 10^{-13}$ at the end of run 2012. Even though a further run is performed in 2013 the expected sensitivity is only $5.7 \cdot 10^{-13}$ and is therefore significantly larger than the aimed sensitivity of 10^{-13} in branching ratio. This means that the original goal of the MEG experiment can only be reached with higher muon stopping rates in the target to increase the collected amount of data. To deal with the related increase of the number of accidental background events, significantly improved detector resolutions will be necessary. Hardware upgrades are therefore essential if the MEG collaboration wants to reach a sensitivity of 10^{-13} of the branching ratio $\mathcal{B}(\mu^+ \rightarrow e^+ + \gamma)$ in the next few years.

8.4 Summary

To reduce the computing time of the confidence level calculation, the information about each event was translated from the five-dimensional observable space to the one-dimensional space of a discriminant variable, that is, the relative signal likelihood. The probability density functions of the relative signal likelihood for each kind of event are obtained by generating many toyMC events. Goodness of fit checks were performed to verify that the event distributions fit to the expected background. As signal and background events are expected to have different relative signal likelihoods, a cut analysis is performed to obtain the confidence interval limits where the optimal cut is found by minimizing the Punzi sensitivity. By counting the number of observed events and calculating the number of expected background events above this cut, the upper and possible lower limits are obtained by using the Feldman-Cousins method. The calculated confidence interval limits tend to be wider than the ones obtained with the official MEG analysis but the required computing time is two orders of magnitude shorter. Therefore, the cut analysis method is a fast tool to estimate the reachable confidence interval limits and to verify the obtained results of the official MEG analysis.

An alternative analysis method based on the relative signal likelihood was proposed to calculate the confidence interval of the branching ratio $\mathcal{B}(\mu^+ \rightarrow e^+ + \gamma)$. As the corresponding probability density functions of radiative muon decays and accidental coincidences are too similar, a separated treatment of those two kinds of background events was not possible.

However, signal and background events are expected to have different relative signal likelihoods. A maximum likelihood analysis was performed to obtain the best fit values for signal and background events. The confidence level curve and therefore the confidence interval was calculated with the Feldman-Cousins unified approach and profile likelihood ordering. The results of the alternative analysis are comparable with the results of the official MEG analysis. For the 2009 and 2010 combined data set, the alternative analysis results in an upper limit of $2.4 \cdot 10^{-12}$ at 90 % C.L. for the branching ratio $\mathcal{B}(\mu^+ \rightarrow e^+ + \gamma)$, which is equal to the result obtained with the official MEG analysis. The major advantage of the alternative analysis is that it is performed 480 times faster than the official MEG analysis. With the currently available computing power of the MEG experiment, the alternative analysis calculates the confidence interval limits within 30 minutes. The newly proposed analysis is therefore a fast alternative to the official MEG analysis method.

Chapter 9

Conclusion and Outlook

In the Standard Model of particle physics, the lepton flavor violating decay $\mu^+ \rightarrow e^+ + \gamma$ is strongly suppressed due to small neutrino masses. However, new theoretical models describing physics beyond the Standard Model predict branching ratios $\mathcal{B}(\mu^+ \rightarrow e^+ + \gamma)$ of up to 10^{-12} . The MEG collaboration is searching for the decay $\mu^+ \rightarrow e^+ + \gamma$ aiming a sensitivity of 10^{-13} for the branching ratio $\mathcal{B}(\mu^+ \rightarrow e^+ + \gamma)$. Therefore, the MEG collaboration will either prove the existence of new physics by observing the decay $\mu^+ \rightarrow e^+ + \gamma$ or it will put stringent constraints on the allowed parameter space of new theoretical models. The MEG collaboration has been taking data since 2008. The analysis of the combined data sets collected in 2009 and 2010 results in a branching ratio of $\mathcal{B}(\mu^+ \rightarrow e^+ + \gamma) < 2.4 \cdot 10^{-12}$ at 90 % C.L., which is the most stringent limit on this decay to date.

In the first part of this thesis, improvements of the MEG drift chamber system to enhance the performance stability and the measurement accuracy were introduced. The automated pressure control system, which regulates the gas flows through the drift chambers and the COBRA magnet, achieves a pressure stability of 0.002 Pa in RMS. The performance of the pressure control system is therefore two orders of magnitude better than the required 1 Pa precision. The sophisticated high voltage system of the drift chambers ensures a stable power supply of 0.02 V in RMS for applied 1840 V. The implemented step-by-step ramping, the fast trip recovery, and the safety features ensure a safe and stable operation of the drift chambers. Furthermore, the data of a new optical survey method using corner cube reflectors were analyzed and it was shown that the accuracy of the new method is significantly better than the one of the previously used optical survey method.

A measuring technique to determine the timing resolution of a DRS4 chip with a precision of 3 ps was proposed. The technique was applied to a DRS4 evaluation board to determine the timing resolution of a DRS4 chip independent of the MEG electronics system. The measurements show that electrical noise has non-negligible impact on the timing resolution. In addition, the impact of swapping clock cables on the timing measurement was studied. The clock cables are used to synchronize the DRS chips of the MEG experiment. It was proven that an exchanged clock cable can affect the timing measurement by up to 65 ps.

In order to analyze the performance of the MEG photon detector for variable beam conditions, the MEG collaboration adopted a monitoring method based on a pulsed neutron generator. The muon beam induced background is subtracted from the collected neutron data by producing a background template. In this thesis, it was shown that the neutron generator method had a stable performance during run 2010 and that beam related performance instabilities of the photon detector can be excluded. In addition, the neutron generator method was used to verify that the dead channel recovery algorithm to compensate broken photomultiplier tubes works as expected.

In the second part of this thesis, analysis methods were proposed to verify that the detection and analysis processes of the MEG experiment behave as expected. In particular, two analysis methods based on goodness of fit checks were introduced that verify the consistency of measured event distributions and background probability density functions. Applying these tests to the 2009 and 2010 data sets results in no significant deviations from the expected background. In addition, the event distributions of the analysis window of the 2009 and 2010 data sets were plotted with the focus placed on events with high relative signal likelihood. By visually checking the plots, neither unexpected dependencies, nor event clusters, nor significant differences between the data sets were recognized.

Finally, to confirm the results obtained with the official MEG analysis, the information about the collected events was transformed from the multidimensional parameter space to the one-dimensional space of the relative signal likelihood. In this thesis, two analysis methods based on the relative signal likelihood were proposed to calculate the confidence interval limits of the branching ratio $\mathcal{B}(\mu^+ \rightarrow e^+ + \gamma)$. First, a cut analysis was proposed where the optimal cut for the relative signal likelihood is determined by minimizing the sensitivity. The calculated confidence interval limits tend to be wider than the ones obtained with the MEG analysis method but the required computing time is two orders of magnitude faster. In particular, the cut analysis results in a branching ratio of $\mathcal{B}(\mu^+ \rightarrow e^+ + \gamma) < 2.9 \cdot 10^{-12}$ at 90 % C.L. for the combined 2009 and 2010 data set and confirms the results of the official MEG analysis. Second, an alternative analysis method was proposed that combines a maximum likelihood analysis and the Feldman-Cousins unified approach with profile likelihood ordering. The alternative analysis method is 480 times faster than the official analysis method and the provided results are comparable to the results of the MEG analysis. For the combined data set of 2009 and 2010, the alternative analysis results in an upper limit of $\mathcal{B}(\mu^+ \rightarrow e^+ + \gamma) < 2.4 \cdot 10^{-12}$ at 90 % C.L., which is equal to the result obtained with the MEG analysis. Therefore, the newly proposed analysis method is a fast alternative to the official MEG analysis method.

The sensitivities that can be reached by the MEG experiment in the next few years were estimated with the alternative analysis method. The results of these prospect calculations showed that the MEG experiment can achieve a sensitivity of $7.2 \cdot 10^{-13}$ at the end of run 2012. This means that the original goal of the MEG collaboration, namely aiming a sensitivity of 10^{-13} , can only be reached within two or three years of data taking by using higher muon stopping rates. To deal with the related increased number of accidental background events, significantly improved detector resolutions are required. The MEG collaboration is now investigating various detector upgrades such as smaller photon sensors for the liquid xenon detector, a very thin silicon vertex tracker near the target to provide an additional

measuring point on the positron track, or an active target made of scintillating fibers. The MEG collaboration will perform a physics data taking run in 2012, followed by detector upgrade work in 2013-2014. Finally, the MEG collaboration expects to take physics data in 2015-2017 with the goal to reach a sensitivity below 10^{-13} .

Appendix A

Graphs of the Event and Background Distribution Checks

The consistency checks described in Chapter 7 include studies about the event distributions and goodness of fit checks to verify that the background distributions fit to the probability density functions. As those consistency checks require a large amount of plots, only the most important ones are shown in Chapter 7. All other plots are presented in this appendix.

Figures A.1 to A.4 show the distributions of the measured observables E_γ , E_e , $\theta_{e\gamma}$, and $t_{e\gamma}$ used for Pearson's χ^2 test. The corresponding cumulative distribution functions used for the Kolmogorov-Smirnov test are shown in Figs. A.5 to A.8. The obtained p -values are listed in Table 7.2 and Table 7.3, respectively. The results do not show any deviations from the expectations.

The muon decay position (vertex) and the location of the photon detection point of events within the analysis window of the 2009 and 2010 data set as a function of the run number are shown in Fig. A.9. In these plots, the high ranked events listed in Table 7.4 are highlighted. Events with a run number less than 70'000 were recorded in 2009 while all other events were collected in 2010. The data break around run number 80'000 is caused by the 2010 charge exchange calibration. The distributions show no time dependencies.

The distributions of the photon detection coordinates plotted in always two spatial coordinates are shown in Fig. A.10. By visually checking the individual plots, neither unexpected spacial dependencies nor event clustering are recognizable.

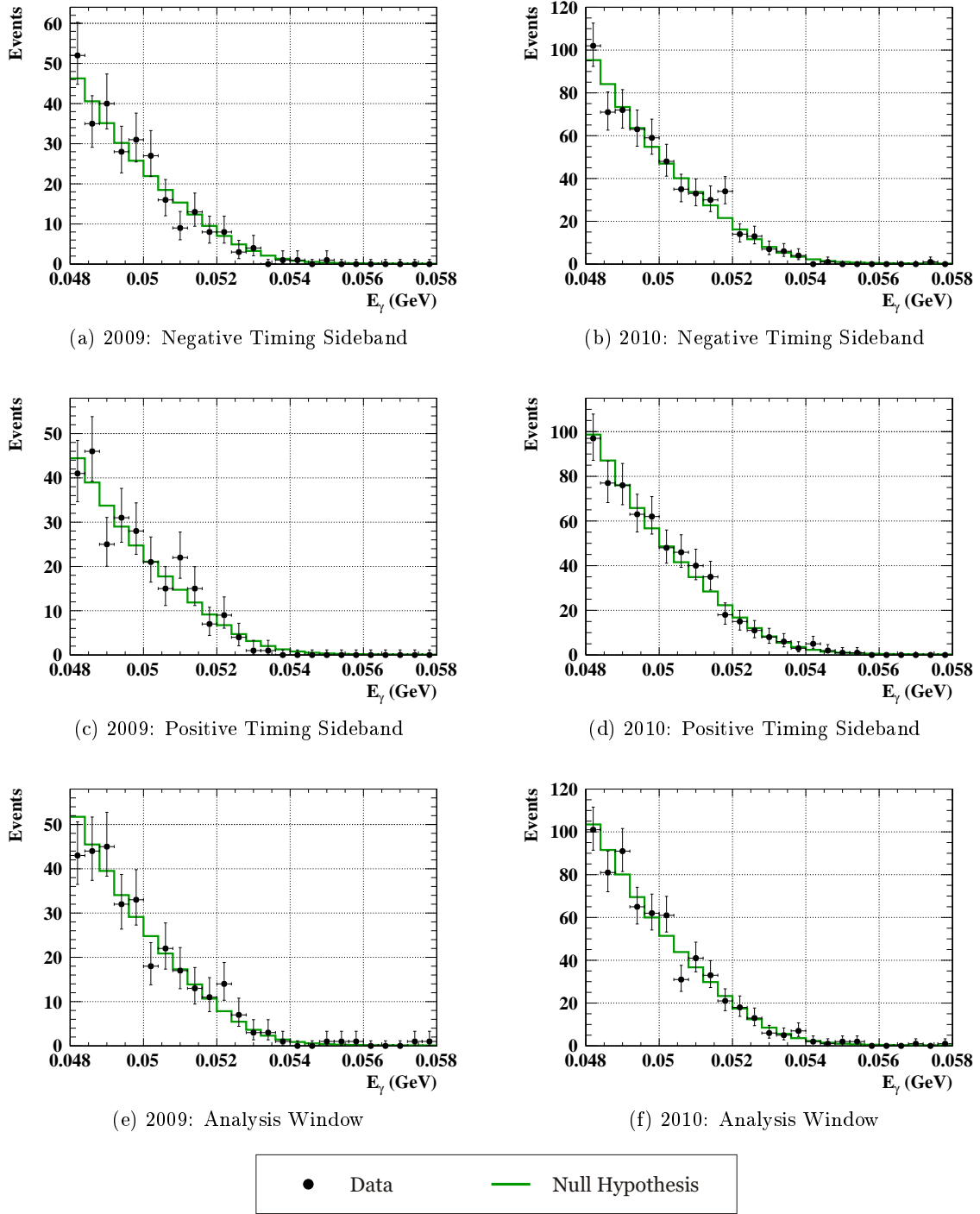


Figure A.1: Distributions of the measured photon energies E_γ within the negative and positive timing sidebands and within the analysis window separately plotted for the 2009 and the 2010 data set. In addition, the corresponding null hypotheses are shown. These plots are used for Paerson's χ^2 test.

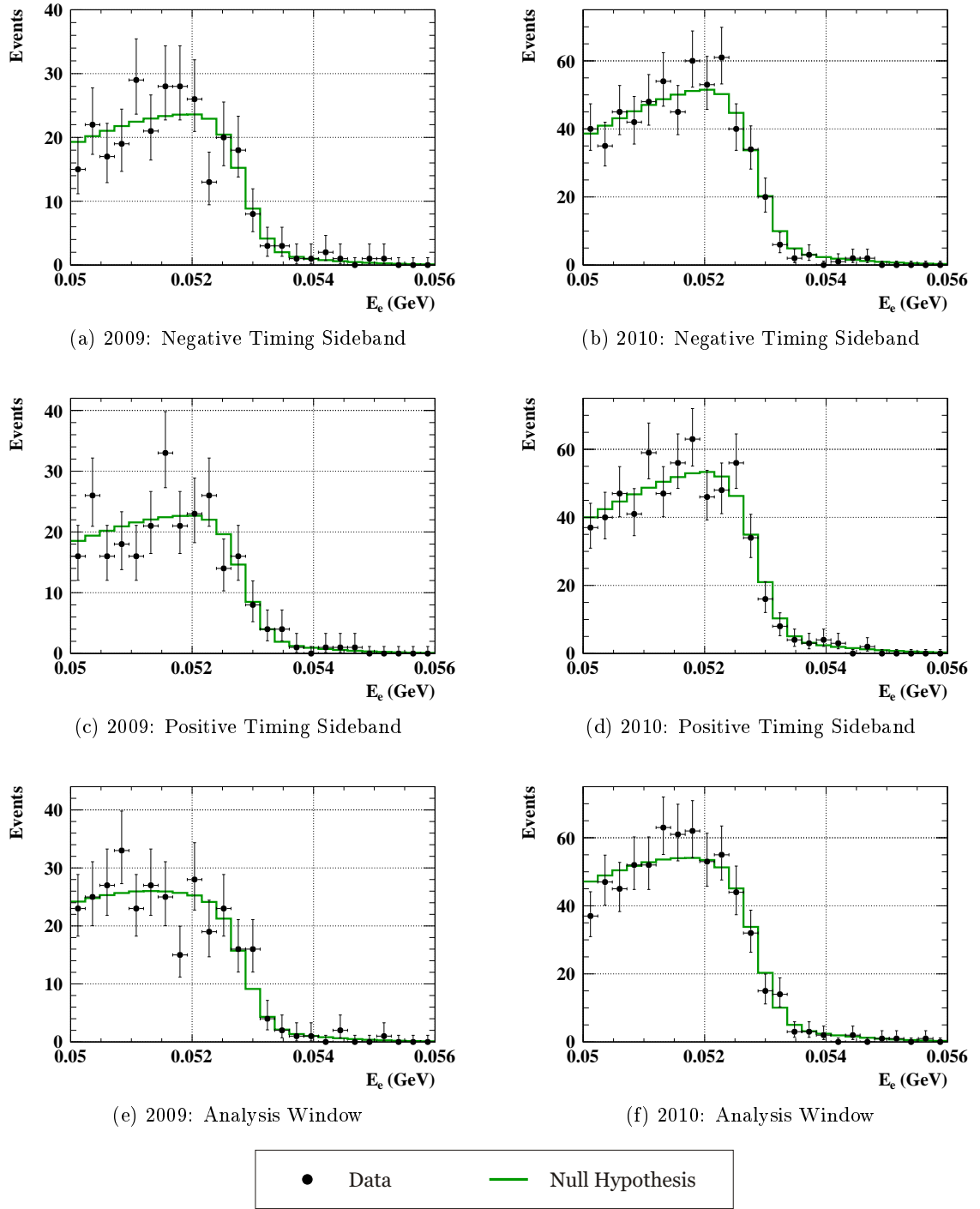


Figure A.2: Distributions of the measured positron energies E_e within the negative and positive timing sidebands and within the analysis window separately plotted for the 2009 and the 2010 data set. In addition, the corresponding null hypotheses are shown. These plots are used for Pearson's χ^2 test.

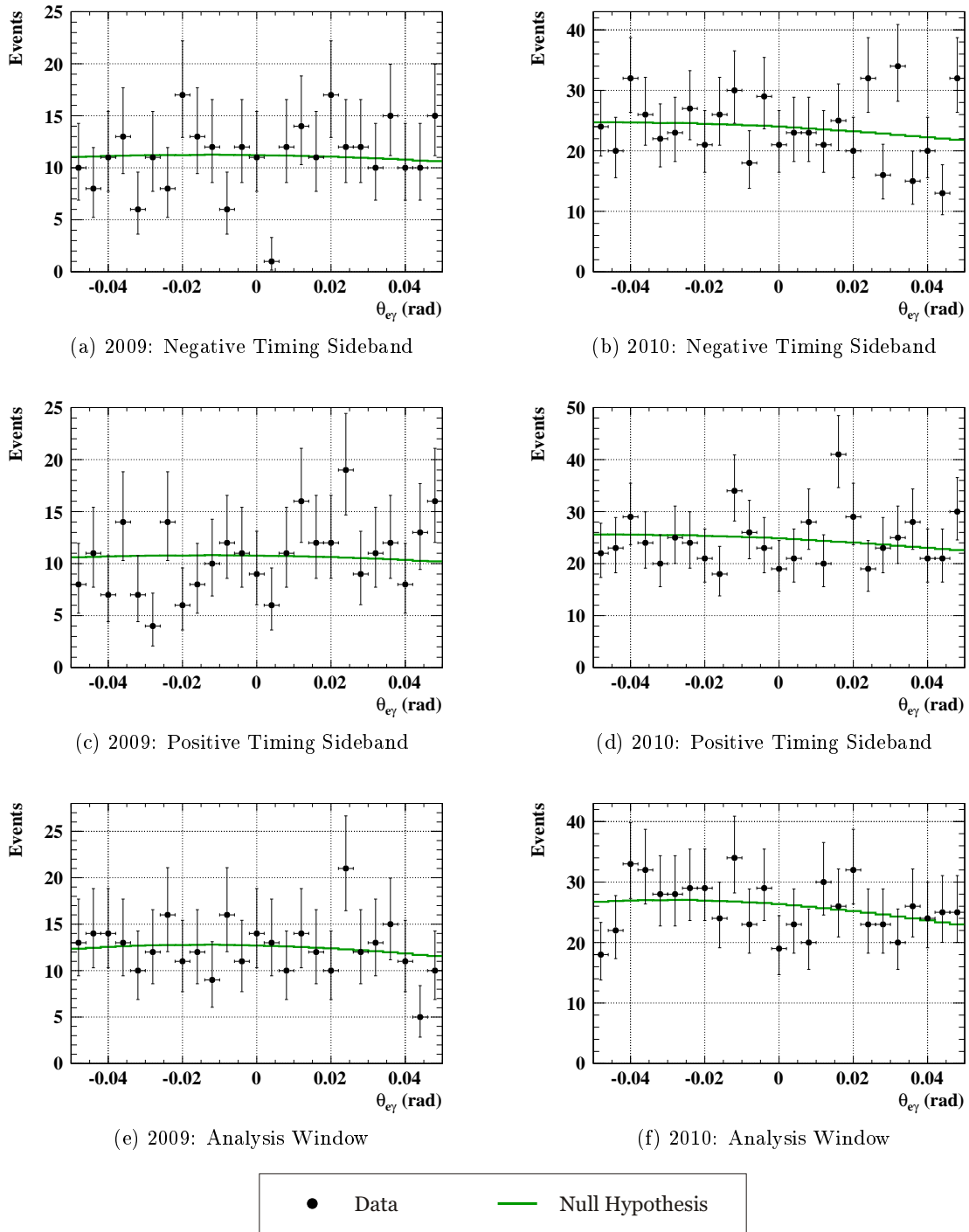
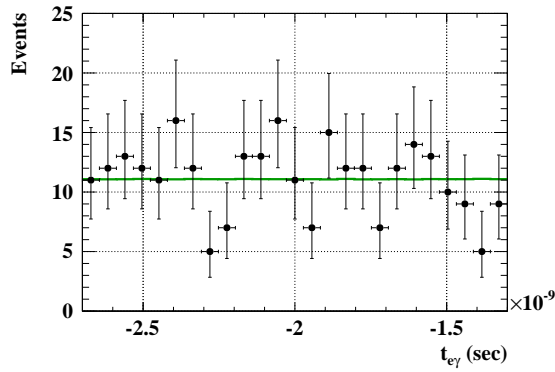
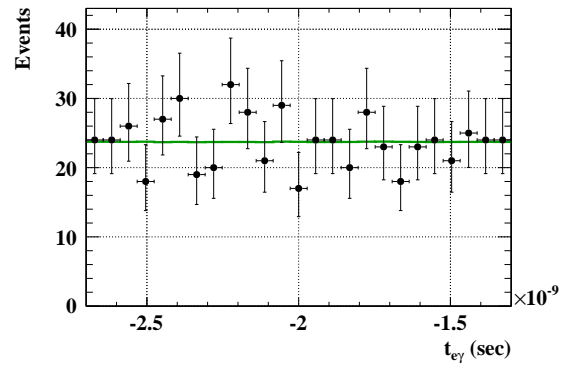


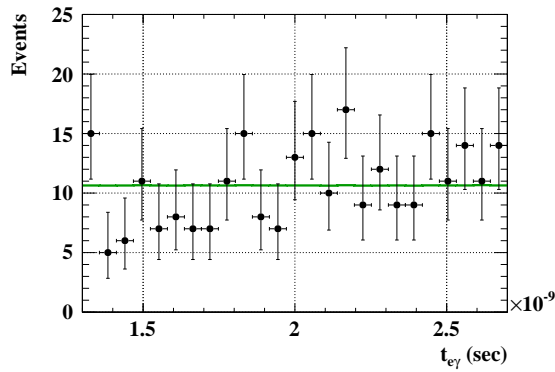
Figure A.3: Distributions of the measured polar angles $\theta_{e\gamma}$ within the negative and positive timing sidebands and within the analysis window separately plotted for the 2009 and the 2010 data set. In addition, the corresponding null hypotheses are shown. These plots are used for Paerson's χ^2 test.



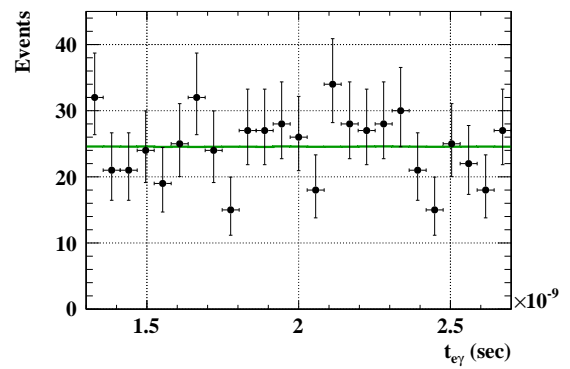
(a) 2009: Negative Timing Sideband



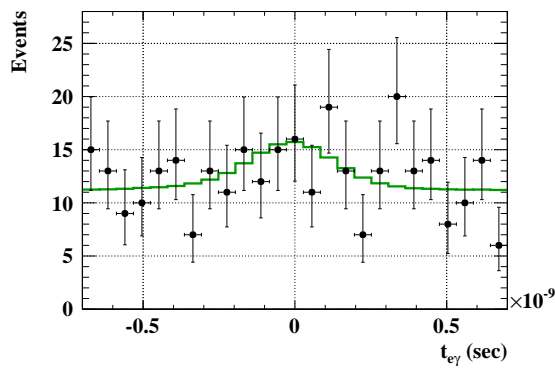
(b) 2010: Negative Timing Sideband



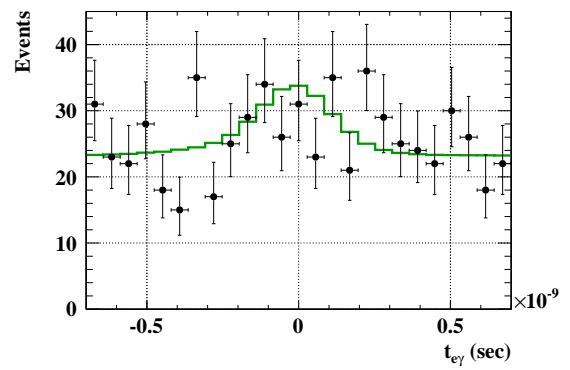
(c) 2009: Positive Timing Sideband



(d) 2010: Positive Timing Sideband



(e) 2009: Analysis Window



(f) 2010: Analysis Window



Figure A.4: Distributions of the measured timing $t_{e\gamma}$ within the negative and positive timing sidebands and within the analysis window separately plotted for the 2009 and the 2010 data set. In addition, the corresponding null hypotheses are shown. These plots are used for Paerson's χ^2 test.

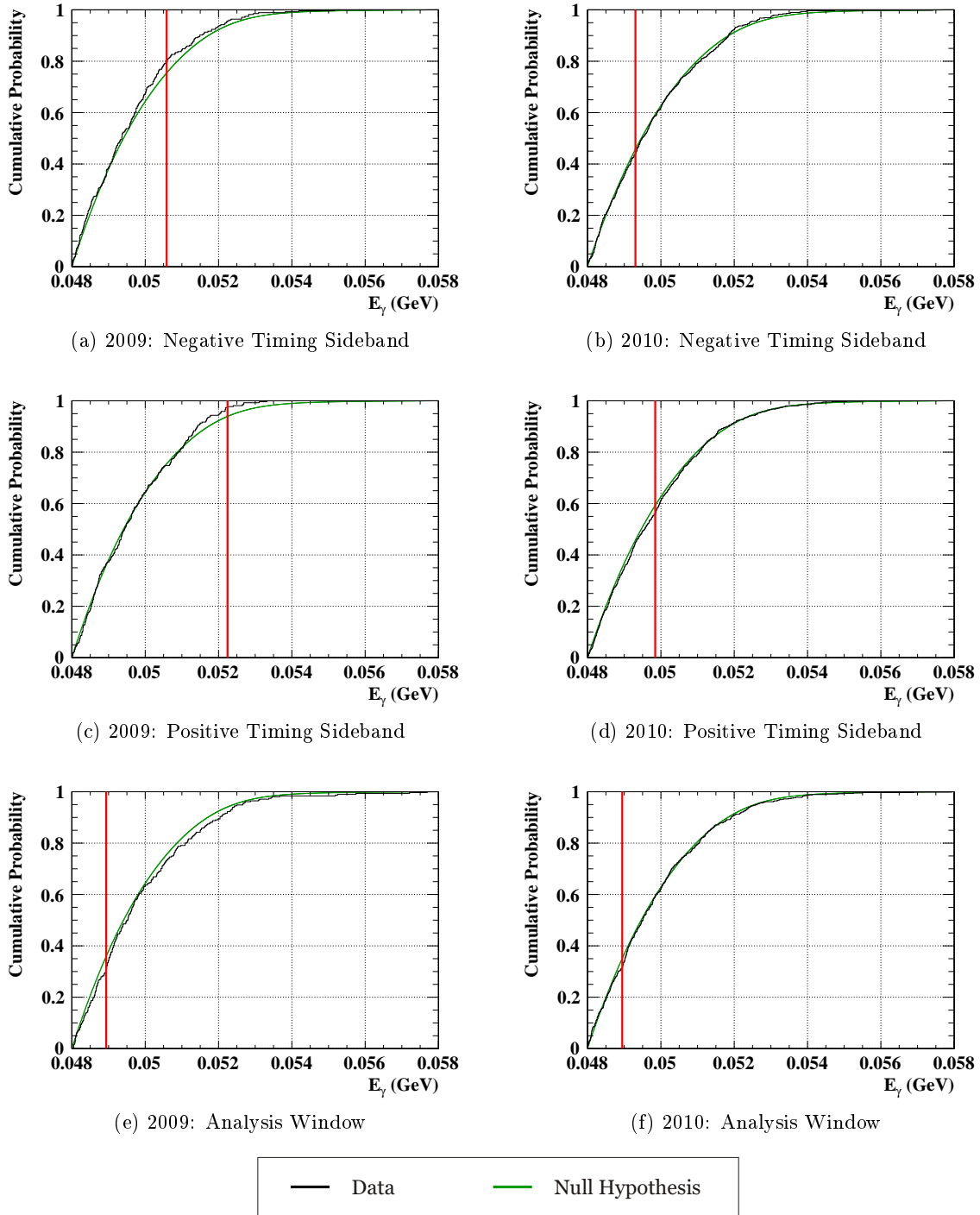


Figure A.5: Cumulative distribution functions of the measured photon energies E_γ and the corresponding null hypotheses within the negative and positive timing sidebands and within the analysis window separately plotted for the 2009 and the 2010 data set. These plots are used for the Kolmogorov-Smirnov test. The position of the largest deviation between data and null hypothesis is highlighted with a vertical line.

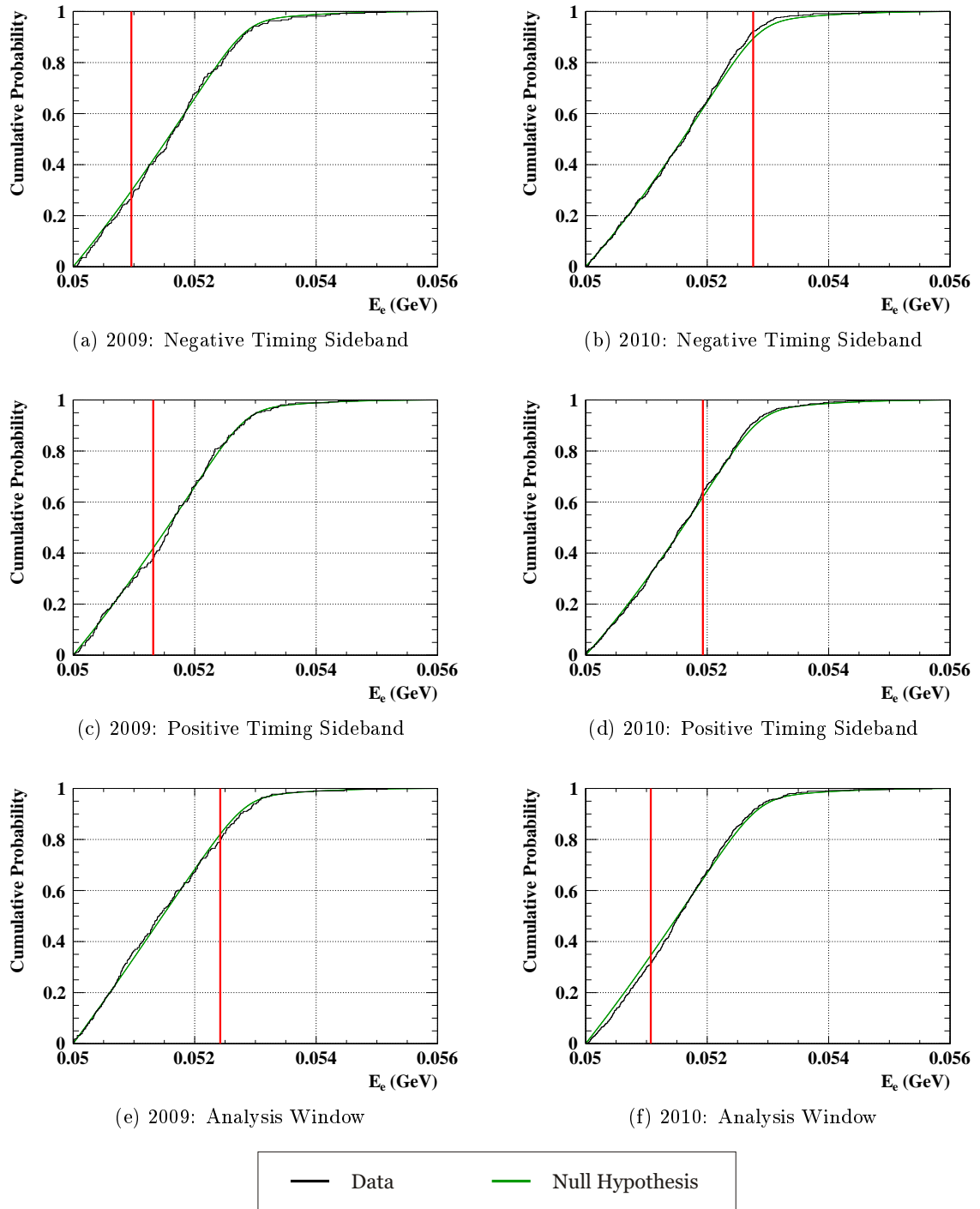


Figure A.6: Cumulative distribution functions of the measured positron energies E_e and the corresponding null hypotheses within the negative and positive timing sidebands and within the analysis window separately plotted for the 2009 and the 2010 data set. These plots are used for the Kolmogorov-Smirnov test. The position of the largest deviation between data and null hypothesis is highlighted with a vertical line.

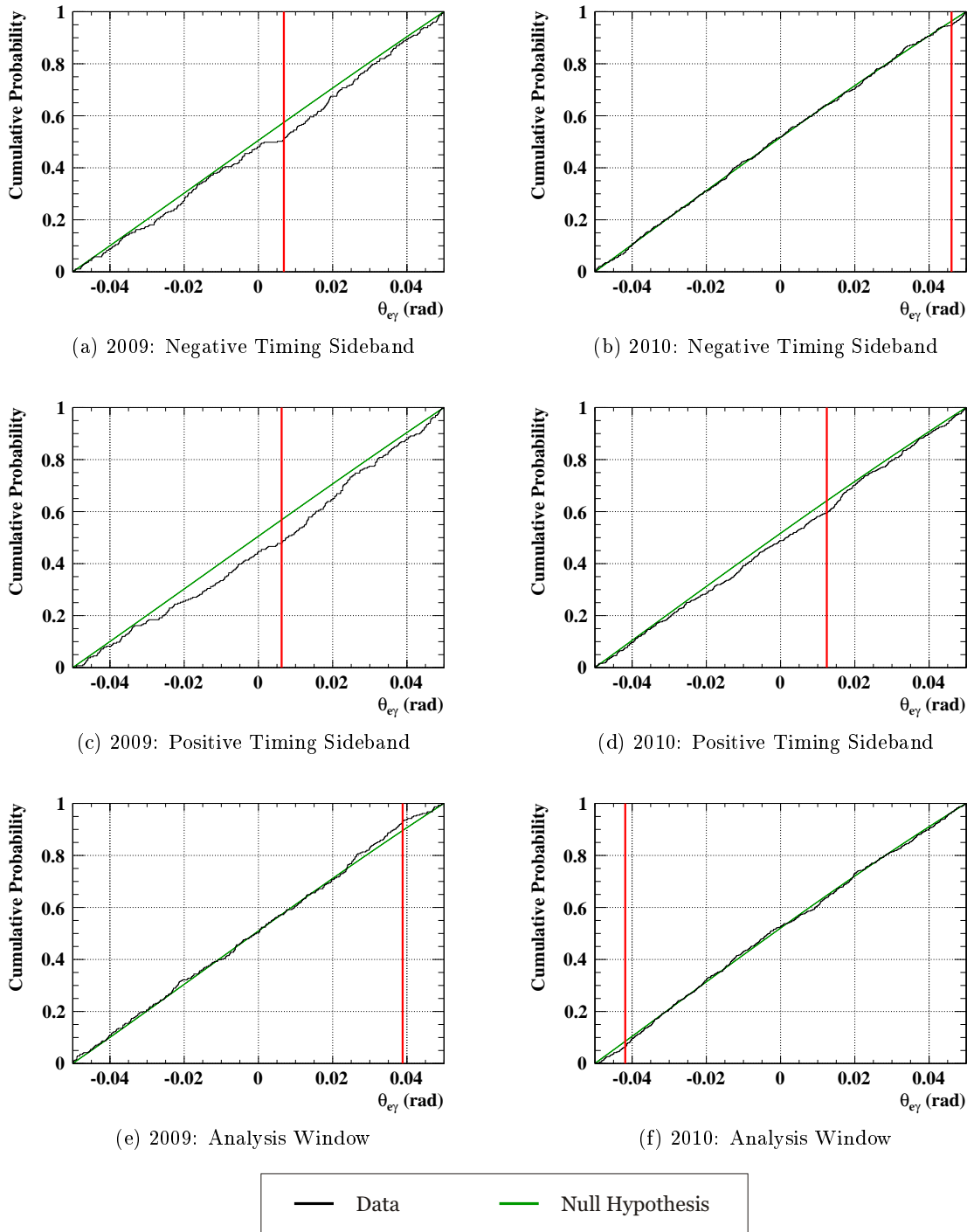
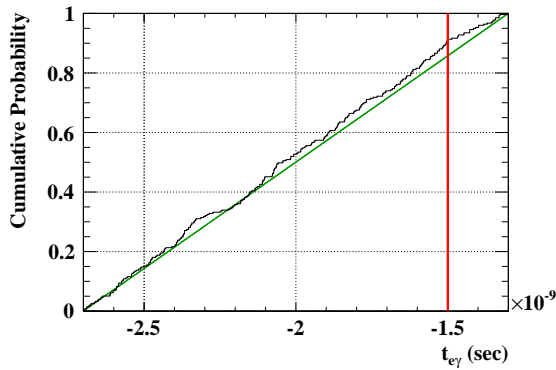
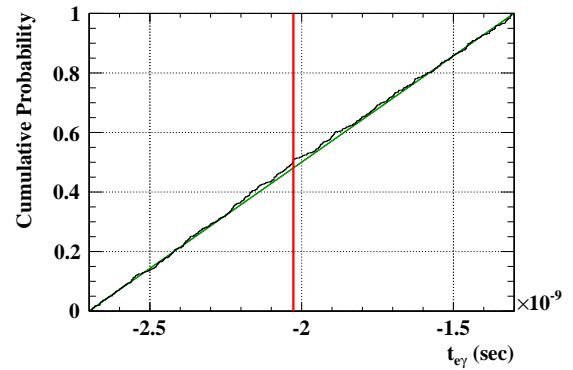


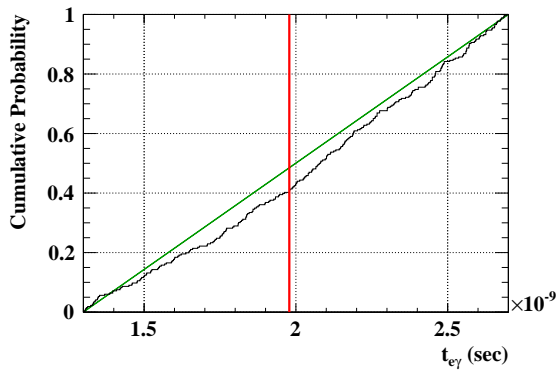
Figure A.7: Cumulative distribution functions of the measured polar angles $\theta_{e\gamma}$ and the corresponding null hypotheses within the negative and positive timing sidebands and within the analysis window separately plotted for the 2009 and the 2010 data set. These plots are used for the Kolmogorov-Smirnov test. The position of the largest deviation between data and null hypothesis is highlighted with a vertical line.



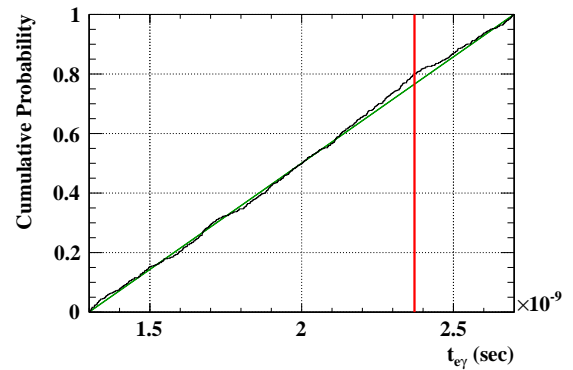
(a) 2009: Negative Timing Sideband



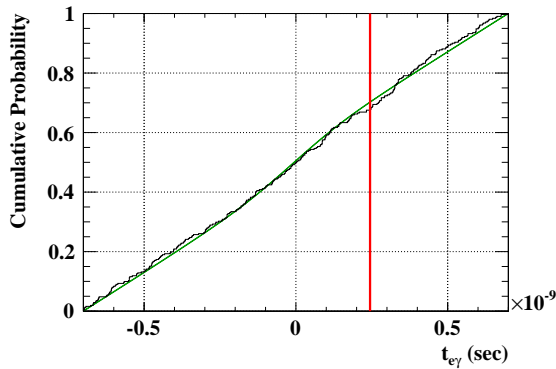
(b) 2010: Negative Timing Sideband



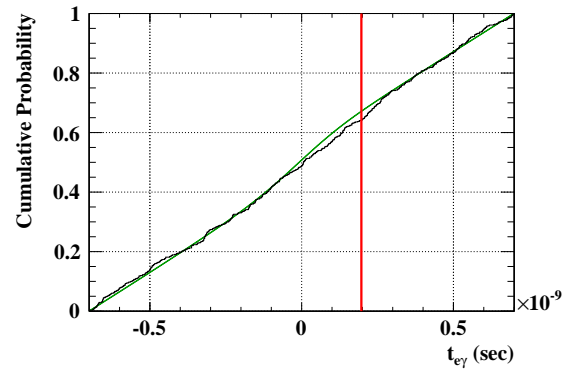
(c) 2009: Positive Timing Sideband



(d) 2010: Positive Timing Sideband



(e) 2009: Analysis Window



(f) 2010: Analysis Window



Figure A.8: Cumulative distribution functions of the measured timing $t_{e\gamma}$ and the corresponding null hypotheses within the negative and positive timing sidebands and within the analysis window separately plotted for the 2009 and the 2010 data set. These plots are used for the Kolmogorov-Smirnov test. The position of the largest deviation between data and null hypothesis is highlighted with a vertical line.

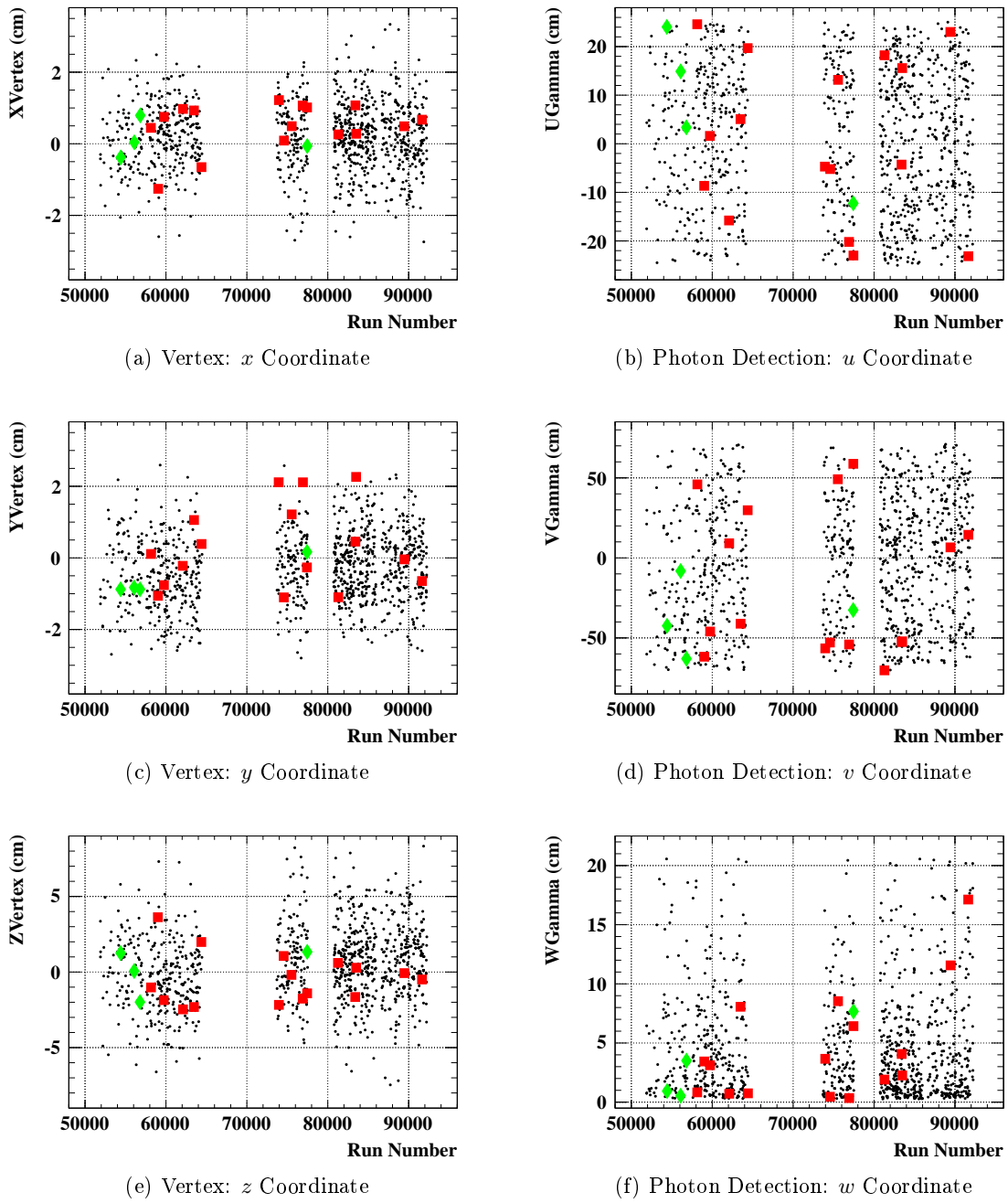
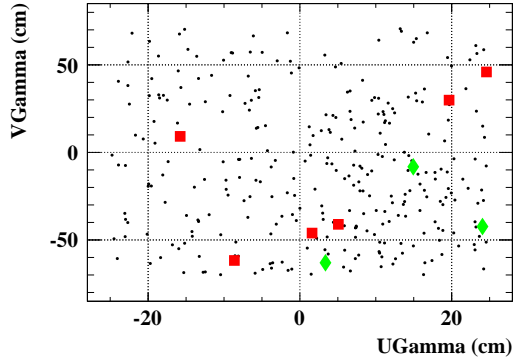
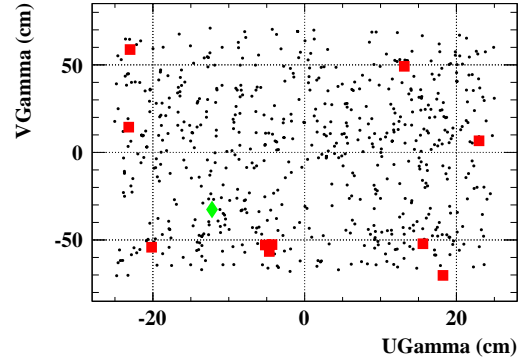


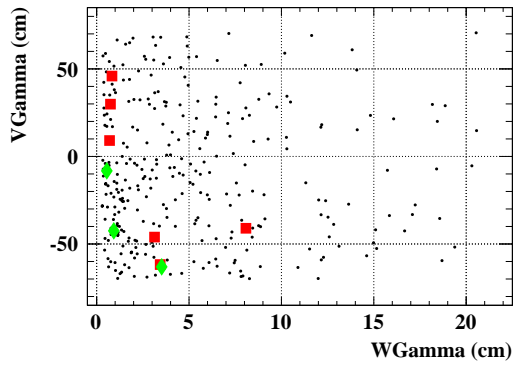
Figure A.9: Event distributions of all events within the analysis window collected in 2009 and 2010. The plots show the coordinates of the reconstructed muon decay vertex (x , y , z) and the coordinates of the photon detection point (u , v , w) as a function of the run number. Events with a run number less than 70'000 were recorded in 2009 while all other events were collected in 2010. The four most high ranked events are identified with diamonds and the other high ranked events presented in Table 7.4 are highlighted with squares.



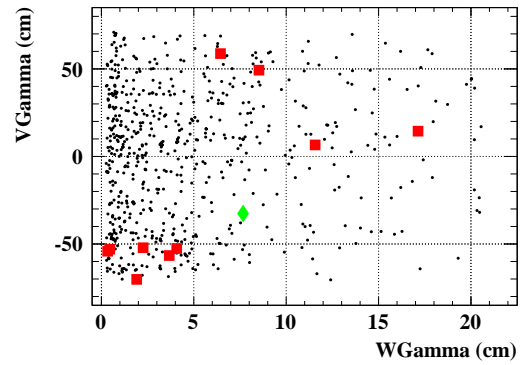
(a) 2009: vu Coordinates Photon Detection



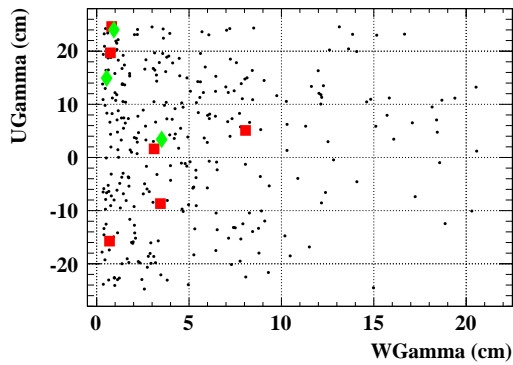
(b) 2010: vu Coordinates Photon Detection



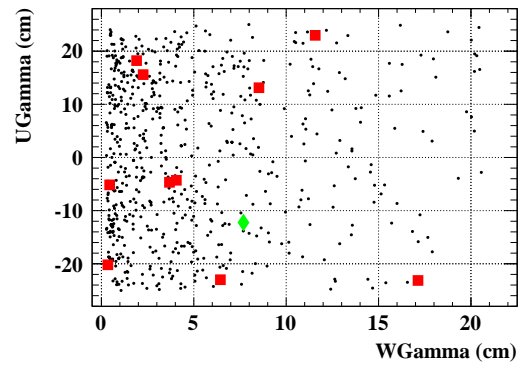
(c) 2009: vw Coordinates Photon Detection



(d) 2010: vw Coordinates Photon Detection



(e) 2009: uw Coordinates Photon Detection



(f) 2010: uw Coordinates Photon Detection

Figure A.10: Event distributions of the photon detection coordinates (u, v, w) separately plotted for the 2009 and 2010 data set. The events are plotted in always two spatial coordinates. The four most high ranked events are identified with diamonds and the other high ranked events presented in Table 7.4 are highlighted with squares.

List of Figures

| | | |
|------|----------------------------------------------------------------------------------------------------------------------------|----|
| 1.1 | Feynman Diagrams for $\mu^+ \rightarrow e^+ + \gamma$ in the Standard Model with Neutrino Oscillations | 5 |
| 1.2 | Feynman Diagrams for $\mu^+ \rightarrow e^+ + \gamma$ in SU(5) SUSY GUT | 6 |
| 1.3 | Calculated Branching Ratio of $\mu^+ \rightarrow e^+ + \gamma$ in SO(10) SUSY GUT | 7 |
| 1.4 | Upper Limits of the Branching Ratio $\mathcal{B}(\mu^+ \rightarrow e^+ + \gamma)$ obtained with past Experiments | 8 |
| 2.1 | Schema of the MEG Detector | 16 |
| 2.2 | Schema of the MEG Beam Transport System | 17 |
| 2.3 | Picture of the MEG Target | 17 |
| 2.4 | Picture and Schema of the COBRA Magnet | 18 |
| 2.5 | Illustrations of the COBRA Magnet Advantages | 19 |
| 2.6 | Picture and Geometrical Details of the MEG Drift Chambers | 20 |
| 2.7 | Picture of one MEG Timing Counter | 22 |
| 2.8 | Geometrical Details of the MEG Liquid Xenon Detector Faces | 23 |
| 2.9 | Pictures of the MEG Liquid Xenon Detector | 23 |
| 2.10 | Simplified Schema of the DRS Chip | 25 |
| 2.11 | Structure of the MEG Software | 26 |
| 2.12 | LEDs and Alpha Sources in the Liquid Xenon Detector | 28 |
| 2.13 | CEX Calibration Principle and Setup | 29 |
| 3.1 | Schema of the Pressure Control System | 36 |
| 3.2 | Picture of the “Aquarium” | 37 |
| 3.3 | Pressure Difference Stability | 38 |
| 3.4 | High Voltage Stability | 39 |

| | | |
|-----|----------------------------------------------------------------------------------------------------|----|
| 3.5 | Illustration of the Trip Recovery and Step-By-Step Ramping | 40 |
| 3.6 | Measured Voltage and Current during Trip and Spike | 41 |
| 3.7 | Pictures of Support Structure Pins and Drift Chamber Crosshairs | 42 |
| 3.8 | Picture and Schema of Corner Cube Reflectors | 43 |
| 3.9 | Measured Drift Chamber Lengths with Original and New Optical Survey Method | 44 |
| | | |
| 4.1 | Timing Calibration of a DRS4 Chip | 48 |
| 4.2 | DRS4 Timing Resolution Measuring Principle | 49 |
| 4.3 | Recorded Signals and Reference Clock for DRS4 Timing Resolution Measure- ments | 49 |
| 4.4 | Measured Time Differences with and without DRS4 Timing Calibration . . . | 51 |
| 4.5 | Results of the DRS4 Timing Resolution Measurements | 52 |
| 4.6 | Measured Clock Periods and their Fourier Transforms | 53 |
| 4.7 | Influence of Swapped Clock Cables | 56 |
| | | |
| 5.1 | Schema of the Neutron Generator Monitoring Setup and Picture of the Neutron Generator | 60 |
| 5.2 | Neutron Generator Energy Spectra with and without Muon Beam | 61 |
| 5.3 | Background Template Subtraction from Neutron Generator Energy Spectrum | 62 |
| 5.4 | Neutron Generator Energy Measurement with Different PMT Gains | 63 |
| 5.5 | Neutron Generator Monitoring Performance in 2010 | 64 |
| 5.6 | Performance of the Dead Channel Recovery Algorithm | 65 |
| | | |
| 6.1 | Visualization of the Blind Box, the Analysis Window, and the Sidebands . . . | 72 |
| 6.2 | Averaged PDFs for the Combined Data Set | 76 |
| 6.3 | Example of a Confidence Level Curve | 80 |
| 6.4 | Upper Limit Distributions from Background-Only toyMC Experiments | 82 |
| 6.5 | Maximum Likelihood Fit Result of the 2009 Data Set | 86 |
| 6.6 | Maximum Likelihood Fit Result of the 2010 Data Set | 87 |
| 6.7 | Maximum Likelihood Fit Result of the Combined Data Set | 88 |
| 6.8 | Confidence Level Curves of the 2009, 2010, and Combined Data Sets | 90 |
| | | |
| 7.1 | χ^2 Test of the Azimuthal Angle $\phi_{e\gamma}$ | 98 |
| 7.2 | Kolmogorov-Smirnov Test of the Azimuthal Angle $\phi_{e\gamma}$ | 99 |

| | | |
|------|-------------------------------------------------------------------------------------------|-----|
| 7.3 | Event Distributions of the Observables and R_{sig} | 102 |
| 7.4 | Event Distributions of the Muon Decay Vertex | 104 |
| 7.5 | Event Distributions of always two Observables | 105 |
| 8.1 | PDFs of R_{sig} for the Combined Data Set | 109 |
| 8.2 | R_{sig} Event Distribution of the Combined Data Set | 110 |
| 8.3 | R_{sig} Event Distributions and Results of the Official MEG Analysis | 111 |
| 8.4 | χ^2 Test of the Relative Signal Likelihood R_{sig} | 112 |
| 8.5 | Kolmogorov-Smirnov Test of the Relative Signal Likelihood R_{sig} | 113 |
| 8.6 | Background Rejection and Signal Efficiency of the Cut Analysis | 115 |
| 8.7 | Cut Analysis Results | 117 |
| 8.8 | PDFs of R_{sig} for Signal and Background Events | 120 |
| 8.9 | Binning of the R_{sig} Alternative Analysis | 123 |
| 8.10 | Sensitivities of the R_{sig} Alternative Analysis | 125 |
| 8.11 | Effect of Fixing the Fraction between Background Events | 127 |
| 8.12 | Statistical Effects | 129 |
| 8.13 | Maximum Likelihood Fit Result of the R_{sig} Alternative Analysis | 130 |
| 8.14 | Confidence Level Curves obtained from the R_{sig} Alternative Analysis | 131 |
| 8.15 | Prospect Calculations with the R_{sig} Alternative Analysis | 135 |
| A.1 | χ^2 Test of the Photon Energy E_γ | 144 |
| A.2 | χ^2 Test of the Positron Energy E_e | 145 |
| A.3 | χ^2 Test of the Polar Angle $\theta_{e\gamma}$ | 146 |
| A.4 | χ^2 Test of the Timing $t_{e\gamma}$ | 147 |
| A.5 | Kolmogorov-Smirnov Test of the Photon Energy E_γ | 148 |
| A.6 | Kolmogorov-Smirnov Test of the Positron Energy E_e | 149 |
| A.7 | Kolmogorov-Smirnov Test of the Polar Angle $\theta_{e\gamma}$ | 150 |
| A.8 | Kolmogorov-Smirnov Test of the Timing $t_{e\gamma}$ | 151 |
| A.9 | Event Distributions of the Muon Decay Vertex and the Photon Detection Point | 152 |
| A.10 | Event Distributions of the Photon Detection Point | 153 |

List of Tables

| | | |
|-----|------------------------------------------------------------------------------------------------------------------------------------------------------------------|-----|
| 1.1 | Muon Decay Modes | 4 |
| 1.2 | Past $\mu^+ \rightarrow e^+ + \gamma$ Search Experiments and Reached Upper Limits of the Branching Ratio $\mathcal{B}(\mu^+ \rightarrow e^+ + \gamma)$ | 8 |
| 2.1 | Overview of MEG Physics Data Taking Periods | 31 |
| 2.2 | MEG Detector Performance in 2009 and 2010 | 33 |
| 4.1 | Influence of Swapped Clock Cables | 58 |
| 6.1 | Expected Number of RMD and ABG Events within the Analysis Window | 74 |
| 6.2 | Normalization Factors | 81 |
| 6.3 | Sensitivities | 83 |
| 6.4 | Results of the Timing Sideband Analysis | 84 |
| 6.5 | Results of the Maximum Likelihood Fit | 85 |
| 6.6 | Results of the Confidence Level Calculation | 89 |
| 6.7 | Relative Contributions of Systematic Uncertainties | 91 |
| 7.1 | Overview of Performed Goodness of Fit Checks | 94 |
| 7.2 | Results of the Goodness of Fit Checks with Timing Sidebands | 96 |
| 7.3 | Results of the Goodness of Fit Checks with the Analysis Window | 97 |
| 7.4 | Properties of the Most High Ranked Events of 2009 and 2010 | 101 |
| 8.1 | Effects of the R_{sig} Condition | 110 |
| 8.2 | Results of the R_{sig} Goodness of Fit Checks | 114 |
| 8.3 | Results of the Cut Analysis | 117 |
| 8.4 | Results of the Cut Analysis of the Timing Sidebands | 118 |

| | | |
|------|----------------------------------------------------------------------------------------------------|-----|
| 8.5 | Expected Number of Background Events Passing the R_{sig} Condition | 121 |
| 8.6 | Sensitivities of the R_{sig} Alternative Analysis | 126 |
| 8.7 | Results of the R_{sig} Alternative Analysis of the Timing Sidebands | 126 |
| 8.8 | Results of the Maximum Likelihood Fit of the R_{sig} Alternative Analysis | 130 |
| 8.9 | Results of the Confidence Level Calculation of the R_{sig} Alternative Analysis | 132 |
| 8.10 | Comparison of Results | 133 |
| 8.11 | Specifications for Prospect Calculations | 134 |
| 8.12 | Results of the Prospect Calculations | 136 |

Bibliography

- [1] M. L. Brooks et al. (MEGA Collaboration), “New Limit for the Lepton-Family-Number Nonconserving Decay $\mu^+ \rightarrow e^+\gamma$ ”, *Phys. Rev. Lett.* **83** (Aug, 1999) 1521–1524. doi:10.1103/PhysRevLett.83.1521.
- [2] T. Mori et al., “Research Proposal to Paul Scherrer Institut: Search for $\mu^+ \rightarrow e^+\gamma$ down to 10^{-14} branching ratio”, (1999). http://meg.web.psi.ch/docs/prop_psi/proposal.pdf [June 2012].
- [3] PSI Home Page, <http://www.psi.ch> [June 2012].
- [4] MEG Experiment Home Page, <http://meg.web.psi.ch/> [June 2012].
- [5] F. Halzen and A. D. Martin, “Quarks and leptons: an introductory course in modern particle physics”. Wiley, 1984.
- [6] N. Schmitz, “Neutrino-physik”. Teubner Studienbücher: Physik. Teubner, 1997.
- [7] S. P. Martin, “A Supersymmetry Primer”, 2011. <http://arxiv.org/pdf/hep-ph/9709356v6.pdf> [June 2012].
- [8] The CMS Collaboration, “Observation of a new boson with a mass near 125 GeV”, (2012). <http://cdsweb.cern.ch/record/1460438/files/HIG-12-020-pas.pdf> [June 2012].
- [9] K. Nakamura et al. (Particle Data Group), “Review of Particle Physics”, *J. Phys. G* **37** (2010), no. 7A, 075021.
- [10] R. R. Crittenden et al., “Radiative Decay Modes of the Muon”, *Phys. Rev.* **121** (Mar, 1961) 1823–1832. doi:10.1103/PhysRev.121.1823.
- [11] W. Bertl et al. (SINDRUM Collaboration), “Search for the decay $\mu^+ \rightarrow e^+e^+e^-$ ”, *Nuclear Physics B* **260** (1985), no. 1, 1–31. doi:10.1016/0550-3213(85)90308-6.
- [12] Y. Fukuda et al. (Super-Kamiokande Collaboration), “Evidence for Oscillation of Atmospheric Neutrinos”, *Phys. Rev. Lett.* **81** (Aug, 1998) 1562–1567. doi:10.1103/PhysRevLett.81.1562.

- [13] Q. R. Ahmad et al. (SNO Collaboration), “Measurement of the Rate of $\nu_e + d \rightarrow p + p + e^-$ Interactions Produced by 8B Solar Neutrinos at the Sudbury Neutrino Observatory”, *Phys. Rev. Lett.* **87** (Jul, 2001) 071301. doi:10.1103/PhysRevLett.87.071301.
- [14] F. P. An et al., “Observation of Electron-Antineutrino Disappearance at Daya Bay”, *Phys. Rev. Lett.* **108** (Apr, 2012) 171803. doi:10.1103/PhysRevLett.108.171803.
- [15] F. Boehm and P. Vogel, “Physics of Massive Neutrinos”. Cambridge University Press, 1992. <http://dx.doi.org/10.1017/CB09780511622571> [June 2012].
- [16] K. S. Hirata et al., “Experimental limits on nucleon lifetime for lepton+meson decay modes”, *Physics Letters B* **220** (1989), no. 1–2, 308–316. doi:10.1016/0370-2693(89)90058-0.
- [17] J. Hisano et al., “Exact event rates of lepton flavor violating processes in supersymmetric $SU(5)$ model”, *Physics Letters B* **391** (1997), no. 3–4, 341–350. doi:10.1016/S0370-2693(96)01473-6.
- [18] L. Calibbi et al., “Lepton flavor violation from supersymmetric grand unified theories: Where do we stand for MEG, PRISM/PRIME, and a super flavor factory”, *Phys. Rev. D* **74** (Dec, 2006) 116002. doi:10.1103/PhysRevD.74.116002.
- [19] S. H. Neddermeyer and C. D. Anderson, “Note on the Nature of Cosmic-Ray Particles”, *Phys. Rev.* **51** (May, 1937) 884–886. doi:10.1103/PhysRev.51.884.
- [20] E. P. Hincks and B. Pontecorvo, “Search for Gamma-Radiation in the 2.2-Microsecond Meson Decay Process”, *Phys. Rev.* **73** (Feb, 1948) 257–258. doi:10.1103/PhysRev.73.257.
- [21] P. Depommier et al., “New Limit on the Decay $\mu^+ \rightarrow e^+\gamma$ ”, *Phys. Rev. Lett.* **39** (Oct, 1977) 1113–1116. doi:10.1103/PhysRevLett.39.1113.
- [22] A. van der Schaaf et al., “A search for the decay $\mu^+ \rightarrow e^+\gamma$ ”, *Nuclear Physics A* **340** (1980), no. 2, 249–270. doi:10.1016/0375-9474(80)90274-2.
- [23] W. W. Kinnison et al., “Search for $\mu^+ \rightarrow e^+\gamma$ ”, *Phys. Rev. D* **25** (Jun, 1982) 2846–2868. doi:10.1103/PhysRevD.25.2846.
- [24] R. D. Bolton et al., “Search for the Decay $\mu^+ \rightarrow e^+\gamma$ ”, *Phys. Rev. Lett.* **56** (Jun, 1986) 2461–2464. doi:10.1103/PhysRevLett.56.2461.
- [25] Y. Uchiyama, “Analysis of the First MEG Physics Data to Search for the Decay $\mu^+ \rightarrow e^+\gamma$ ”. PhD thesis, University of Tokyo, 2009. http://meg.web.psi.ch/docs/theses/uchiyama_phd.pdf [June 2012].
- [26] nEDM Home Page, <http://nedm.web.psi.ch/> [June 2012].
- [27] UCN Home Page, <http://ucn.web.psi.ch/> [June 2012].

- [28] W. J. Marciano et al., “Charged Lepton Flavor Violation Experiments”, *Ann. Rev. Nucl. Part. Sci.* **58** (2008), no. 1, 315–341. doi:10.1146/annurev.nucl.58.110707.171126.
- [29] J. L. Hewett et al., “Fundamental Physics at the Intensity Frontier”, (2012). <http://arxiv.org/abs/1205.2671> [June 2012].
- [30] A. Blondel et al., “Letter of Intent for an Experiment to Search for the Decay $\mu \rightarrow eee$ ”, (2012). http://www.physi.uni-heidelberg.de/Forschung/he/mu3e/documents/LOI_Mu3e_PSI.pdf [June 2012].
- [31] U. Bellgardt et al. (SINDRUM Collaboration), “Search for the decay $\mu^+ \rightarrow e^+e^+e^-$ ”, *Nuclear Physics B* **299** (1988), no. 1, 1–6. doi:10.1016/0550-3213(88)90462-2.
- [32] R. M. Carey et al. (Mu2e Collaboration), “Letter of Intent: A Muon to Electron Conversion Experiment at Fermilab”, (2007). <http://inspirehep.net/record/774138/files/fermilab-tm-2396.PDF> [June 2012].
- [33] Fermilab Home Page, <http://www.fnal.gov/> [June 2012].
- [34] D. Bryman et al. (COMET Collaboration), “An Experimental Proposal on Nuclear and Particle Physics Experiments at the J-PARC 50 GeV Proton Synchrotron: An Experimental Search for Lepton Flavor Violating $\mu^- \rightarrow e^-$ Conversion at Sensitivity of 10^{-16} with a Slow-Extracted Bunched Proton Beam”, (2007). http://j-parc.jp/researcher/Hadron/en/pac_0801/pdf/Kuno.pdf [June 2012].
- [35] J-PARC Home Page, <http://j-parc.jp/index-e.html> [June 2012].
- [36] M. Aoki et al. (PRISM/PRIME Group), “A Letter of Intent on Nuclear and Particle Physics Experiments at the J-PARC 50 GeV Proton Synchrotron: An Experimental Search for A $\mu^- \rightarrow e^-$ Conversion at Sensitivity of the Order of 10^{-18} with a Highly Intense Muon Source: PRISM”, (2006). http://j-parc.jp/researcher/Hadron/en/pac_0606/pdf/p20-Kuno.pdf [June 2012].
- [37] W. Bertl et al. (SINDRUM II Collaboration), “A search for $\mu \rightarrow e$ conversion in muonic gold”, *The European Physical Journal C - Particles and Fields* **47** (2006) 337–346. doi:10.1140/epjc/s2006-02582-x.
- [38] PSI π E5 Beam Line Home Page, http://aea.web.psi.ch/beam2lines/beam_pie5.html [June 2012].
- [39] H. Nishiguchi, “The MEG positron spectrometer”, *Nucl. Instrum. Methods Phys. Res. A* **581** (2007), no. 1–2, 538–541. doi:10.1016/j.nima.2007.08.044.
- [40] W. Ootani et al., “Development of a Thin-Wall Superconducting Magnet for the Positron Spectrometer in the MEG Experiment”, *IEEE Transactions on Applied Superconductivity* **14** (june, 2004) 568–571. doi:10.1109/TASC.2004.829721.

- [41] M. Hildebrandt, “The drift chamber system of the MEG experiment”, *Nucl. Instrum. Methods Phys. Res. A* **623** (2010), no. 1, 111–113. doi:10.1016/j.nima.2010.02.165.
- [42] D. F. Anderson et al., “A simple “vernier” method for improving the accuracy of coordinate read-out in large wire chambers”, *Nucl. Instrum. Methods Phys. Res.* **224** (1984), no. 1–2, 315–317. doi:10.1016/0167-5087(84)90482-4.
- [43] J. Allison et al., “The diamond shaped cathode pads of the OPAL muon barrel drift chambers”, *Nucl. Instrum. Methods Phys. Res. A* **310** (1991), no. 1–2, 527–534. doi:10.1016/0168-9002(91)91094-C.
- [44] H. Nishiguchi, “An Innovative Positron Spectrometer to Search for the Lepton Flavour Violating Muon Decay with a Sensitivity of 10^{-13} ”. PhD thesis, University of Tokyo, 2008. http://meg.web.psi.ch/docs/theses/nishiguchi_phd.pdf [June 2012].
- [45] B. A. Golden, “In Pursuit of the Rare Decay $\mu^+ \rightarrow e^+\gamma$: A Window to the UV Completion of the Standard Model”. PhD thesis, University of California, Irvine, 2012. <http://meg.web.psi.ch/docs/theses/BenThesis.pdf> [June 2012].
- [46] R. Valle, “Development of the Timing Counter for the MEG experiment”. PhD thesis, University of Genova, 2006. http://meg.web.psi.ch/docs/theses/valle_phd.pdf [June 2012].
- [47] S. Dussoni et al., “The Timing Counter of the MEG experiment: Design and commissioning”, *Nucl. Instrum. Methods Phys. Res. A* **617** (2010), no. 1–3, 387–390. doi:10.1016/j.nima.2009.08.089.
- [48] M. De Gerone et al., “The MEG timing counter calibration and performance”, *Nucl. Instrum. Methods Phys. Res. A* **638** (2011), no. 1, 41–46. doi:10.1016/j.nima.2011.02.044.
- [49] S. Mihara, “MEG liquid xenon detector”, *Journal of Physics: Conference Series* **308** (2011), no. 1, 012009. doi:10.1088/1742-6596/308/1/012009.
- [50] R. Sawada, “A Liquid Xenon Scintillation Detector to Search for the Lepton Flavor Violating Muon Decay with a Sensitivity of 10^{-13} ”. PhD thesis, University of Tokyo, 2008. http://meg.web.psi.ch/docs/theses/sawada_phd.pdf [June 2012].
- [51] T. Haruyama et al., “Development of a High-Power Coaxial Pulse Tube Refrigerator for a Liquid Xenon Calorimeter”, *AIP Conf. Proc.* **710** (2004) 1459–1466. doi:10.1063/1.1774839.
- [52] T. Iwamoto et al., “Development of a large volume zero boil-off liquid xenon storage system for muon rare decay experiment (MEG)”, *Cryogenics* **49** (2009), no. 6, 254–258. doi:10.1016/j.cryogenics.2008.09.003.
- [53] S. Mihara et al., “Development of a liquid-xenon photon detector—towards the search for a muon rare decay mode at Paul Scherrer Institute”, *Cryogenics* **44** (2004), no. 4, 223–228. doi:10.1016/j.cryogenics.2003.12.002.

- [54] S. Mihara et al., “Development of a method for liquid xenon purification using a cryogenic centrifugal pump”, *Cryogenics* **46** (2006), no. 9, 688–693.
doi:10.1016/j.cryogenics.2006.04.003.
- [55] MIDAS Home Page, <http://midas.psi.ch> [June 2012].
- [56] TRIUMF Home Page, <http://www.triumf.ca> [June 2012].
- [57] L. Galli, “A real time glance at the Lepton Flavor Violating decay $\mu \rightarrow e\gamma$ in the MEG experiment”. PhD thesis, University of Pisa, 2010.
<http://meg.web.psi.ch/docs/theses/GalliThesis.pdf> [June 2012].
- [58] DRS Chip Home Page, <http://drs.web.psi.ch> [June 2012].
- [59] R. Pegna et al., “A GHz sampling DAQ system for the MAGIC-II telescope”, *Nucl. Instrum. Methods Phys. Res. A* **572** (2007), no. 1, 382–384.
doi:10.1016/j.nima.2006.10.375.
- [60] S. Ritt et al., “Application of the DRS chip for fast waveform digitizing”, *Nucl. Instrum. Methods Phys. Res. A* **623** (2010), no. 1, 486–488.
doi:10.1016/j.nima.2010.03.045.
- [61] S. Ritt, private communication.
- [62] MSCB Home Page, <http://midas.psi.ch/mscb> [June 2012].
- [63] National Instruments Home Page, <http://www.ni.com> [June 2012].
- [64] GEANT Home Page, <http://wwwasd.web.cern.ch/wwwasd/geant> [June 2012].
- [65] ROOT Home Page, <http://root.cern.ch> [June 2012].
- [66] P. W. Cattaneo et al., “The architecture of MEG simulation and analysis software”, *The European Physical Journal Plus* **126** (2011) 1–12.
doi:10.1140/epjp/i2011-11060-6.
- [67] A. Papa, “Search for the lepton flavour violation in $\mu^+ \rightarrow e^+\gamma$. The calibration methods for the MEG experiment”. PhD thesis, University of Pisa, 2009.
<http://meg.web.psi.ch/docs/theses/Angela.pdf> [June 2012].
- [68] A. Baldini et al., “A radioactive point-source lattice for calibrating and monitoring the liquid xenon calorimeter of the MEG experiment”, *Nucl. Instrum. Methods Phys. Res. A* **565** (2006), no. 2, 589–598. doi:10.1016/j.nima.2006.06.055.
- [69] J. Adam et al. (MEG Collaboration), “Calibration and monitoring of the MEG experiment by a proton beam from a Cockcroft-Walton accelerator”, *Nucl. Instrum. Methods Phys. Res. A* **641** (2011), no. 1, 19–32. doi:10.1016/j.nima.2011.03.048.
- [70] Year Plans of the PSI Beams Home Page,
<http://abe.web.psi.ch/schedule/yearplan.php> [June 2012].

- [71] J. Adam et al. (MEG Collaboration), “A limit for the $\mu \rightarrow e\gamma$ decay from the MEG experiment”, *Nuclear Physics B* **834** (2010), no. 1–2, 1–12.
doi:10.1016/j.nuclphysb.2010.03.030.
- [72] M. Schneebeli, “The drift chambers of the MEG experiment and measurement of the ρ -parameter in the Michel spectrum of the muon decay”. PhD thesis, ETH Zurich, 2008. <http://meg.web.psi.ch/docs/theses/matthias.pdf> [June 2012].
- [73] F. Xiao, “Measurement of the Radiative Muon Decay Branching Fraction in the MEG Experiment”. PhD thesis, University of California, Irvine, 2010.
<http://meg.web.psi.ch/docs/theses/FengThesis.pdf> [June 2012].
- [74] G. F. Franklin et al., “Feedback Control of Dynamic Systems”. Addison-Wesley, 1994.
- [75] J. Adam, “Geometrical Alignment of the Drift Chamber System and Target of the MEG Experiment”, Master’s thesis, ETH Zurich and Paul Scherrer Institute, 2008.
http://meg.web.psi.ch/docs/theses/Diploma_Thesis_Jeanine_Adam_2008.pdf [June 2012].
- [76] DRS4 Evaluation Board Home Page, <http://drs.web.psi.ch/evaluation/> [June 2012].
- [77] D. W. Marquardt, “An Algorithm for Least-Squares Estimation of Nonlinear Parameters”, *Journal of the Society for Industrial and Applied Mathematics* **11** (1963), no. 2, 431–441.
- [78] S. Ritt, “Plans for the DRS5 Switched Capacitor Array”, in *Workshop on Microelectronics beyond the GigaHertz*. 2011.
http://clrwww.in2p3.fr/www2008/giga/doc/S_Ritt.pdf [June 2012].
- [79] A. Papa, private communication.
- [80] Y. Nishimura, “A Search for the Decay $\mu^+ \rightarrow e^+\gamma$ Using a High-Resolution Liquid Xenon Gamma-Ray Detector”. PhD thesis, University of Tokyo, 2010.
http://meg.web.psi.ch/docs/theses/nishimura_phd.pdf [June 2012].
- [81] J. Adam et al. (MEG Collaboration), “New Limit on the Lepton-Flavor-Violating Decay $\mu^+ \rightarrow e^+\gamma$ ”, *Phys. Rev. Lett.* **107** (Oct, 2011) 171801.
doi:10.1103/PhysRevLett.107.171801.
- [82] J. R. Klein and A. Roodman, “Blind Analysis in Nuclear and Particle Physics”, *Ann. Rev. Nucl. Part. Sci.* **55** (2005) 141–163.
doi:10.1146/annurev.nucl.55.090704.151521.
- [83] S. Adrián-Martínez et al., “Search for relativistic magnetic monopoles with the ANTARES neutrino telescope”, *Astroparticle Physics* **35** (2012), no. 10, 634–640.
doi:10.1016/j.astropartphys.2012.02.007.

- [84] V. A. Andreev et al. (MuCap Collaboration), “Measurement of the Muon Capture Rate in Hydrogen Gas and Determination of the Proton’s Pseudoscalar Coupling g_P ”, *Phys. Rev. Lett.* **99** (Jul, 2007) 032002. doi:10.1103/PhysRevLett.99.032002.
- [85] D. M. Webber et al. (MuLan Collaboration), “Measurement of the Positive Muon Lifetime and Determination of the Fermi Constant to Part-per-Million Precision”, *Phys. Rev. Lett.* **106** (Jan, 2011) 041803. doi:10.1103/PhysRevLett.106.041803.
- [86] K. Arisaka et al. (E791 Collaboration), “Improved Upper Limit on the Branching Ratio $B(K_L^0 \rightarrow \mu^\pm e^\mp)$ ”, *Phys. Rev. Lett.* **70** (Feb, 1993) 1049–1052. doi:10.1103/PhysRevLett.70.1049.
- [87] V. M. Abazov et al. (D0 Collaboration), “Search for the Flavor-Changing Neutral Current Decay $B_s^0 \rightarrow \mu^+ \mu^-$ in $p\bar{p}$ Collisions at $\sqrt{s} = 1.96$ TeV with the D0 Detector”, *Phys. Rev. Lett.* **94** (Feb, 2005) 071802. doi:10.1103/PhysRevLett.94.071802.
- [88] R. Aaij et al. (LHCb Collaboration), “Search for the rare decays $B_s^0 \rightarrow \mu^+ \mu^-$ and $B^0 \rightarrow \mu^+ \mu^-$ ”, *Physics Letters B* **699** (2011), no. 5, 330–340. doi:10.1016/j.physletb.2011.04.031.
- [89] MINUIT Home Page,
<http://lcgapp.cern.ch/project/cls/work-packages/mathlibs/minuit/home.html>
[June 2012].
- [90] Y. Kuno and Y. Okada, “Muon decay and physics beyond the standard model”, *Rev. Mod. Phys.* **73** (Jan, 2001) 151–202. doi:10.1103/RevModPhys.73.151.
- [91] G. J. Feldman and R. D. Cousins, “Unified approach to the classical statistical analysis of small signals”, *Phys. Rev. D* **57** (Apr, 1998) 3873–3889. doi:10.1103/PhysRevD.57.3873.
- [92] F. James and M. Winkler, “MINUIT User’s Guide”. CERN, 2004.
<http://seal.web.cern.ch/seal/documents/minuit/mnusersguide.pdf> [June 2012].
- [93] F. James and M. Roos, “Minuit - a system for function minimization and analysis of the parameter errors and correlations”, *Computer Physics Communications* **10** (1975), no. 6, 343–367. doi:10.1016/0010-4655(75)90039-9.
- [94] G. Cowan, “Statistical Data Analysis”. Oxford Science Publications. Clarendon Press, 1998.
- [95] W. H. Press et al., “Numerical Recipes in C: The Art of Scientific Computing”. Cambridge University Press, 2 edition, 1992. <http://apps.nrbook.com/c/index.html>
[June 2012].
- [96] V. Blobel and E. Lohrmann, “Statistische und numerische Methoden der Datenanalyse”. Teubner Studienbücher: Physik. Teubner, 1998.

- [97] G. Punzi, “Sensitivity of searches for new signals and its optimization”, in *Proceedings of the International Conference on Statistical Problems in Particle Physics, Astrophysics, and Cosmology (PHYSTAT2003), SLAC Stanford, California*. 2003. arXiv:physics/0308063.

Acknowledgements

First of all, I would like to thank Prof. Dr. Günther Dissertori for agreeing to supervise me during this thesis even though his research group was not involved in the MEG experiment. I would also like to thank Prof. Dr. Klaus Kirch and Prof. Dr. André Schöning for co-examining this thesis.

I am heartily thankful for the support and advise of Dr. Stefan Ritt and Dr. Malte Hildebrandt who already supervised me during my diploma thesis and encouraged me to do this thesis. They taught me a lot about the DRS chip and the MEG drift chambers and helped me whenever necessary during my thesis. A special thank goes to Dr. Peter-Raymond Kettle and Dr. Angela Papa from whom I learned much about the MEG beamline and the different calibration methods.

I am also very grateful for the help and guidance of the Japanese MEG crew, especially Prof. Dr. Toshinori Mori, Prof. Dr. Satoshi Mihara, Prof. Dr. Wataru Ootani, Prof. Dr. Toshiyuki Iwamoto, Dr. Hajime Nishiguchi, Dr. Ryu Sawada, and Dr. Yusuke Uchiyama. They taught me everything about the MEG analysis principles and supervised me during my own analysis. I am thankful for all the fruitful discussions about physics, but also the interesting conversations about the differences between the Japanese and Swiss culture.

I enjoyed being part of the MEG experiment and I would like to thank all members of the MEG collaboration and the Institute for Particle Physics at ETH who contributed to this thesis directly or indirectly.

I would like to sincerely thank my family and my friends for their patient support and help during the last years. I am incredible sad that my mother did not live long enough to see this thesis being finished.

Finally, I am deeply thankful to my love Lars who has been encouraging and supporting me since more than a decade in so many ways. Thank you so much!

Curriculum Vitae

Personal Data

Name: Jeanine Adam
Date of Birth: 23 March 1985
Nationality: Swiss

Education

09/2008 – 08/2012 PhD in Particle Physics, ETH Zurich, Switzerland
Advisor: Prof. Dr. Günther Dissertori
Thesis Topic: “New Analysis Method to Confirm the Upper Limit of the Branching Ratio $\mathcal{B}(\mu^+ \rightarrow e^+ + \gamma)$ from the MEG Experiment”

10/2003 – 08/2008 Master of Science, ETH Zurich, Switzerland
Graduation with Distinction
Major: Particle Physics
Thesis Topic: “Geometrical Alignment of the Drift Chamber System and Target of the MEG Experiment”

08/1999 – 08/2003 Eidgenössische Matura, Kantonsschule Solothurn, Switzerland
Major: Physics and Applied Mathematics
Award: Bernhard-Baertschi-Award

Professional Experience

09/2008 – 08/2012 Research and Teaching Assistant at the Institute for Particle Physics, ETH Zurich, Switzerland